Molecular Simulation Studies of Metal Organic Frameworks Focusing on Hydrogen Purification

Ana-Maria Banu

PhD

The University of Edinburgh

Institute for Materials and Processes

2014

Declaration

I hereby declare that this thesis is a presentation of my own original work, carried out in the School of Engineering, at the University of Edinburgh, except where explicitly acknowledged in the text. This thesis has been composed by myself, and has not been submitted for any other degree or professional qualification.

Date: August 27th, 2013 ………………………………

Ana-Maria Banu

Abstract

The process of purifying hydrogen gas using pressure swing adsorption columns heavily relies on highly efficient adsorbents. Such materials must be able to selectively adsorb a large amount of impurities, and must also be regenerated with ease. The work presented in this thesis focuses on a novel class of porous solids, metal-organic frameworks (MOFs), and their potential for use as adsorbents in hydrogen purification processes. MOFs are tuneable structures, a property that can be exploited in order to achieve the desired characteristics that are beneficial for a specific application. The design or selection of MOFs for any separation process however, relies on a thorough understanding of the relationship between a framework's characteristics and its adsorption and selective properties.

In order to identify favourable MOF characteristics for the separation of hydrogen from typical impurities a systematic molecular simulation study is performed on a large group of MOFs. Features such as the presence of short linkers, amine groups and additional aromatic rings, and a high density of linker groups are found to increase the adsorbate - framework interaction strength, and reduce the free volume available inside the pores. Both of these effects are shown to enhance MOF selectivity for impurities. Two promising materials, exhibiting desirable features, Mn MIL-53 and MIL-47, are studied further through a variety of approaches.

A combination of experimental work and molecular simulations are employed in order to assess the level of flexibility in Mn MIL-53 on uptake of CO_2 and CH_4. An investigation of the experimental and simulation adsorption and characterization data indicates that the framework undergoes structural changes, in order to accommodate CO_2 molecules, but not CH_4. The form of the framework during CO_2 uptake is also shown to be strongly influenced by temperature.

In the case of MIL-47, adsorption isotherms simulated for a wide range of gases overpredict experimental adsorption data, leading to an in-depth investigation of

non-porous effects, force field suitability, and framework rigidity. *Ab initio* molecular dynamics studies of MIL-47 indicate that the benzene dicarboxylate linkers rotate about their symmetry axis to reach more energetically favourable configurations, an effect responsible for the discrepancies between simulated and experimental isotherms.

The effect of MOF flexibility on adsorption is further highlighted in a study of Sc_2BDC_3, a material able to undergo structural changes in order to accommodate a variety of adsorbates. Molecular simulations show that structural changes in the framework are responsible for the creation of additional CO_2 adsorption sites as pressure is increased, whereas methanol adsorption sites occupied at extreme pressure are stabilized by the formation of hydrogen bonds.

Finally, the exceptionally robust UiO-66(Zr) and UiO-67(Zr) families of MOFs are analysed using a multi-scale simulation study combining molecular level and process-scale computational work, seeking to compare the materials to commercial adsorbents, and assess whether they are suitable for H_2 purification through pressure swing adsorption (PSA). Of the four MOFs studied, UiO-66(Zr)-Br is the most promising, as it significantly outperforms commercial zeolites and activated carbons in H_2 purification from steam methane reformer offgas.

Acknowledgements

First, I would like to thank my supervisor Tina Düren for her constant support and guidance over the last four years. I am deeply grateful to her for opening my eyes to the world of research, and for patiently helping me find my own way forward. This thesis would not have been possible without her invaluable advice, and encouragement.

I would also like to thank David Fairen-Jimenez for the time he spent helping and teaching me, for the interesting discussions we had, and for his support. I am very grateful to our collaborators from The University of St. Andrews, John Mowat and Paul Wright, for their help with synthesis and characterization work. From the Université aix Marseille, I would like to thank Phillip Llewewllyn and Sandrine Bourrelly, for taking the time to show me their labs and train me to use their adsorption equipment. I would also like to thank Stefano Brandani and Daniel Friedrich from the University of Edinburgh, for allowing me to use their CySim model and for their help with the breakthrough curve analysis.

I would like to thank my colleagues in the Institute for Materials and Processes for their support and friendship. I am especially grateful to Zoe Kapetaki, Jovana Radulovic, Peyman Zoroufchian Moghadam, Linjiang Chen, Matthew Lennox, Naomi Cessford, and Jennifer Williams, who made my time in the Sanderson Building, and in Edinburgh very enjoyable.

I am so grateful to my wonderful family, and especially to my parents, Marin and Laura Banu, and my brother, Andrei Banu for inspiring me to be the person I am today. With their constant love and support, I have always felt them close to me despite the distance. I would also like to thank my loving fiancé, Gareth Tomlinson, for being my rock, for believing in me, and for being there for me every step of the way. Meeting him has truly changed my life.

Finally, I would like to thank the University of Edinburgh computing departments, for providing me with access to the CLX, Eddie and Hector clusters, as well as the EPSRC for providing the funding for this project.

Table of Contents

1 Introduction

In recent years environmental concerns have led to an increased demand for clean energy sources. Consequently, a great amount of research has been focused on the production and purification of hydrogen fuel for future applications including automotive fuel cells as well as industrial applications. Hydrogen-rich streams resulting from engineering processes such as steam reformers, refineries, ethylene offgas, and coke oven offgas have been identified as important future fuel sources. In order to obtain the >99.99% H_2 purity required for most applications, these streams must first be recovered and separated from the impurities present, which in the case of steam methane reformer offgas (SMROG) are CO, CO_2, CH_4, N_2, and H_2O.[1] Currently the technology of choice for such purification processes involves four-bed, or polybed pressure swing adsorption (PSA) units,[2] depending on the production quantity.

Porous solids are an essential part of modern gas adsorption and separation processes, including hydrogen purification. While theoretically any microporous material may be used in order to separate the components of a gas stream, the most frequently used adsorbents are activated carbons, zeolites, activated alumina, and silica gels.[2] The choice of adsorbents is dependent on the mixture components to be separated, as well as the type of separation process taking place, such as equilibrium adsorption, kinetic and steric separations. Naturally, the match between an adsorbent and its application is such that the specific adsorptive properties of the material are exploited. For example, activated carbons are well suited for adsorbing non-polar gases and organic vapours from wet streams, due to their large pore surfaces that are either nonpolar or only weakly polar.[2] On the other hand, zeolites have well-defined pore sizes, and the presence of cations, such as Ca^{+2}, Na^{+}, or K^{+} results in a polar pore surface.[2] As a result zeolites are often used either as molecular sieves in steric separations of gases with kinetic diameters that are larger/smaller than the limiting pore diameter, or in competitive adsorption separations involving mixtures of gases with different polarities.[2]

Metal organic frameworks (MOFs) are a new class of porous materials, characterized as having remarkably high surface areas, high pore volumes and medium adsorption strength. Over the last two decades, these materials have attracted a lot of attention with studies focusing on a wide variety of applications[3-5] including gas storage,[6-9] gas separation,[10-12] catalysis,[13-15] sensing,[16,17] and drug delivery.[18,19] One of the most interesting traits of MOFs is that they are assembled in a building block fashion from metal clusters and organic linkers, the choice of which ultimately dictates the framework produced. The large variety of organic and inorganic secondary building units (SBUs) results in seemingly infinite structural possibilities.[3] Interestingly, while most MOFs are fairly rigid structures, certain combinations of SBUs form flexible frameworks, which can exhibit a breathing behaviour or gate-opening effects in response to changes in pressure or temperature, or interactions with guest molecules.[3] The ability to select specific building units in order to create materials with desirable pore shapes, sizes, functionalities, and flexibility, enables the optimization of host-guest interactions, and opens the door towards material design for specific uses, such as gas separations. A great number of MOFs have already been reported, many of which may meet the requirements for certain applications.

The overwhelming diversity of MOF structures, and therefore MOF properties, has resulted in a need for innovative combinations of simulation methods to complement experimental work not only for the thorough characterization of such materials, but also for the comparison and selection of promising MOFs. Classical molecular simulations are particularly advantageous as they can be performed in a short period of time and provide information on the adsorption, separation and diffusion of gases inside a framework. Ab initio methods on the other hand are essential in understanding finer framework characteristics, such as structural changes, which are difficult to observe using experimental set-ups. Finally, a complete understanding of a material’s separation efficiency can be gained using full-scale process modeling, thereby avoiding lengthy experimental procedures.

The work presented here focuses on the adsorption and separation of hydrogen from SMROG in MOFs in order to assess their potential use as adsorbents in hydrogen purification. The main objective is firstly to determine desirable framework characteristics by understanding the relationship between pore shape, size and functionality and a material's adsorption and separation abilities. The findings are then complemented by in depth studies of the most promising MOFs using fitting combinations of experimental methods and molecular simulations, in order to understand the impact of slight structural changes on adsorption sites and therefore adsorption behavior. Additionally, process simulations of full-scale separation columns, are used to compare the separation abilities of a robust family of MOFs to commercial adsorbents.

1.1 Thesis Outline

Chapter 2 provides a description of metal organic frameworks, as well as the classical and ab initio molecular simulation methods that were used in studying these structures. Grand canonical Monte Carlo, molecular dynamics, and ab initio molecular dynamics methods are discussed in detail.

Chapter 3 entails an investigation into how the uptake of SMROG gases correlates with MOF properties such as the accessible surface area, free volume and heat of adsorption. The findings are then used in order to understand the relationship between a MOF's selectivity for impurities and various framework characteristics, namely the length of the organic linkers, the presence of amine groups and additional aromatic rings, as well as a more rarely studied characteristic, the density of the linker groups present in the framework. The ability of an adsorbent performance indicator to validate the findings, and provide a more complete evaluation of an adsorbent's potential is also studied. Promising structures for hydrogen purification applications are identified.

Chapter 4 presents a combined experimental and simulation study of the structure and adsorption behaviour of an Mn^{II} analogue of the MIL-53 framework. Synthesis and activation optimization studies are used to improve product purity, and the effectiveness of solvent evacuation procedures. A combination of experimental characterization of structural form and adsorption capacity, and molecular simulation studies, provides an understanding of the material's ability to adsorb CO_2, and CH_4, at 196 K as well as 303 K. The results present new insight into the structure's flexible nature, and its response to guest-framework interactions.

In Chapter 5, a three-pronged approach is used in order to determine the root cause of disagreement between experimental and simulated adsorption isotherms of various gases and gas mixtures in the MIL-47 framework, which was identified as a promising material for hydrogen purification. The study includes an investigation into non-porous effects, the adsorbate-framework interaction strength described by generic force fields, as well as the flexibility of this rigid MOF. First principles methods facilitate a study of the dynamic nature of the framework, and determine the effect of linker rotation on the internal energy of the structure, whereas classical methods are used to study the effect of structural changes on adsorption.

Chapter 6 provides a detailed look at the adsorption of CO_2 and methanol in the small-pore MOF, Sc_2BDC_3. The influence of variations in temperature and pressure on CO_2 adsorption sites is assessed and correlated to two stages of slight structural changes observed experimentally, and with the help of ab initio molecular dynamics studies. Methanol adsorption sites at high pressure are identified with the help of molecular dynamics simulations, and the stabilizing role of hydrogen bonds is investigated.

In Chapter 7 a thorough evaluation of four MOFs belonging to the UiO-66 and UiO-67 families, concentrating on hydrogen purification from SMROG is presented. This work involves molecular simulation studies of adsorption and separation, as well as molecular dynamics studies of the diffusion of mixture components through each MOF. The results are used as direct input for full-scale process simulation studies, in order to obtain breakthrough curves for five component mixtures through single and two-layered MOF adsorption columns. The four MOFs are compared to commercial zeolites and activated carbons in terms of their impurity retention as well as their ease of regeneration, the latter of which is made possible by desorption simulations.

In Chapter 8, a general summary of the findings is presented, and recommendations for future studies are provided.

1.2 Publications

“A Multiscale Study of MOFs as Adsorbents in H_2 PSA Purification”, Ana-Maria Banu, Daniel Friedrich, Stefano Brandani, and Tina Düren, *Industrial and Engineering Chemistry Research*, 2013, 52 (29), 9946-9957

“Hydrogen thermal desorption spectra: insights from molecular simulation”, Claudia Prosenjak, Ana-Maria Banu, Alistair D. Gellan and Tina Düren, *Dalton Transactions*, 2012, 41, 3974-3984

“Structural Chemistry, Monoclinic-to-Orthorhombic Phase Transition, and CO_2 Adsorption Behavior of the Small Pore Scandium Terephthalate, $Sc_2(O_2C_6H_4CO_2)_3$, and Its Nitro- And Amino-Functionalized Derivatives”, John P. S. Mowat, Stuart R. Miller, John M. Griffin, Valerie R. Seymour, Sharon E. Ashbrook, Stephen P. Thompson, David Fairen-Jimenez, Ana-Maria Banu, Tina Düren, and Paul A. Wright, *Inorganic Chemistry*, 2011, 50 (21), 10844-10858

1.3 Presentations

A.-M. Banu, D. Friedrich, S. Brandani, T. Düren
"*A multi-scale study of MOFs as adsorbents in H_2 PSA purification*", oral presentation
11th International Conference on the Fundamentals of Adsorption, Baltimore 2013

A.-M. Banu, D. Friedrich, S. Brandani, T. Düren
"*A multi-scale study of MOFs as adsorbents in H_2 PSA purification*", oral presentation
3rd International Conference on Metal-Organic Frameworks and Open Framework Compounds, Edinburgh 2012

A.-M. Banu, D. Fairen-Jimenez, N. A Seaton, S. Bourrelly, P. Llewellyn, T. Düren
"*Parameterisation of New Force Fields for Adsorption on Metal-Organic Frameworks*", poster presentation
9th International Symposium on the Characterisation of Porous Solids, Dresden 2011

A.-M. Banu, D. Fairen-Jimenez, T. Düren
"*An Evaluation of Metal-Organic Frameworks as Adsorbents for Hydrogen Purification*", poster presentation
34th Annual British Zeolite Association Conference, Edinburgh 2011

A.-M. Banu, D. Fairen-Jimenez, S. Bourrelly, P. Llewellyn, T. Düren
"*Deviation Between Simulated and Experimental Isotherms in MIL-47: Pore Volume and Force Field Effects*", poster presentation
Gas Separation and Gas Storage Using Porous Materials (workshop), Lausanne 2010

A.-M. Banu, D. Fairen-Jimenez, T. Düren
"*An Evaluation of Metal-Organic Frameworks as Adsorbents for Hydrogen Purification*", oral presentation
Scottish Atomistic Simulation Group Meeting, Glasgow 2010

2 Materials and Simulation Methods

2.1 Metal Organic Frameworks

The studies presented in this thesis focus on porous materials belonging to the metal-organic framework (MOF) class, also known as porous coordination polymers (PCPs) and porous coordination networks (PCNs). These materials combine organic and inorganic groups, connected through strong coordination bonds, to form highly porous crystalline structures.[3,20-22] The discovery of two important structures, IRMOF-1[23] and HKUST-1[24] (Figure 2-1), and the seemingly limitless structural possibilities of MOF synthesis, sparked scientific curiosity leading to the reported synthesis of over 37,000 structures according to the Cambridge Structural Database (CSD).[25]

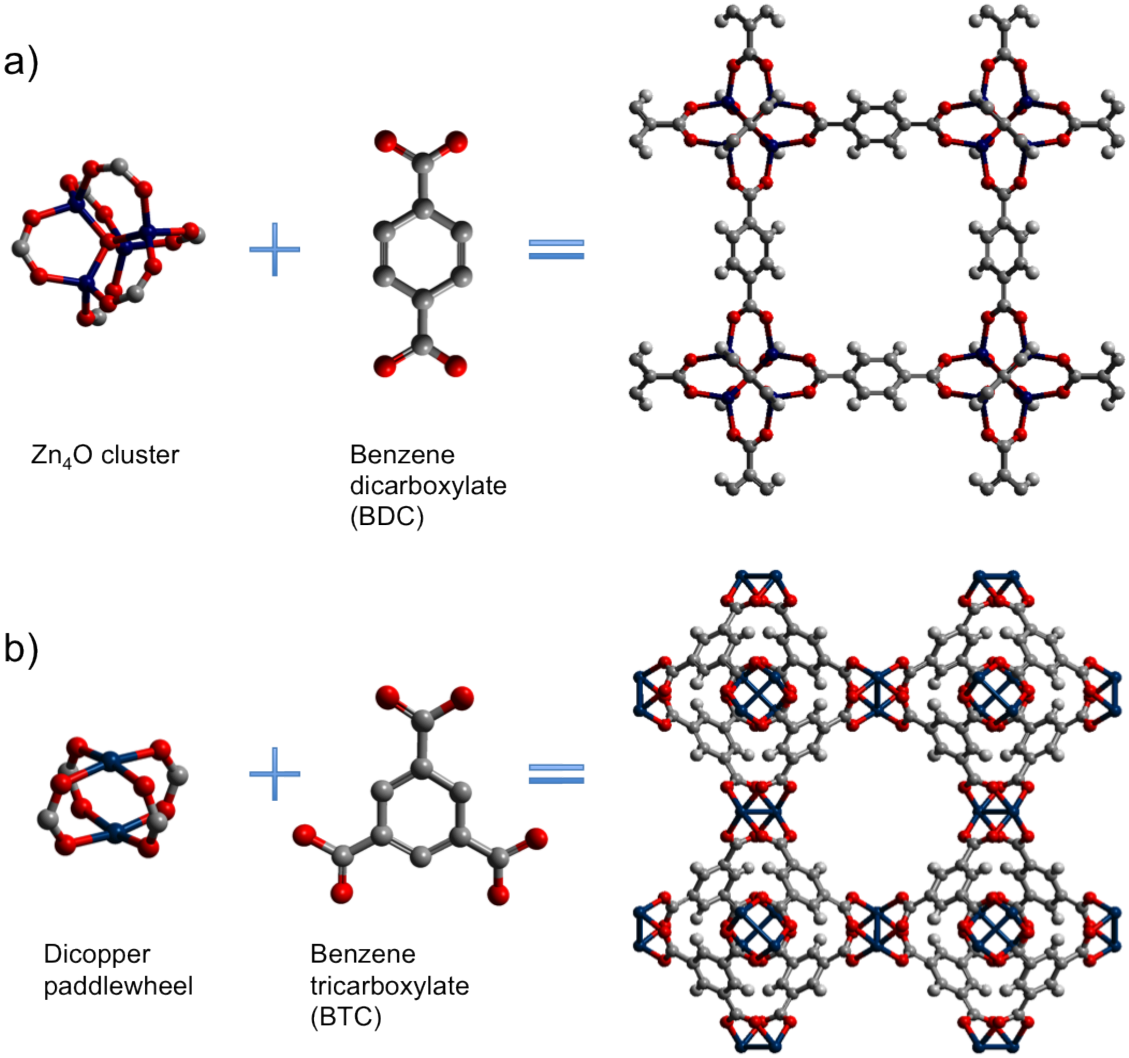

Figure 2-1: a) IRMOF-1[23] and b) HKUST-1[24] organic and inorganic building blocks and resulting frameworks.

In general, MOFs are produced through relatively simple, one-pot synthesis reactions, performed under mild conditions.[3] The chosen organic and inorganic building units are assembled in a building block fashion, giving rise to well-ordered, infinite frameworks. The inorganic building units can be arranged in the form of metal oxide clusters, or chains, whereas the organic linkers can vary widely in terms of size, connection mode, and chemistry. In many cases, the frameworks are robust enough to allow for the evacuation of solvent molecules from within the pores, and are able to retain their porosity once activated.[3] The exact framework structures can then be elucidated via diffraction experiments, allowing for a detailed study of the sizes and shapes of the pores.

A significant benefit of working with MOFs is the potential for structural design targeting specific applications. The design opportunities stem not only from the ability to select the particular organic and inorganic building units making up the framework, but also from the possibility of post-synthesis functionalization[26] in order to achieve the desired linker chemistry. In theory a chosen set of building units could be used to create a variety of frameworks with different topologies.[27] For example, building units with a tetrahedral geometry can be used to create more than 100 unique types of nets.[23,27] The vast majority of reported structures however, are simple frameworks in which the underlying net has the highest symmetry achievable with the chosen building units.[27] It is believed that through the tuning of synthesis conditions, a greater variety of structures can be achieved, yet this approach is still in its infancy.

In an attempt to keep pace with the growing number of reported MOF structures, a staggering number of studies have focused on the characterization of MOFs, in order to identify promising structures for a variety of applications.[5] Studies often combine a variety of experimental and simulation methods in order to study the adsorptive capacities, selectivities, hydrothermal stabilities, and flexibilities of MOF structures. The studies presented in this thesis were performed principally through the use of classical molecular simulations, but incorporated ab initio methods, experimental work, and large-scale process simulations. An overview of the classical and ab initio simulation methods is provided in Section 2.2, and 2.3, respectively, whereas experimental work and process simulation details are provided within the chapters pertaining to those particular studies.

2.2 Classical Molecular Simulation Methods

2.2.1 Statistical Mechanics

Statistical mechanics facilitates the study of many-body systems by applying mathematical tools in order make the connection between the microscopic and macroscopic properties of a system.[28] In the study of gas adsorption or diffusion in porous solids, a microstate is described by microscopic properties, namely in the instantaneous positions and velocities of gas molecules inside the pores.[29] As the molecules move around inside the pores, the system passes through numerous instantaneous microstates.[29] On the macroscopic level, the same system at equilibrium is simply described using temperature, pressure and volume, forming a macrostate.

Statistical mechanics makes use of microstates in order to determine desired macrostate properties. For a given macrostate there are a large number of possible microstates. One of the underlying principles of statistical mechanics is that over time, the number of microstates that the system passes through increases. As time approaches infinity, all possible microstates of a system at equilibrium are obtained. The properties of the macrostate then correspond to the time averaged properties of the system, and can be simply obtained by observing the system over time, as is done in molecular dynamics (MD) simulations. However, for an ergodic system, statistical mechanics states that the average properties of an ensemble, that is a collection of a very large number of microstates all satisfying the constraints of the macroscopic system, would be the same as those of the macrostate (MC).[28] In other words, the average properties determined by averaging over a large number of microstates that are not connected in time (randomly selected as in MC), are the same as the average properties of a system obtained by observing the system over time. For a desired property M this means[30]

$$M_{observed} = \langle M \rangle_{ensemble} = \sum_i M_i \, P_i \qquad \text{Eq 2-1}$$

where $M_{observed}$ is the value of M obtained by averaging over time, and $<M>_{ensemble}$ is obtained by summing the value of M for each microstate i in the ensemble, M_i, multiplied by a weighing factor representing the likelihood of finding that particular microstate in the ensemble, P_i. Ergodicity means that the properties of the system are independent of the starting configuration.[28] This property is essential in Monte Carlo simulations, as it makes it possible to obtain macroscopic information from an ensemble of microstates, which do not necessarily succeed one another in time.

While all systems in this work were assumed to be ergodic, this is not always the case, and care must be taken when studying non-ergodic processes.

Microstates making up an ensemble must share three constant properties. Some of the most often encountered ensembles are the:

- Microcanonical ensemble: Constant number of molecules, volume and energy
- Canonical ensemble: Constant number of molecules, volume and temperature
- Grand canonical ensemble: Constant chemical potential, volume and temperature
- Isobaric-isothermal ensemble: Constant number of molecules, pressure and temperature

The most suitable ensemble for the study of adsorption is the grand canonical ensemble, as the volume, temperature and chemical potential of a system are kept constant, while the number of molecules is allowed to change. At equilibrium the chemical potential and temperature in the adsorbed phase must be the same as in the bulk phase reservoir. In order to reach equilibrium, the number of molecules is allowed to change either by removing molecules from the simulation cell or by introducing molecules from the bulk reservoir. This very much resembles an experimental set-up for adsorption where an adsorbent is in contact with a bulk fluid, and a transfer of molecules from the bulk phase to the adsorbed phase leads to equilibrium.

Considering that the work presented in this thesis focuses on adsorption processes, the remainder of this Monte Carlo discussion will use the grand canonical ensemble as an example. A grand canonical ensemble is made up of microstates all having the same chemical potential, volume and temperature. The partition function of such an ensemble is defined as the sum over of all possible microstates. The microstates at a chosen temperature T can vary in energy, E_k, following a Boltzmann distribution, and also in the number of molecules in the system N consistent with the ensemble T and μ, which can also be described by the Boltzmann distribution. The partition function, *Ξ(μ,V,T),* which is a sum across all microstates, must therefore take into consideration all combinations of E_k and *N*.[29]

$$\Xi(\mu, V, T) = \sum_{k,N} \left(e^{-\beta E_k}\right)\left(e^{\beta \mu N}\right) \qquad \text{Eq 2-2}$$

where

$$\beta = {}^{1}/_{k_B T} \qquad \text{Eq 2-3}$$

Therefore the probability of encountering a microstate *k* with *N* particles and energy E_k in a grand canonical ensemble of microstates is as follows:

$$P_{k,N} = \frac{\left(e^{-\beta E_k}\right)\left(e^{\beta \mu N}\right)}{\Xi(\mu, V, T)} \qquad \text{Eq 2-4}$$

The ensemble average of a desired property can then be determined by summing the value of the property at each microstate *k* and using $P_{k,N}$ as a weighing factor in order to reflect the likelihood of its occurrence.

$$\langle M \rangle_{\mu,V,T} = \sum_{k,N} M_k P_{k,N} = \frac{1}{\Xi(\mu, V, T)} \sum_{k,N} M_k (e^{-\beta E_k})(e^{\beta \mu N}) \qquad \text{Eq 2-5}$$

Eq 2-5 is extremely difficult to compute due to the sheer size of such an ensemble. In order to evaluate <*M*> it is necessary to shift from this quantum mechanical definition to a classical expression. This is done by first assigning each microstate, described by the positions and momenta of all molecules in the system, to a point in phase space. Selecting only the positions and orientations of the molecules renders a configuration space – a subspace of the phase space. Property *M* can be expressed as an integral across the phase space that is evaluated over all momenta, $\boldsymbol{q}$, and positions, $\boldsymbol{s}$:

$$M = \int M(\boldsymbol{q}, \boldsymbol{s})\, \rho(\boldsymbol{q}, \boldsymbol{s}) d\boldsymbol{q}\; d\boldsymbol{s} \qquad \text{Eq 2-6}$$

where *ρ* is used to denote the probability distribution in classical mechanics. In order to simplify this expression it is useful to assume that the total energy can be divided into a potential energy term dependent only on the positions, and a kinetic term dependent only on the momenta. The potential energy, here denoted as $U(\boldsymbol{s})$, is a result of intermolecular interactions, and is therefore dependent on the positions of the molecules in the system. The kinetic term is determined using the expression for the kinetic energy of a monoatomic particle:

$$E_k = {}^{V}\!/_{\Lambda^3} \quad \text{where} \quad \Lambda = \hbar\sqrt{\frac{\beta}{2\pi m}} \qquad \text{Eq 2-7}$$

Here Λ is the de Broglie wavelength of the particle, ħ is the Planck's constant, and m is the mass of the particle. The classical probability distribution ρ thus becomes,

$$\rho(\boldsymbol{s}^N) = \frac{1}{\Xi(\mu, V, T)} \frac{V^N}{N!\,\Lambda^{3N}} \left(e^{\beta\mu N}\right)\left(e^{-\beta U(\boldsymbol{s}^N)}\right) \qquad \text{Eq 2-8}$$

The classical expression equivalent to Eq 2-5 is therefore:

$$\langle M \rangle_{\mu,V,T} = \frac{1}{\Xi(\mu, V, T)} \sum_N \frac{V^N}{N!\,\Lambda^{3N}} \int M(\boldsymbol{s}^N)\left(e^{\beta\mu N}\right)\left(e^{-\beta U(\boldsymbol{s}^N)}\right) d\boldsymbol{s}^N \qquad \text{Eq 2-9}$$

For additional information on statistical mechanics the reader is referred to the textbook of Hill. [28]

2.2.2 The Monte Carlo Method

The Monte Carlo method consists of integrating Eq 2-9 at a series of randomly chosen points in order to evaluate a macroscopic property <*M*>.[30] In the simplest form of the Monte Carlo algorithm, random sampling is carried out evenly across the configuration space, and the contribution of each point to the value of the overall integral is unweighted.[29] The drawback of this approach is that computational time is wasted on the integration of points at which the $e^{-\beta U}$ factor is small, and which therefore have a small contribution to the evaluation of the integral. Importance sampling is a method designed to bypass this limitation, so that calculations are concentrated on points with large contributions to the integral evaluation. Using this approach, sampling points are chosen according to a probability distribution favouring high $e^{-\beta U}$ factor regions, and weighing factors are used in order to account for the sampling bias.

One frequently used importance sampling method is the Metropolis Monte Carlo scheme, whereby a distribution of configurations $\rho(\boldsymbol{s})$ can be sampled based only on probability ratios, without knowing the density distribution explicitly. The algorithm consists of a random walk through the phase space where the moves generate a Markov chain of configurations. A Markov chain is a "memory-less" sequence of configurations, where the decision to move to a new configuration is only affected by the current configuration, and not by previous configurations.[29] The walk starts from an arbitrary old configuration *(o)*. In order to sample a new point, a new trial configuration *(n)* is created by adding a small random displacement to the old configuration. The probability of moving from an old configuration *(o)* to a new configuration *(n)* is called the transition probability, $\pi(o \rightarrow n)$. One of the conditions of the Metropolis method is that the number of moves out of a state *(o)* to a new state *(n)* must be equal to the number of moves into state *(o)* from state *(n)*. This is known as detailed balance, and it can be expressed as follows:[29]

$$\pi(o \to n)\rho(o) = \pi(n \to o)\rho(n) \qquad \text{Eq 2-10}$$

The transition probability $\pi(o \rightarrow n)$ is composed of two factors: the probability of attempting a move from *(o)* to *(n)* when the system is in *(o)*, denoted as $\alpha(o \rightarrow n)$, and the probability of accepting that move, $acc(o \rightarrow n)$.

$$\pi(o \to n) = \alpha(o \to n)acc(o \to n) \qquad \text{Eq 2-11}$$

Although this is not "strictly required", the Metropolis method defines α as a symmetric matrix, and therefore α(o→n) = α(n→o). For this particular case the detailed balance condition can be expressed as:

$$acc(o \to n)\rho(o) = acc(n \to o)\rho(n) \qquad \text{Eq 2-12}$$

There are numerous ways to define $acc(o \rightarrow n)$ and $acc(n \rightarrow o)$ such that the detailed balance condition is satisfied. Metropolis et al.[31] defined the highest of the acceptance probabilities $acc(o \rightarrow n)$ and $acc(n \rightarrow o)$, corresponding to the move resulting in a decrease in potential energy, to equal 1.[30] In other words, if the acceptance probability of moving from state *(o)* to state *(n)* is greater than that for moving from state *(n)* to state *(o)*, the trial move $o \rightarrow n$ will always be accepted.[29] The acceptance criteria can then be expressed as follows:

$$acc(o \to n) = min\left(1, \frac{\rho(n)}{\rho(o)}\right) \qquad \text{Eq 2-13}$$

and

$$acc(n \to o) = min\left(1, \frac{\rho(o)}{\rho(n)}\right) \qquad \text{Eq 2-14}$$

In the case where $acc(o \rightarrow n) < acc(n \rightarrow o)$ the decision of whether to accept or reject the move is made by comparing the value of $acc(o \rightarrow n)$ to a randomly generated number. The move $o \rightarrow n$ is accepted if the random number is smaller than $acc(o \rightarrow n)$, and rejected otherwise.

2.2.3 Grand Canonical Monte Carlo (GCMC) Simulations

In this work, the Monte Carlo method in the grand canonical ensemble was used to study gas adsorption in nanoporous solids. In the grand canonical ensemble, a Markov chain is created by alternating between the following trial moves:[29]

- Inserting a molecule at a random position
- Deleting a randomly chosen molecule
- Moving a molecule to a random new position

Moves are accepted or rejected according to acceptance rules, and detailed balance is conserved.[29] For a trial move where one molecule is randomly moved to a new position while the total number of molecules remains the same, the acceptance probability is,

$$acc(o \rightarrow n) = min(1, exp\{-\beta(U(n) - U(o))\}) \qquad \text{Eq 2-15}$$

and conversely,

$$acc(n \rightarrow o) = min(1, exp\{-\beta(U(o) - U(n))\}) \qquad \text{Eq 2-16}$$

A trial move where a molecule is randomly inserted is accepted with the probability,

$$acc(o \rightarrow n) = \min\left(1, \frac{V}{\Lambda^3(N+1)} e^{[\beta(\mu - U(N+1) + U(N))]}\right) \qquad \text{Eq 2-17}$$

Here *acc(o→n)* can be written as a function of fugacity instead of the chemical potential by using the engineering definition for μ:

$$\mu = \frac{1}{\beta}\ln(\beta f \Lambda^3) \qquad \text{Eq 2-18}$$

therefore,

$$acc(o \rightarrow n) = \min\left(1, \frac{\beta f V}{(N+1)} e^{[-\beta(U(N+1) - U(N))]}\right) \qquad \text{Eq 2-19}$$

The fugacity of the bulk phase at a given pressure can be easily determined using an equation of state. The studies presented in this work employed the Peng Robinson equation of state.[32] For a trial move involving the destruction of a randomly chosen molecule, the acceptance probability is expressed as,

$$acc(o \rightarrow n) = \min\left(1, \frac{N}{\beta f V} e^{[-\beta(U(N) - U(N+1))]}\right) \qquad \text{Eq 2-20}$$

In the case of gas mixtures, acceptance criteria for insertion and deletion trials must also take into account the number of species, and the number of molecules of each species present in the system.

In GCMC simulations of large molecules, such as butane for example, the probability of successfully inserting a molecule in a nanoporous framework simulation cell, without resulting in an overlap of atoms, is low. As a result a very large number of trial steps must be used in order to reach an equilibrium loading. In such cases, a configurational-bias grand canonical Monte Carlo (CB-GCMC) method can be used order to increase the acceptance of trial moves while ensuring that the detailed balance condition is satisfied. CB-GCMC algorithms involve the calculation of a molecule's so-called Rosenbluth weight, or alternatively the ideal gas configurational integral.[33] A number of possible orientations are generated at each sampling point, of which one is selected, and the Rosenbluth weights of the new and old configurations, which reflect the orientation dependent likelihood of acceptance, are used in deciding whether to accept or reject the trial move. More details on CB-GCMC algorithms can be found in the molecular simulation textbook of Frenkel and Smit.[29]

2.2.4 Molecular Dynamics

Unlike the stochastic approach used in Monte Carlo simulations, molecular dynamics is a deterministic computational tool. MD simulations are normally used in order to study the behaviour of a many-body system in time by determining the motion of all molecules within the system. Starting from an initial set of positions, orientations and velocities, calculations are performed by integrating Newton's equations of motion in order to determine a new set of positions, orientations and velocities at each simulation time step. As a result the points do not form a Markov chain, but are connected in time allowing for the study of equilibrium as well as dynamic properties.

As is the case for Monte Carlo simulations, in molecular dynamics the interactions between molecules are modeled using force fields. The intermolecular potential energy, U_{inter}, is obtained by taking a sum of the interaction energies calculated for each pair of molecules in the system, $u(r_{ij})$, separated by a distance, r_{ij}:

$$U_{inter} = \sum_i \sum_j u(r_{ij}) \qquad \text{Eq 2-21}$$

The force acting on each molecule is then a partial derivative of the intermolecular potential energy as follows:

$$\mathbf{F}_{\boldsymbol{i}} = -\frac{\partial U_{inter}(\mathbf{r}^N)}{\partial \mathbf{r}_i} \qquad \text{Eq 2-22}$$

Where $\boldsymbol{F}_i$ is the force acting on a molecule i, and $\boldsymbol{r}_i$ is the position vector of molecule i. Once the forces acting on each molecule within the system have been computed, the new molecular positions can be determined using Newton's equations of motion. Newton's second law relates the motion of molecules to the external forces acting on them, therefore:

$$\mathbf{F}_{\boldsymbol{i}} = -\frac{\partial U_{inter}(\mathbf{r}^N)}{\partial \mathbf{r}_{\boldsymbol{i}}} = m\frac{d^2\mathbf{r}_{\boldsymbol{i}}}{dt^2} \qquad \text{Eq 2-23}$$

where m is the mass of the molecule. Numerous procedures, such as the Verlet, velocity-Verlet, and Leap-Frog algorithms, have been developed in order to integrate the equations of motion based on a Taylor series of particle coordinates as a function of time. Such algorithms, explained in detail in Frenkel and Smit,[29] and Haile,[34] allow for the calculation of a new set of coordinates, positions and velocities at each time step. Usually the time steps used in MD simulations are in the order of femtoseconds, while the simulation time is in the order of picoseconds, consisting of an equilibration period, and a production period. During the equilibration period the system, having been assigned initial starting conditions, including molecular positions and velocities, moves towards an equilibrium state. This period must be sufficiently long in order to allow all the properties of the system to reach fairly stable values that are no longer affected by the starting conditions. Naturally the equilibration period required depends on how far away from equilibrium the starting conditions were. The production period of the MD simulation is used to record and average the required system properties over time. The accuracy of the measurements increases with increasing simulation time.

As was the case for MC simulations, MD makes use of a variety of ensembles. In this work MD simulations were performed in the NVT ensemble, which can be thought of as a constant volume system containing a constant number of molecules that is surrounded by a constant temperature heat bath. In order to maintain a constant temperature over the course of an MD simulation, a thermostat must be applied. The goal of a thermostat is to ensure that the temperature of the system is the desired temperature, while allowing for the small temperature fluctuations expected of a canonical ensemble. Simple velocity scaling thermostats, and variations thereof, such as the Berendsen thermostat, can be used to ensure that the system remains at a constant temperature, however they can have an unrealistic influence on the molecular velocities, and fail to reproduce the canonical temperature distribution. The thermostat used in this work is the Nosé-Hoover thermostat, in which the heat bath is considered to be part of the system. As a result, the interaction between the heat bath and the system leads to a kinetic energy transfer, resulting in a temperature that is not constant, but which fluctuates near the desired value. This approach ensures that the positions and momenta of the particles over the simulation time follow a canonical distribution. The temperature is coupled to the motion of particles by adding the energy contributions of an artificial parameter with an artificial mass into the Langrangian expression of the system, forming an extended-Lagrangian. The thermostat formulation is discussed in detail in Frenkel and Smit,[29] and Rapaport.[35]

2.2.5 Diffusion Calculations Using Equilibrium and Non-Equilibrium MD

Molecular dynamics can be used to study systems that are at equilibrium (EMD) as well as systems that are away from equilibrium (NEMD). EMD simulations are performed on closed systems, in which the number of molecules is constant, whereas NEMD is used to study systems under the influence of an external field. EMD simulations are useful for determining the self-diffusivities, D_s, of molecules, which are essentially a measure of Brownian motion. Self diffusivity, which can also be thought of as the movement of a tagged molecule in a system filled with untagged molecules, is calculated using the Einstein relation:

$$D_s = \lim_{t \to \infty} \frac{\langle |r(t) - r(0)|^2 \rangle}{(2d)t} \qquad \text{Eq 2-24}$$

Where d is the number of dimensions, $r(0)$ is the initial position of the molecule, and $r(t)$ is its position at time t.

The simulations performed in this work however, focused on determining the transport diffusivity of gas molecules through the pores of MOFs. Transport diffusivities are of greater interest for engineering applications as they reflect the movement of molecules due to the presence of a chemical potential gradient, which mirrors the physical transport process. Transport diffusivities can be determined using a variety of methods including equilibrium molecular dynamics (EMD), external field nonequilibrium molecular dynamics (EF-NEMD) and dual control volume grand canonical molecular dynamics simulations, (DCV-GCMD). Arya et al.[36] and Chempath et al.[37] studied these three methods in detail and compared their level of accuracy in calculating the transport diffussivities of pure components, and mixtures components, respectively, and found that EF-NEMD simulations result in the smallest calculation errors. In this work all transport diffusivity calculations were performed using EF-NEMD.

In EF-NEMD, an external force is applied to the guest molecules inside a framework in order to imitate a chemical potential gradient effect. This results in a movement of molecules along the direction of the applied force, and the molecular flux can then be measured. The flux, J, can be calculated using the following expression:

$$\langle J \rangle = \frac{1}{V\tau_{sim}} \left\langle \sum_{k=1}^{N} \left[r_k(t) - r_k(0) \right] \right\rangle \qquad \text{Eq 2-25}$$

where r_k refers to the position of molecule k along the direction in which the force was applied, V represents the unit cell volume and τ is the time span of the simulation. The sum of the molecular displacements at each time point is also known as the displacement correlation function (DCF).

Fick’s law of diffusion defines the molecular diffusive flux, ***J***, as a function of transport diffusivity, D_t, and concentration gradient, ∇c.

$$\mathbf{J} = -D_t \nabla c \qquad \text{Eq 2-26}$$

It is more useful, however to think of flux in terms of a chemical potential gradient, $\nabla\mu$ and this is done using the Onsager formulation:

$$J = -L\nabla\mu \qquad \text{Eq 2-27}$$

where L is sometimes referred to as an Onsager coefficient. This method has been described in detail in other works,[37,38] and a summary of its application for the simplest case, single component diffusion, is provided here.

The Onsager coefficient can be determined from EF-NEMD simulations as a ratio of average molecular flux to the applied force:

$$L = \frac{\langle J \rangle}{F} \qquad \text{Eq 2-28}$$

The transport diffusion coefficient D_t can then be related to the Onsager coefficient, L as follows:

$$D_t = L\Gamma \text{ where } \Gamma = \frac{RT}{c}\frac{d\ln f}{d\ln c} \qquad \text{Eq 2-29}$$

The d(ln *f*)/d(ln *c*) term is also known as the thermodynamic correction factor and can be determined directly from a single component adsorption isotherm. For example, for the dual-site Langmuir isotherm ,

$$c = c_A + c_B = \frac{c_{sat,A} b_A P}{1 + b_A P} + \frac{c_{sat,B} b_B P}{1 + b_B P} \qquad \text{Eq 2-30}$$

the thermodynamic correction factor is given by:[39]

$$\Gamma = \frac{1}{\frac{c_A}{c}\left(1 - \frac{c_A}{c_{sat,A}}\right) + \frac{c_B}{c}\left(1 - \frac{c_B}{c_{sat,B}}\right)} \qquad \text{Eq 2-31}$$

In Eq 2-30 and Eq 2-31 c_A and c_B are used to denote the loadings at each of the two sites at a given pressure, and $c_{sat,A}$ and $c_{sat,B}$ are the saturation loadings.

It should be noted that the simple model presented here applies only to the single component diffusion case. For the diffusion of mixture components, a matrix of Onsager coefficients must be determined in order to characterize the diffusion of each species through like and unlike molecules, which are also referred to as main-term and cross-term coefficients. Further details on this method are provided in the works of Chempath et al.[37] and Williams et al.[38]

2.2.6 Potentials

In classical molecular simulations such as GCMC and MD, potential energies are calculated using force fields in order to take into account fluid-fluid as well as fluid-framework interactions. The total potential energy is a sum over all bonded and non-bonded interactions:

$$U_{total} = U_{bonded} + U_{non-bonded} \qquad \text{Eq 2-32}$$

$$U_{bonded} = \sum_{bonds} U_{stretch} + \sum_{bends} U_{bend} + \sum_{torsions} U_{torsions} \qquad \text{Eq 2-33}$$

$$U_{non-bonded} = \sum_{pairs} U_{vdW} + \sum_{pairs} U_{Coulombic} \qquad \text{Eq 2-34}$$

Bonded interactions include bond stretching, angle-bending, and torsional movements, while non-bonded interactions are divided into van der Waals interactions and Coulombic interactions.

In this work dispersion interactions were calculated using the Lennard-Jones (LJ) 12-6 potential model as follows:[34]

$$u_{ij}(r_{ij}) = 4\varepsilon_{ij}\left[\left(\frac{\sigma_{ij}}{r_{ij}}\right)^{12} - \left(\frac{\sigma_{ij}}{r_{ij}}\right)^{6}\right] \qquad \text{Eq 2-35}$$

where $u_{ij}(r_{ij})$ is the intermolecular energy between two LJ spheres, i and j, separated by a distance r_{ij}, ε_{ij} is the depth of the potential well, and σ_{ij} is the LJ sphere diameter. Each simulation sphere is defined using a size parameter, σ_{ii}, and an interaction strength parameter, ε_{ii}. For pairs of LJ spheres of different types, i and j, the cross-interaction parameters are determined using the Lorentz-Berthelot mixing rules:

$$\sigma_{ij} = \frac{\sigma_{ii} + \sigma_{jj}}{2} \qquad \text{Eq 2-36}$$

$$\square_{ij} = \sqrt{\square_{ii}\square_{jj}} \qquad \text{Eq 2-37}$$

The total dispersion and repulsion energy contribution for a system is then determined using a pairwise additive approach:

$$U_{vdW} = \underset{i}{\square}\,\underset{j<i}{\square}\, u_{ij} \qquad \text{Eq 2-38}$$

For a pair of molecules separated by a large r_{ij}, the dispersion interaction described by the Lennard-Jones potential is close to zero. As a result such interactions can be considered negligible. In GCMC or MD simulations, a cut-off value is normally assigned for the calculation of dispersion interactions, beyond which all contributions are considered to be null. Such an approach is justified as the Lennard-Jones potential approaches zero at high separation distances. In MD simulations however, care must be taken in order to ensure that the cut-off value sufficiently high in order to reduce the risk of discontinuities in the force calculations.

For polar and quadrupolar fluid molecules, simulations must take into account dispersion as well as electrostatic, or Coulombic interactions. Each LJ interaction centre, whether it is part of the framework, or part of a fluid molecule, is assigned a partial charge. Based on these partial charges, the Coulombic potential energy for the system being modelled is calculated as follows:

$$U_{Coulombic} = \sum_{i=1}^{N} \sum_{j=i+1}^{N} \frac{\gamma_i \gamma_j}{4\pi\varepsilon_0 r_{ij}} \qquad \text{Eq 2-39}$$

where γ_i and γ_j are partial charges assigned to sphere i and j, separated by a distance, r_{ij}, N is the total number of interaction spheres, and ε_0 is the permittivity in vacuum. These long range interactions are evaluated using the Ewald summation method, which is described in detail by Frenkel and Smit.[29]

Normally, framework atoms are represented using LJ parameters taken from generic force fields, such as the Universal Force Field (UFF),[40] the Dreiding force field,[41] and the OPLS force field.[42] In this work MOF atoms were modeled using either the UFF or the Dreiding force fields. Fluid molecules on the other hand, are usually represented using force field parameters that were fitted to reproduce vapour-liquid equilibrium data.[43-46] The LJ parameters for the fluid molecules simulated in this work are summarized in Table 2-1. The number of LJ centres required to represent each molecule depends on its size and polarity. A small, non-polar, spherical molecule such as methane can be represented using only one LJ centre, while a molecule with a dipole moment such as CO requires three, or four depending on the model. Here, alkane and alkene molecules were represented with the TraPPE force field, which uses a united-atom approach to describe each carbon atom and its surrounding hydrogen atoms as one LJ sphere with one set of parameters.[43,44] N_2, O_2 and CO_2 were modelled as three-centred molecules using the TraPPE force field.[47] In the case of N_2 and O_2, dummy LJ spheres, located in the centre of mass of the molecules, were used in order to describe the charge distribution in the molecules. H_2 was modelled as a two-centred Lennard-Jones molecule as described by Yang et al.[45] CO was represented either using the model introduced by Piper et al.[48] using four LJ spheres (one at the centre of each atom, and two dummy spheres), or the more recent model of Martín-Calvo et al. which uses only three LJ spheres (one at the centre of each atom, and one dummy sphere).[49] The arrangement of the carbon, oxygen and dummy atoms associated with the two CO models are shown in Figure 2-2. The dipole moment of the molecule is overestimated by the Piper et al. model (0.43 D), whereas the model of Martín-Calvo et al. results in a dipole moment of 0.112 D, which is in agreement with experimental data.[49] In addition the three-centred model of Martín-Calvo et al. has been shown to correctly reproduce the vapour-liquid equilibrium curve, while the model of Piper et al fails to do so.[49]

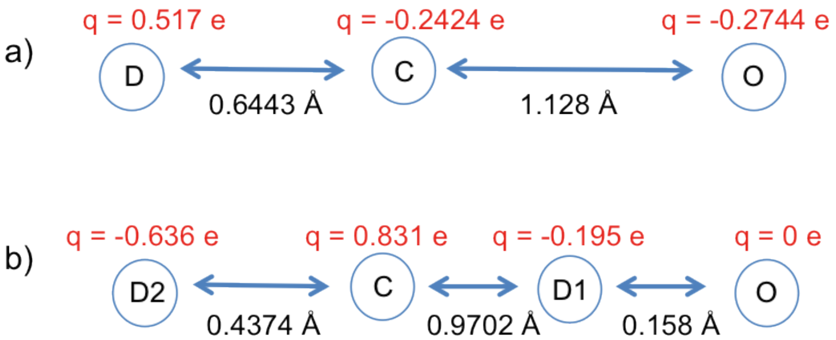

Figure 2-2: Depiction of the positions and charges of the LJ interaction spheres as described by the CO models of a) Martín-Calvo et al.[49] and b) Piper et al.[48]

Table 2-1: LJ parameters and partial charges for various simulated molecules.

Fluid	LJ Sphere	σ (Å)	ε/kB (K)	q (e)	Ref.

CH_4	$[CH_4]$	3.73	148	-	43
C_2H_6	$[CH_3]$-CH_3	3.75	98	-	43
C_3H_8	$[CH_3]$-CH2-CH_3	3.75	98	-	43
	CH_3-$[CH_2]$-CH_3	3.95	46	-	
C_3H_6	$[CH_3]$-CH=CH_2	3.75	98	-	44
	CH_3-CH=$[CH_2]$	3.68	85	-	
	CH_3-[CH]=CH_2	3.71	52	-	
C_4H_{10}	$[CH_3]$-CH_2-CH_2-CH_3	3.75	98	-	43
	CH_3-$[CH_2]$-CH_2-CH_3	3.95	46	-	
N_2	N-	3.31	36	-0.482	47
	Dummy	0	0	0.964	
H_2	H-	2.72	10	-	45
O_2	O-	3.02	49	-0.113	47
	Dummy	0	0	0.226	
CO_2	C-	2.8	27	0.66	47
	O-	3.05	79	-0.33	
CO	C-	3.385	39.89	0.831	48
	O-	2.885	61.57	0	
	Dummy1	0	0	-0.636	
	Dummy2	0	0	-0.195	
CO	C-	3.636	16.141	-0.2424	49
	O-	2.979	98.041	-0.2744	
	Dummy	0	0	0.5168	
CH_3OH	$[CH_3]$-O-H	3.75	98	0.265	50
	CH_3-[O]-H	3.02	93	-0.7	
	CH_3-O-[H]	0	0	0.435	

Simulations of flexible molecules must take into account non-bonded as well as bonded interactions. In this work, all bond lengths were maintained constant, and are provided in Table 2-2.

Table 2-2: Bond lengths for all adsorbate molecules studied in this work.

Fluid	Bonded Pair	Bond Length (Å)	Ref.
C_2H_6	$[CH_3]$-CH_3	1.54	43
C_3H_8	$[CH_3$-$CH_2]$-CH_3	1.54	43
	CH_3-$[CH_2$-$CH_3]$	1.54	
C_3H_6	$[CH_3$-$CH]$=CH_2	1.33	44
	CH_3-$[CH$=$CH_2]$	1.54	
C_4H_{10}	$[CH_3$-$CH_2]$-CH_2-CH_3	1.54	43
	CH_3-$[CH_2$-$CH_2]$-CH_3	1.54	
	CH_3-CH_2-$[CH_2$-$CH_3]$	1.54	
N_2	[N-Dummy]-N	0.55	47
	N-[Dummy-N]	0.55	
H_2	H-H	0.74	45
O_2	[O-Dummy]-O	0.65	47
	O-[Dummy-O]	0.65	
CO_2	[O=C]=O	1.16	47
	O=[C=O]	1.16	
CO	[D2-C]-D1-O	0.4374	48
	D2-[C-D1]-O	0.9702	
	D2-C-[D1-O]	0.158	
CO	[Dummy-C]-O	0.6443	49
	Dummy-[C-O]	1.128	
CH_3OH	$[CH_3$-$O]$-H	1.43	50
	CH_3-$[O$-$H]$	0.945	

In many cases, however, a harmonic expression is used in order to represent the bond stretching potential, as follows:

$$U_{stretch} = \frac{k_r}{2}\left(r - r_{eq}\right)^2 \qquad \text{Eq 2-40}$$

where r_{eq} is the equilibrium bond length, r is the distance between two bonded LJ spheres, and k_r is the bond force constant. Similarly the bending potential is also calculated using a harmonic function, this time based on the angle formed by three bonded atoms:

$$U_{bend} = \frac{k_\theta}{2}(\theta - \theta_{eq})^2 \qquad \text{Eq 2-41}$$

where θ_{eq} is the equilibrium bond angle, θ the angle between the three LJ spheres, and k_θ is the bending force constant. Finally the torsional contribution can be expressed as:

$$U_{torsion} = c_0 + c_1\left[1+\cos(\phi)\right] + c_2\left[1-\cos(2\phi)\right] + c_3\left[1+\cos(3\phi)\right] \qquad \text{Eq 2-42}$$

where c_0, c_1, c_2 and c_3 are the force constants and ϕ is the dihedral angle of a chain of four bonded atoms. In this work, adsorption simulations performed for propane and propene using an angle bending potential gave identical results to simulations performed using rigid molecules, therefore the angle bending potential was not included in the final simulations for these molecules. Simulations of methanol and butane molecules were performed using the TraPPE force field,[43,50] and took into account angle bending, and in the case of butane, torsional movements, while maintaining the bond lengths fixed. The TraPPE force field parameters used to represent the bonded interactions for butane and methanol are provided in Table 2-3 and Table 2-4.

Table 2-3: TraPPE[43,50] force field parameters for angle bending energy contributions.

Molecule	**Bending Angle**	**ϑ (°)**	**k_ϑ/k_B [K]**
Butane	[CH_3-CH_2-CH_2]-CH_3	114.0	62,500
	CH_3-[CH_3-CH_2-CH_3]	114.0	62,500
Methanol	CH_3-O-H	108.5	55,400

Table 2-4: TraPPE[43] force field parameters for torsional energy contributions.

Molecule	**Torsional Angle**	**φ (°)**	**c_0/k_B [K]**	**c_1/k_B [K]**	**c_2/k_B [K]**	**c_3/k_B [K]**
Butane	CH_3-CH_2-CH_2-CH_3	180.0	0.00	355.03	-68.19	791.32

2.2.7 Periodic Boundary Conditions

In a classical molecular simulation run, the number of atoms being modelled is very small (in the order of a few thousand) compared to the number of atoms involved in experimental set-ups. In such small simulation boxes, the ratio of the number of atoms located near the surface of the box to the total number of atoms is large, leading to surface effects that are not representative of a bulk phase. In order to minimize surface effects it is desirable to simulate an infinite, continuous system, which can be done using periodic boundary conditions. This method essentially replicates the primary simulation cell in all directions, generating image cells, as shown in Figure 2-3. Using the so-called minimum image convention, each atom in the primary simulation cell is only allowed to interact with the closest representation of every other atom in the system. As a result, the cutoff radius chosen for the calculation of dispersion interactions must be shorter than half of the shortest simulation cell length.

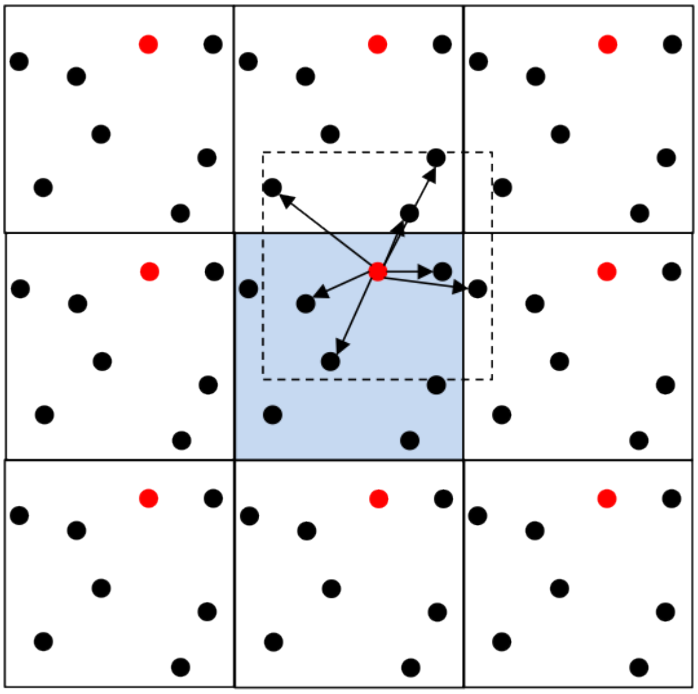

Figure 2-3: Visualization of periodic boundary conditions in 2D. Blue shading is used to indicate the primary simulation cell. Red spheres used to show the replication of an atom in each surrounding image cell. Dashed box is used to select the nearest image of each atom interacting with the atom marked in red.

2.3 First Principles Methods

The classical simulations performed in this work made use of the assumption that the framework atoms remain fixed in their crystallographic positions. In reality, atoms are in constant motion, and their movement can have a strong impact on the adsorption or diffusion of guest molecules. As a result it is sometimes necessary to study the positions of framework atoms over time, in order to determine whether the crystallographic positions are accurately describing the framework, and whether the positions of atoms can change depending on temperature, pressure, or guest-framework interactions, resulting in important structural changes.

Ab Initio Molecular Dynamics (AIMD) simulations are similar to classical simulations in the sense that the movement of atoms at each time step is calculated by integrating Newton’s equations of motion. Classical MD simulations rely on the use of force fields in order to describe the potential energy associated with each atom in the system. The accuracy of force fields is strongly dependent on the systems used in their calibration, and as a result the development of a system specific force field is necessary. One major advantage of using the AIMD method is that the energy of the system is calculated from first principles. This approach overcomes the need for force field design, and more importantly, results in a significant increase in simulation accuracy.

2.3.1 Electronic Structure Theory

In quantum mechanics, the state of a system composed of atoms or molecules is expressed using a wave function, Ψ, which is a function of the coordinates of all elementary particles and of time.[51] The simplest form of the Schrödinger equation describes the behaviour of a system using the wave function as follows:

$$\hat{H}\Psi = E\Psi \qquad \text{Eq 2-43}$$

where $\hat{H}$ is the Hamiltonian operator, and E is the total energy of the system. Such an equation can be solved exactly only for very simple cases, such as the particle in a box example.[52] The Hamiltonian operator is dependent on the nature of the system being studied. For a single particle system, the Hamiltonian operator is defined as:

$$\widehat{H} = -\frac{\hbar^2}{2m}\nabla^2 + V_{total} \qquad \text{Eq 2-44}$$

where $\hbar$ is the Planck's constant, m is the mass of the particle, ∇^2 is the Laplacian operator, and V_{total} is the total potential energy. For a many particle system, the expression becomes more complex, and $\hat{H}$ can be written as follows:

$$\widehat{H} = \widehat{T}_e + \widehat{T}_n + \widehat{V}_{ne} + \widehat{V}_{ee} + \widehat{V}_{nn} \qquad \text{Eq 2-45}$$

T_e and T_n are the kinetic energy contribution due to the movement of electrons, and nuclei, respectively, whereas V_{ne}, V_{ee}, and V_{nn} are the potential energy contributions from electron-nucleus, electron-electron, and nucleus-nucleus interactions. Each of the terms can be expressed in atomic units as follows:

$$\widehat{H} = -\frac{1}{2}\sum_{i=1}^{N}\nabla_i^2 - \frac{1}{2}\sum_{A=1}^{M}\nabla_A^2\frac{1}{M_A} - \sum_{i=1}^{N}\sum_{A=1}^{M}\frac{Z_A}{r_{iA}} + \sum_{i=1}^{N}\sum_{j>1}^{N}\frac{1}{r_{ij}} + \sum_{A=1}^{M}\sum_{B>A}^{M}\frac{Z_A Z_B}{R_{AB}} \qquad \text{Eq 2-46}$$

where M and N are the number of nuclei and electrons in the system, respectively, M_A is the mass of a nucleus A, r_{iA} is the distance between an electron i and a nucleus A, r_{ij} is the distance between two electrons, R_{AB} is the distance between two nuclei, and Z_A and Z_B are the atomic numbers of A and B.

In order to simplify the problem, it is useful to consider the difference in size between the electrons and the atomic nuclei of a system. The nuclei are much heavier than the electrons (1836 times, to be precise), therefore the electrons are able to move much faster in response to certain interactions. As a result, quantum mechanical calculations of a system's energy normally make use of the Born-Oppenheimer approximation,[53] to assume that the slow movement of the nuclei can be calculated using classical methods, and that the electrons can be considered to be in a ground state. The relatively still nuclei generate a potential field, which then influences the movement of the electrons. As a result of adopting this approximation, the kinetic energy contribution of the nuclei, T_n, is considered to be zero, and the nucleus-nucleus repulsive potential energy, V_{nn}, is constant. The Hamiltonian can then be expressed for a system in which the electrons move in a field described by stationary nuclei as follows:

$$\hat{H}_{elec} = -\sum_{i=1}^{N}\frac{1}{2}\nabla^2 - \sum_{i=1}^{N}\sum_{A=1}^{M}\frac{Z_A}{r_{iA}} + \sum_{i=1}^{N}\sum_{j>i}^{N}\frac{1}{r_{ij}} \qquad \text{Eq 2-47}$$

where $\hat{H}_{elec}$ is the electronic Hamiltonian. The Schrödinger equation can then make use of the electronic Hamiltonian to describe the electronic wave function:

$$\hat{H}_{elec}\Psi_{elec} = E_{elec}\Psi_{elec} \qquad \text{Eq 2-48}$$

The total energy of the system can then be thought of as a sum of the electronic energy contribution and the constant repulsive potential energy due to interactions between the stationary nuclei. For a thorough understanding of quantum mechanical methods, the reader is referred to the textbooks of McQuarrie[51] and Atkins and Friedman.[54]

2.3.2 Density Functional Theory

In order to calculate the energy of a many particle system, classical ab initio methods focus on determining the molecular wave function. Such methods calculate the approximate electronic wave function based on the wave functions of each electron in the system, which comes at a high computational cost particularly for systems with a large number of electrons. In contrast to wave function based methods, Density Functional Theory (DFT)[55,56] is an energy minimization method used to approximately determine the energy of a many particle system based on a functional of electron density. The main advantage of using DFT is a lower computational cost, which enables the study of larger systems. This section provides a brief overview of the DFT method. For a more detailed look at this method, the reader is referred to the textbooks of Martin,[57] and Parr and Yang.[58]

The density of electrons at a particular point, **r**, in the system can be written as a conjugate of individual electron wave functions as follows:

$$\rho(\mathbf{r}) = 2\sum_{i}\Psi_i(\mathbf{r})\cdot\Psi(\mathbf{r}) \qquad \text{Eq 2-49}$$

In order to calculate the energy as a function of the electron density, DFT makes use of two fundamental theorems developed by Hohenberg and Kohn.[55] The first theorem states that, "*The ground-state energy from Schrödinger's equation is a* *unique functional of the electron density*”.[55] What this means is that given an equation describing the electron density in the system, a unique energy value can be determined. In the same way that a function uses a number to give a number, a functional uses a function to give a number.

The second theorem states that, “*The electron density that minimizes the energy of the overall functional is the true electron density corresponding to the full solution of the Schrödinger equation*”.[55] This second theorem presents a method for calculating the energy: for a given functional, an initial trial electron density can be tested and adjusted in order to obtain the minimum energy. Based on the Hohenberg-Kohn theorems,[55] the electronic energy can be expressed as:

$$E = E[\rho(\mathbf{r})] \qquad \text{Eq 2-50}$$

In order to perform DFT calculations, it is useful to express the energy as a sum of known and unknown terms:

$$E[\{\Psi_i\}] = E_{known}[\{\Psi_i\}] + E_{XC}[\{\Psi_i\}] \qquad \text{Eq 2-51}$$

The exchange correlation term, E_{XC} includes all non-classical energy contributions. The known term, E_{known} can be considered as the energy of a fictitious system of non-interacting electrons with the same electron density as the true system of interacting electrons. The known energy term is a sum of the electronic kinetic energy, the nuclear-electron potential energy due to classical Coulombic interactions, and the Coulombic part electron-electron potential energy, and can be written as:

$$\begin{aligned} E_{known} = \frac{\hbar^2}{m}\sum_i \int \Psi_i * \nabla^2\Psi_i \, d^3\mathbf{r} + \int V_{ne}(\mathbf{r})\rho(\mathbf{r})d^3\mathbf{r} \\ + \frac{e^2}{2}\int\int \frac{\rho(\mathbf{r})\rho(\mathbf{r}')}{|\mathbf{r}-\mathbf{r}'|} d^3\mathbf{r}d^3\mathbf{r}' \end{aligned} \qquad \text{Eq 2-52}$$

The benefit of working with a fictitious system of non-interacting electrons, is that the contribution of each electron to the total electron density can be treated separately, using what are known as Kohn-Sham orbitals.[56] The Kohn-Sham expression for a single non-interacting electron is as follows:

$$\left(\frac{\hbar^2}{2m}\nabla^2 + V_{ne}(\mathbf{r}) + \int \frac{\rho(\mathbf{r}')}{|\mathbf{r}-\mathbf{r}'|} d\mathbf{r}' + E_{XC}(\mathbf{r})\right)\Psi_i(\mathbf{r}) = \mathcal{E}_i\Psi_i(\mathbf{r}) \qquad \text{Eq 2-53}$$

The first term of the equation is the kinetic energy for the non-interacting system, $V_{ne}(\mathbf{r})$ is the energy contribution from nucleus-electron Coulombic interactions, the third term is Coulombic electronic interaction energy, also known as the Hartree energy, and $E_{XC}(\mathbf{r})$ is the exchange correlation energy term. The Kohn-Sham expressions[56] can be evaluated and used to approximate the electron density.

The iterative, self-consistent method used for calculating the total system energy can then be summarized as follows:

- Choose an initial $\rho(\mathbf{r})$
- Solve a set of Kohn-Sham equations to obtain the wave functions for each particle
- Calculate a new electron density corresponding to the Kohn-Sham wave functions
- If the initial chosen electron density is the same as the newly calculated calculated density, then it can be used to calculate the ground state energy. Otherwise, modify the initial electron density and repeat the process.

2.3.3 Functionals

The known terms in Eq 2-53 can be calculated analytically, however no exact expression exists for calculating the exchange correlation energy term, E_{XC}. As a result E_{XC} must be approximated, using methods such as the local density approximation (LDA) method, or the generalized gradient approximation (GGA) method. Exchange and correlation functionals are developed in order to account for electron-electron non-classical interactions, as well as differences in kinetic energy resulting from interactions between particles, which are not described for a non-interacting system. Examples of GGA methods include BLYP,[59-61] PBE,[62] and BP86.[59,63] In this work only GGA methods were employed.

2.3.4 Basis Sets

Electronic wave functions, also known as molecular orbitals, can be expressed as linear functions of atomic orbitals. A set of atomic orbitals that can be used to represent the electrons of a particular atom are called basis functions. Basis functions can be of the Slater type orbital (STO) or atom-centred Gaussian type orbital (GTO). STOs are more accurate but are difficult to use during integral computation, therefore a common approach is to use multiple GTOs (often three) to approach the accuracy of an STO. Such basis functions obtained using a combination of GTOs are called contracted Gaussian type orbitals (CGTOs). The molecular orbitals can be calculated by using the basis functions and a set of coefficients. The set of functions used to describe a molecular orbital is known as a basis set. In order to increase the accuracy of the molecular orbital calculation, basis sets using multiple functions to represent each atomic orbital are employed. Such basis sets are also known as double-zeta, triple-zeta, quadruple-zeta, and so on, depending on the number of functions incorporated.

2.3.5 Pseudopotentials

When working with large systems, such as MOFs for example, a large number of basis functions are required to describe all molecular orbitals, which comes at a high computational cost. Especially in the case of metals, a large amount of computational power is spent on describing the molecular orbitals of inner core electrons. While valence electrons play an important role in bonded interactions and must be defined explicitly, the potential energy of the inner core electrons can be described using simpler expressions. In order to reduce the computational demand associated with performing calculations with a large number of basis functions, the inner core electrons of atoms are often described using pseudopotentials, also known as effective core potentials. This method is also known as a split-valence approach. In this work, the pseudopotentials developed by Goedecker Teter and Hutter (GTH),[64,65] were employed in all simulations.

2.3.6 Ab Initio Molecular Dynamics

Ab Initio Molecular Dynamics (AIMD) is a powerful tool that enables the study of molecules over time based on on-the-fly energy calculations from first principles. In this work all simulations were performed using the Quickstep[66] module of the CP2K package[67] (/http://cp2k.berlios.de/). This program makes use of a hybrid Gaussian and plane wave[68] (GPW) basis set. The atom-centred Gaussian-type basis set is applied in order to describe the wave functions, whereas the auxiliary plane wave basis set describes the density. As a result a high level of accuracy is ensured, and the wave functions can be computed using Fast Fourier Transforms (FFT) resulting in a low computational cost for Hartree energy calculations.

3 Hydrogen Separations

Hydrogen purification processes require columns filled with highly selective adsorbents that are capable of retaining a large amount of impurities while allowing hydrogen to pass through. The adsorbents must also be able to release the adsorbed impurities with ease upon a reduction in pressure, in order to allow for column regeneration. Metal-organic frameworks (MOFs) have been shown to exhibit these desirable characteristics[11,69] and are therefore of interest in improving the separation efficiencies of H_2 purification processes. The first step in selecting MOFs suitable for hydrogen purification applications is to identify which structural characteristics are most likely to result in highly efficient adsorbents and are therefore desirable. To date, several studies have focused on determining the effect of pore shape, size and functionality on the uptake of various gases.[70,71] Far fewer studies, however, have been reported in which the relationship between such characteristics and adsorption selectivity is assessed.[3,12]

One such selectivity study, carried out by Liu et al.,[72] simulated adsorption of CH_4/H_2 mixtures in three pairs of interpenetrated and noninterpenetrated IRMOFs. It was concluded that in interpenetrated IRMOFs, the presence of smaller pores results in a greater difference in the adsorbate – framework interactions of H_2 and CH_4 molecules, therefore a much higher methane selectivity is observed than in their noninterpenetrated counterparts. Liu et al.[73] carried out a similar study for CO_2/N_2 and CH_4/N_2 mixtures on the same set of IRMOFs, and concluded that the CO_2 and CH_4 selectivities, respectively, were also higher in catenated IRMOFs. Bae et al.[74] on the other hand, looked at the influence of linker functionalization on CO_2/N_2 and CO_2/CH_4 separations, and showed that the addition of -CF_3 functional groups resulted in a marked improvement in CO_2 selectivity for both mixtures. The increase in selectivity was attributed to both, an increase in Coulombic interaction strength proportional to the (quadru)polar moment of the adsorbate, as well as a smaller pore size.[74] While the earlier work of Bae et al.[74] focused on variations of a single structure, the recent study of Bae and Snurr looked at a group of 40 MOFs with the aim of identifying correlations between pore size, surface area, pore volume and heats of adsorption, and five adsorbent selection criteria, including CO_2 uptake and selectivity from CO_2/CH_4, and CO_2/N_2 mixtures. While no clear correlations could be identified for the purely structural properties, weak correlations were observed with the heat of adsorption.

In this chapter, a two-step approach is used in identifying desirable MOF characteristics for the separation of H_2 from mixtures containing CH_4, CO_2, CO and N_2. The study focuses on 11 MOFs, specifically chosen in order to enable the study of isolated characteristics and their impact on adsorption and selectivity. The materials are described in Section 3.1, and the simulation details for studying single component and binary mixture adsorption, as well as for structure characterization are given in Section 3.2. In Section 3.3 the influence of surface area (SA), free volume (FV), and heat of adsorption (Q_{st}) on single component uptake is described for each of the five components of an SMROG stream. The impact of SBU characteristics influencing SA, FV, Q_{st}, such as linker length, linker functional groups, and density of linkers present in the framework, on binary mixture adsorption is assessed in Section 3.4. The findings are summarized in Section 3.5.

3.1 Materials

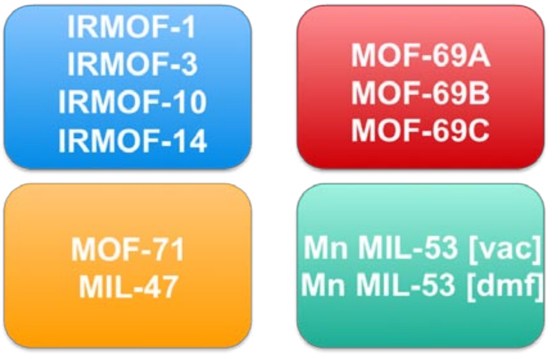

Figure 3-1: The 11 MOFs studied, arranged by isoreticular or isostructural group.

The 11 MOFs chosen in this comparison study are IRMOF-1, IRMOF-3, IRMOF-10, IRMOF-14, MOF-69A, MOF-69B, MOF-69C, MOF-71, MIL-47 and Mn MIL-53 in both, a narrow pore form, [vac] and a large pore form, [dmf]. They incorporate a variety of linkers, as shown in Figure 3-2, and adopt different topologies depending on the inorganic SBUs, resulting in a range of pore sizes, as provided in Table 3-1. By choosing isoreticular and isostructural groups of MOFs as shown in Figure 3-1, it is possible to study the isolated influences of linker properties on adsorption and selectivity. In addition, some members of the MOF families in this study have the same linkers as members of the other groups. For example the BDC linker is found in at least one member of each of the four groups of MOFs. These similarities allow for an investigation into the influence of linker arrangement within a MOF.

BDC
1,4-benzenedicarboxylate
IRMOF-1, MIL-47, MOF-69C, MOF-71
Mn MIL-53 [vac], Mn MIL-53 [dmf]

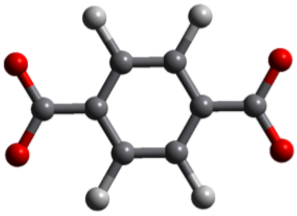

ABDC
2-amino-1,4-benzenedicarboxylate
IRMOF-3

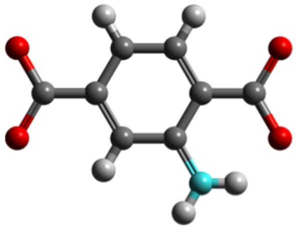

NDC
2,6-naphthalenedicarboxylate
MOF-69B

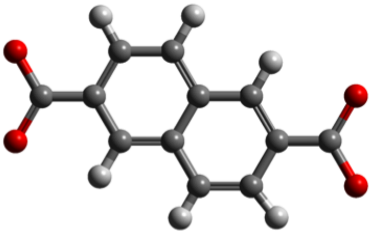

BPDC
Biphenyl-4,4’-dicarboxylate
MOF-69A, IRMOF-10

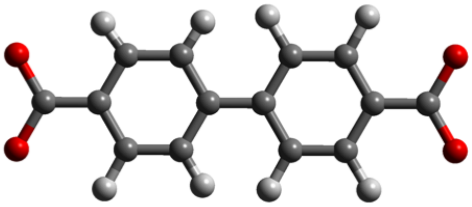

BPNO
4,4’-bipyridine N,N’-dioxide
Mn MIL-53 [vac], Mn MIL-53 [dmf]

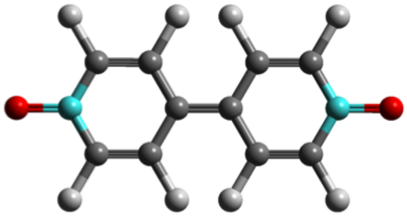

PYDC
pyrene-2,7-dicarboxylate
IRMOF-14

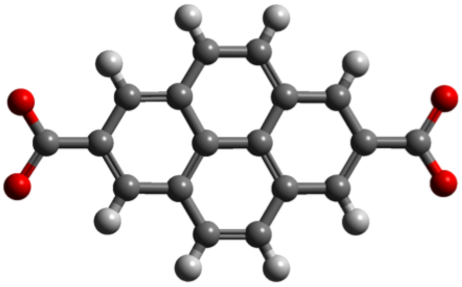

Figure 3-2: Linker groups incorporated in the 11 MOFs investigated. Colour key: oxygen – red, carbon – dark grey, hydrogen – light grey, nitrogen – light blue.

Table 3-1 Pore diameters calculated[75] for each of the 11 MOFs.

Material	**Pore Diameter(s) (Å)**
IRMOF-1	11.1, 14.3
IRMOF-3	9.5, 14.3
IRMOF-10	16.8, 20.0
IRMOF-14	14.9, 20.1
MOF-69A	10.3
MOF-69B	9.0
MOF-69C	6.8
MIL-47	7.4
MOF-71	3.9
Mn MIL-53 [vac]	4.6
Mn MIL-53 [dmf]	5.6

The IRMOF[70] family is well-suited to systematic structural comparison work due to the wide range of linkers that can be incorporated into these structures, while maintaining the topology unchanged. The IRMOF-1, IRMOF-3, IRMOF-10 and IRMOF-14 structures chosen here are composed of Zn_4O clusters joined together by different organic linkers, respectively, as shown in Figure 3-3. The simplest framework, IRMOF-1, is obtained using benzene dicarboxylate (BDC) linkers. IRMOF-3 is obtained by functionalizing each benzene ring with one amine group, a change that alters the distribution of partial charges in the linkers and is expected to lead to increased Coulombic interactions with polar and quadrupolar adsorbate molecules. IRMOF-10 on the other hand is obtained by using the longer BPDC linkers, which contain two benzene rings. These linkers result in an increase in pore size, and free volume. The fourth member of the IRMOF family studied here is IRMOF-14, whose PYDC linkers are similar in length to the BPDC linkers of IRMOF-10, but contain two additional benzene rings. These paddle-shaped linkers are expected to result in an increase in adsorbate – framework interactions compared to IRMOF-10, as molecules adsorbed on these surfaces can interact with a high number of framework atoms simultaneously.

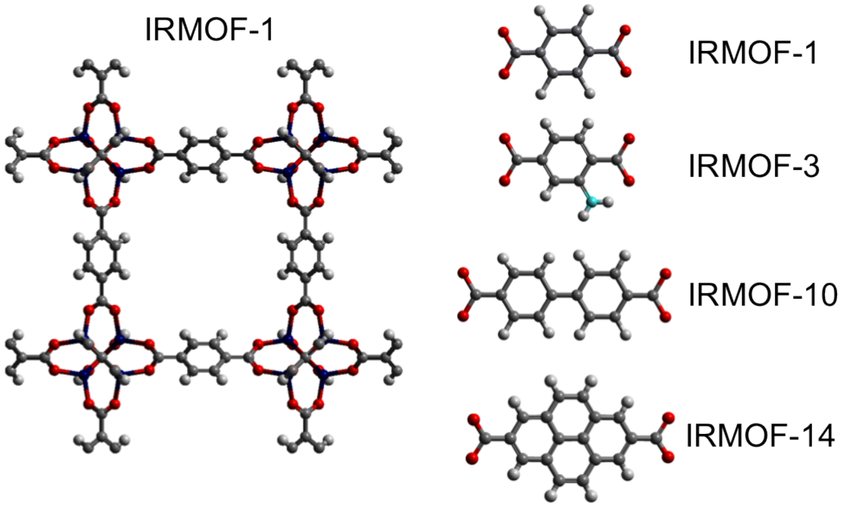

Figure 3-3: The underlying structure of IRMOFs, and the linkers corresponding to IRMOF-1, IRMOF-3, IRMOF-10, IRMOF-14. Colour key: oxygen – red, carbon – dark grey, hydrogen – light grey, nitrogen – light blue, zinc – navy.

The MOF-69 group[76] shown in Figure 3-4 is another zinc-based isoreticular family, however in this case the inorganic SBUs are chains of zinc oxide, forming 1D, rhombic channels. The Zn(II) atoms adopt tetrahedral and octahedral arrangements, which are then linked to each other via μ_3-OH groups as well as to two and four organic linkers each, respectively. The MOF-69C framework contains the same short BDC linkers used in IRMOF-1. The linkers of MOF-69A and B are made up of two benzene rings each, however they differ in the way in which the linkers are connected. In MOF-69A the linkers used to join the metal chains are biphenyl dicarboxylates, whereas MOF-69B contains naphthalene dicarboxylates. As a result the linkers of MOF-69B are longer than those of MOF-69C and shorter than those of MOF-69A.

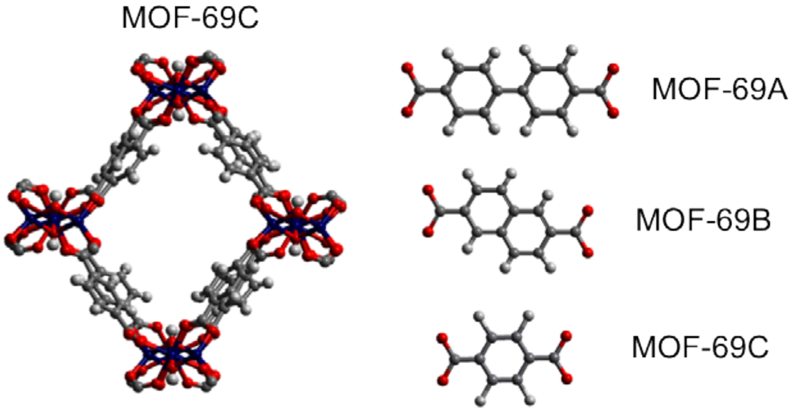

Figure 3-4: The underlying structure and linkers of MOF-69 A, B and C. Colour key: oxygen – red, carbon – dark grey, hydrogen – light grey, zinc – navy.

MOF-71[76] and MIL-47[77] are isostructural frameworks, both having BDC linkers arranged in 1D diamond-shaped pores. The inorganic SBUs in MOF-71 are made up of cobalt oxide chains while in MIL-47 the chains contain vanadium oxide. Unlike the inorganic chains of MOF-69 structures, the V and Co metal centers adopt a corner linked octahedral arrangement. The use of different metals results in a difference in the angles between the BDC linkers joined to each inorganic chain. As a result, the pores of MIL-47 (7.4 Å) are larger than the pores of MOF-71 (3.9 Å), as can be seen in Figure 3-5.

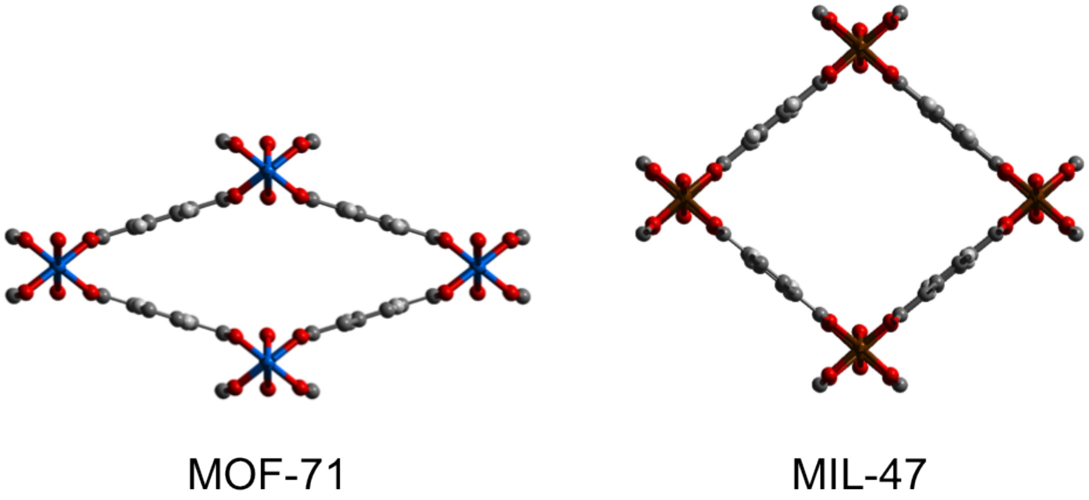

Figure 3-5: The isostructural frameworks MOF-71 and MIL-47. Colour key: oxygen – red, carbon – dark grey, hydrogen – light grey, cobalt – blue, vanadium – brown.

Mn MIL-53 is also made up of rod-like inorganic SBUs, and contains BDC linkers as well as BPNO. The framework was reported to change upon adsorption of DMF, ethanol and a variety of aromatic molecules.[78] Here two forms of the structure are investigated: an evacuated narrow-pore form [vac], and a guest-free larger pore form, [dmf] that is obtained upon dmf adsorption (Figure 3-6).

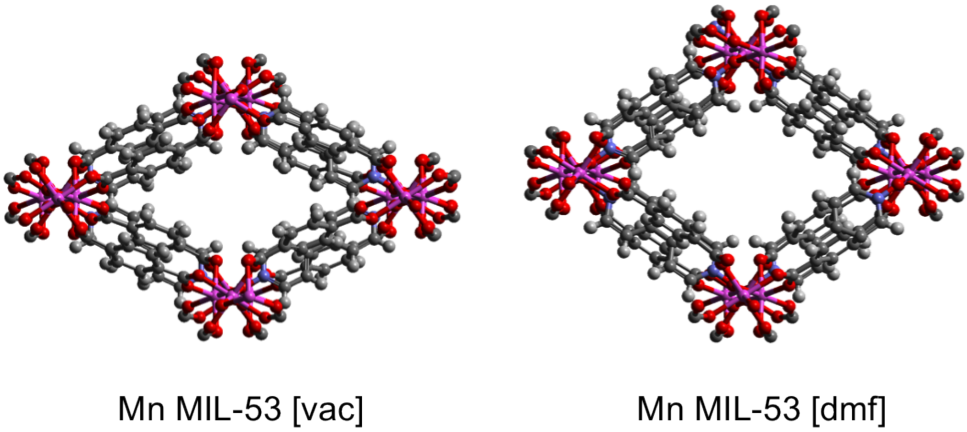

Figure 3-6: Two forms of Mn MIL-53: narrow pore [vac], and large pore [dmf]. Colour key: oxygen – red, carbon – dark grey, hydrogen – light grey, manganese – pink.

3.2 Simulation Details

Pure component as well as mixture adsorption isotherms were calculated using GCMC simulations in the multipurpose simulation code (Music).[79] The simulations were carried out using atomistic models for all frameworks. The atoms were maintained fixed at their crystallographic positions.[70,76,77,80-82] The LJ parameters for framework atoms were represented using the Universal Force Field (UFF).[40] Partial charges for MIL-47[83] and the IRMOF frameworks[84,85] were taken from the literature, while partial charges for the MOF-69 family and MOF-71 were approximated using the method of Xu and Zhong.[86] The connectivity-based atom contribution (CBAC) method of Xu and Zhong assumes that the partial charges for an atom in a certain bonding connectivity is the same for all MOFs.[86] Their study made use of density functional theory (DFT) derived partial charges for 30 MOFs in order to obtain mean partial charge values for a set of common atom types.[86] Partial charges calculated using DFT are the most accurate method for describing electrostatic interactions, however the work presented in this chapter is a comparison study, hence the approximations used in the case of MOF-69 and MOF-71 were deemed acceptable. Partial charges for the Mn MIL-53 frameworks, which are examined in more detail in Chapter 4, were calculated using DFT methods by Linjiang Chen at the University of Edinburgh, and are provided in Chapter 4.

Adsorbate molecules were represented using the LJ parameters provided in Table 2–1 of Chapter 2. CO molecules were modeled using the four-centred model of Piper et al.[48] and a cutoff distance of 12.8 Å was applied for all simulations. Adsorbate-adsorbate and adsorbate-framework Coulombic interactions for N_2, CO and CO_2 were calculated using the Ewald summation method.

Using the simulated mixture adsorption isotherm data, the selectivity of each MOF for one component over another was calculated as follows:

$$S_{AB} = \frac{x_A / x_B}{y_A / y_B} \quad \text{Eq 3-1}$$

Here y_A and y_B are the mole fractions of components A and B in the bulk phase, whereas x_A and x_B are the mole fractions in the adsorbed phase.

The working capacities of each MOF, Δq_i, that is the amount of CH_4, CO_2, CO and N_2 adsorbed from each binary mixture at a chosen high pressure, $q_{i,highP}$, minus what remains adsorbed at a certain low, desorption pressure, $q_{i,lowP}$, were calculated as follows:

$$\Delta q_i = q_{i,highP} - q_{i,lowP} \quad \text{Eq 3-2}$$

The differential enthalpy of adsorption (Q_d) and the isosteric heat of adsorption (Q_{st}) were calculated from simulation data for each of the adsorbates as follows[87] :

$$-Q_d = h_{res,bulk} + RT(1 - z_{bulk}) - \frac{\langle U_{ads} N_{ads} \rangle - \langle U_{ads} \rangle \langle N_{ads} \rangle}{\langle N_{ads}^2 \rangle - \langle N_{ads} \rangle \langle N_{ads} \rangle} \quad \text{Eq 3-3}$$

N_{ads} is the number of adsorbed molecules, and U_{ads} is the potential energy of the adsorbed molecules. If the gas can be assumed to behave as an ideal gas, the bulk phase residual enthalpy, $h_{res,bulk}$ is zero, and the compressibility factor z_{bulk} is 1. Q_{st} is then calculated by subtracting RT from $-Q_d$. In this chapter Q_{st} values were obtained for all 11 MOFs in the low loading regions for each of the five adsorbates.

The geometric free volume and accessible surface area were calculated for each framework using the methods described by Frost, Düren and Snurr.[71] For the surface area calculations, a probe molecule with a diameter of 3.681 Å was rolled over the pore surface of each MOF. The size of the probe molecule was chosen to be equal to the diameter of an N_2 molecule in order to determine the surface area accessible to such molecules. In the case of MOF-71 the pore diameter of 3.9 Å is very similar in size to the probe diameter. This is expected to result in a large error in the accessible surface area calculation, as the probe molecule is too large to access the entire pore volume, in particular the pore corners of the framework. Here the surface areas calculated are used solely for trend and correlation studies. The free volume was calculated using a 0 Å probe molecule to perform trial insertions into the pore space. This results in a geometric measurement of the free volume available inside each MOF.[71]

The calculated Q_{st}, geometric pore volume (FV) and accessible surface area (SA) for each MOF are given in Table 3-2.

Table 3-2: SA, FV and Q_{st} for the 11 MOFs. Q_{st} was determined at 298 K and low loading.

	SA (m^2/g)	**FV (cm^3/g)**	**Q_{st} (kJ/mol)**				
			CH_4	**N_2**	**CO**	**CO_2**	**H_2**
IRMOF-1	3653.36	1.394	11.75	8.79	10.04	14.33	6.07
IRMOF-3	3250.51	1.284	12.33	8.84	10.12	16.13	6.01
IRMOF-10	4974.81	2.747	8.61	7.06	8.07	13.45	3.79
IRMOF-14	4918.52	2.429	9.82	7.96	8.92	15.26	4.04
MOF-69A	1801.88	0.756	16.38	12.56	15.76	21.95	8.58
MOF-69B	1609.54	0.681	17.11	13.34	15.40	22.40	8.56
MOF-69C	1147.68	0.459	18.27	14.53	15.16	23.09	10.61
MIL-47	1534.09	0.641	17.05	13.11	14.79	22.66	7.67
MOF-71	167.42	0.273	18.73	16.50	22.76	42.91	7.77
Mn MIL-53 vac	288.87	0.221	24.33	19.26	20.27	37.81	10.83
Mn MIL-53 dmf	730.46	0.352	21.77	16.85	18.25	30.69	9.78

3.3 Influence of Q_{st}, SA and FV on Gas Uptake

Single component isotherms were simulated for the five components of dry SMROG, namely carbon dioxide, methane, carbon monoxide, nitrogen and hydrogen. The simulated isotherms for each of the 11 investigated structures are all Type 1, and are plotted on a semi-log scale in Figure 3-7 to Figure 3-11 in order to enable a closer a look at the low pressure regions. The highest CO, CO_2, CH_4 and N_2 loadings in the low pressure region of the isotherm correspond to MOF-71, MOF-71, MIL-47, and the [dmf] form of Mn MIL-53, respectively. These MOFs have relatively small pores, resulting in a high potential overlap, and therefore strong adsorbate-framework interactions. At high pressure the highest loading of CO, CO_2, N_2 and CH_4 is observed in IRMOF-10 and IRMOF-14, which can be explained by the presence of large open pores that are able to accommodate a greater number of molecules. On the other hand, the highest H_2 loading corresponds to IRMOF-10 and IRMOF-14 across the entire pressure range. As reported by Frost et al. H_2 uptake at 298 K is correlated with the pore volume at low as well as high pressure,[88] which explains the H_2 loadings observed in each of the 11 MOFs in Figure 3-11.

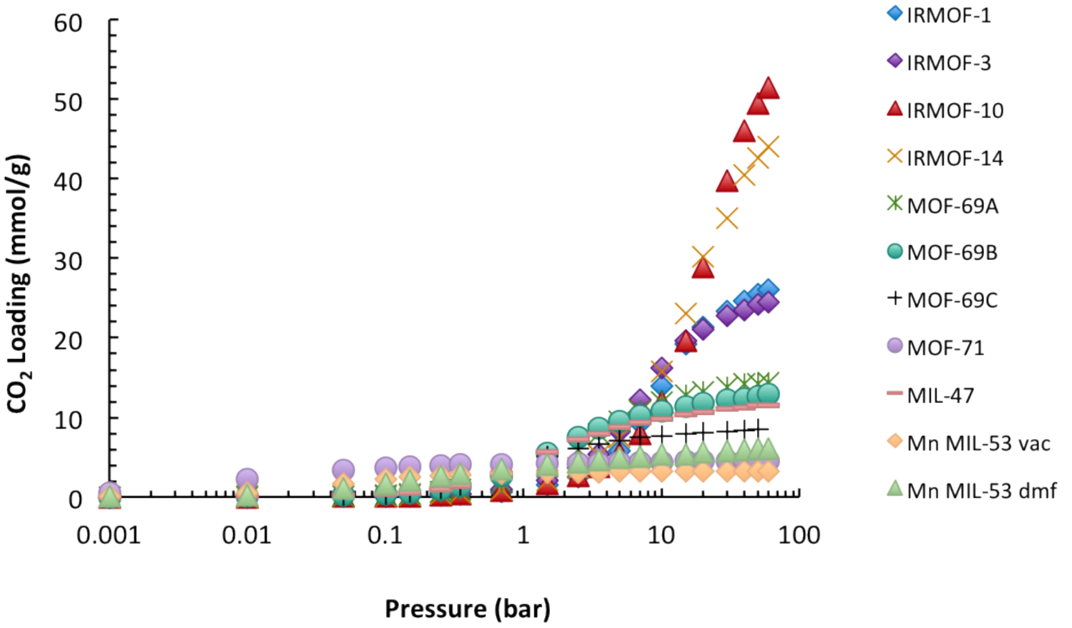

Figure 3-7: Simulated CO_2 adsorption isotherms in 11 MOFs at 298 K.

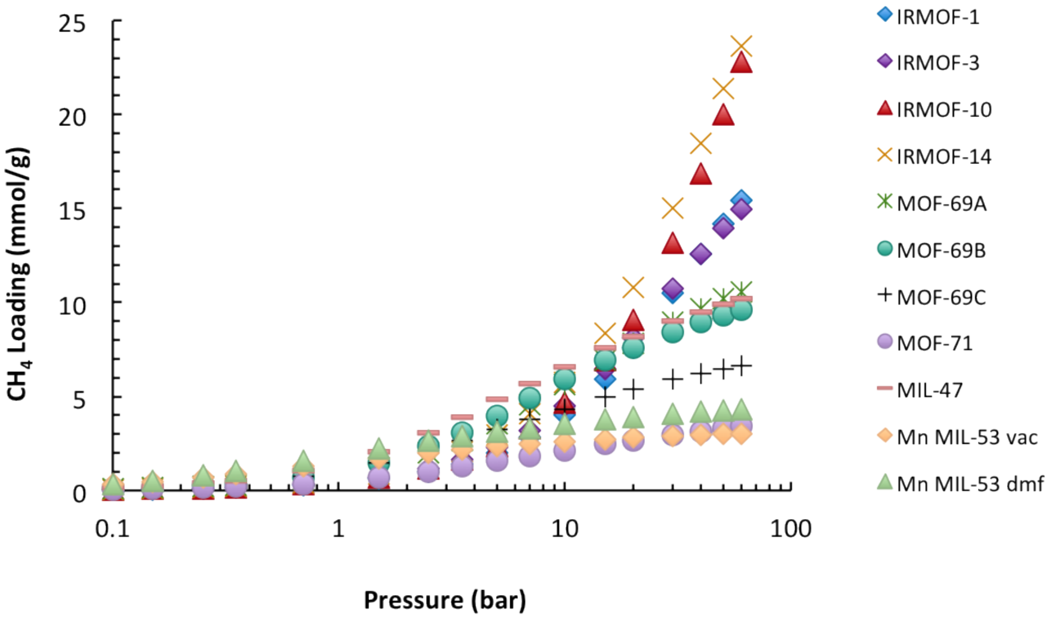

Figure 3-8: Simulated CH_4 adsorption isotherms in 11 MOFs at 298 K.

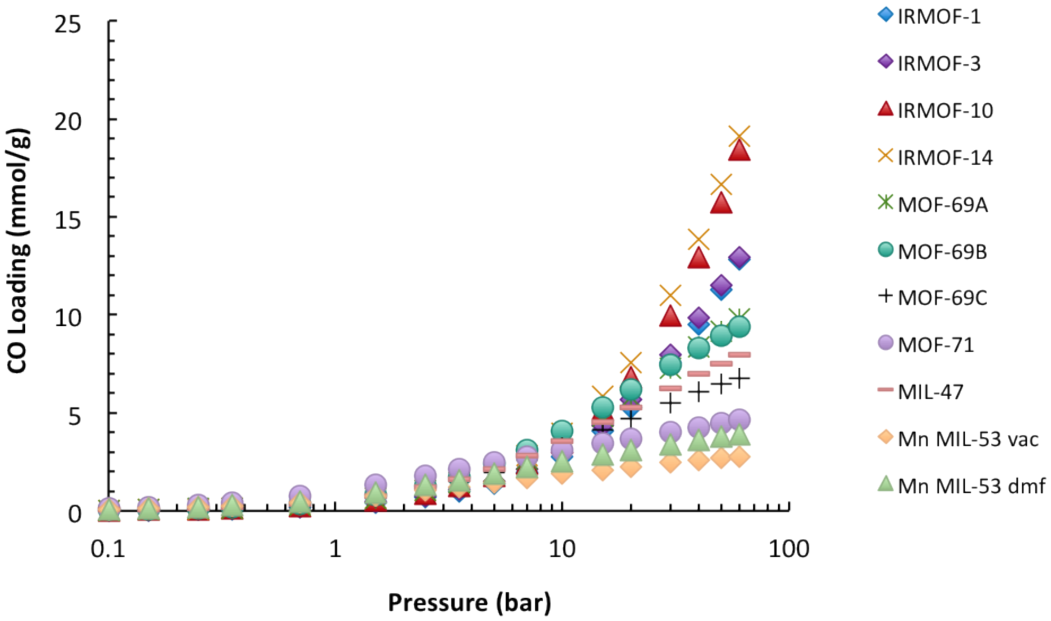

Figure 3-9: Simulated CO adsorption isotherms in 11 MOFs at 298 K.

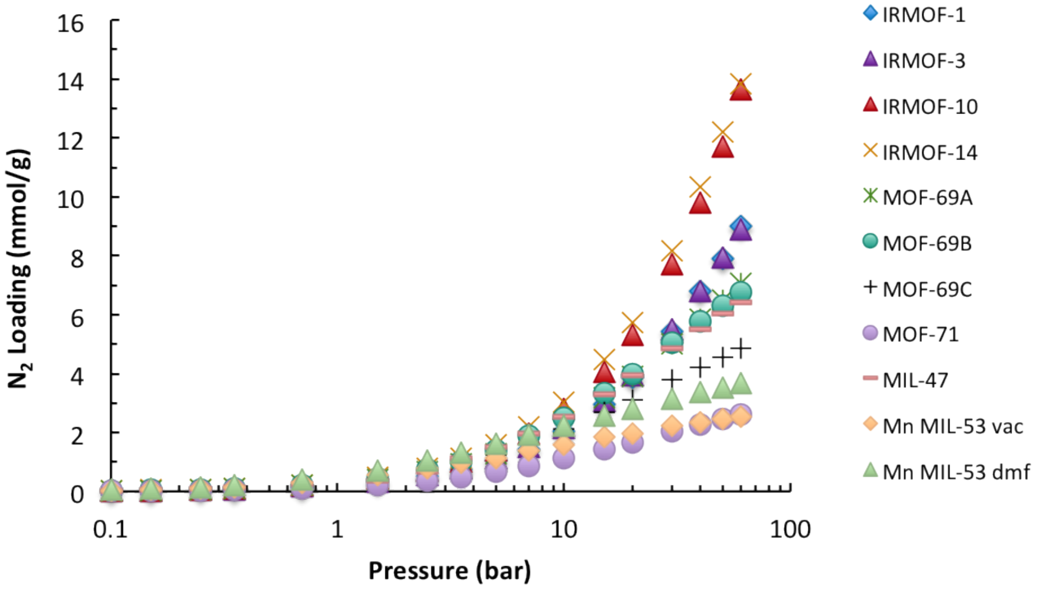

Figure 3-10: Simulated N_2 adsorption isotherms in 11 MOFs at 298 K.

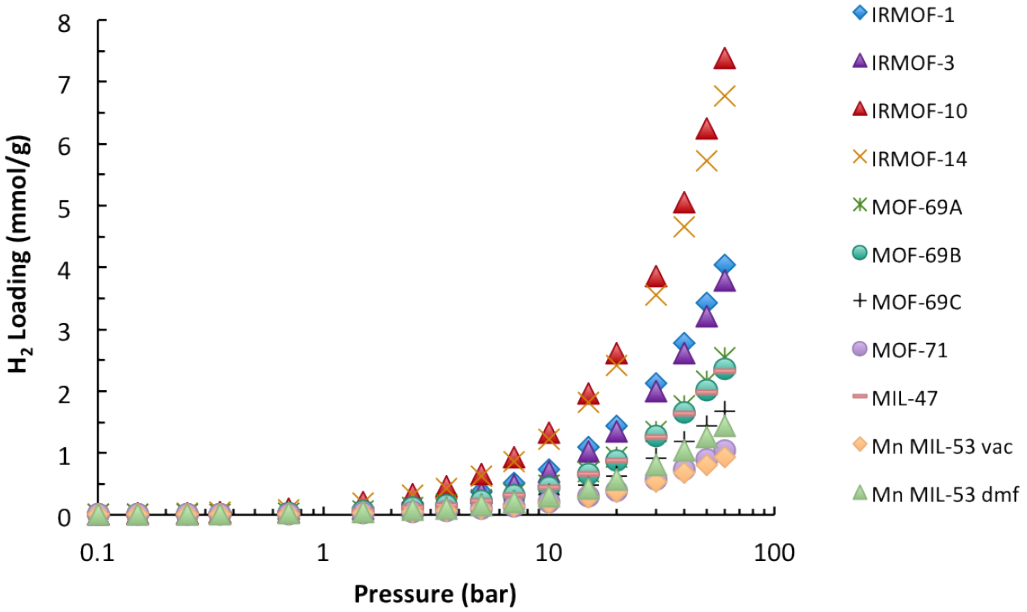

Figure 3-11: Simulated H_2 adsorption isotherms in 11 MOFs at 298 K.

The correlation studies of Frost et al.[88] are essential in understanding how H_2 adsorption in MOFs is influenced by pore volume, surface area and isosteric heat of adsorption. In this work, the same correlations were studied for the remaining four SMROG components, and compared to those observed for H_2. Detecting differences in the factors influencing the uptake of hydrogen compared to the remaining four SMROG components can help identify opportunities for creating a more competitive adsorption process for gas mixtures by facilitating the search for effective adsorbents.

In order to understand the relationship between MOF characteristics and the adsorption of each of the five gases, the degree of correlation between gas uptake and the isosteric heat of adsorption at low loading (Q_{st}), the accessible surface area (SA), and the free volume (FV) provided in Table 3-2 were analyzed. Scatter plots of uptake as a function of each of the three factors were fitted using linear trendlines, and the R^2 coefficients of determination were recorded. The goodness-of-fit R^2 coefficients reflect how well the change in loading with FV, SA and Q_{st} can be represented by a linear relationship. The analysis was repeated over the isotherm pressure range in order to determine how the correlations change with loading, and the results for each of the five gases are plotted in Figure 3-12.

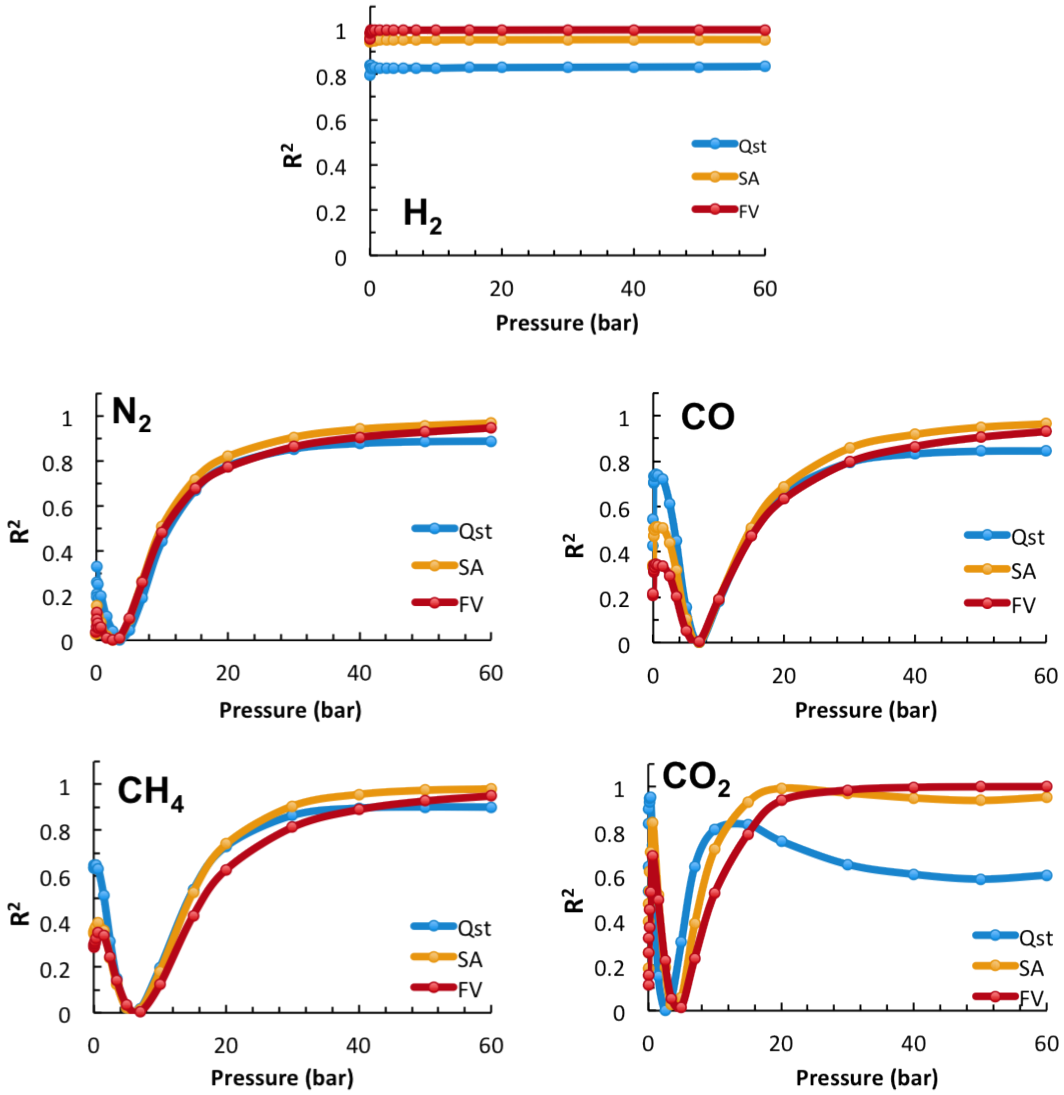

Figure 3-12: R^2 coefficient of determination representing the goodness of fit for linear trendlines used to correlate uptake with Q_{st}, SA and FV.

The trends observed for H_2 adsorption are in agreement with the correlations reported by Frost et al.,[88] showing that H_2 uptake is strongly correlated with the pore volume and surface area over the whole pressure range. H_2 uptake is also observed to have a weaker correlation with Q_{st}, however this is due to the relationship between FV, SA and Q_{st} in MOFs. In general, MOFs with high accessible surface areas tend to have large open pores, resulting in a weak potential overlap and therefore weaker adsorbate-framework interactions, which results in low Q_{st} values. These relationships are highlighted by the strong correlations between the FV and SA and between SA and Q_{st} provided in Figure 3-13, which were determined using the data corresponding to the 11 MOFs. The correlation curves for CO, CH_4, N_2 and CO_2 on the other hand, while similar to one another, are strikingly different from those of H_2. In the high pressure region CO_2, CO, CH_4 and N_2 uptake is strongly correlated with the accessible surface area and free volume. In the case of CO, CH_4, and N_2, a negative correlation with Q_{st} at high pressure is also observed, which can once again be attributed to the link between the free volume and the isosteric heat of adsorption. This negative correlation of uptake with Q_{st} in the high pressure region is weaker for CO_2, an effect that is due to a cooperative adsorption process. As pressure increases the adsorption of additional CO_2 molecules is facilitated by CO_2-CO_2 interactions, which also results in an increase in Q_{st}. The R^2 values plotted in Figure 3-12 were determined using Q_{st} values determined at low loading and therefore do not reflect the increase in Q_{st} with loading. This effect is not observed for CO, CH_4, N_2 and H_2, as Q_{st} does not change significantly with pressure for these molecules.

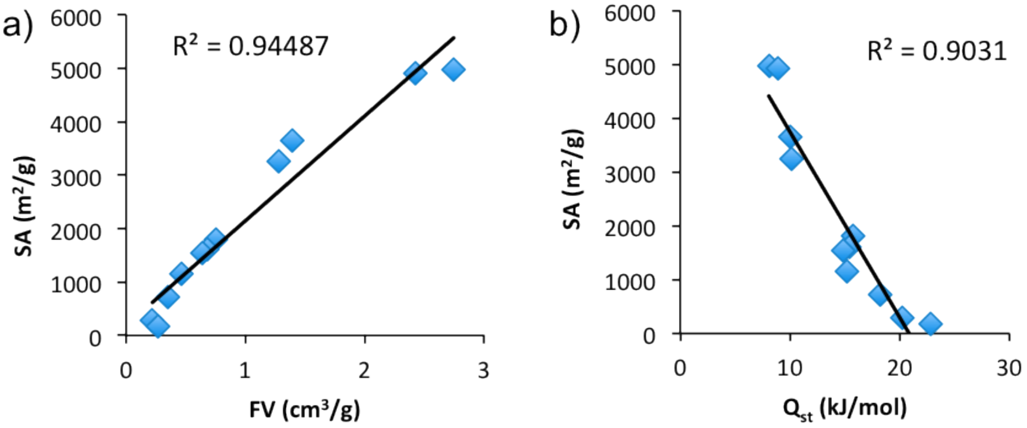

Figure 3-13: Coefficients of determination from correlation plots obtained for a) SA and FV and b) SA and Q_{st}.

The correlation curves for CO, CO_2, CH_4 and N_2 show a dip to zero at medium pressures. In order to better understand the reason for this behavior, the scatter plots showing the relationship between gas uptake and FV, SA and Q_{st} were examined at low, medium and high pressure. The same general trends were observed for all four gases, and in Figure 3-14 scatter plots of the CO uptake correlations at 0.05 bar, 7 bar and 40 bar with each of the three factors are provided. At 0.05 bar, CO uptake correlates well with the low loading Q_{st}, while weaker negative correlations with FV and SA can also be observed. As mentioned earlier, such weak negative correlations are due to the relationship between Q_{st} and FV and SA in MOFs. At 7 bar there is no correlation between uptake and each of the three factors. The reason for this is that as pressure increases, some of the small pore MOFs, with high Q_{st} values, approach their saturation loading, while in larger pore MOFs, with lower Q_{st} values, uptake continues to increase with increasing pressure. This results in a decrease in the correlation of loading with Q_{st} in the medium pressure range. The link between Q_{st} and the FV and SA, results in a similar dip in the FV and SA correlations. This dip in the correlation plots is occurs at the same pressure at which the isotherms in Figure 3-9 are observed to cross. At this point, the isotherms corresponding to MOFs with a large FV are steep due to a strong dependence of uptake on Qst. On the other hand the isotherms corresponding to the small pore MOFs have more gentle slopes as the high interaction sites have been occupied, and adsorption is now at the pore filling stage. As pressure increases further to 40 bar, the uptake in the larger pore MOFs becomes proportional to the amount of space available inside the MOF pores. This results in an increase in correlation of uptake with FV. Therefore, when going from low to high pressure there is a change from weak negative FV and SA correlations with uptake towards strong positive correlations, while the reverse is true for Q_{st}. Once molecules start to adsorb in the centres of the pores, rather than on the pore wall surfaces uptake becomes less correlated with Q_{st} and increasingly correlated with FV. While only CO correlations are shown in Figure 3-14, the same trends were also observed for CH_4, CO_2 and N_2.

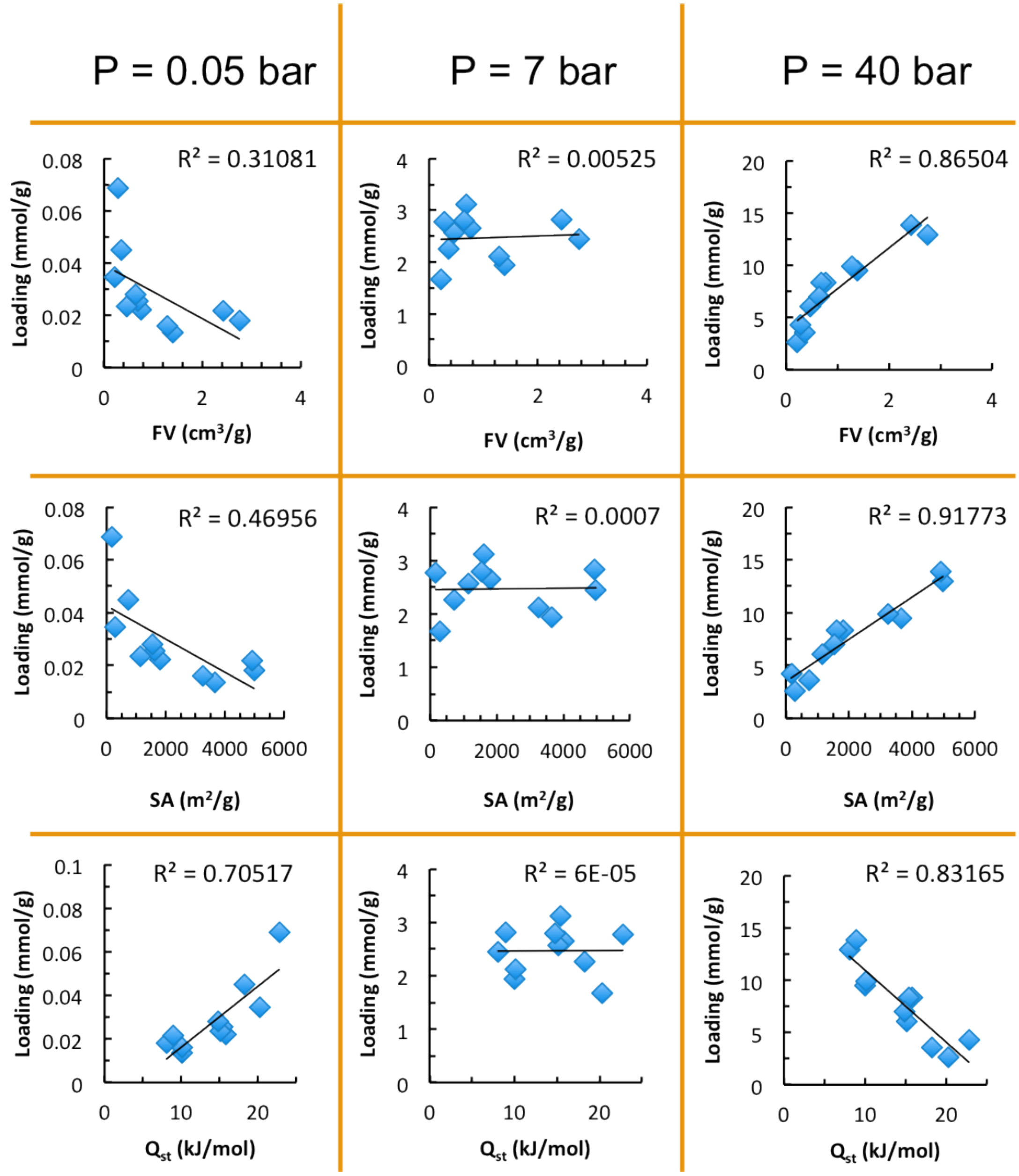

Figure 3-14: Coefficients of determination for linear fitting of scatter plots of CO loading as a function of the free volume, FV, (top row), the accessible surface area, SA (middle row) and the low loading isosteric heat of adsorption, Q_{st} (bottom row), calculated for three different pressures: 0.05 bar (left column), 7 bar (middle column) and 40 bar (right column).

It must also be mentioned that a significant improvement in low pressure correlations is observed when the data points for MOF-71 are not included. An example of the improvement observed for the N_2 correlation of uptake with Q_{st} at 0.05 bar is provided in Figure 3-15. The pores of MOF-71 are nearly the same size as the kinetic diameter of N_2 molecules, resulting in a very high potential overlap and therefore high Q_{st}. The narrow pores however are only able to accommodate a limited number of molecules, therefore the data point obtained for MOF-71 does not follow the same trend that is observed for the other 10 MOFs. A similar effect is observed for CO_2, CO and CH_4, for all three factors considered the exclusion of MOF-71 data from the correlation analysis was not observed to change the shape of the curves in Figure 3-12.

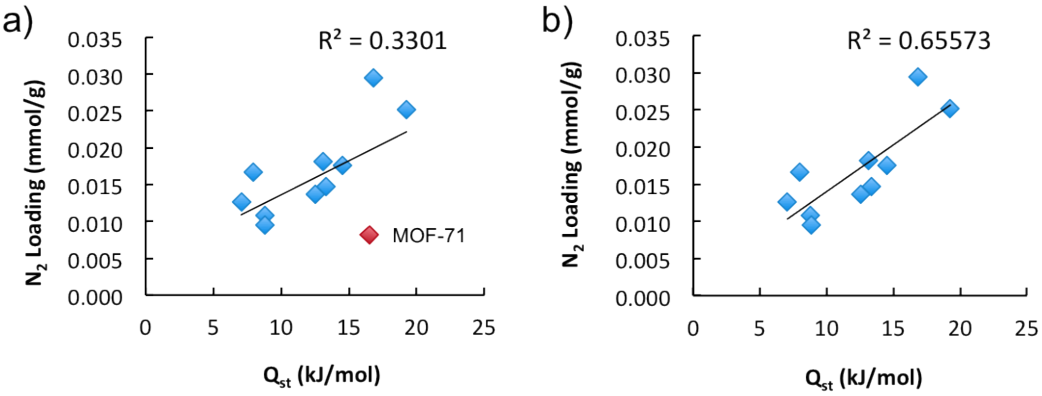

Figure 3-15: Goodness of fit for scatter plots of N_2 uptake at 0.05 bar and 298 K as a function of the isosteric heat of adsorption, Q_{st}, obtained by a) including MOF-71 data, and b) excluding MOF-71 data.

Considering that the partial charges employed in MOF-71 simulations were obtained using an approximation method, it is important to understand the sensitivity of gas uptake to inaccuracies in the assigned partial charges. Figure 3-16 presents a comparison of CO_2 uptake in MOF-71 using the initially appointed charges, to the uptake simulated using partial charges artificially increased or decreased by 10%. It is clear that modifying the MOF-71 partial charges by ±10% has a minimal influence on uptake above 0.05 bar. As a result the outlying MOF-71 data point is not caused by insufficiently accurate partial charges, but by the size of the pores.

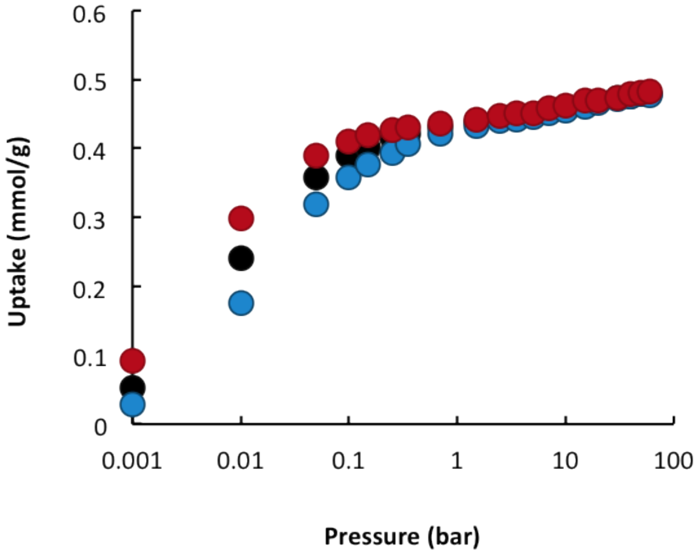

Figure 3-16: CO_2 uptake in MOF-71 simulated using the originally appointed partial charges (black), partial charges artificially decreased by 10% (blue), and partial charges artificially increased by 10% (red).

At low and medium pressures, there is a remarkable difference between the correlation curves observed for H_2 adsorption and those obtained for the remaining four gases shown in Figure 3-12. Adsorption of H_2 is strongly correlated with FV and SA across the entire pressure range, whereas CO, CH_4, CO_2 and N_2 show a correlation with Q_{st} at low pressure, followed by a dip towards zero correlations at medium pressures. The reason for this difference is explained in Figure 3-17 using a comparison of CO and H_2 correlations at low pressure (0.05 bar). H_2 uptake shows a positive correlation slope with FV, and as a consequence of the link between FV and Q_{st}, has a negative Q_{st} correlation slope. The opposite is true for CO uptake, which shows a strong positive correlation with Q_{st}, and a weak negative correlation with FV. These differences can be exploited in order to increase a material's uptake of CO, CH_4, N_2, and CO_2, while simultaneously decreasing its H_2 uptake. Moving along the x-axes of the graphs shown in Figure 3-17, it is clear that a decrease in FV, or an increase in Q_{st} results in a decrease in H_2 uptake and an increase in CO uptake. The correlations observed in Figure 3-12 can be used to optimize MOF properties, and increase a material's selectivity for CO, CO_2, CH_4 and N_2, from H_2 mixtures. Several strategies can be used in order to increase Q_{st} by increasing the adsorbate-framework interaction strength, as well as the density of highly selective sites in MOFs. Three such strategies are discussed in the next section.

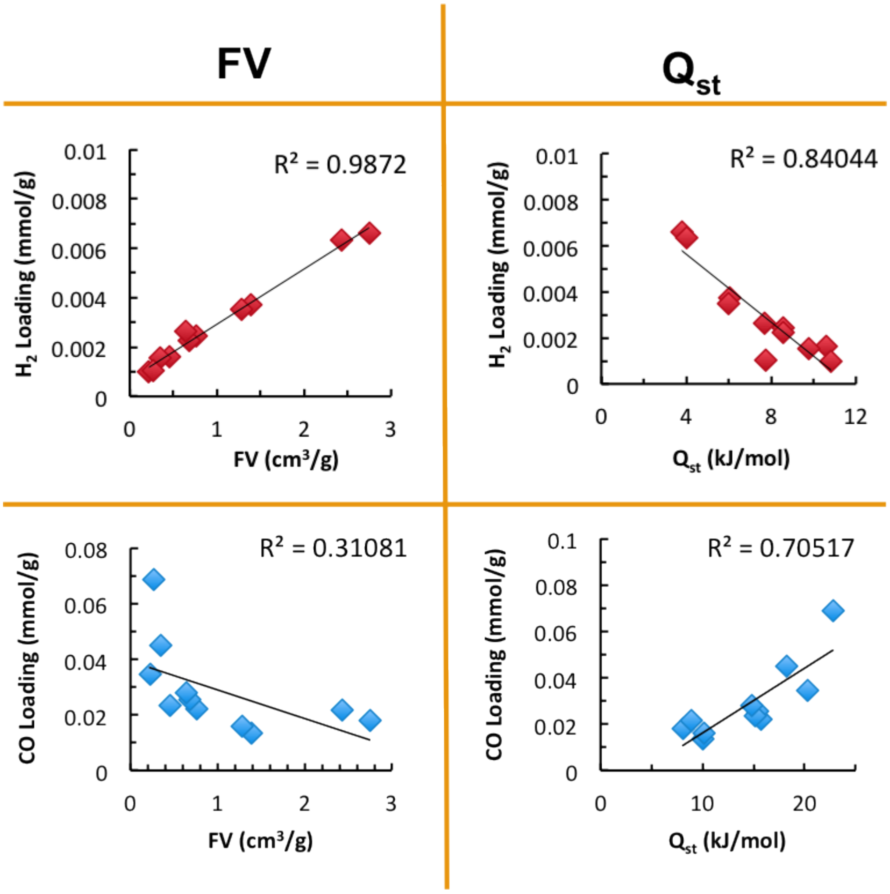

Figure 3-17: Scatter plots and coefficients of determination for the linear fitting of H_2 loading (red), and CO loading (blue) as a function of the FV (left column), and the low loading Q_{st} (right column), calculated at 0.05 bar.

3.4 Factors Influencing MOF Selectivity

Having identified a strategy for improving the ability of MOFs to separate hydrogen from four other gases, it is now important to identify effective methods for eliciting the desired changes in MOF properties. In this section, a mixture adsorption study performed on a chosen set of MOFs is used in order to assess whether an increase in Q_{st} and a decrease in FV can be achieved through certain structural changes. The adsorption of four binary mixtures, each containing 70% H_2, which is the same as the hydrogen content of an SMROG stream, and a balance of CH_4, CO, CO_2, or N_2 was studied using GCMC simulations. The simulations were carried out for all 11 MOFs at 298 K for pressures ranging from 1x10^{-4} to 40 bar. Mixture adsorption data was then used to determine the CH_4/H_2, CO_2/H_2, CO/H_2 and N_2/H_2 selectivities of each structure. Differences in framework selectivity were then used in order to assess the influence of a variety of framework characteristics on the adsorption of each mixture. The framework features considered in this work include the length of the organic linkers, the presence of NH_3^+ functional groups or additional aromatic rings, and the density of the organic linkers present in the framework, the latter of which is heavily influenced by the form of the inorganic SBU. The frameworks compared were chosen in such a way as to allow for the study of one isolated property at a time.

3.4.1 Linker Length

The MOF-69A, B, and C frameworks contain unfunctionalized linkers of incrementally shorter lengths, and are therefore perfectly suited for the study of the influence of linker length on selectivity. The calculated selectivities for the N_2:H_2, CO_2:H_2, CO:H_2, and CH_4:H_2 mixtures are presented in Figure 3-18. The framework with the shortest linkers, MOF-69C, has the highest CO_2, CO, N_2 and CH_4 selectivities, followed by MOF-69B and MOF-69A. This behaviour is linked to the trends observed in the correlation plots. An increase in linker length causes an increase in FV, resulting in higher uptake of H_2 over the entire pressure range. In addition, longer linkers lead to lower Q_{st} values for all adsorbates as shown in Table 3-2, thereby reducing the uptake of CO_2, CO, CH_4 and N_2. As a result, in order to increase MOF selectivity for each of the four gases over H_2 it is important to minimize the length of the linkers making up the framework.

The drawback of incorporating short linkers into frameworks is the comparatively low gas uptake at high pressure, which can lead to low working capacities in gas separation applications. As a result, selectivity and capacity should be studied together when selecting the organic linkers of MOFs.

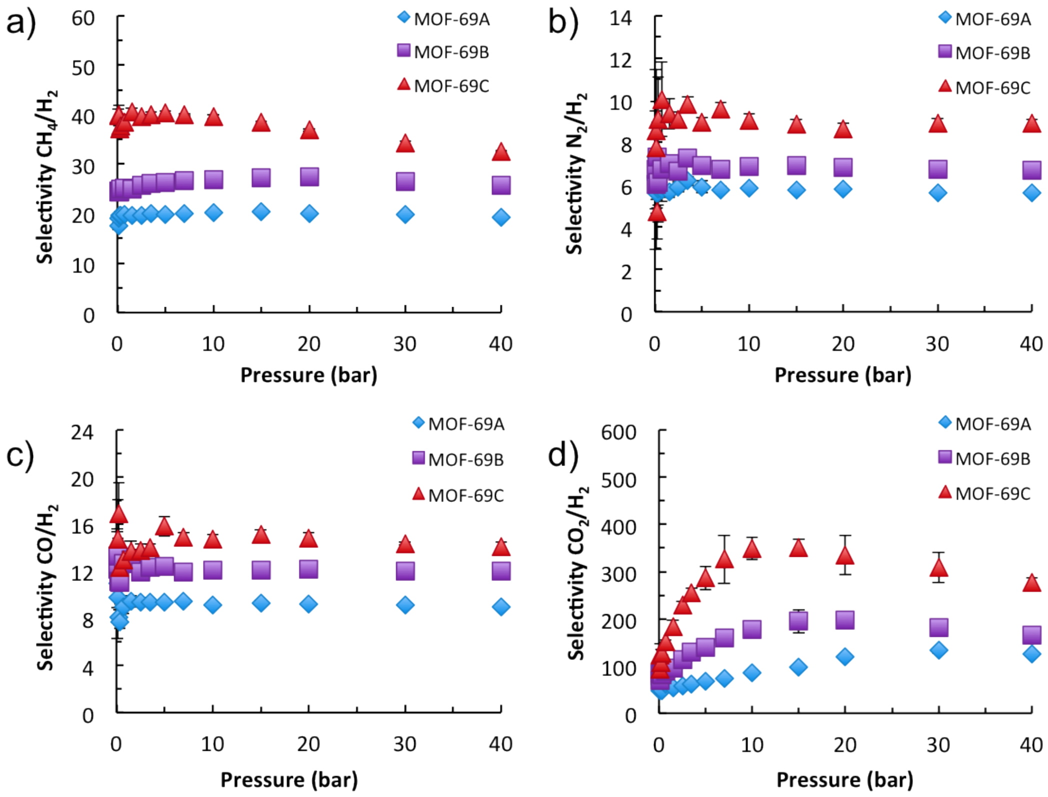

Figure 3-18: Selectivity plots for MOF-69A, B and C from adsorption simulations of 30:70 mixtures of a) CH_4:H_2, b) N_2:H_2, c) CO:H_2, and d) CO_2:H_2. The error bars are shown in black.

3.4.2 Linker Functionalization

How the selectivity changes with linker functionalization can be studied on two pairs of MOFs: IRMOF-1 and IRMOF-3, and IRMOF-10 and IRMOF-14. The ABDC linker of IRMOF-3 is obtained by adding an amine group to the BDC linker of IRMOF-1. On the other hand, the difference between the IRMOF-10 BPDC linkers and the IRMOF-14 PYDC linkers lies in the number of aromatic rings incorporated while the pore size remains the same. The PYDC linkers are not produced through the addition of aromatic rings to BPDC linkers, but through a complex synthesis pathway, and are therefore not a true example of functionalization. Nevertheless it is important to consider the influence of aromatic groups on selectivity. It should be noted that the presence of functional groups causes IRMOF-3 and IRMOF-14 to have lower free volumes than IRMOF-1 and IRMOF-10. All four MOFs however, have relatively large pore sizes, therefore adsorption and selectivity will be most strongly influenced by the strength of adsorbate-framework interactions rather than by the free volume. The selectivities determined from GCMC simulations of the four 30:70 mixtures are shown in Figure 3-19. IRMOF-3 results in higher selectivities than IRMOF-1 indicating that amine groups are beneficial in the separation of H_2 from each of the four gases. The amine group is responsible for generating stronger Coulombic interactions between the (quadru)polar adsorbates and the framework. In the case of CO_2 the increased electrostatic interactions in IRMOF-3 result in higher uptake of CO_2, and at the same time facilitate a cooperative adsorption process, as additional CO_2 molecules are able to interact with a greater number of already adsorbed CO_2 molecules. This effect is not as strong for $CO:H_2$ mixtures, as CO-framework interactions are particularly weak in IRMOFs, resulting in relatively low uptakes even at high pressure. A comparison of mixture adsorption in IRMOF-14 and IRMOF-10 shows that a larger number of aromatic rings in each linker results in higher selectivities for all four mixtures. The addition of amine groups, or aromatic rings causes a decrease in FV and an increase in Q_{st}, resulting in higher framework selectivity.

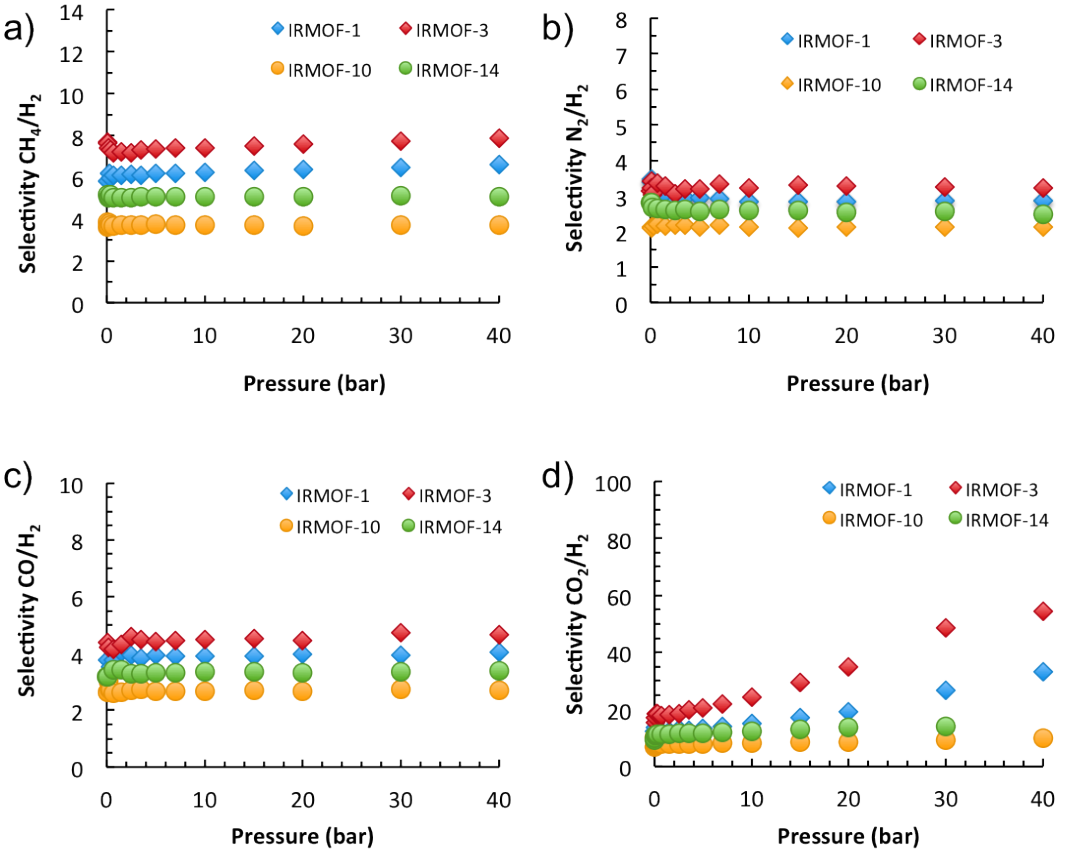

Figure 3-19: Selectivity plots for IRMOF-1, -3, -10 and -14 from adsorption simulations of 30:70 mixtures of a) CH_4:H_2, b) N_2:H_2, c) CO:H_2, and d) CO_2:H_2.

3.4.3 Density of Linker Groups

In addition to determining the effect of linker length and functional groups on selectivity, it is also important to study how the arrangement of linkers within a MOF affects adsorption of gas mixtures. The challenge in studying this particular factor stems from the vast array of underlying nets that can be exhibited by MOFs. The extensive research of O'Keefe and coworkers[89-91] has led to the characterization of numerous structures, and the identification of their underlying topology based on SBU geometries and coordinations. The Reticular Chemistry Structure Resource (RCSR) database developed by O'Keefe et al.[91] contains approximately 1600 periodic nets, which can be used to describe and classify a variety of MOF frameworks. A comparison of the influence of each type of net on selectivity would be a thorough, yet mountainous undertaking. The task can be simplified by focusing on a structural property that is heavily influenced by SBU arrangement: the density of linker groups.

The inorganic building units of MOFs can be arranged in a wide array of clusters, or rods, with various degrees of coordination. In addition, organic SBUs can also differ in terms of connection modes. The chosen metal and organic SBU arrangements dictate the number of organic linkers present in a given volume of MOF, which is here referred to as linker density. The densities of linkers in five of the 11 MOFs are provided in Table 3-3.

Table 3-3: Density of linkers in 5 MOFs, expressed as no. of linkers per unit of volume.

	Linkers per Unit Cell	**Unit Cell Volume (nm^3)**	**Linker Density (No. Linkers/ nm^3)**
IRMOF-1	24	17.24	1.39
MOF-69C	12	4.40	2.72
MIL-47	4	1.53	2.61
Mn MIL-53 [vac]	12	3.03	3.96
Mn MIL-53 [dmf]	12	3.38	3.55

The linker density of a MOF influences both, the free volume available inside the pores, as well as the extent of potential energy overlap, and therefore the isosteric heat of adsorption. In Figure 3-20, the correlations between CO loading and the linker density are plotted at the same three pressure regimes that were investigated in Figure 3-13. The correlations of uptake with linker density mirror the correlations that were observed between CO loading and Q_{st}. The same trends were observed for CO_2, N_2 and CH_4. This indicates that at low pressure a higher linker density will result in a higher uptake of CO due to a higher Q_{st}, whereas at high pressure, MOFs with a lower linker density would result in a greater uptake.

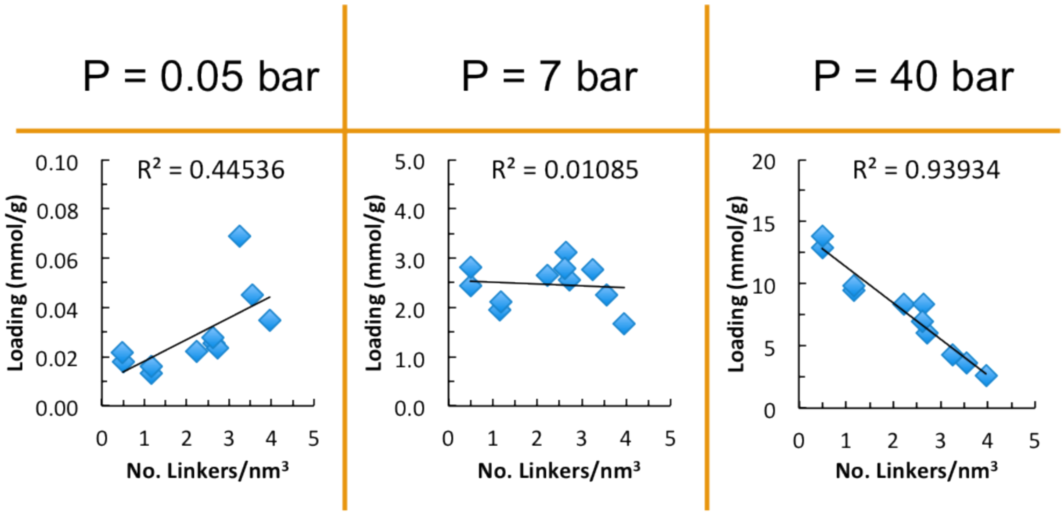

Figure 3-20: Coefficients of determination for linear fitting of scatter plots of CO loading as a function of the linker density at three different pressures: 0.05 bar, 7 bar and 40 bar.

In this work, the effect of linker density on MOF selectivity is first assessed through a comparison of the CO_2, CO, N_2 and CH_4 selectivities observed for IRMOF-1, MOF-69C and MIL-47, which are plotted in Figure 3-21. The three MOFs all contain BDC linkers, however the inorganic SBU of each structure is different: IRMOF-1 contains zinc oxide clusters, MOF-69C has zinc oxide rods, while MIL-47 has vanadium oxide rods. The similarity between the MOF-69C and MIL-47 inorganic SBUs generate structures with similar linker densities, while IRMOF-1 clusters lead to a significantly lower density of linker groups. As shown in Figure 3-21, a higher linker density results in higher selectivities for all four mixtures, which can be explained by the shorter distances between neighbouring linkers, leading to a greater potential overlap. Naturally, the higher linker density also results in a decrease in FV, reducing H_2 uptake.

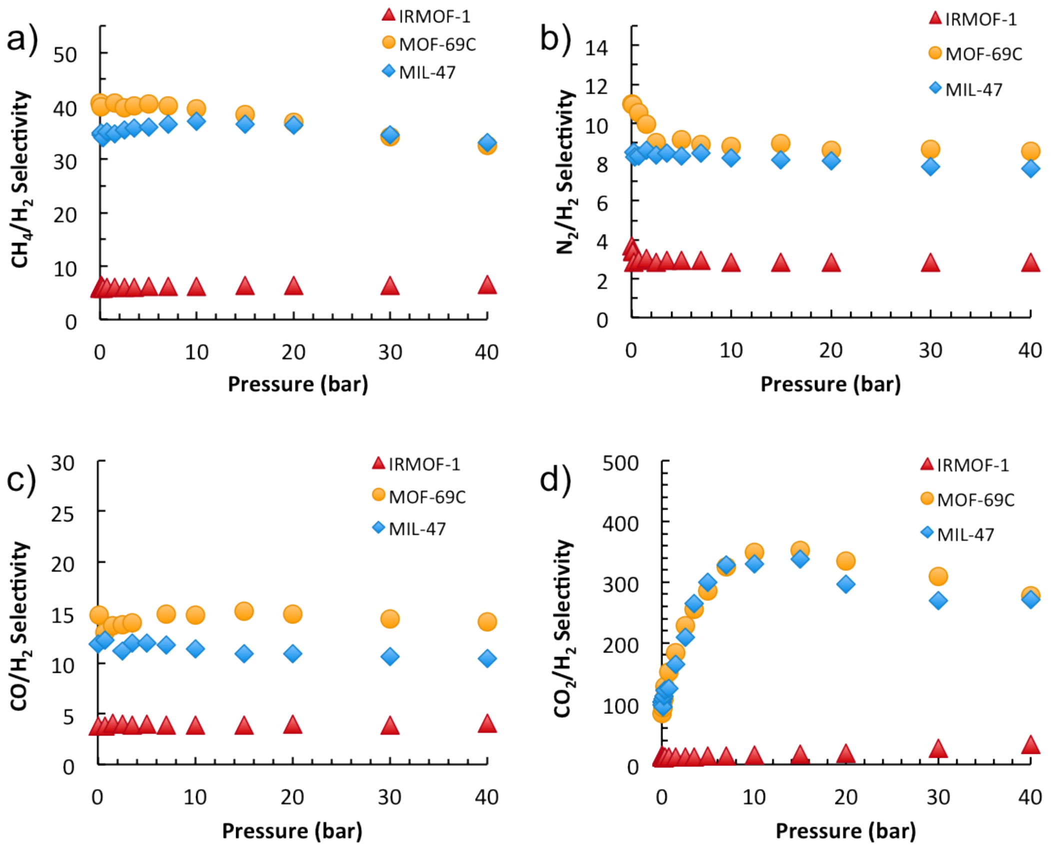

Figure 3-21: Selectivity plots for IRMOF-1, MOF-69C and MIL-47 from adsorption simulations of 30:70 mixtures of a) CH_4:H_2, b) N_2:H_2, c) CO:H_2, and d) CO_2:H_2.

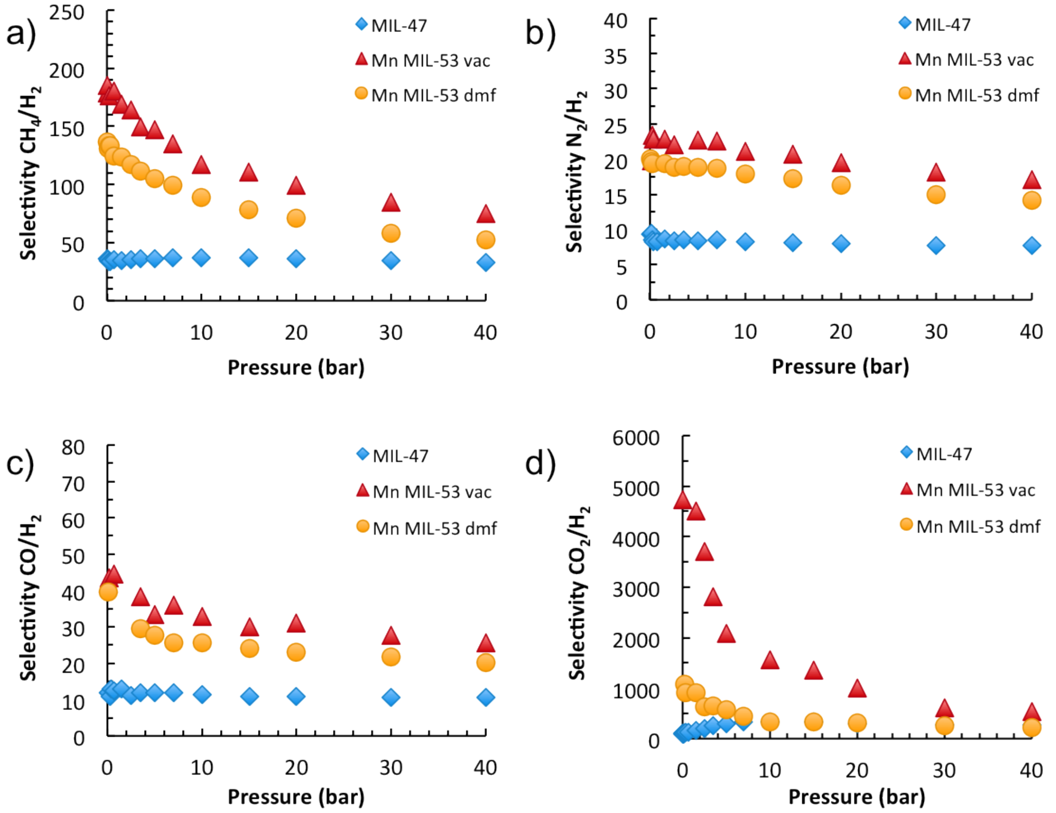

Figure 3-22: Selectivity plots for MIL-47, Mn MIL-53 [vac] and Mn MIL-53 [dmf] from adsorption simulations of 30:70 mixtures of a) CH_4:H_2, b) N_2:H_2, c) CO:H_2, and d) CO_2:H_2.

The influence of linker density is studied further using a second set of MOFs, namely MIL-47, Mn MIL-53 [dmf] and Mn MIL-53 [vac], the selectivities of which are shown in Figure 3-22. The Mn MIL-53 structures contain BPNO linkers in addition to a similar arrangement of BDC linkers as in MIL-47. The two forms of Mn MIL-53 therefore have higher densities of linker groups than MIL-47. The smaller pores of the [vac] form lead to a lower unit cell volume than in [dmf], further increasing the linker density. Following the same trend observed with the first group of MOFs, the highest selectivities for CO_2, CO, N_2 and CH_4 correspond to the Mn MIL-53 [vac]. In the case of $S_{CO2/H2}$, the large difference between the [dmf] and [vac] forms of Mn MIL-53 is likely due to an efficient packing of CO_2 molecules in the small pores of the [vac] form. The studies performed on the two sets of MOFs show that an increase in linker density leads to a significant improvement in the selectivity of MOFs in all four mixtures, which can be attributed to an increase in the solid-fluid interactions, and is therefore an important parameter to consider when selecting or designing materials for separation applications. In addition, the selectivities of both forms of Mn MIL-53 observed in Figure 3-22 make this MOF potentially suitable for H_2 purification applications. In order to determine the structure's capacity for impurities however, it is important to assess which form is adopted during the adsorption of various gases. The characteristics of Mn MIL-53 are discussed further in Chapter 4.

3.4.4 Adsorbent Performance Indicator

While adsorption selectivity is an important characteristic to examine in choosing MOFs for separation and purification applications, separation efficiency is also heavily influenced by a material's working capacity, that is its ability to adsorb a large amount of impurities at high pressure and then release them at low pressure. In order to enable a material's potential for a variety of gas separations to be studied while simultaneously taking into account its selectivity, working capacity and the heat of adsorption for the most strongly adsorbed mixture component, Wiersum et al. developed an Adsorbent Performace Indicator (*API*)[92] which can be calculated as follows:

$$API = \frac{\left(S_{i/j} - 1\right)^{A} WC_{i}^{B}}{\left|Q_{st,i}\right|^{C}} \qquad \text{Eq 3-4}$$

Here *A*, *B* and *C* are weighing factors that can be adjusted in order to increase the contribution of the selectivity, $S_{i/j}$, the working capacity *WC* and the heat of adsorption for the more strongly adsorbed component Q_{st}, respectively. In this work A, B and C were all set to 1, and the *API* was evaluated for all 11 MOFs. In order to study the separation efficiency of the materials under different separation conditions, two working scenarios were considered: a separation where adsorption takes place at 10 bar and desorption is carried out at 1 bar, and a process where adsorption is performed at 20 bar with desorption carried out at 1 bar. The *API* was evaluated for each of the four binary mixtures discussed in the previous sections, and the results are shown in Figure 3-23.

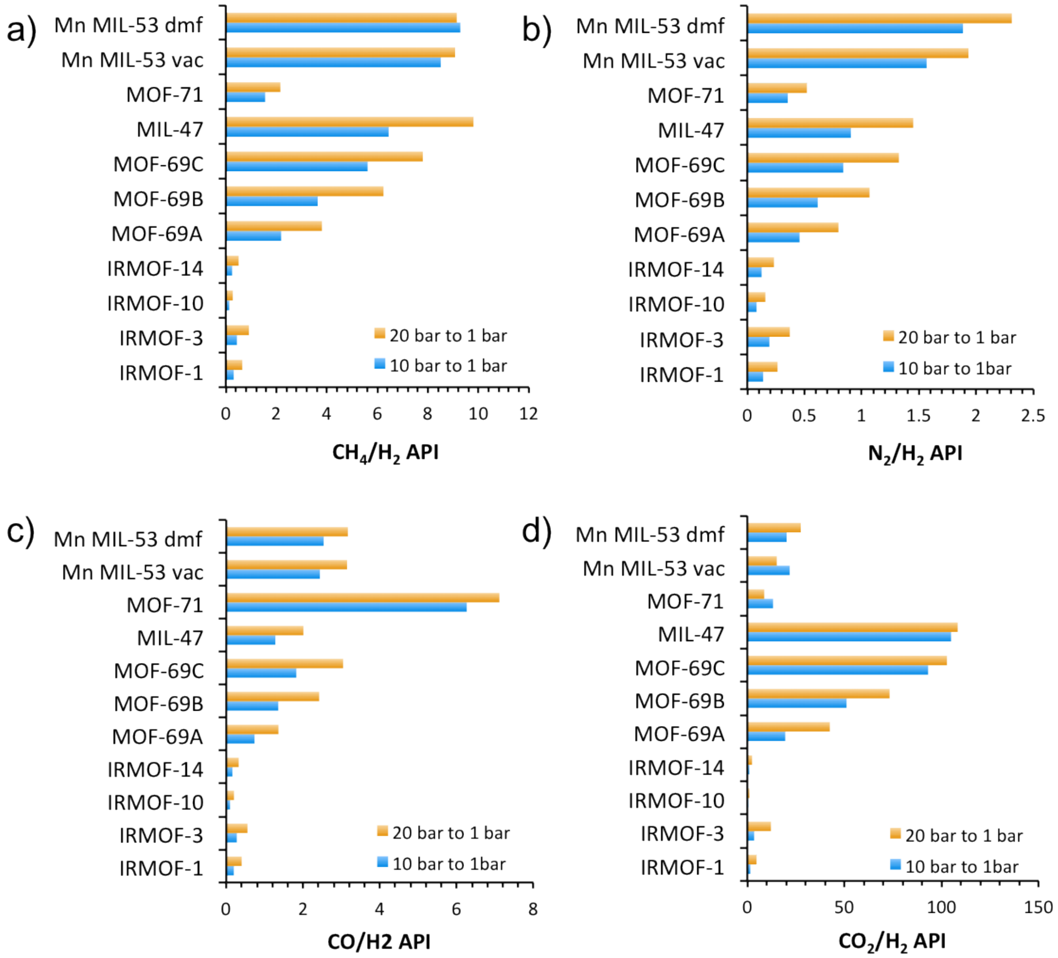

Figure 3-23: Adsorbent Performance Indicator determined for each of the 11 MOFs for separations of a) CH_4:H_2, b) N_2:H_2, c) CO:H_2, and d) CO_2:H_2 mixtures under two operating scenarios.

Despite their high capacities, the IRMOF materials have very low *API* values due to their low selectivities for all four mixtures. These materials would therefore be very poor adsorbents for H_2 separation applications. Nevertheless the increase in selectivity due to the amine groups in IRMOF-3, and the additional aromatic rings in IRMOF-14, is reflected by higher *API*s compared to IRMOF-1 and IRMOF-10, respectively. The MOF-69 family has higher *API*s than the IRMOF group, which increase with decreasing linker length, and can be expected to perform much better. MOF-69C and MIL-47 have the highest *API* for CO_2/H_2 separations, and this can be attributed to a high linker density as well as a large available FV in both of these materials. The narrow pores of MOF-71 are only able to accommodate a small number of CH_4, N_2 and CO_2 molecules, resulting in a low *API* despite the high selectivity for these molecules. The small pore size however is advantageous in CO/H_2 separations, as it matches the size of the CO molecules, resulting in a high Q_{st}, and a sufficiently high loading to generate a significantly higher *API* than the remaining 10 MOFs. It is clear that the *API* factors give a more complete starting picture of the capabilities of a material in separating hydrogen from a variety of gases. As shown in Figure 3-23, the *API* values calculated here do not lose any of the information previously gained from selectivity studies, but incorporate important data regarding each material's working capacity, in order to provide an improved perspective. According to Figure 3-23 CH_4/H_2 and N_2/H_2 separations can be performed most efficiently with the use of Mn MIL-53, either in its narrow pore form [vac] or in its larger pore form, [dmf]. These materials can also perform relatively well in CO/H_2 separations, having the second and third highest *API* values. Despite a high selectivity due to a high linker density, Mn MIL-53 does not have a sufficiently high capacity for CO_2/H_2 separations, which is reflected in low *API* values for this mixture. The larger pore volume of the MIL-47 framework, and relatively good selectivity, results in a high *API* for CO_2 separations. This material is also is well suited for CH_4 and N_2 separations, particularly at high pressure.

For the group of MOFs investigated here, the *API* is able to summarize the effects of working capacity, selectivity and interaction strength. The major shortcoming of this approach however, results from an ambiguous choice of the relative influence of each factor, which is reflected by the values of the A, B and C parameters. As discussed by Maring and Webley[93] it remains unclear exactly how to classify the separation efficiency of a material based on working capacities and selectivities alone. This problem is exacerbated when working with mixtures with more than two components, as the working capacities from binary mixtures are significantly different from those of more complex mixtures. Another important issue raised by Maring and Webley[93] is the influence of temperature on adsorption and regeneration. The endothermic nature of the desorption process can significantly reduce the working capacity, especially for strongly interacting adsorbates, and this effect must be taken into account when ranking the separation efficiency of materials.

3.5 Conclusions

The wide variety of existing, as well as potential MOF structures presents an unprecedented opportunity for selecting or designing materials that are perfectly suited for specific applications, such as H_2 purification. The drawback of working with such an array of structures is the time required to assess and characterize each material in turn. Nevertheless it is essential to understand which characteristics are desirable, and how they can be obtained. Such an understanding can be acquired by studying trends of how the adsorption of pure gases and gas mixtures is influenced by various structure properties. In this work, 11 MOFs were chosen in order to study pure component adsorption of steam methane reformer offgas components. The correlations of three framework characteristics, namely free volume, accessible surface area, and isosteric heat of adsorption, with the uptake of each gas was assessed. While H_2 loading correlates most strongly with the FV and SA and only to a lesser extent to Q_{st}, at low pressure the uptake of CO_2 is strongly correlated with Q_{st}. Adsorption of N_2, CH_4 and CO are also most strongly influenced by Q_{st}. An increase in a framework's uptake of CO_2, CO, CH_4, and N_2 accompanied by a decrease in H_2 adsorption, can be achieved by decreasing the FV and increasing the Q_{st}. In order to achieve such framework properties, three types of modifications were investigated: changes in linker length, additional functional groups, and changes in linker density. A decrease in linker length, the addition of amine groups or aromatic rings, and an increase in the density of linker groups in the framework, are all modifications that lead to higher selectivities for CO_2, CO, N_2 and CH_4 due to a higher Q_{st} and a lower FV. While in this work, only the amine functional group was studied, numerous other functionalization possibilities exist, and their effect on selectivity may differ. In addition to framework selectivity, it is also important to consider a material's working capacity under certain conditions. A simple way of assessing the suitability of a material for separating the components of a binary mixture based on both of these factors is through the use of the Adsorbent Performance Indicator. This indicator however, should be used with caution, as the relative influence of the working capacity, selectivity and heat of adsorption on a particular separation process is not known in advance. The trends observed in this work are essentially tools that can be used in choosing MOFs for H_2 purification. Of the 11 MOFs studied here, Mn MIL-53 presents an excellent potential for H_2 purification applications and is examined in detail in Chapter 4. MIL-47 is another promising material for such separation applications, and is studied further in Chapter 5.

4 Characterization of $Mn_2(BDC)_2(BPNO)$: Experiments and Simulations

The studies presented in Chapter 3 identified Mn MIL-53 as a material with excellent potential for use as an adsorbent in hydrogen separation applications. The work presented in this chapter is an investigation into the structure and characteristics of this newly reported Mn^{II} – based MIL-53 analogue. The Mn MIL-53 framework, also referred to as $Mn_2(BDC)_2(BPNO)$, consists of Mn^{II} oxide chains that are linked together by two types of linkers: 1,4-benzenedicarboxylic acid (BDC) and 4,4'-bipyridine-N,N'-dioxide (BPNO) shown in Figure 4-1 a). The structure is similar to the MIL-47 and MIL-53 frameworks[77], however instead of having bridging μ_2-oxo groups as in MIL-47, or μ_2-OH groups as in other MIL-53 frameworks, the metal cations are connected by μ_4-$\eta^2\eta_2$ BPNO ligands.[78] The role of the BPNO linkers is therefore not only to connect pairs of Mn^{II} cations within the same chain, but also to crosslink the neighbouring inorganic chains as shown in Figure 4-1 b). Moreover, Xu et al. have shown that the BPNO linkers within the framework interact with each other through parallel displaced $\pi - \pi$ interactions.[78]

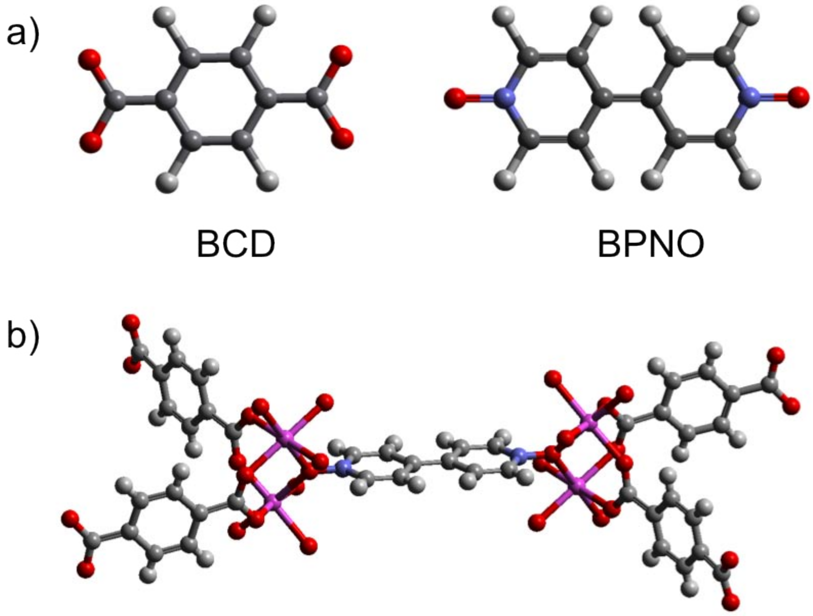

Figure 4-1: a) Organic linkers: 1,4-benzenedicarboxylic acid (BDC) and 4,4'-bipyridine-N,N'-dioxide (BPNO), and b) $Mn_2(BDC)_2(BPNO)$ bridging and chain connection of the BPNO linker. Colour key: oxygen – red, nitrogen – blue, carbon – dark grey, hydrogen – light grey, manganese - pink.

One of the most interesting properties of $Mn_2(BDC)_2(BPNO)$, or MIL-53(Mn^{II}), is its flexibility upon adsorption of a variety of molecules. The pores of the as-synthesized material are filled with DMF molecules. The DMF molecules can either be evacuated by heating the MOF under vacuum conditions, or they can be exchanged with smaller ethanol molecules by soaking the material in pure ethanol. The evacuation of DMF molecules from the pores of $Mn_2(BDC)_2(BPNO)$ results in a structural change towards a more narrow pore configuration, a transformation that is comparable to the breathing observed in other MIL-53 analogues, but smaller in magnitude. Similarly the exchange of DMF with ethanol molecules results in a structure with slightly smaller pores than $Mn_2(BDC)_2(BPNO)\bullet(DMF)_2$. The immersion of the evacuated material in C8 aromatics such as xylenes and ethylbenzene results in no uptake, however the material is able to adsorb benzene, toluene and chlorobenzene.[78] The adsorption of these aromatic molecules is accompanied by a significant increase in pore size, a process which appears to be driven by $\pi - \pi$ interactions and pairwise stacking.[78] The changes in the $Mn_2(BDC)_2(BPNO)$ pore size upon adsorption are detailed in Figure 4-2.

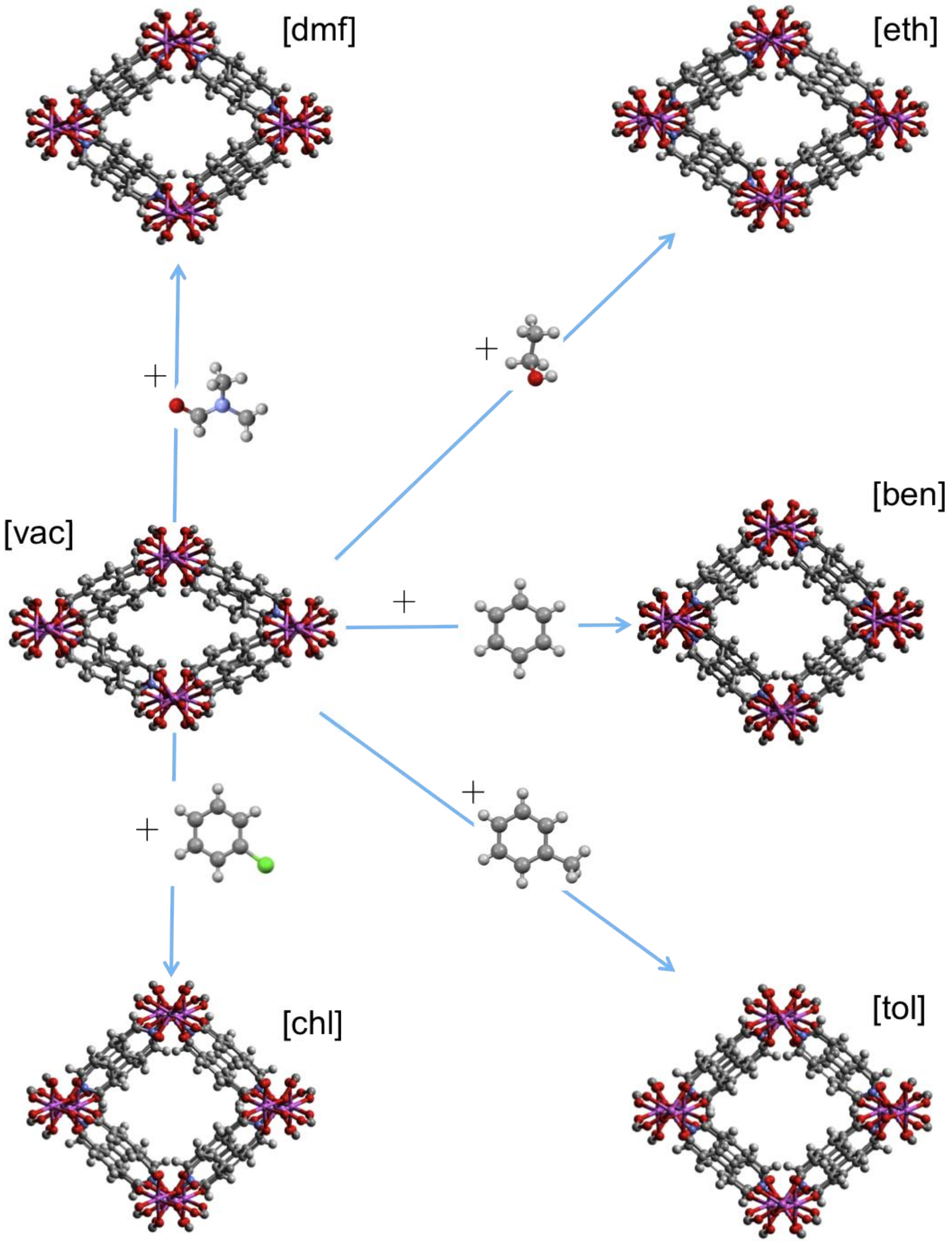

Figure 4-2: Flexibility of $Mn_2(BDC)_2(BPNO)$ upon adsorption of DMF, ethanol, benzene, toluene and chlorobenzene.[78] Colour key: oxygen – red, nitrogen – blue, carbon – dark grey, hydrogen – light grey, manganese – pink, chlorine – green.

The work of Xu et al. provides good insight into the behaviour of $Mn_2(BDC)_2(BPNO)$ with regards to the adsorption and separation of C6-C8 aromatics. To date however, no experimental work has been published in which the material's capacity and selectivity for lighter gases, such as H_2, CO, CO_2, N_2 and

CH_4 is assessed. This framework is particularly interesting as the presence of short linkers results in relatively small 1D rhombic pores, with pore diameters between 4.5 and 6 Å depending on the degree of pore opening, as well as a high density of linkers. As was shown in Chapter 3, these characteristics are desirable in a MOF for H_2 purification from SMROG, and are expected to result in high selectivities for CO, CO_2, N_2 and CH_4. Given the flexibility of the structure, a combination of experimental and simulation techniques is required in order to assess its potential for H_2 purification.

The work presented in this chapter focuses on studying the form of $Mn_2(BDC)_2(BPNO)$ during adsorption of light gases such as CO_2 and CH_4, at low temperature and room temperature. The study encompasses simulation work as well as experimental work. The $Mn_2(BDC)_2(BPNO)$ material was synthesized at the University of St. Andrews using a scale-up of the originally reported method. Optimization studies were carried out for the synthesis process, detailed in Section 4.2.1, as well as the activation of the samples, presented in Section 4.2.2, resulting in significant improvements in the purity of the synthesized product, and the evacuation of solvent molecules from its pores. In order to help characterize the pore form of the synthesized sample during gas adsorption, the pore size and pore limiting diameter of each of the previously reported $Mn_2(BDC)_2(BPNO)$ configurations[78] were evaluated in Section 4.3.1. In Section 4.3.2 a comparison of experimental and simulation adsorption studies carried out at 196 K and 303 K is used to determine the degree of pore opening in the material under such conditions. The findings are summarized in Section 4.4.

4.1 Simulation Details

4.1.1 Grand Canonical Monte Carlo Simulations

The adsorption of pure gases in each of the six reported configurations of $Mn_2(BDC)_2(BPNO)$ was simulated using the GCMC method in the Multipurpose Simulation Code (Music).[79] The simulations were carried out at 303 K and 196 K.

The $Mn_2(BDC)_2(BPNO)$ structures were simulated using an atomistic model. The framework atoms were kept fixed at their crystallographic positions,[78] and periodic boundary conditions were applied in order to mimic infinite structures. At each pressure point, the GCMC simulation was composed of 1.2×10^7 equilibration steps, and 1.8×10^7 steps for data collection. A cut-off radius of 12.8 Å was applied to all LJ interactions. The LJ parameters for CH_4 and CO_2 molecules are provided in Table 2-1 of Chapter 2.[43,47] The framework atoms were represented using the Dreiding force field[41] with the exception of manganese atoms which were modeled with UFF[40] parameters. Similar trends were observed from simulations performed using the UFF, and the Dreiding force field. The latter resulted in slightly better agreement with the experimental data, therefore unless indicated otherwise all simulated data presented in this chapter was obtained using Dreiding. Partial charges for the framework atoms were calculated in Gaussian 03,[94] using DFT with a B3LYP/6-31+G* level of theory by Linjiang Chen, a PhD student in Tina Düren's group at the University of Edinburgh. The partial charges and LJ parameters for each framework atom shown in Figure 4-3 are given in Table 4-1.

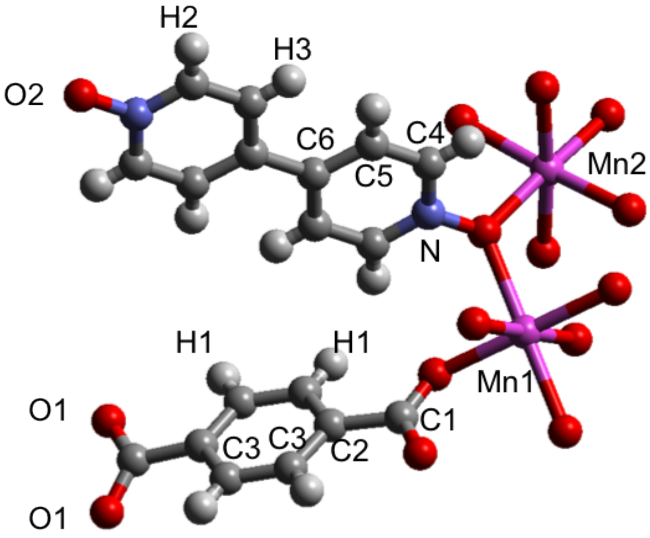

Figure 4-3: Atom labels corresponding to the atomic types given in Table 4-1.

Table 4-1: Lennard-Jones parameters and partial charges assigned to each atomic type.

	σ (Å)	ε/k_B (K)	q (e)
C1	3.473	47.856	0.97453
C2	3.473	47.856	-0.15074
C3	3.473	47.856	-0.05814
C4	3.473	47.856	-0.29137
C5	3.473	47.856	-0.09016
C6	3.473	47.856	0.04047
H1	2.846	7.649	0.07636
H2	2.846	7.649	0.23482
H3	2.846	7.649	0.09342
O1	3.033	48.158	-0.88915
O2	3.033	48.158	-0.77241
Mn1	2.638	6.542	1.51518
Mn2	2.638	6.542	1.46366

4.2 Experimental Methods

4.2.1 $Mn_2(BDC)_2(BPNO)$ Synthesis

The synthesis of $Mn_2(BDC)_2(BPNO)$ was carried out at The University of St. Andrews, with the help of John Mowat and Paul Wright, by scaling up the procedure detailed by Xu et al.[78] A mixture containing $Mn(NO_3)\bullet 4H_2O$ (Sigma Aldrich, >97%, 0.26208 g, 1.04 mmol), 1,4-benzenedicarboxylic acid (BDC, Sigma Aldrich, 98%, 0.1768g, 1.06 mmol), 4,4'-bipyridine-N,N'-dioxide (BPNO, Sigma Aldrich, 98%, 0.11288 g, 0.6 mmol), 0.5 mL H_2O, and 48 mL dimethylformamide (DMF, 99.8%) was prepared in a 100 mL Teflon-lined stainless steel Parr autoclave. The solution was stirred thoroughly prior to being placed in a conventional oven and heated at 120 °C for 6 hours. The autoclave was then cooled to room temperature. The product, in the form of large, red, needle-like crystals was filtered, washed thoroughly with ethanol, and finally dried in an oven at 50 °C.

In the work of Xu et al.[78] the formation of a non-porous impurity, Mn(BDC)(DMF), in the shape of small white crystals, alongside the desired red needle-like crystals was reported. Small-scale synthesis carried out in 17 mL Teflon-lined stainless steel Parr autoclaves, using the original amount of water specified in the procedure of Xu et al.[78] resulted in the formation of the reported impurity as well as the $Mn_2(BDC)_2(BPNO)•(DMF)_2$ product. The impurity was also observed using a direct 8× scale-up of the procedure of Xu et al. The mechanical separation of crystals resulted in a significant loss of the desired product, while the manual separation required a large amount of time.

In an effort to minimize the formation of impurities, an optimization study was carried out focusing on the amount of water added during synthesis. The original procedure specified the use of a 50 wt% $Mn(NO_3)_2$ aqueous solution. The optimization study was carried out using large-scale syntheses (8× scale-up) in which the reagent amounts were proportional to those specified by Xu et al.,[78] while the amount of water added was varied, as shown in Table 4-2.

Table 4-2: Synthesis optimization for $Mn_2(BDC)_2(BPNO)•(DMF)_2$: mixture composition of each preparation.

	$Mn(NO_3)_2$	**H_2O**	**TPA**	**BPNO**	**DMF**
Trial 1	0.26208 g	0.25 mL	0.1768 g	0.11288 g	48 mL
Trial 2	0.26208 g	0.4 mL	0.1768 g	0.11288 g	48 mL
Trial 3	0.26208 g	0.5 mL	0.1768 g	0.11288 g	48 mL
Trial 4	0.26208 g	0.6 mL	0.1768 g	0.11288 g	48 mL
Trial 5	0.26208 g	2.0 mL	0.1768 g	0.11288 g	48 mL

Trials 3 and 4 resulted in the formation of pure red crystals, while the remaining three trials resulted in the formation of large amounts of impurities. Additionally, in Trials 1, 2 and 5, very little $Mn_2(BDC)_2(BPNO)•(DMF)_2$ was produced. As a result, all $Mn_2(BDC)_2(BPNO)•(DMF)_2$ samples were prepared with Trial 3 mixture compositions. Due to an increase in the amount of H_2O added during synthesis, the formation of impurities was prevented, and a visually pure product was obtained, which is shown in Figure 4-4.

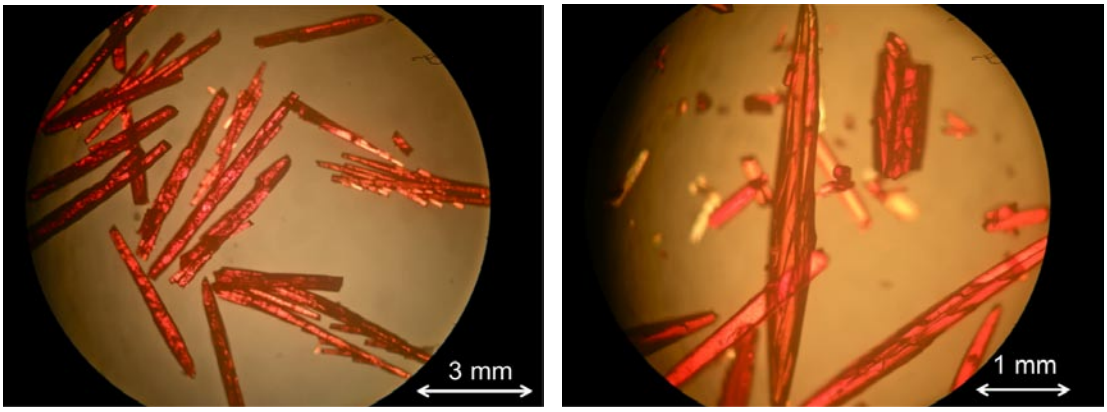

Figure 4-4: Visually pure synthesized product: red needle-like crystals of $Mn_2(BDC)_2(BPNO)\bullet(DMF)_2$.

4.2.2 Sample Activation

The synthesis of $Mn_2(BDC)_2(BPNO)•(DMF)_2$ was confirmed by a comparison of the powder X-ray diffraction pattern of the as-synthesized product to the simulated powder pattern of $Mn_2(BDC)_2(BPNO)•(DMF)_2$, resulting in excellent agreement as shown in Figure 4-5.

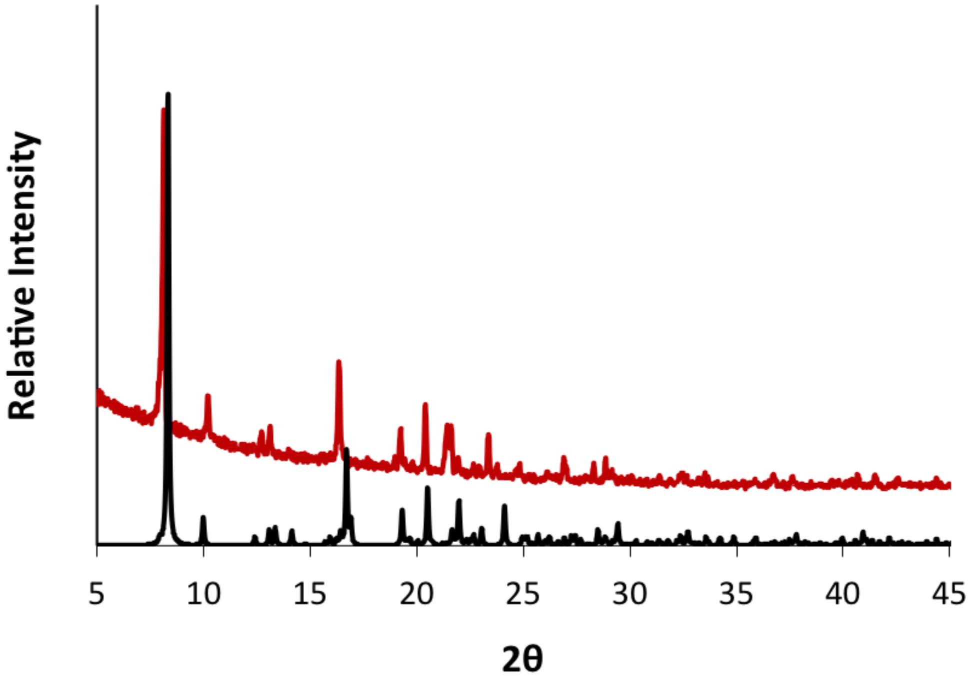

Figure 4-5: Powder X-ray diffraction pattern obtained for the synthesized product (red) and simulated powder pattern for $Mn_2(BDC)_2(BPNO)•(DMF)_2$.

Thermogravimetric analysis (TGA) was performed on the $Mn_2(BDC)_2(BPNO)•(DMF)_2$ crystals synthesized at the University of St. Andrews, and the results are shown as the black curve in Figure 4-6. The curve shows three steps of weight loss, followed by complete decomposition above 653 K, which is in agreement with the originally reported TGA.[78] The first two steps can be assigned to the loss of DMF molecules, while the third step was found to correspond to BPNO breakdown.[78]

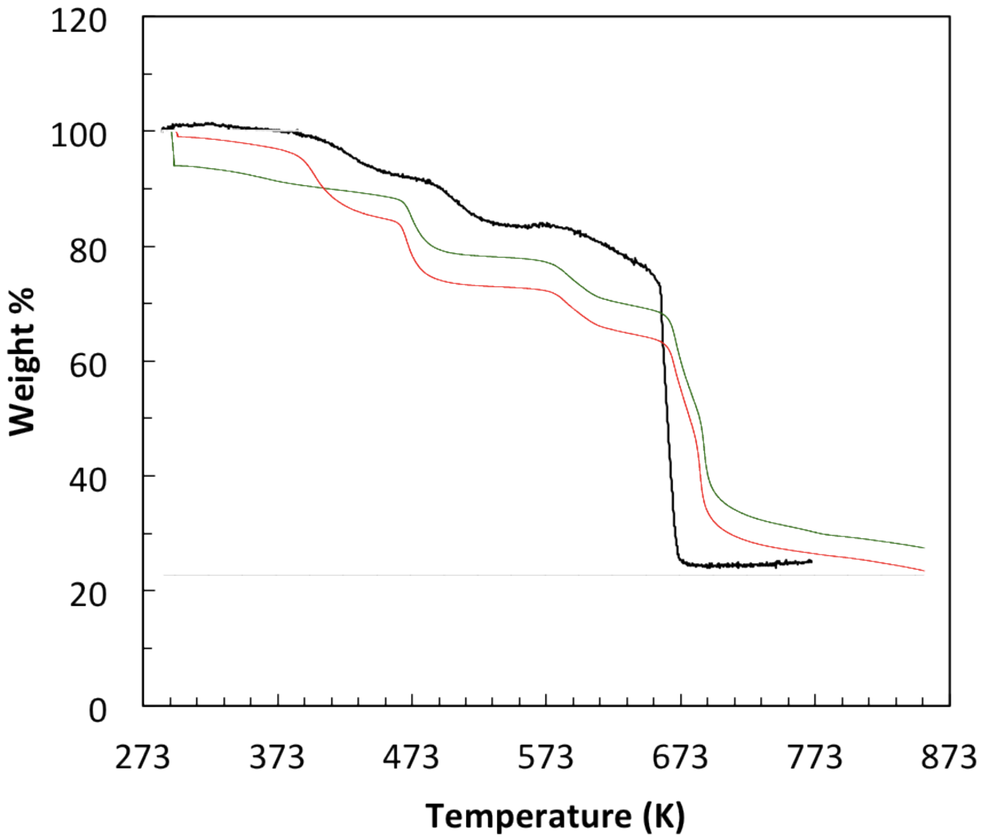

Figure 4-6: TGA curves performed on a fresh $Mn_2(BDC)_2(BPNO)•(DMF)_2$ sample at The University of St. Andrews shown in black, and at the Université Aix Marseille on an untreated sample, $Mn_2(BDC)_2(BPNO)•(DMF)_2$, shown in red, as well as an ethanol-soaked sample, $Mn_2(BDC)_2(BPNO)•(Ethanol)_2$, shown in green.

In the work of Xu et al.[78] $Mn_2(BDC)_2(BPNO)•(DMF)_2$ activation was carried out by heating the samples at 120 °C under vacuum conditions for 5 hours. This procedure resulted in the removal of DMF molecules and the formation of a narrow-pore $Mn_2(BDC)_2(BPNO)$ configuration.[78] Alternatively the removal of DMF molecules was achieved by soaking $Mn_2(BDC)_2(BPNO)•(DMF)_2$ crystals in pure ethanol for 2 days,[78] resulting in a large-pore, ethanol filled configuration $Mn_2(BDC)_2(BPNO)•(Ethanol)_2$.

The activation of fresh samples at the University of St. Andrews was successfully performed by John Mowat using the method reported by Xu et al..[78] At the Laboratoire MADIREL, Université Aix Marseille, with the help of Sandrine Bourrelly, the same activation method using samples that had been stored in air for a long period of time (approximately 3 months), resulted in an incomplete evacuation of solvent molecules. This problem was overcome by either increasing the outgassing temperature to 250 °C, or by soaking samples in pure ethanol for 9 days prior to outgassing at 120 °C, or 250 °C. A comparison of TGA curves obtained for unsoaked samples and the soaked samples, shown in Figure 4-6 in red and green respectively, indicates that samples soaked in ethanol can be activated more easily than untreated samples. While the location of the second weight loss step occurs at approximately 200 °C for both samples, the first step is significantly more shallow for soaked samples.

Considering the wide temperature range corresponding to the removal of solvent molecules from untreated samples, two outgassing temperatures, 120 °C and 250 °C, were tested for the activation of $Mn_2(BDC)_2(BPNO)\bullet(DMF)_2$. Samples were placed in quartz capillaries and outgassed for 6 hours at each of the chosen temperatures in vacuo. Powder X-ray diffraction patterns were obtained for each flame-sealed capillary tube, and the results are presented in Figure 4-7.

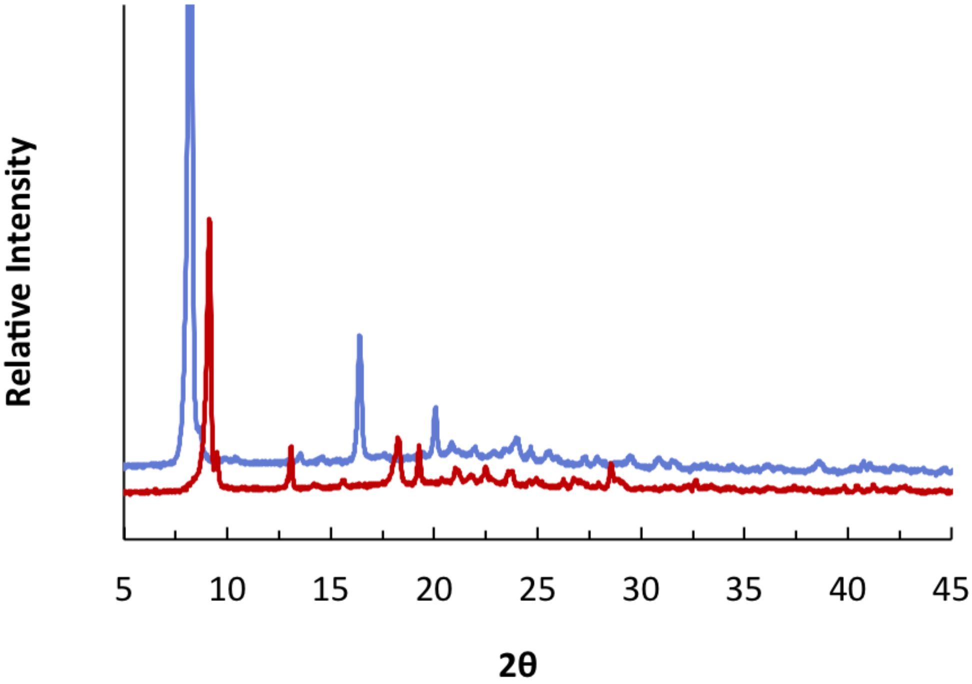

Figure 4-7: X-ray diffraction patterns for samples activated at 120°C (red) and 250°C (blue) collected on a capillary diffractometer.

The two different activation temperatures result in strikingly different crystal structures. A visual comparison of the experimental patterns presented in Figure 4-7 to patterns simulated based on the six reported configurations of Xu et al.[78] was performed. As shown in Figure 4-8 good agreement is observed between the 120 °C activated structure and the evacuated, narrow-pore $Mn_2(BDC)_2(BPNO)$, which will be referred to as [vac] from here on. On the other hand, the pattern obtained for the 250 °C activated sample was found to match the pattern simulated for the larger-pore [dmf] configuration, with slight differences possibly due to the removal of DMF molecules. These observations suggest that the activation of $Mn_2(BDC)_2(BPNO)$ at 250 °C results in a retention of the larger pore [dmf] form following the removal of DMF molecules, while activation at 120 °C results in a closing of the pores and a structural change towards the narrow pore [vac] configuration. In this work, both outgassing temperatures were used in sample activation in order to enable adsorption studies on a [vac] starting form, as well as on a larger pore [dmf] form. It must be mentioned however, that the 120 °C activations were preceded by an ethanol soak, unless the samples were freshly synthesized, or stored in ethanol.

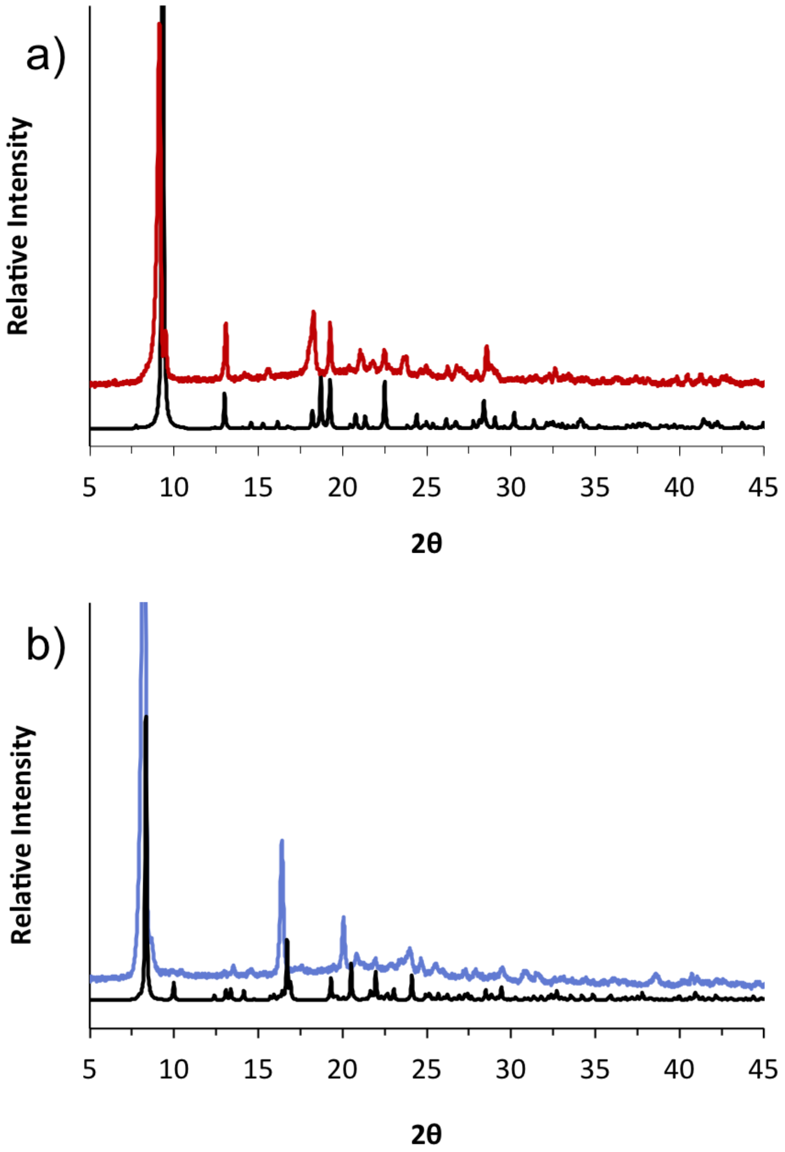

Figure 4-8: a) Experimental XRD pattern for sample activated at 120°C (red) and simulated XRD pattern (black) for evacuated $Mn_2(BDC)_2(BPNO)$, b) Experimental XRD pattern for sample activated at 250°C (blue) and simulated XRD pattern (black) for $Mn_2(BDC)_2(BPNO)(DMF)_2$.

4.3 Experimental and Simulation Studies

4.3.1 Pore Size Characterization

The maximum pore diameter as well as the limiting pore diameter, that is the smallest opening through which molecules must diffuse in order access the entire length of the channels, were determined for each of the $Mn_2(BDC)_2(BPNO)$ configurations shown in Figure 4-2. The calculations were performed using the method developed by Sarkisov and Harrison[95] and are presented in Table 4-3. The diameters of CH_4 and CO_2 molecules are estimated to be approximately 3.8 Å and 3.4 Å, respectively while the size of benzene molecules is much larger, approximately 6 Å. Due to its flexible nature, $Mn_2(BDC)_2(BPNO)$ is able to adsorb aromatic molecules, a process driven by T-shaped as well as parallel displaced $\pi - \pi$ interactions.[78] Similarly DMF molecules are able to interact with the framework through hydrogen bonds that form between the BPNO hydrogen atoms and the DMF oxygen atoms,[78] resulting in an increase in maximum pore size as well as pore-limiting diameters.

Table 4-3: Maximum diameter and pore limiting diameter calculated for each $Mn_2(BDC)_2(BPNO)$ configuration.

Structure	Maximum Diameter (Å)	Pore-limiting Diameter (Å)
[vac]	4.6	3.1
[eth]	5.1	4.2
[dmf]	5.6	4.7
[ben]	6.0	5.1
[tol]	6.0	5.0
[chl]	6.0	5.1

Based on the pore-limiting diameters shown in Table 4-3, CO_2 and CH_4 molecules would not be able to diffuse into the pores of [vac]. If the configuration of the structure following activation is [vac], as is obtained by outgassing at 120 °C, adsorption of CO_2 or CH_4 would only be possible if the framework – adsorbate interactions are sufficiently strong in order to cause a change in configuration resulting in larger pores. On the other hand, if the configuration of the material upon activation is [dmf]-like, as observed with outgassing at 250 °C, both CH_4 and CO_2 molecules would be expected to diffuse through the pores of the structure. The activation procedure has a strong influence on the initial form of the material, which could have a strong impact on the adsorption behavior observed.

CO_2 molecules have a quadrupole moment, usually resulting in strong interactions with MOF pore walls, and have been shown to drive framework breathing in MIL-53 structures. Of the MIL-53 family, MIL-53(Fe) is perhaps the most similar structure to $Mn_2(BDC)_2(BPNO)$ as its solvent-free form is of a closed-pore nature.[96] On the other hand, MIL-53 structures with Al or Cr atoms forming the metal-oxide chains are in an open-pore configuration following solvent removal. In MIL-53(Fe), the initially closed-pore structure transitions through an intermediate, narrow pore, and finally large pore configuration upon increasing CO_2 relative pressure.[97] The transitions observed were deemed to result from strong interactions between the μ_2-OH groups and CO_2 molecules. In the case of CH_4 adsorption in MIL-53(Fe) however, Llewellyn et al. have shown that even at pressures as high as 40 bar, structural flexibility is limited, and only the intermediate structure can be achieved.[96] In order to determine the level of flexibility induced by CO_2 and CH_4 adsorption in $Mn_2(BDC)_2(BPNO)$, a combination of experiments and molecular simulations was employed.

4.3.2 CO_2 and CH_4 Adsorption

Low pressure adsorption studies were performed at the University of St. Andrews with the help of John Mowat and Paul Wright, while high pressure adsorption studies were carried out at the Université Aix Marseille with the help of Sandrine Bourrelly and Phillip Llewellyn.

CO_2 adsorption isotherms were obtained gravimetrically at 196 K on two separately prepared samples of $Mn_2(BDC)_2(BPNO)$. The samples were activated immediately prior to carrying out the adsorption experiments by outgassing at 120 °C under secondary vacuum for 6 hours. The use of an activation temperature of 120 °C ensured that the starting configuration of the sample was [vac]. This approach enabled a study of whether the CO_2 molecules are able to interact with the framework atoms in order to cause a change from the [vac] form towards a larger pore form. The CO_2 isotherms obtained are Type I, with a maximum uptake of approximately 7 mmol/g as shown in Figure 4-9.

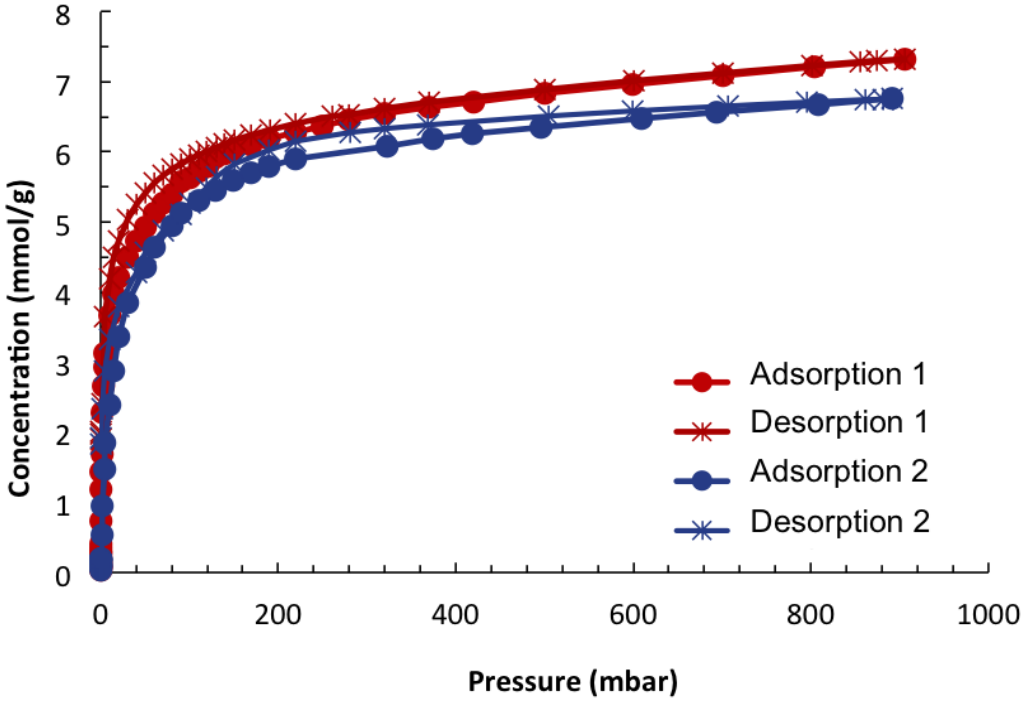

Figure 4-9: CO_2 adsorption/desorption isotherms measured experimentally for two samples of $Mn_2(BDC)_2(BPNO)$ at 196 K.

GCMC simulations were carried out for the [vac], [dmf], [eth], [ben], [tol] and [chl] configurations shown in Figure 4-2, in order to determine the uptake of CO_2 at 196 K, and assess whether the experimental isotherm can be accurately described by simulations performed on one of the six known configurations. The simulated isotherms are presented along with the experimental data in Figure 4-10. As expected, the maximum loading simulated strongly depends on the pore size, and therefore pore volume of each configuration. The maximum uptake observed experimentally appears to be between the maximum loading values observed for [dmf] and [ben]. This indicates that for CO_2 adsorption at 196 K, the $Mn_2(BDC)_2(BPNO)$ framework assumes a relatively open configuration, with a pore size between that of [dmf], 5.55 Å, and [ben], 5.98 Å. This behavior is potentially due to strong interactions between CO_2 and the framework atoms. The good agreement observed in Figure 4-10 b) between the experimental isotherm and the [dmf] simulated isotherm indicates that the material is in this open pore configuration even at low pressure. In addition, the isotherm does not exhibit any steps, a feature normally associated with structural changes in MOFs. The [vac] simulated isotherm was omitted from Figure 4-10 b) for clarity, however the disagreement between the experimental isotherm and the [eth] simulation data confirms the presence larger [dmf]-like pores rather than smaller [eth]-like pores.

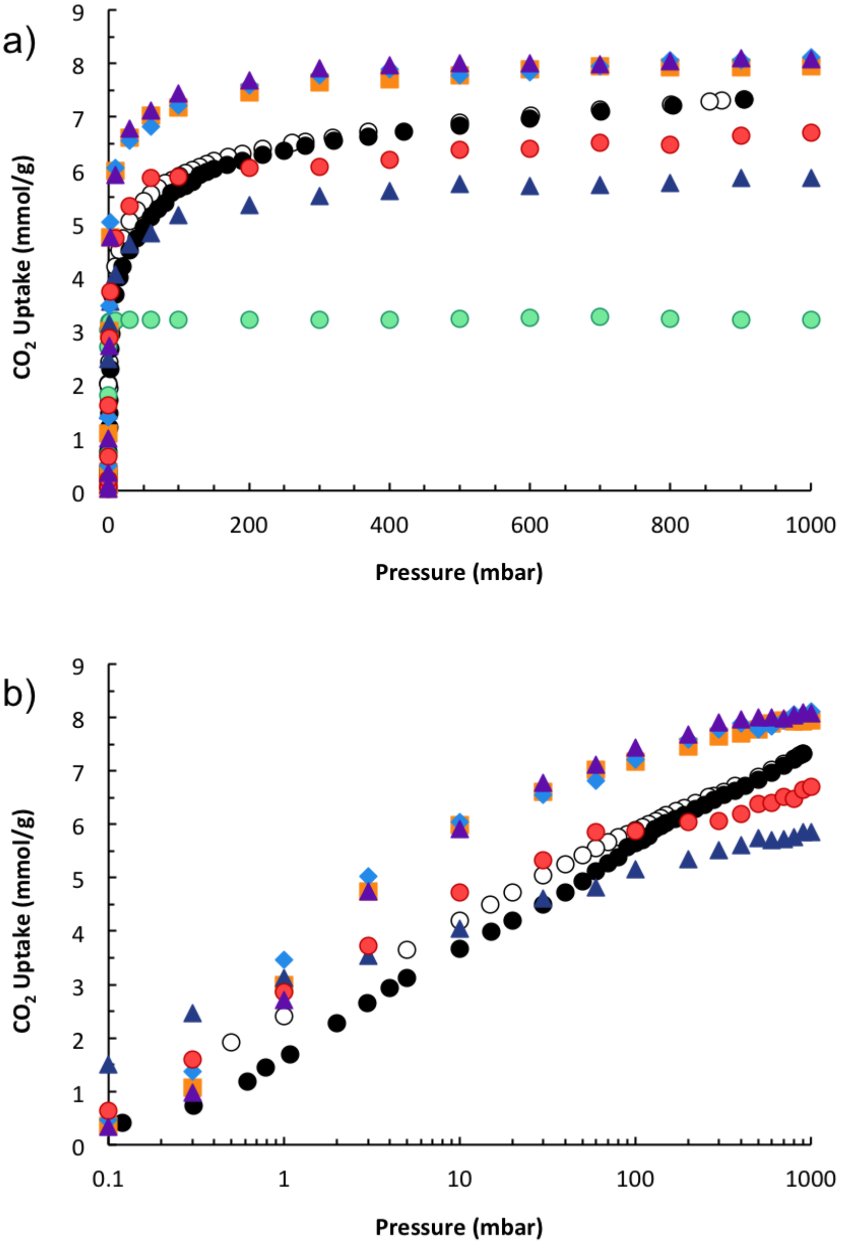

Figure 4-10: a) normal scale and b) semi-log scale plots of CO_2 adsorption isotherms at 196 K simulated based on six reported configurations: [vac] –green spheres, [eth] – dark blue triangles, [dmf] – red spheres, [ben] – light blue diamonds, [tol] – orange squares, and [chl] – purple triangles. Experimental adsorption and desorption data – solid and open spheres, respectively.

In order to determine whether $Mn_2(BDC)_2(BPNO)$ would be a suitable material for H_2 PSA purification processes, it was important to assess adsorption of CO_2 and CH_4 at ambient temperature. Adsorption experiments at 303 K were carried out at the Université Aix Marseille with the help of Sandrine Bourrelly. The samples prepared at the University of St. Andrews were initially stored in air in glass vials. Activation of samples stored in air by outgassing at 120 °C was found to be ineffective, resulting in minimal CO_2 uptake. As shown in Figure 4-11, samples stored in air were successfully activated by outgassing at 250°C. It is possible that samples stored in air were affected by air moisture. Water is strongly adsorbed in most zeolites and MOFs, therefore if water was present in the MOF pores it would have been more difficult to remove during outgassing. Samples stored in air, then soaked in ethanol for 9 days, and samples stored in ethanol immediately following synthesis showed similar activation effectiveness. This similarity between the two samples is observed for an outgassing temperature of 120 °C as well as of 250 °C. Samples stored in ethanol, and activated at 250 °C were found to have the highest CO_2 uptake at low pressure.

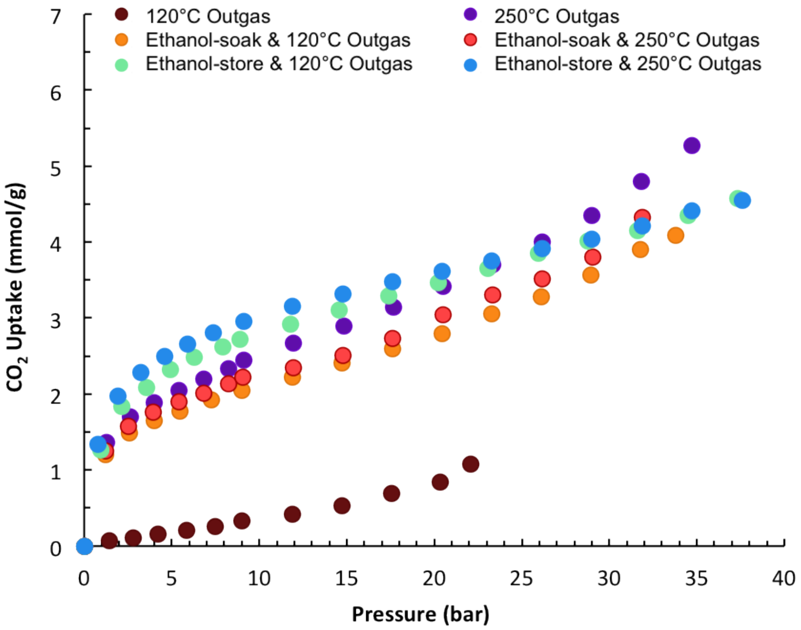

Figure 4-11: Effect of activation conditions on experimental CO_2 adsorption on $Mn_2(BDC)_2(BPNO)$ at 303 K.

The CO_2 adsorption isotherm obtained experimentally at 303 K, is compared to simulated isotherms in each of the six published configurations of $Mn_2(BDC)_2(BPNO)$ in Figure 4-12. The experimental uptake is markedly lower than the simulated [dmf] and [ben] loading, yet exceeds the loading simulated for [vac]. At low pressure, the experimental isotherm is below the [vac] simulated isotherm, whereas at pressures above 30 bar, the experimental uptake exceeds the simulated loading for [eth]. The semi-log plot shows that there are only small differences in the Henry region uptake for each of the simulated isotherms, therefore the experimental uptake at low pressure is not significantly affected by the form of framework. The low uptake observed experimentally at low pressure may be due to incomplete solvent removal, or the presence of water molecules inside the pores. Another possibility is that at low pressure the diffusion of CO_2 molecules into the pores is very slow, and therefore the experimentally measured uptake does not reflect the equilibrium uptake. This may be verified in future work through desorption experiments. At higher pressure the disagreement between the simulated [dmf] isotherm and the experimental data may be caused by a trapping effect: as CO_2 molecules are adsorbed, they interact with the framework atoms, possibly causing the framework to mold around the adsorbed molecules. As pressure is increased further, the isotherm does not appear to reach a plateau region. This effect may be due to molecules adsorbing on the outside of the MOF crystals. Considering the flexible nature of Mn MIL-53, and the variety of pore sizes that this framework has been shown to adopt, a more likely cause for the continued increase in uptake at high pressure is that a series of very gradual structural changes are taking place. The experimental isotherm does not contain a step, indicating the activation energy associated with any structural changes that may be taking place is small. This behavior differs from other MIL-53 analogues, where CO_2 uptake causes step-wise transitions between two or three distinct energy minima. The changes associated with CO_2 uptake in Mn MIL-53 could be studied in more detail either through GCMC simulations employing flexible force fields to describe the framework atoms, thereby allowing for structural changes to occur in response to CO_2 adsorption, or by performing in situ XRD experiments.

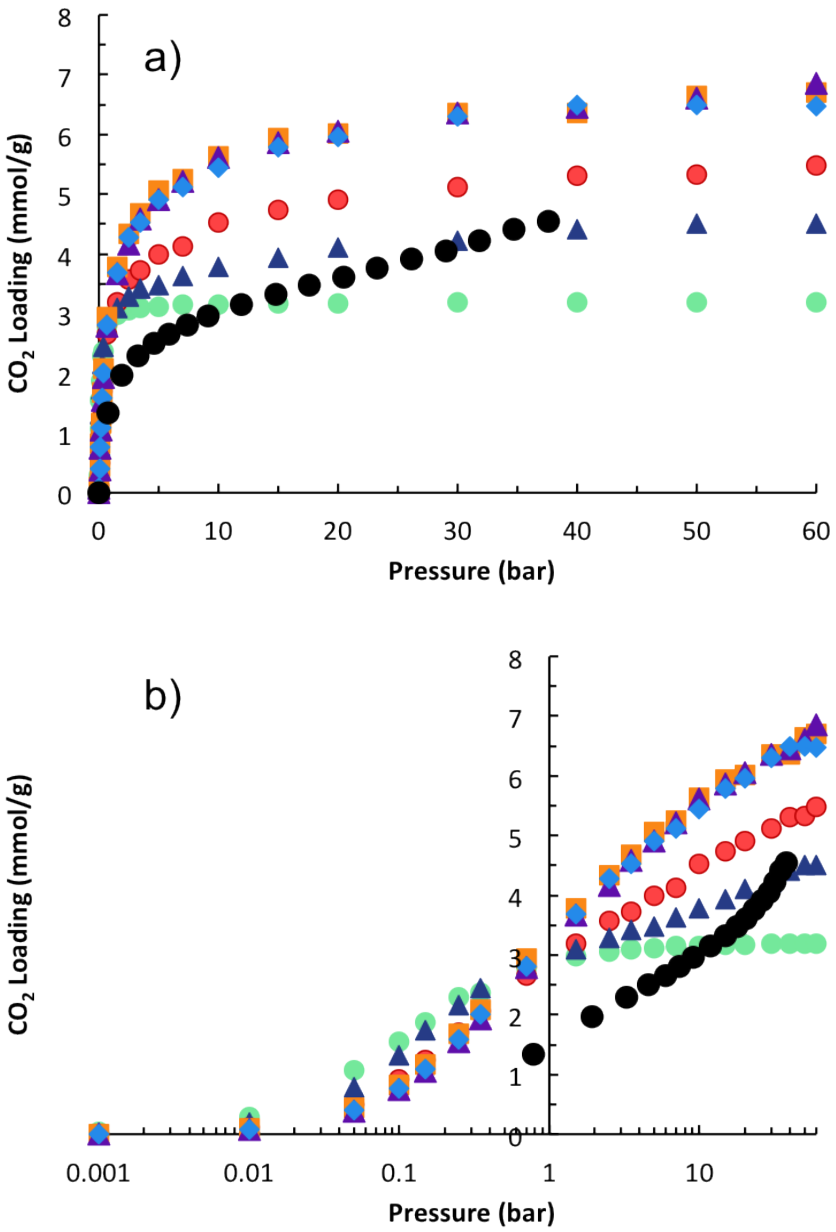

Figure 4-12: Experimental (black spheres) and simulated CO_2 adsorption isotherms on $Mn_2(BDC)_2(BPNO)$ at 303 K ploted on a) a normal scale, and b) a semi-log scale. [vac] – green spheres, [dmf] – red spheres, [ben] – light blue diamonds, [eth] – dark blue triangles, [chl] – purple triangles, [tol] – orange squares.

The arrangement of CO_2 molecules observed in [vac] indicates a particularly favourable arrangement, consisting of a pairing of CO_2 molecules along the length of the pore as shown in Figure 4-13. As a result, the incremental adsorption of additional CO_2 molecules with each step increase in pressure would be accompanied by a slight structural adjustment. Such trapping behavior has been previously reported in a study of the molecular sieve OSM-2, where samples were aged through exposure to CO_2 for 20 hours prior to adsorption measurements.[98] Aged samples resulted in lower uptake than fresh samples.[98] In the case of $Mn_2(BDC)_2(BPNO)$, although samples were not aged, the material has a tendency to be in its [vac] configuration at zero loading, and changes towards a larger pore size require strong adsorbate-framework interactions. This tendency can be overcome by CO_2-framework interactions at 196 K, however at higher temperatures adsorbate-framework interactions are weaker, and cannot drive the framework towards a more open configuration unless a significant amount of pressure is applied.

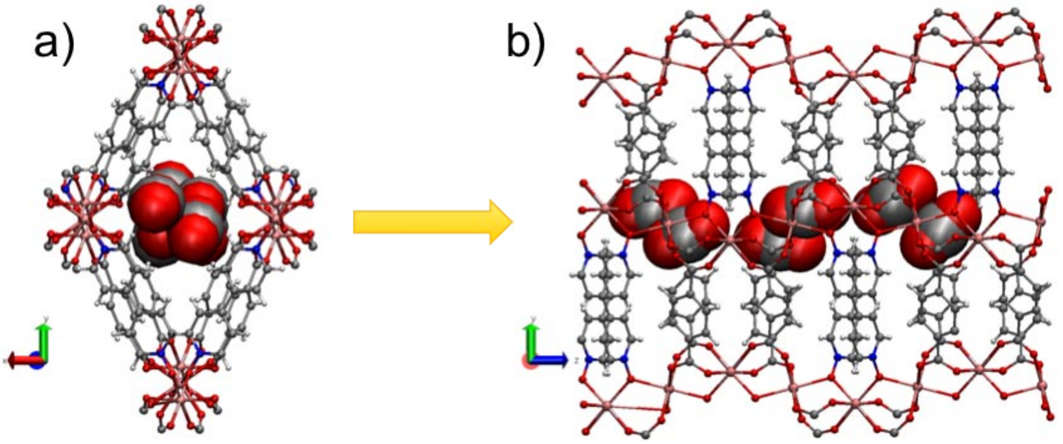

Figure 4-13: Arrangement of CO_2 molecules in [vac] at a saturation loading of 8molec/uc shown a) along the xy plane and b) along the yz plane. Colour index: C – dark grey, H – light grey, O – red, Mn – pink, N – blue.

Methane adsorption experiments performed on samples activated at 120 °C and 250 °C, resulted in a similar low uptake at 303 K as shown in Figure 4-14. The simulated adsorption isotherm based on the [vac], [eth], [dmf] and [ben] configurations show significantly higher loading across the entire pressure range. As discussed in Section 4.2.2, an outgassing of samples at 120 °C results in a [vac] form of the material, while outgassing at 250 °C allows for a [dmf]-like form of the material to be maintained. The methane adsorption experiments however, were performed on samples that had been stored in ethanol prior to outgassing, and were therefore initially in an [eth] configuration. If the [eth] from can be maintained upon outgassing at 250 °C, then the form of the material at the start of the adsorption experiment would be expected to be a solvent free [eth] configuration rather than a [dmf] configuration. It is however possible that outgassing of ethanol stored samples at 250 °C results in a narrow pore [vac] form. In the case of CH_4 adsorption, the kinetic diameter of the molecules is 3.8 Å, which is comparable to the pore limiting diameters of [vac] and [eth], of 3.1 Å and 4.2 Å, respectively. The low experimental uptake observed in the low pressure region for both outgassing temperatures suggests that the $Mn_2(BDC)_2(BPNO)$ framework is in a narrow-pore configuration. The interactions between methane molecules and the framework are therefore not strong enough to cause a change in the MOF configuration. The simulated high uptake in the low pressure region indicates that if CH_4 molecules were able to enter the pores of $Mn_2(BDC)_2(BPNO)$, the adsorbate – framework interactions would be relatively strong due to the presence of small pores. One possible explanation for the slightly higher experimental uptake observed at 22 bar could be that methane molecules are being forced through the pores, an effect that may be accompanied by slight structural changes. It is clear however, that even at high pressure a large fraction of the pore space remains unoccupied.

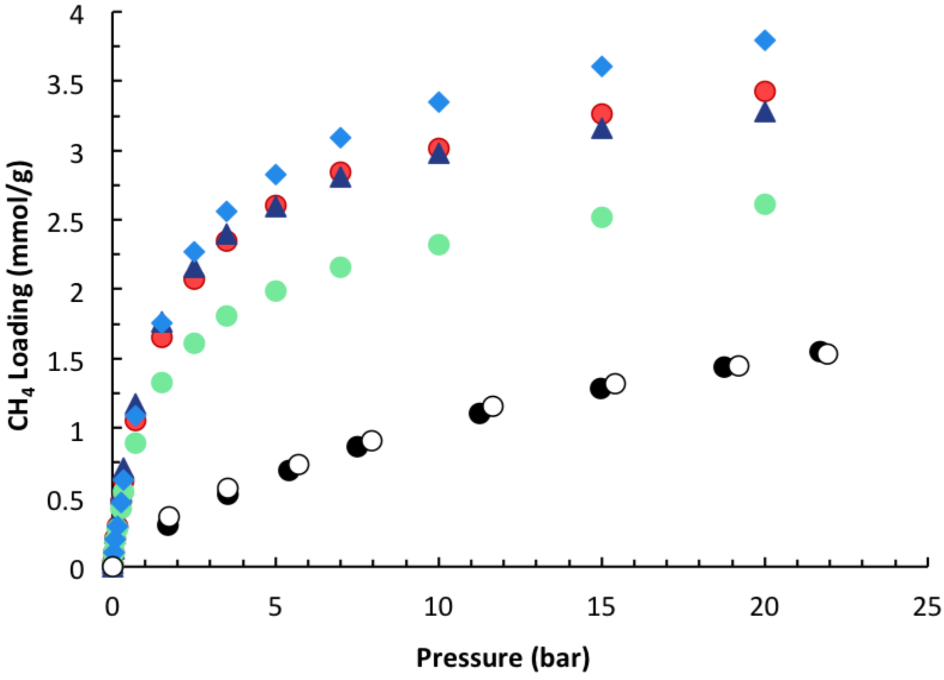

Figure 4-14: Experimental data obtained from samples activated at 250 °C (closed spheres) and 120 °C (open spheres) compared to simulated CH_4 adsorption isotherms on $Mn_2(BDC)_2(BPNO)$ at 303 K. [vac] – green spheres, [dmf] – red spheres, [ben] – light blue diamonds, [eth] – dark blue triangles.

The experimental results presented in this work indicate that $Mn_2(BDC)_2(BPNO)$ adopts a relatively open pore configuration during CO_2 adsorption and a closed pore form during CH_4 adsorption. It is unclear however, precisely what the [CO_2] configuration is, and how it is affected by temperature. An attempted AIMD investigation of the $Mn_2(BDC)_2(BPNO)$ structure is presented in Appendix A, and possible causes of the unsuccessful trials are discussed.

4.4 Conclusions

$Mn_2(BDC)_2(BPNO)$ undergoes structural changes on uptake of ethanol, DMF, as well as C6 and C7 aromatic molecules, stabilizied by strong adsorbate-framework interactions including hydrogen bonds and $\pi - \pi$ interactions.[78] In this work the flexibility of $Mn_2(BDC)_2(BPNO)$ framework upon adsorption of CO_2 and CH_4 was investigated through a combination of experimental and simulation studies. GCMC simulations were performed on six known (adsorbate-removed) configurations of $Mn_2(BDC)_2(BPNO)$. At 196 K the framework adsorbs CO_2 with ease, reaching a maximum loading of 7 mmol/g. The agreement between experimental and [dmf] simulated CO_2 adsorption isotherms at 196 K indicates that the configuration of $Mn_2(BDC)_2(BPNO)$ on CO_2 uptake is similar to the [dmf] configuration. At 303 K however, the experimental CO_2 uptake exceeds the [vac] and [eth] simulated isotherms, yet does not match the [dmf] simulated isotherm. Considering that the pore-limiting diameter of [vac] is smaller than the kinetic diameter of CO_2 molecules, the maximum observed uptake of 4.5 mmol/g at 303 K, indicates that structural changes are taking place in order to allow CO_2 molecules to diffuse into the pores. The disagreement in CO_2 isotherm shape and uptake may be due to a tendency of the framework to assume its [vac] configuration, as well as the pairwise packing of CO_2 molecules observed through GCMC simulations on [vac]. At 196 K CO_2-framework interactions are sufficiently strong in order to drive the framework towards a larger pore configuration, however at 303 K this effect is only achieved at high pressures. In the case of CH_4 molecules, the adsorbate-framework interactions are not sufficiently strong in order to drive structural changes. At high pressure, the molecules are forced through the narrow pores of [vac], however the maximum observed uptake remains below the simulated isotherms for all configurations. The selective flexibility of $Mn_2(BDC)_2(BPNO)$ is an interesting feature, and should be explored further in order to identify opportunities for its use in gas separation and purification applications.

5 Simulating Gas Adsorption in MIL-47

Discrepancies between adsorption isotherms obtained using experimental and simulation methods have often been credited to a difference in the quality of the structures being analysed. In simulation studies, the crystals are assumed to be perfect and fully activated, that is, void of any solvent molecules or unreacted reagents that may have been left over from the synthesis. Experimental samples however, may be subject to partial framework collapse, incomplete activation or the presence of dense impurities,[99-102] causing experimental uptakes to be lower than those predicted in simulation work.[71,103,104] On the other hand, accurate GCMC adsorption data can only be achieved through a correct representation of the interactions between the adsorbate and framework atoms. While generic force fields, such as Dreiding[41] and UFF[40], give very good predictions of adsorbate-framework interactions for some MOFs, in many cases they lead to large deviations from experimental data, especially at low pressures.

To get a better understanding of the nature of the differences between experimental and simulated adsorption isotherms, an investigation was carried out focusing on the vanadium terephthalate MIL-47 framework, shown in Figure 5-1. This material is of interest as it is a relatively simple MOF from a structural point of view, containing one-dimensional rhombic pores (free diameter ~ 8 Å), and does not have any specific adsorption sites such as OH groups or open metal sites. Having been first synthesized by Barthelet *et al.*,[77] MIL-47 has been the focus of a number of adsorption studies combining experimental and classical simulation methods.[10,73,83,99,100,105-108]

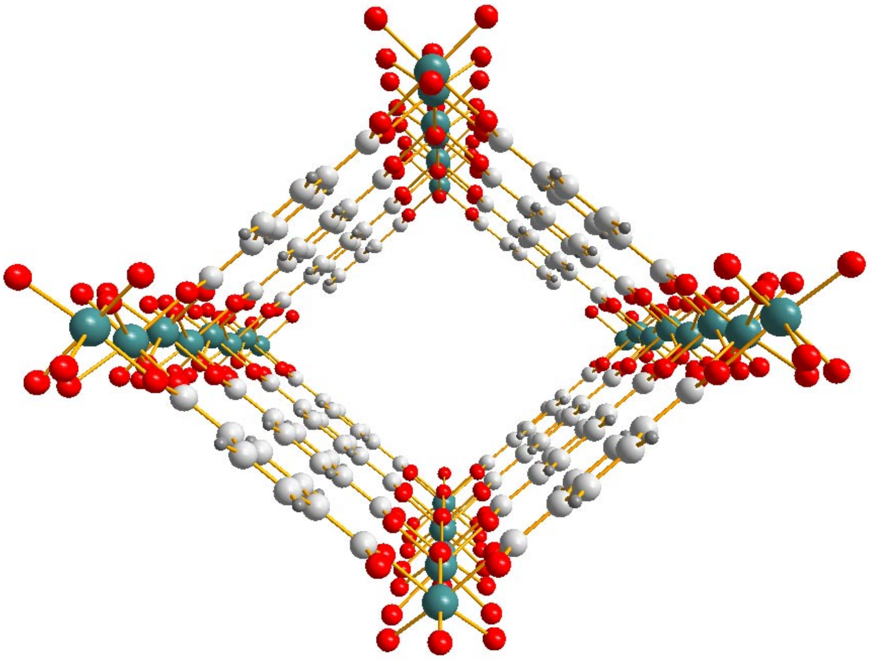

Figure 5-1: The MIL-47 framework. Key: teal, V; red, O; dark grey, H; light grey, C.

In several of the previous studies where the UFF, Dreiding, or OPLS force fields were used to represent this MOF some disagreement between simulated and experimental isotherms was observed. For example, predictions using the OPLS, Dreiding and UFF force fields were compared by Fairen-Jimenez et al. and all three force fields gave very similar simulation results for methane adsorption in MIL-47, overpredicting the experimental uptake.[100] An overestimation in the simulated uptake was also reported by Ramsahye et al. in their study on CO_2 adsorption,[83] and by Rosenbach et al. for the adsorption of light hydrocarbons.[99] Disagreements were also observed in the work of Castillo et al. on xylene adsorption in MIL-47 at three different temperatures. In their study, good agreement was reported for pure *o*-, *p*- and *m*-xylene isotherms at 423 K, however a significant overprediction of *o*- and *p*-xylene uptake was observed at 343 K.[10] In addition, at 383 K, the *o*- and *p*- isotherms were underpredicted at low pressure and overpredicted at high pressure. Liu and Smit on the other hand, using adjusted force fields, achieved very good agreement between simulated and experimental isotherms for pure CO_2, N_2 and CH_4 as well as mixtures of CO_2/N_2 and CH_4/N_2.[73] Some studies chose to adopt a hybrid force field, combining Dreiding parameters for the inorganic rods with UFF parameters for the organic linkers.[105,106] While Déroche et al. found an improved agreement between experimental and simulated isotherms of long-chain alkanes when using the hybrid force field instead of the UFF,[105] the n-hexane and n-octane isotherms were overpredicted in the low-medium pressure region, and the n-nonane isotherm was overpredicted across the entire pressure range.

In this chapter, an adsorption study of ten pure components and six mixtures on MIL-47 is presented. Absolute adsorption isotherms for O_2, H_2, N_2, CO, CO_2, CH_4, C_2H_6, C_3H_8, C_3H_6, and C_4H_{10} in the MIL-47 framework at 303 K were modeled through GCMC simulations and compared to experimental measurements carried out by Sandrine Bourrelly and Phillip Llewellyn at the Université Aix Marseille. Apart from hydrogen, for which excellent agreement is observed, the gas loading is considerably over-predicted in all cases, as shown in Figure 5-2.

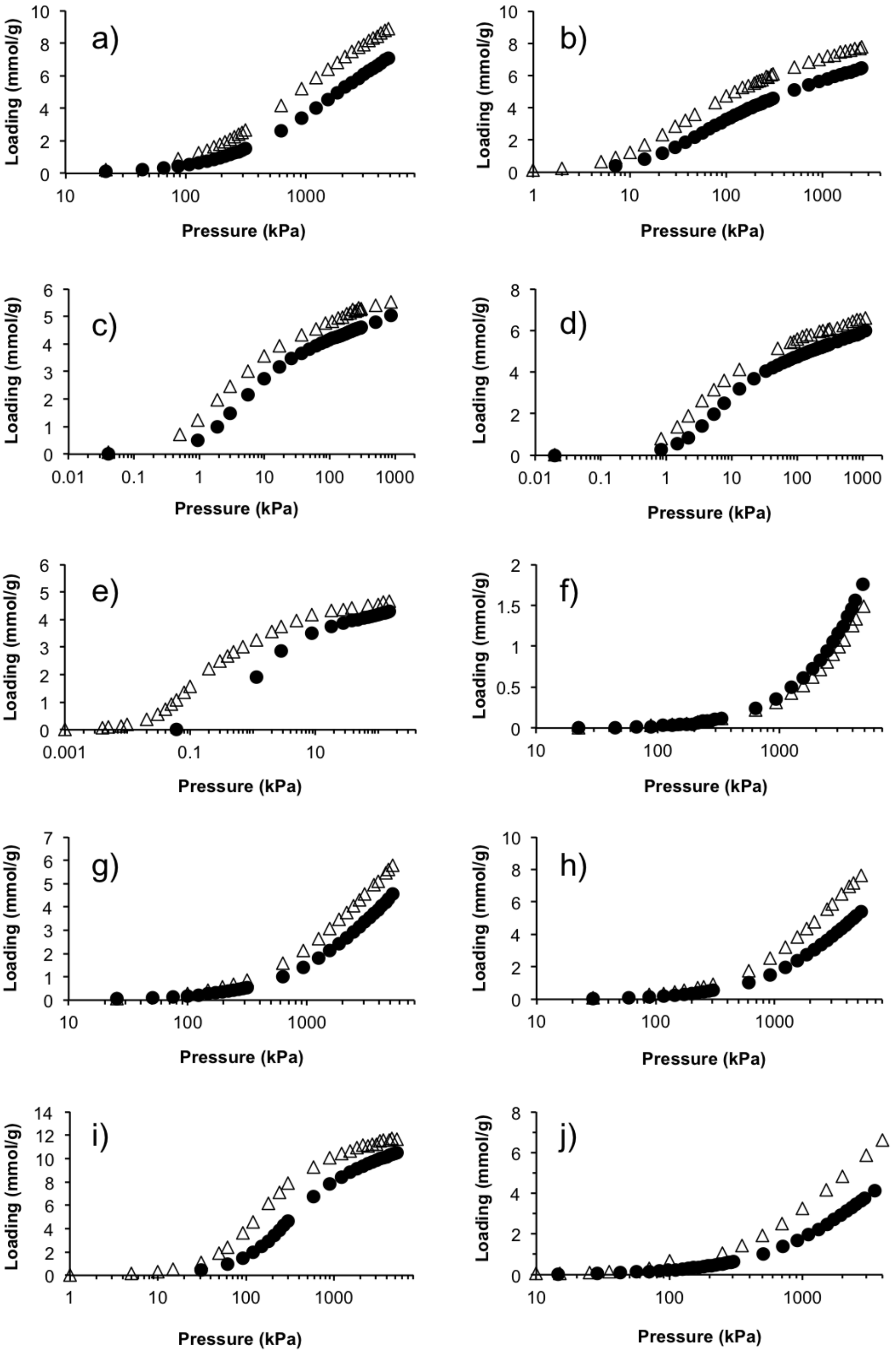

Figure 5-2: Dreiding[41] (open triangles) and experimental (closed spheres) adsorption isotherms in MIL-47 at 303 K for a) methane, b) ethane, c) propane, d) propene, e) butane, f) hydrogen, g) nitrogen, h) oxygen, i) carbon dioxide and j) carbon monoxide.

The simulated isotherms in Figure 5-2 were determined using the Dreiding force field, however a similar overprediction of experimental uptake is observed for isotherms simulated using UFF, as shown in Appendix B. Slightly better agreement between experimental and simulated isotherms is obtained when the Dreiding force field is used as opposed to the UFF. As a result, unless explicitly stated otherwise, the simulation results presented in this chapter were obtained using the Dreiding force field.

All simulation details for the work presented in this chapter are provided in Section 5.1. In order to identify the reason for the disagreement between simulated and experimental isotherms, three possible causes are investigated. Firstly, there may be a difference between the pore volume of the perfect, infinite crystals used in the simulations and the volume that is truly accessible in the experimental sample, possibly due to incomplete solvent or reactant removal during activation, partial framework collapse or mixture with a dense phase (non-porous coordination compound or metal oxide/hydroxide). This would result in the largest overprediction being observed at high pressure, corresponding to the pore filling stage of adsorption where the pore volume plays the largest role. The influence of such non-porous defects in MIL-47 is studied in Section 5.2, through both, isotherm scaling as well as through simulations performed on a framework with partially blocked pores. Secondly, the chosen framework force field, Dreiding, not having been developed specifically for MOFs, may lead to an overprediction of adsorbate-framework interactions resulting in a simulated uptake that is higher than the experimental uptake, particularly at low pressure where the adsorbate-framework interactions have the strongest effect on adsorption. Section 5.3 focuses on the adsorbate – framework interaction strength described by the Dreiding force field and its effect on adsorption simulations, and the comparison of mixture data is verified with the help of the ideal adsorbed solution theory (IAST). Finally the common assumption made while performing GCMC simulations, that the MIL-47 framework can be considered to be rigid, with the atoms fixed at their crystallographic positions, may lead to an inaccurate representation of the atomic positions at any given point in time. The dynamic properties of the MIL-47 framework are discussed in Section 5.4. The positions of the framework atoms were studied using Ab Initio Molecular Dynamics simulations, and the influence of linker rotation on pure component and mixture adsorption was evaluated. Another commonly observed cause for discrepancies between experimental and simulated isotherms in MOFs is the presence of inaccessible parts of the pore network as discussed in the recent work of Barbarao *et al.*[109], however such effects can be disregarded when considering the unobstructed 1D pores of MIL-47. The findings resulting from the three investigations are summarized in Section 5.5.

5.1 Experimental and Simulation Methods

5.1.1 Sample Preparation

MIL-47 or V(O)(L) (L = terephtahalate) was synthesized by Thomas Devic and Christian Serre at the Institut Lavoisier, Université de Versailles, according to the reported procedure.[77]

5.1.2 Single gas and mixture isotherm measurement

The static single component and mixture adsorption experiments were performed by Sandrine Bourrelly and Phillip Llewellyn at the Université Aix-Marseille. The experiments were carried out at 303 K using a laboratory made gas dosing system connected to a commercial gravimetric adsorption device (Rubotherm Präzisionsmeßtechnik GmbH).[110-112] Further experimental details are provided in Appendix C.

5.1.3 Grand Canonical Monte Carlo (GCMC) Simulations

GCMC simulations were carried out at 303 K and the pure gas and mixture fugacities were calculated with the Peng-Robinson equation of state. [32] The MIL-47 structure was simulated using an atomistic model. The framework atoms were kept fixed at their crystallographic positions.[77] At each pressure, the GCMC simulation was composed of 1.2×10^7 equilibration steps, and 1.8×10^7 steps for data collection. A cut-off radius of 12.8 Å was applied to all LJ interactions. The framework atoms were represented using the Dreiding force field[41] as well as the UFF[40] force field, as shown in Table 5-1. Vanadium atoms were represented using UFF[40] in all simulations.

Table 5-1: Dreiding and UFF LJ parameters used for modelling the interaction with the MIL-47 framework atom. [a] Vanadium parameters were taken from the UFF.

Atom	**Dreiding**		**UFF**	
	σ (Å)	**ε/k_B (K)**	**σ (Å)**	**ε/k_B (K)**
Hydrogen	2.846	7.649	2.571	22.142
Carbon	3.473	47.856	3.431	52.838
Oxygen	3.033	48.158	3.118	30.193
Vanadium	2.801[a]	8.052[a]	2.801	6.039

The LJ parameters used to represent the adsorbate molecules are provided in Table 2 – 1 of Chapter 2. Coulombic interactions and quantum effects were not included in the hydrogen simulations as they are negligible at 303 K. CO was represented with the three-centred model introduced by Martín-Calvo et al.[49] Partial charges for the framework atoms were taken from the DFT calculations of Ramsahye et al.[83] Coulombic interactions were included in all simulations involving N_2, O_2, CO and CO_2 using the Ewald summation method.[113]

5.1.4 Ideal Adsorbed Solution Theory (IAST)

The IAST method[114] can be used to predict mixture adsorption isotherms from single component adsorption data by treating the adsorbate mixtures as ideal solutions. IAST assumes that the surface potential of the mixture is equal to the surface potential of each of the components. For each of the components the surface potential is defined as a function of the amount of pure component adsorbed at the same temperature. In order to optimise IAST results, pure component adsorption data must be fitted to equations that best describe the isotherms. In this study, the experimental and simulated isotherms of each gas were carefully fitted to the Jensen-Seaton isotherm equation.[115] The IAST technique was then used to solve the continuous functions representing each of the single component isotherms in order to determine first the mixture spreading pressure, and then the molar fraction of each component in the adsorbed phase. Full details of the IAST method are given elsewhere.[116]

5.1.5 Ab Initio Molecular Dynamics (AIMD) Simulations

All AIMD and DFT single point energy calculations were performed using the QUICKSTEP module[66] of the CP2K package.[67] The simulations were carried out using the Becke-Lee-Yang-Parr BLYP exchange correlation functional,[59,60] and dispersion corrections were included using the DFT-D3 method developed by Grimme.[117] Oxygen, hydrogen and carbon atoms were represented using double-ζ valence plus polarization basis sets optimized for the Goedecker-Teter-Hutter (GTH) pseudopotential[64,65,118] and the BLYP functional, while vanadium atoms were represented using the MOLOPT basis set.[119] A plane wave basis set energy cutoff of 300 Ry and a corresponding Gaussian basis set relative cutoff energy of 40 Ry were applied. The self-consistent field (SCF) cycles were assigned an energy convergence criteria of 1.0×10^{-6} Hartree. The AIMD simulations were carried out in the NVT ensemble, in order to ensure that the unit cell parameters remained unchanged. The simulation cell contained 1×2×2 MIL-47 unit cells, and periodic boundary conditions were applied. The temperature was set to 298 K and controlled using a Nosé-Hoover thermostat.[120] The pressure was set to 1.0 bar and a barostat coupling time constant of 300 fs was applied. The equations of motion were integrated using a time step of 1.0 fs. The geometry optimization calculations were performed using a convergence criterion 3×10^{-3} Bohr for the maximum geometry change, 1.5×10^{-3} Bohr for the root-mean-square geometry change, 4.5×10^{-4} Hartree/Bohr for the maximum force and 3.4×10^{-4} for the root-mean-square maximum force.

5.2 Pore Volume Effects

In previous MIL-47 studies,[99-102] scaling factors proportional to the ratio between theoretical and experimental maximum uptakes,[100] surface areas,[99] or pore volumes,[101,102] have been applied in order to account for non-porous defects. In this work, the influence of a decrease in the accessible pore volume of MIL-47 on the adsorption isotherm shape was evaluated using both isotherm scaling and pore blocking simulations. The first method involves fitting the simulated and experimental isotherms to the Jensen-Seaton[115] equation in order to extend the isotherms to a high pressure plateau region corresponding to complete pore filling. The simulated isotherms are then scaled to match the expected maximum experimental loading. For the ten adsorption isotherms investigated, the scaling factors required vary widely in order to account for various degrees of over-prediction, ranging from 0.90 in the case of CO_2 to 0.66 observed for CO. The scaling factors are essentially the ratio between the experimental and the simulated accessible pore volume, and should therefore have the same magnitude for all isotherms measured on the same experimental sample. The wide range of scaling factors required indicates that the disagreement between experimental and simulated isotherms is not solely due to non-porous effects.

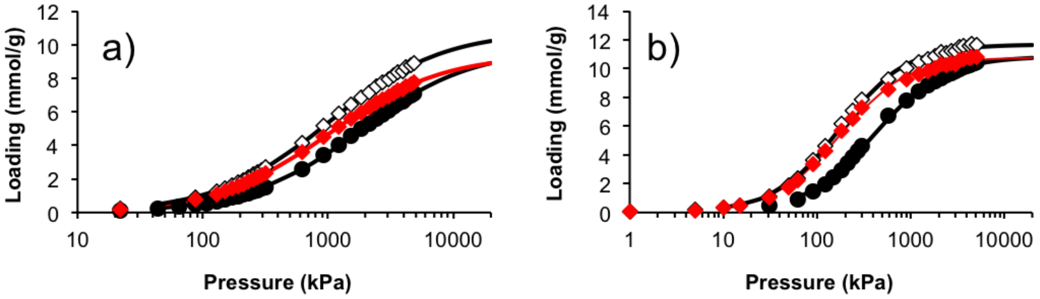

Figure 5-3: Experimental (filled spheres), simulated (open diamonds) and scaled simulated (red diamonds) adsorption isotherms for a) CH_4 and b) CO_2 in MIL-47 at 303 K. The lines indicate curves fit to the Jensen Seaton equation. Scaled isotherms were obtained by multiplying the simulated adsorption amounts by a constant factor equal to the ratio between the maximum experimental and simulated uptake calculated using the fitted isotherms.

The CH_4 and CO_2 experimental, simulated, and scaled adsorption isotherms are plotted in Figure 5-3, while all other scaled isotherms are provided in Appendix D. The scaling factors employed for CH_4 and CO_2 were 1.2 and 1.1, respectively. It should be noted that the simulated hydrogen adsorption isotherm required no scaling in order to match the experimental data, and this particularly important case will be discussed separately. The CH_4 and the CO_2 simulated isotherms overpredict experimental loading by 15% and 8% respectively, at a pressure of 20,000 kPa. Considering that CH_4 uptake in MOFs is correlated with the isosteric heat of adsorption at low pressure, with the surface area at medium pressure, and with the pore volume at high pressure,[88] a difference in simulated and experimental pore volume would have the greatest influence on uptake at high pressure, with only a minimal impact in the low pressure region. As expected the scaled isotherm in Figure 5-3 a) matches the experimental isotherm in the extended high pressure region, namely above 15,000 kPa, yet it greatly overpredicts adsorption in the low pressure region. Similar observations can be made in the case of CO_2 adsorption in Figure 5-3 b). The scaled CH_4 and CO_2 isotherms fail to account for the disagreement between the simulated and experimental isotherms, as they do not match the shape of the experimental isotherms in the low and medium pressure regions.

One important assumption made when seeking to account for non-porous effects through scaling is that there is a uniform reduction in adsorption sites, regardless of the strength of interaction at the various sites. It is possible however, that an incomplete activation during sample synthesis would result in residual solvent or reactant molecules being adsorbed in the high-interaction sites of MIL-47, namely in the pore corners as shown in Figure 5-4.

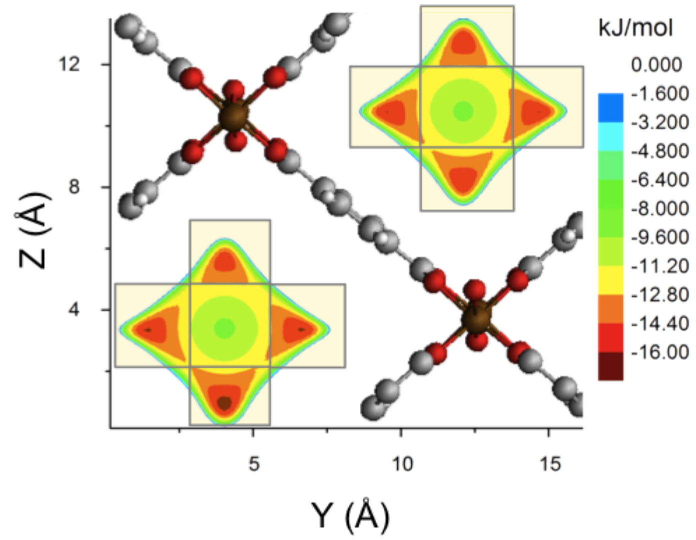

Figure 5-4: MIL-47 contour plot of the potential energy of a methane molecule with the framework, sliced through the yz plane. The grey squares indicate the pore corner sites that were intentionally made inaccessible during the pore blocking simulations.

In order to determine whether a reduced number of high-interaction adsorption sites is the source of disagreement between the simulated and experimental isotherms, GCMC simulations were carried out on a MIL-47 framework where the pore corners were intentionally blocked. The simulated methane isotherms obtained with full, partial, and no pore blocking applied are compared with the experimental isotherm in Figure 5-5. Once again the isotherms were fitted to the Jensen Seaton equation, and extended to the plateau region. When 25% of the pore corners, equivalent to one pore per unit cell, are artificially blocked, the simulated isotherm is in excellent agreement with the experimental data at high pressure, however the low pressure region continues to be significantly overpredicted. The low pressure disagreement is similar in magnitude to the overprediction observed with isotherm scaling. This indicates that the disagreement between simulated and experimental isotherms is not due to a reduced number of accessible high interaction sites. In order to achieve agreement in the low loading region, as much as 70% of the pore corners must be artificially blocked as shown in Figure 5-5, however this results in a simulated pore volume that is much lower than the pore volume of the sample, resulting in a severe underprediction of adsorption at high pressure.

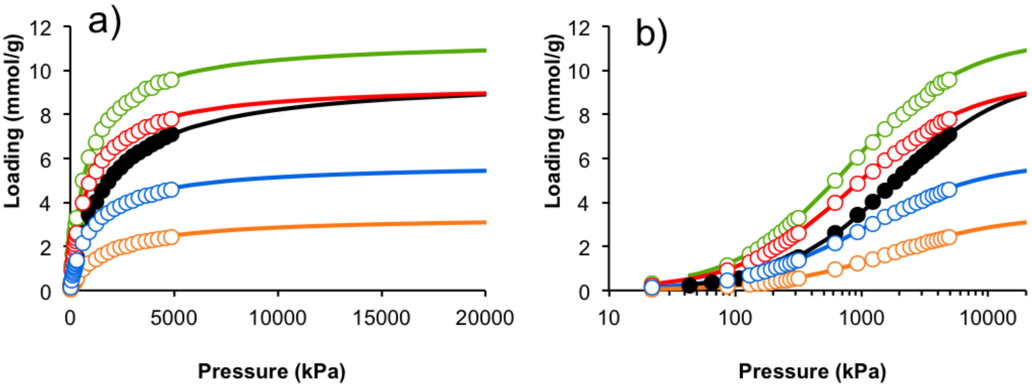

Figure 5-5: CH_4 adsorption isotherms at 303 K obtained from experimental work (filled spheres), and simulations (open spheres) plotted on a) a conventional scale and b) a semi-log scale. Simulations were carried out with fully-accessible pores (green), fully blocked pore corners (orange), 25% of pore corners blocked (red), and with 70% of pore corners blocked (blue). The simulations were carried out using the UFF.[40] The lines indicate curves fitted to the Jensen Seaton equation.

Furthermore, although the isotherms in Figure 5-5 were obtained without accounting for interactions between the methane molecules and residual solvent molecules blocking the high adsorption sites, taking into account residual solvent molecules explicitly results in a higher affinity leading to an even greater overprediction of uptake in the low pressure region, as shown in Figure 5-6 which shows CO_2 uptake in a MIL-47 framework containing two H_2O molecules per unit cell. It can therefore be concluded that regardless of the fraction of inaccessible corner sites, pore blocking simulations fail to match the experimental data across the entire pressure range and that pore blocking is therefore unlikely to be the cause for the differences. The isotherms presented in Figure 5-6 were obtained using the UFF, however similar results can be expected with the Dreiding force field.

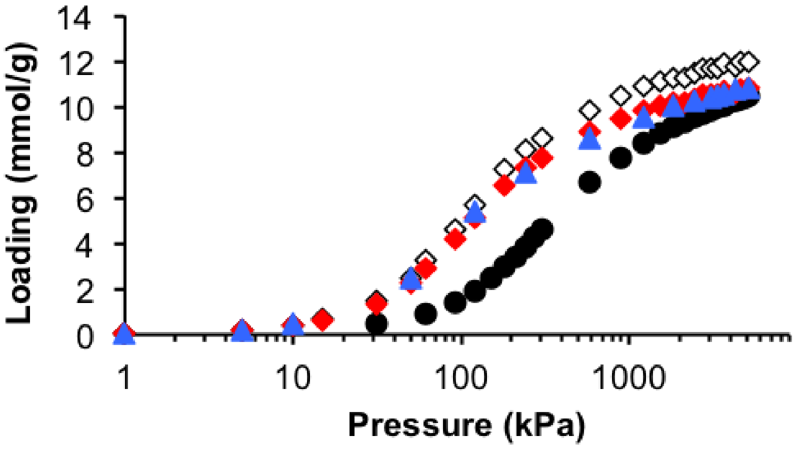

Figure 5-6: UFF[40] simulated adsorption isotherm of CO_2 in a MIL-47 framework containing 2 H_2O molecules per unit cell (blue triangles), UFF[40] simulated isotherm on empty MIL-47 structure (open diamonds), scaled UFF isotherm (red diamonds), experimental (black spheres) adsorption isotherm in MIL-47 at 303 K.

The overprediction of CH_4 and CO_2 uptake at low and medium pressure is present even after scaling factors are applied. In other words, in a simulated MIL-47 structure with the same pore volume as the experimental sample, a larger amount of CH_4, CO_2, (and other gases as shown in Appendix D) are adsorbed compared to the experimental structure. Additionally, the adsorption isotherms simulated on a MIL-47 framework with partially obstructed pores, plotted in Figure 5-5, demonstrate that this over prediction cannot be explained by the presence of inaccessible high interaction sites. This means that the adsorbate-framework interactions being modelled are stronger than what is observed experimentally, causing a greater amount of molecules to become adsorbed at low pressure.

5.3 Force Field Modifications

The second possible cause for the overprediction of gas uptake in MIL-47 is an overprediction of the interactions between the adsorbates and the framework in the GCMC simulations. The overprediction is observed for both, non-polar and polar molecules for which electrostatic interactions are taken into account, indicating that the dispersive fluid-framework interactions, which are modelled with the Dreiding (or the UFF as shown in Appendix E) force field, are too large in the simulations. While the Coulombic interactions were determined using partial charges calculated by DFT studies specifically for MIL-47, the dispersion interactions between adsorbates and the framework were calculated using parameters taken from the Dreiding[41] and UFF[40] generic force fields, which were not developed for MOFs in particular.

In order to determine whether the disagreement between simulated and experimental isotherms is due to a misrepresentation of adsorbate-framework interactions when using the general Dreiding LJ parameters, the effect of reduced adsorbate-framework interaction strengths on the simulated isotherms was studied. Unlike the method used by Yang and Zhong,[121] who adjusted force field parameters for each adsorbate studied, in this work a single set of framework parameters was obtained by adjusting the Dreiding force field in order to accurately describe the experimental methane isotherm, and its transferability to other pure components and mixtures was tested. The key advantage of the experimental data used in this work stems from the use of a single MIL-47 sample for all experimental adsorption isotherms. This presents the rare opportunity of investigating adsorbate-framework interactions based on a very consistent set of experimental data, for a wide range of gases, without having to account for differences in the quality of the sample, which might vary from batch to batch. Hence, all of the adsorbates interacted with the same MIL-47 sample, and more specifically with the same pore surface. An inaccurate description of the adsorbate-framework interactions would therefore require the same framework force field corrections to be applied for all adsorbates. As a result, the suitability of the Dreiding force field was determined by testing whether a set of modified Dreiding parameters fitted for one adsorbate could be directly transferred to all other adsorbates in order to obtain quantitative agreement between simulated and experimental isotherms.

The force field parameters representing each of the adsorbates were not adjusted, as this would have affected both the fluid – fluid interactions and the fluid – framework interactions. Adjustments were made to the force field parameters representing the framework atoms by adjusting the Dreiding LJ parameters based on the methane adsorption isotherm. The benefit of working with the methane isotherm is that the molecules are modelled using a single LJ sphere, and Coulombic interactions do not play a role. By excluding steric and electrostatic factors, the effect of adjustments made to the framework LJ parameters on the adsorption isotherm was isolated, thus ensuring the transferability of the modifications to more complex systems. If the disparity between the original simulations and the experimental isotherms was due to inaccurate framework LJ parameters, the corrected LJ parameters determined for a methane isotherm should be transferable to adsorption simulations of any gas on MIL-47 without additional changes.

In the LJ model describing the dispersive adsorbate-adsorbate and adsorbate-framework interactions, the strength of the interaction between two atoms is governed by the depth of the potential well, ε/k_B. In order to reduce the interaction between adsorbate molecules and MIL-47, the ε/k_B parameters used to describe the framework atoms were adjusted, while the original σ values were preserved. The best agreement between experimental and simulated methane adsorption isotherms over the whole pressure range was obtained with an ε/k_B reduction of 25%. This set of parameters is given in Table 5-2, and will be referred to as Dreiding* (modified Dreiding) from here on.

Table 5-2: Dreiding* LJ parameters used for modelling the interaction with the MIL-47 framework atom.

	σ (Å)	**ε/k_B (K)**
Hydrogen	2.846	5.737
Carbon	3.473	35.892
Oxygen	3.033	36.119
Vanadium	2.801	6.039

In Figure 5-7, the methane adsorption isotherms simulated using Dreiding, Dreiding*, as well as the experimental methane isotherm are compared. In Figure 5-7 b), the isotherms are shown on a log-log plot in order to indicate the level of agreement observed in the Henry's law region. In this low loading section, the adsorption process is governed by the adsorbate-framework interactions, while the adsorbate-adsorbate interactions are negligible. The excellent fit observed between the experimental and the Dreiding* simulated isotherms in the Henry's law region indicates that the adsorbate-framework interactions observed experimentally are being correctly represented. As the pressure is increased and more molecules are adsorbed, adsorbate-adsorbate interactions start to play an increasingly important role in the adsorption process, and at high pressure the amount adsorbed is determined by the pore volume. As shown in Figure 5-7 a), the Dreiding* simulated isotherm is able to accurately predict the uptake of methane at high pressure, therefore it is not necessary to use additional scaling factors in order to account for non-porous effects.

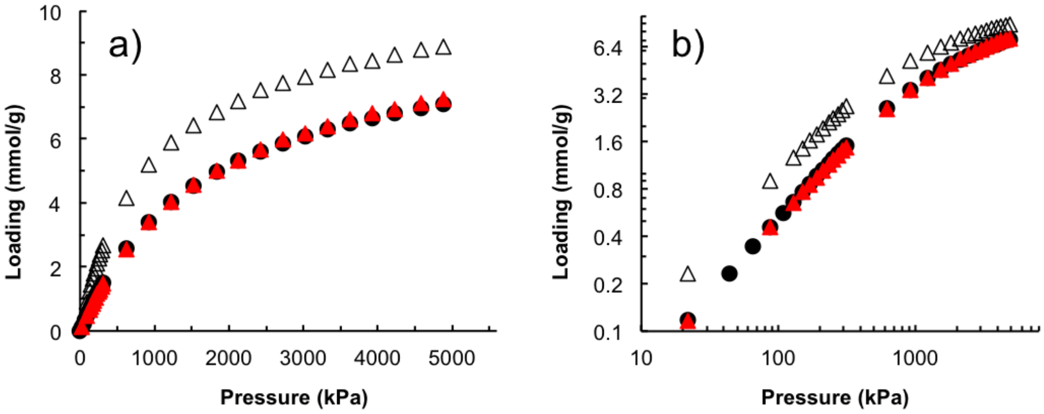

Figure 5-7: MIL-47 methane isotherms at 303 K obtained experimentally (closed spheres), and simulated using the original Dreiding (open triangles), and Dreiding* (red triangles) plotted on a) a normal scale and b) a log-log scale.

5.3.1 Pure Component Isotherms

In order to determine whether Dreiding* is transferable to other adsorbates, the entire set of single components was simulated using Dreiding*. The Dreiding and

Dreiding* simulated isotherms for C_2H_6, C_3H_8, C_3H_6, C_4H_{10}, H_2, N_2, O_2, CO_2, and CO are plotted along with the experimental isotherms in Figure 5-8. All isotherms calculated using Dreiding* show excellent agreement with the experimental results, and do not require any further scaling. In the case of propene, a slight underprediction can be observed in the low pressure region, while butane uptake is slightly overpredicted in the low pressure region. The ability to model the adsorption of a large range of gases using the same force field adjustments, that is Dreiding*, indicates that the disagreement observed between the original Dreiding simulations and the experimental isotherms are due to an overprediction of the adsorbate-framework interaction strength. These results are not unique to the Dreiding force filed. Similar results were obtained by using the same approach with the UFF force field and reducing ε/k_B by 30%, as shown in Appendix E.

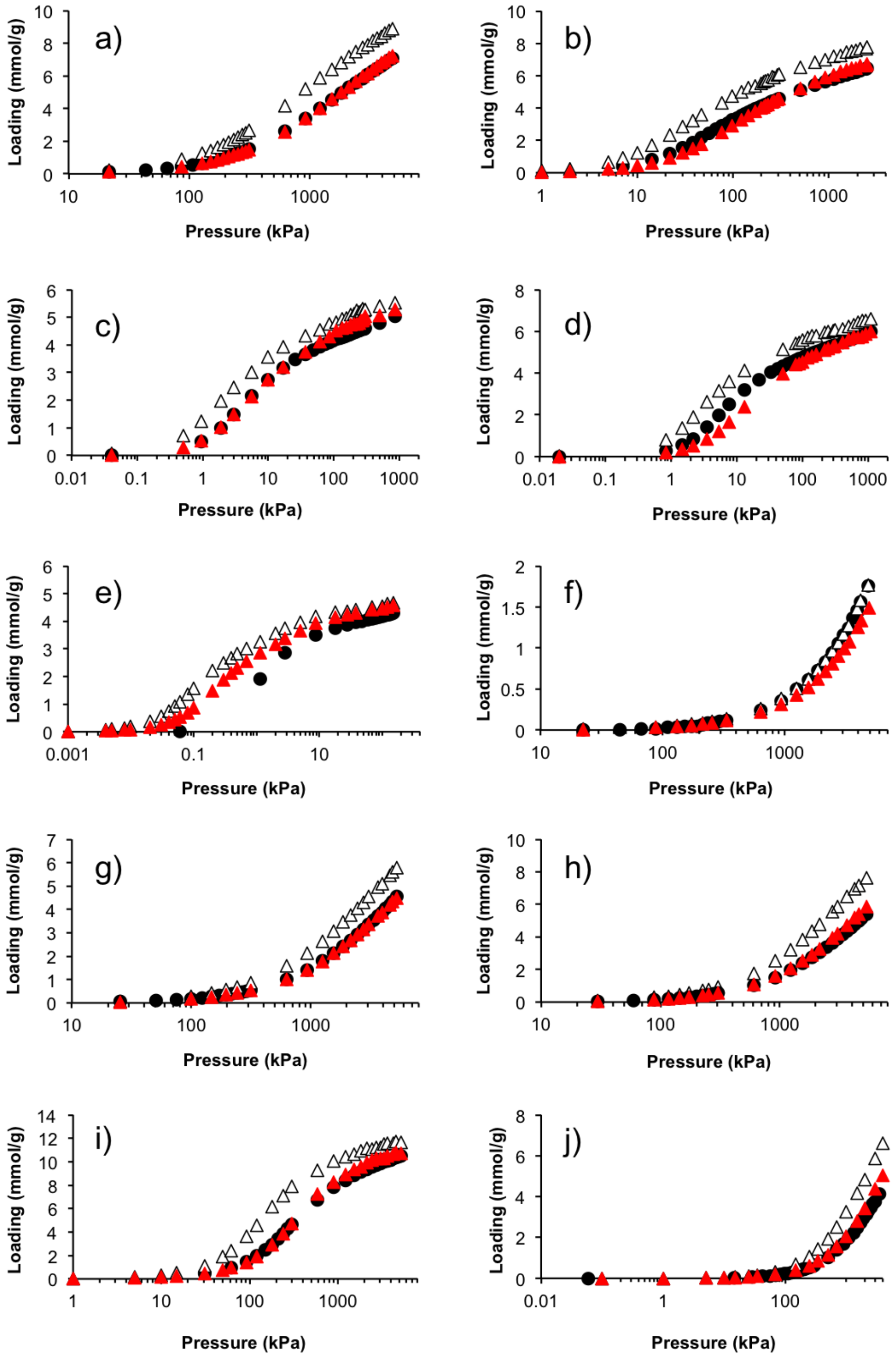

Figure 5-8: Dreiding (open triangles), Dreiding* (red triangles) and experimental (closed spheres) adsorption isotherms in MIL-47 at 303 K for a) methane, b) ethane, c) propane, d) propene, e) butane, f) hydrogen, g) nitrogen, h) oxygen, i) carbon dioxide and j) carbon monoxide.

In the case of hydrogen, the interaction between molecules and MOF framework atoms is weak, and does not have a large influence on uptake. Hence, hydrogen uptake does not correlate with the isosteric heat of adsorption, and the simulated hydrogen isotherm is effectively ‘immune’ to the inherent errors of the Dreiding LJ parameters. As shown in Figure 5-8 f) both the Dreiding and Dreiding* simulated hydrogen isotherms match the experimental data very well, and there is only a minor underprediction of loading in the high-pressure region when using the Dreiding* parameters. The high level of agreement observed for hydrogen with the original force field however only mirrors the findings of Frost and Snurr,[88] who found that H_2 uptake at room temperature is most heavily correlated with the free volume of a material, and is not an indication that the Dreiding parameters accurately model adsorbate-framework interaction strength.

The effect of the weak dispersive interactions between hydrogen and the framework on adsorption behaviour is further illustrated in Figure 5-9, which contains the density distribution plots obtained for H_2, CH_4, and CO_2. While the strongly adsorbing CH_4 and CO_2 are preferentially adsorbed in the pore corners (the differences between the CH_4 and CO_2 distribution plots are caused by differences in the shape of the molecules), H_2 interacts only weakly with the framework, and is adsorbed evenly throughout the pore space. It is therefore not surprising that while the reduction in ε/k_B values has a substantial effect on all other strongly-interacting adsorbates, in the case of hydrogen this effect is not observed.

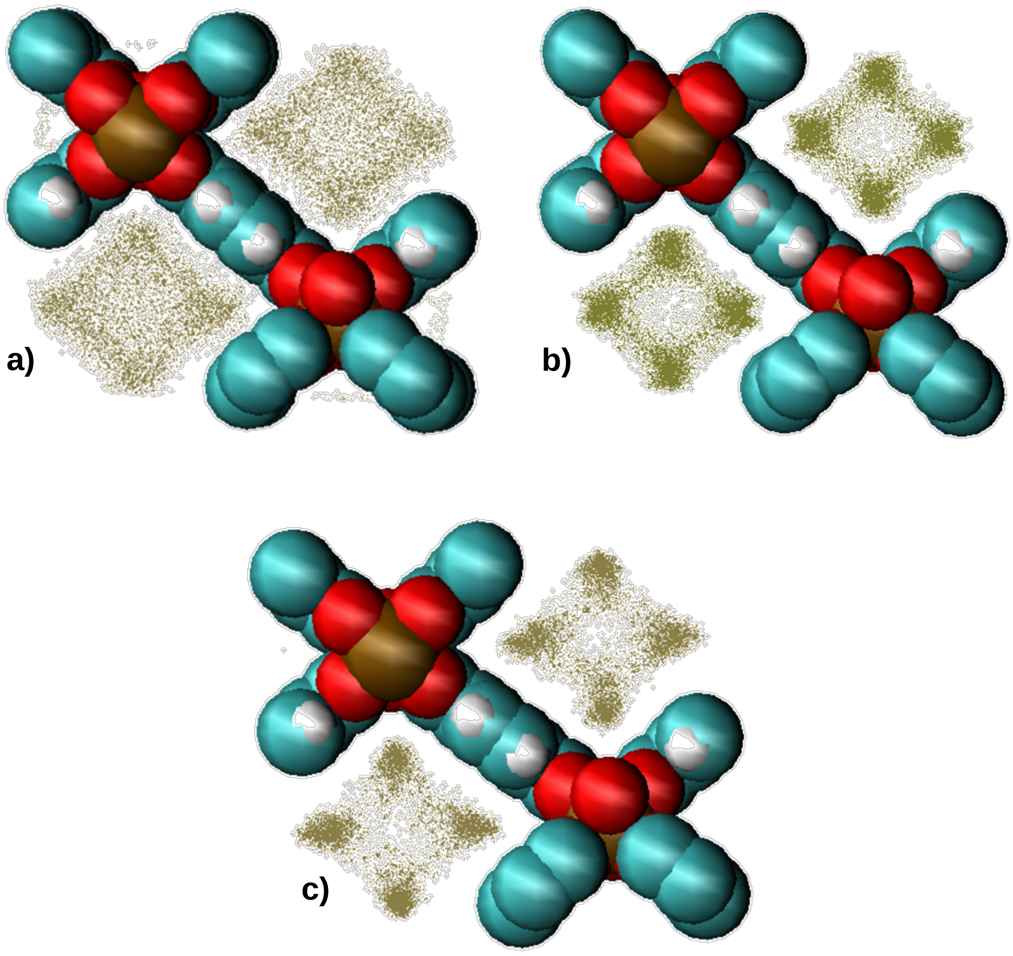

Figure 5-9**:** Density distribution plots for the adsorption of a) H_2, b) CH_4, and c) CO_2 in MIL-47. Each dot represents the position of the centre of mass of a molecule during the simulation at 303 K.

5.3.2 Mixture Adsorption

The use of correct fluid-solid interactions in the prediction of adsorption isotherms is of fundamental importance not only for single components but also for mixtures. As a further validation of the findings, adsorption simulations for three different mixtures were carried out using Dreiding and Dreiding*, and the results were compared with adsorption isotherms obtained experimentally. Figure 5-10 provides a comparison of experimental and simulated adsorption isotherms using Dreiding and Dreiding* for mixtures composed of C_2H_6:CO_2 20:80, CO_2:CO 20:80, and CO:CH_4 20:80 at 303 K. Not surprisingly, the simulations using the unmodified Dreiding failed to correctly describe mixture uptake in MIL-47 due to the overprediction of the adsorbate-framework interactions. The isotherms simulated with Dreiding*, however, show very good agreement with the experimental isotherms, especially considering that the errors in the experimental data were estimated to be +/-10%.[122]

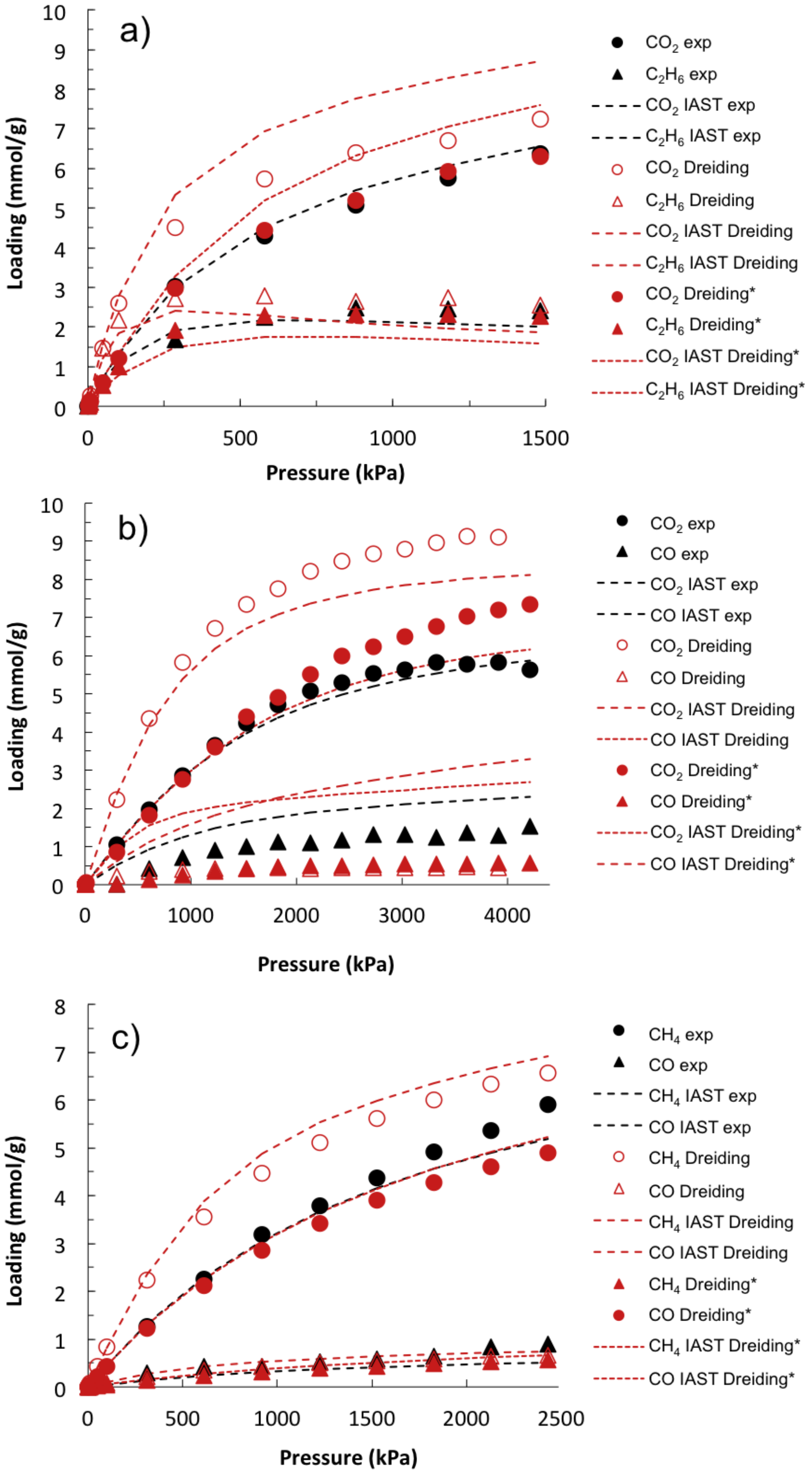

Figure 5-10: MIL-47 mixture adsorption isotherms at 303 K: a) C_2H_6:CO_2 20:80 b) CO_2:CO 20:80, and c) CO:CH_4 20:80.

All Dreiding* mixture adsorption isotherms are in excellent agreement with the experimental data in the low pressure region, indicating that the adsorbate-framework interactions are correctly represented. In the medium and high pressure regions however, Dreiding* presents some deviations from experimental isotherms, especially in the case of the two mixtures containing CO. For the CH_4:CO mixture shown in Figure 5-10 c), CO adsorption is predicted well over the entire pressure range, while CH_4 adsorption is slightly underpredicted at high pressure. The Dreiding* simulation results for the CO_2:CO mixture given in Figure 5-10 b), show an overprediction of the CO_2 uptake and a small underprediction of CO uptake at high pressure. In the case of the C_2H_6:CO_2 20:80 mixture (Figure 5-10 a)), both the C_2H_6 and the CO_2 Dreiding* isotherms are in excellent agreement with the experimental isotherms. As mixture adsorption data may contain a significant experimental error margin (+/-10%), the IAST method was used as verification in order to predict the adsorption of each mixture from experimental single component isotherms, as well as Dreiding* simulated single component isotherms. Similar to the Dreiding* simulation results, the IAST(exp) calculations are in very good agreement with the experimental uptake of mixture components (black dashed lines in Figure 5-10), with few deviations observed. While good agreement is observed using IAST(exp) and IAST(Dreiding*), the IAST(Dreiding) isotherms show large deviations from the experimental uptakes (as expected from the single component predictions), and cannot be used to determine mixture adsorption in MIL-47.

Further confirmation that the Dreiding* force field can be used to correctly predict mixture adsorption regardless of the bulk phase composition is illustrated in Figure 5-11 which shows the amount of CH_4 and CO adsorbed at 303 K and 612 kPa for varying mole fractions of CH_4. The figure shows the available experimental data, IAST predictions based on the experimental pure component isotherms (which are in excellent agreement with the experimental data) and the simulation results using the unmodified Dreiding (Figure 5-11 a)) and Dreiding* (Figure 5-11 b)). As before, the Dreiding simulations over-predict the uptake of both components for all mixture compositions while the isotherms simulated with Dreiding* match IAST(exp) isotherms and the experimental data extremely well.

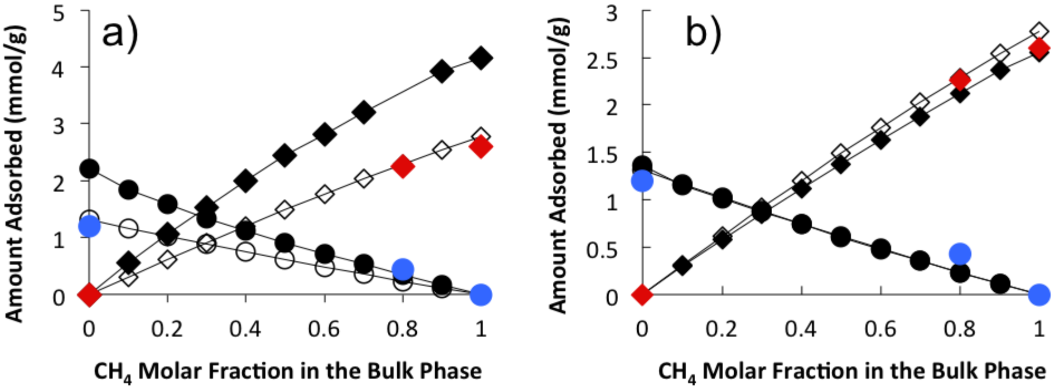

Figure 5-11: Adsorption of CH_4 (diamonds) and CO (spheres) from CH_4:CO mixtures at 303 K and 612 kPa as a function of bulk phase composition determined using a) Dreiding and IAST(exp) and b) Dreiding* and IAST(exp). Dreiding and Dreiding* data - full symbols, IAST - open symbols, experimental data: CH_4- red, CO_2 - blue.

5.4 Investigation into Structure Rigidity

Another potential source of error in the simulated isotherms stems from the assumption that the MIL-47 framework atoms are maintained fixed at their crystallographic locations. The crystal structure of MIL-47 was determined by of Barthelet et al.[77] from single crystal X-ray diffraction performed on the activated framework, and has been used with periodic boundary conditions in all simulated isotherms presented thus far. The thermal ellipsoid representation of the structure is shown in Figure 5-12 indicating the positions of the framework atoms with a 50% and 90% probability in a) and b), respectively. The relatively large thermal factors of the carbon atoms indicate that there is some freedom of movement associated with the BDC linkers. The aromatic rings are connected to the metal rods through carboxylate bonds, and therefore have the ability to rotate around their axis.

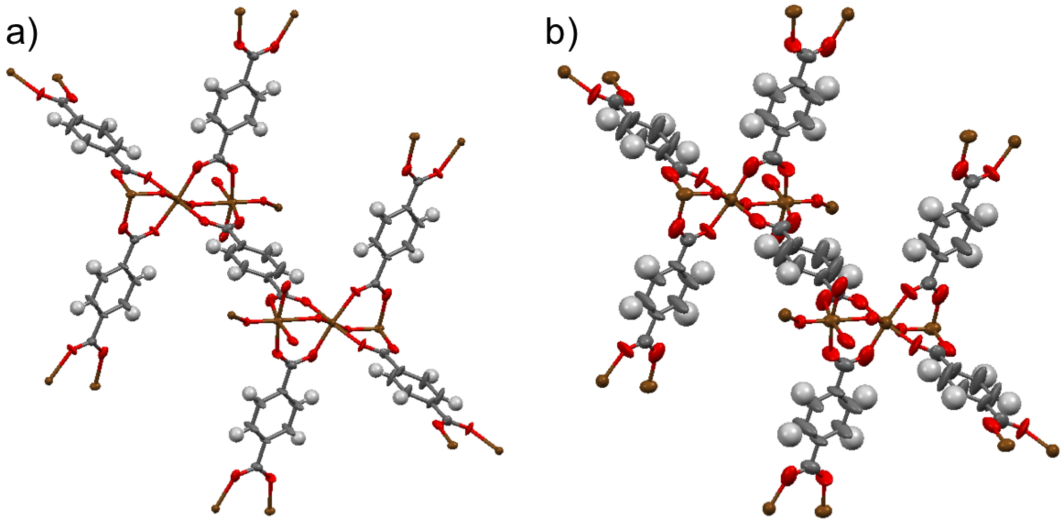

Figure 5-12: MIL-47 crystal structure with atoms shown as thermal ellipsoids of a) 50% and b) 90% probability. Colour key: vanadium – brown; oxygen – red; carbon – dark grey; hydrogen – light grey.

Recently, several studies have focused on assessing the ‘rigidity’ of the MIL-47 framework.[123-125] The work of Kolokolov et al. used ^{2}H NMR spectroscopy in order to confirm that the benzene rings in the MIL-47 linkers can undergo π flips about their symmetry axis at temperatures above 300 K, potentially affecting the adsorption process for small molecules.[123] A different approach used by Yot et al., consisting of a combination of Hg-porosimetry and molecular dynamics simulations, elucidated the breathing behavior of MIL-47 at high pressure, and revealed a transition of the framework towards closed pore form at 340 MPa, accompanied by a reduction in the unit cell volume by half.[124] The flexible nature of the MIL-47 framework was further confirmed in the work of Wang et al., in which the framework was observed to adapt upon adsorption of aromatic and cyclohexane molecules through a variety of deformations including breathing, twisting accompanied by chain rotation, and bending of the ligands.[125] In this work, ab inito molecular dynamics studies enabled an inspection of the atomic positions of the guest free MIL-47 framework. The findings were compared to the crystallographic structure published in the cif file[77] and the impact on adsorption simulations was assessed.

Initially a geometry optimization simulation was carried out for the MIL-47 framework in order to determine the minimum energy configuration of MIL-47. This was followed by a study of the variation in the orientation of BDC linkers with time, performed using ab-initio molecular dynamics simulations. An average configuration was obtained by averaging the atomic positions over 10,000 structures obtained at regular time step intervals (1.0 fs) over the simulation duration of 10 ps. In order to verify that the averaged structure was indeed a good representation of the atomic positions observed for MIL-47, the simulation time was extended to 20 ps. A second averaged structure was then obtained using 20,000 configurations obtained over the 20 ps simulation time. No significant differences could be observed between the AIMD averaged structures, therefore the AIMD averaged configuration obtained at 10 ps, which will be referred to as MIL-47(AIMD) from here onwards, was deemed to be an accurate representation of the MIL-47 atomic positions obtained from ab-initio simulations, and was analyzed further.

In Figure 5-13 the original crystallographic configuration of MIL-47[77] is compared to the geometrically optimized structure and the AIMD averaged configuration. In MIL-47(AIMD) the BDC linkers are rotated around their axis, whereas the linkers of the original crystallographic structure are perpendicular to the yz plane. Over the course of the AIMD simulation, the linkers were observed to rotate with ease back and forth about their symmetry axis, however no full rotations were identified. The linkers appeared to be rotated by some degree over the entire simulation time, and were seldom directly perpendicular to the yz plane (0°) as shown in the spatial distribution plots in Figure 5-14, which were obtained using the Travis[126] analysis package. The rotation of adjacent linkers seemed to be independent of each other and we did not observe any concerted movement. The degree of rotation in the time-averaged structure varies between the linkers from 2° to 22°, however the largest observed rotation angle was significantly greater. The presence of a slightly smaller rotation in the BDC linkers was also observed in the geometrically optimized structure, as shown in Figure 5-13 b), ranging from 2° to 15°. Although its degree of linker rotation is not as great as what was observed for MIL-47(AIMD), the presence of linker rotation in the energy minimized structure confirms that the MIL-47(AIMD) framework is an accurate representation of time-averaged linker positions, and is not simply a result of an insufficiently long simulation time.

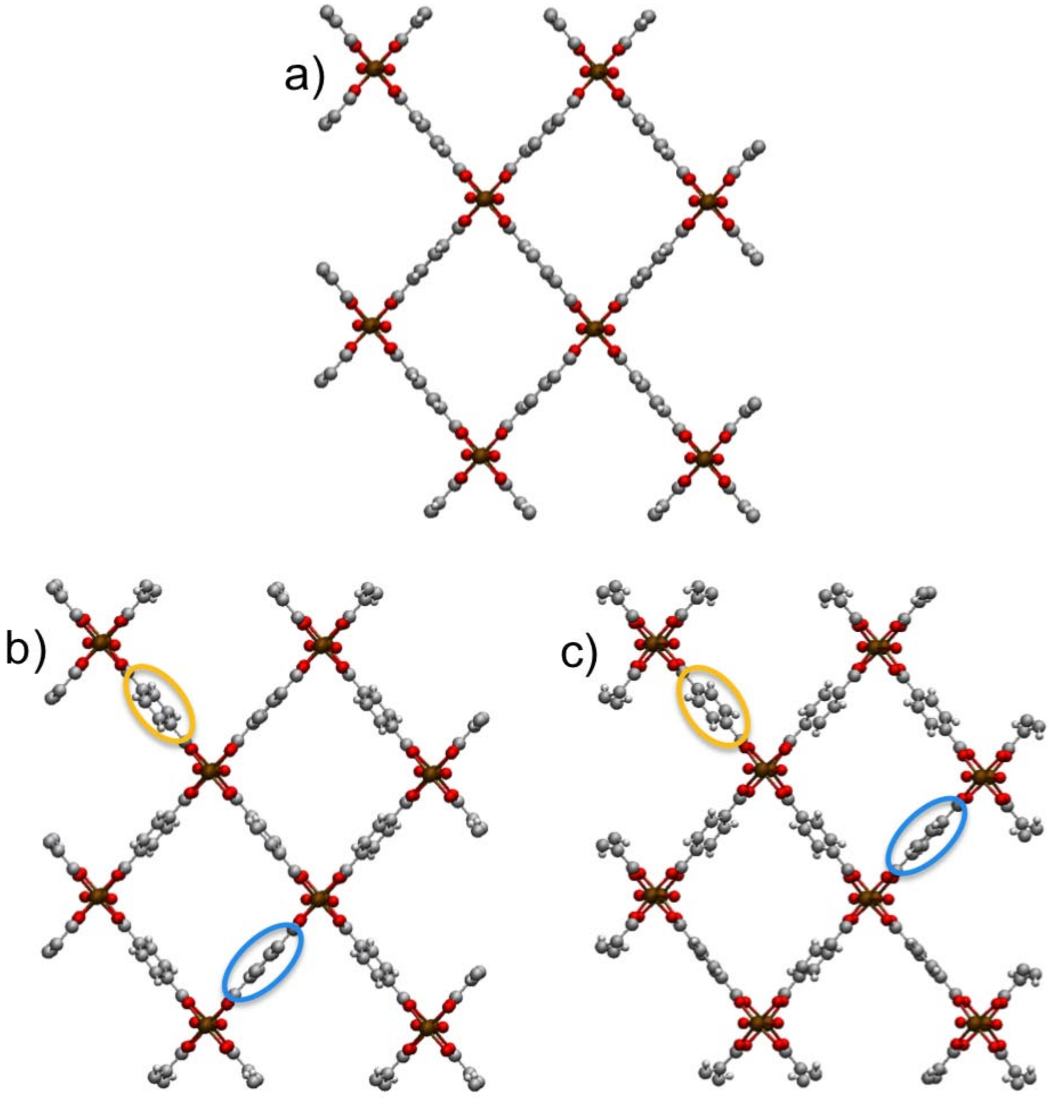

Figure 5-13: a) The crystallographic MIL-47 framework, b) the geometry optimized MIL-47, and c) MIL-47(AIMD). Colour key: vanadium – brown, oxygen – red, carbon – dark grey, hydrogen – light grey. Orientation: yz plane, with the positive x-axis directed into the page. Yellow highlighting in b) and c) is used to indicate linkers rotated by 15°, and 22°, respectively. Blue highlighting in b) and c) is used to indicate linkers rotated by 2° compared to the crystallographic structure.

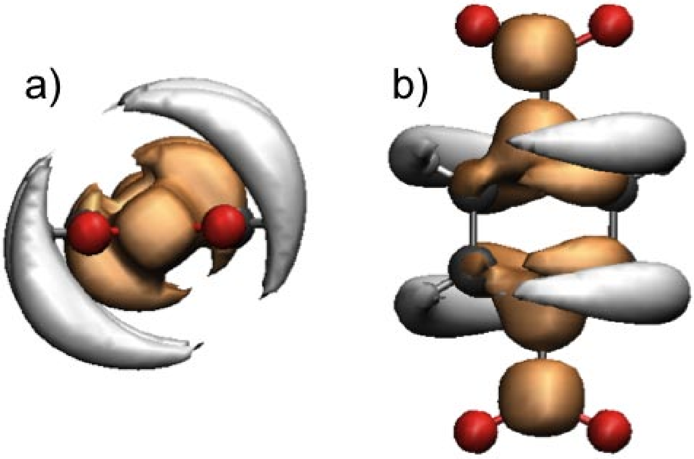

Figure 5-14: Spatial distribution function obtained using Travis,[126] for the carbon (orange) and hydrogen (light grey) atoms of the MIL-47 linkers obtained over the course of the AIMD trajectory viewed a) along the symmetry axis, and b) facing the linker plane. Crystallographic linker position: oxygen – red, carbon – dark grey, hydrogen – light grey.

5.4.1 Pure Component and Mixture Adsorption Simulations with MIL-47(AIMD)

GCMC simulations were first carried out using the Dreiding force field in order to study the adsorption of all pure components on MIL-47(AIMD). The isotherms were compared to the experimental data as well as to the simulated isotherms determined for the crystallographic MIL-47 structure. The comparisons for CH_4, CO_2, CO, O_2, N_2 and H_2 are presented in Figure 5-16, and show that while simulations on the original crystallographic structure result in an overprediction of uptake for all gases except H_2, the isotherms simulated using the MIL-47(AIMD) structure are in excellent agreement with the experimental data across the entire pressure range. As shown in Figure 5-15 a twist in the linkers results in a slight reduction of the low loading isosteric heat of adsorption for CO_2 and CH_4. This reduction in interaction strength results in a lower uptake in the lower pressure region when simulations are performed using MIL-47(AIMD) as opposed to the crystallographic MIL-47 structure.

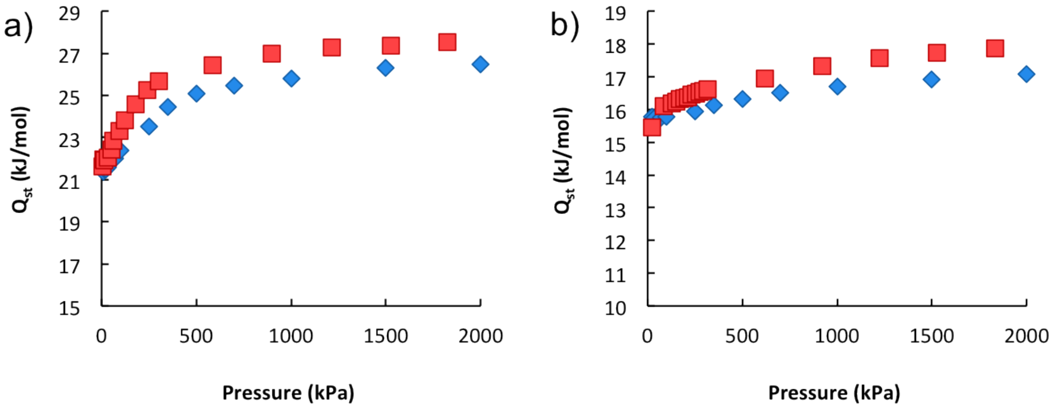

Figure 5-15: Isosteric heats of adsorption determined from a) CO_2 and b) CH_4 simulations performed on the crystallographic MIL-47 structure (red squares) and the MIL-47(AIMD) structure (blue diamonds).

The agreement observed in Figure 5-16 indicates that the crystal configuration obtained from AIMD simulations is a more suitable representation of the atomic positions in MIL-47 than the original crystallographic structure for simulating adsorption of a variety of gases. Unlike the approach presented in Section 5.3, entailing a force field adjustment, the use of MIL-47(AIMD) is based on a concrete physical justification. The work of Chen et al[127] provided detailed proof that AIMD methods give reliable predictions of structural changes resulting from gas uptake and temperature changes. In this work, AIMD simulations show that MIL-47 linkers are usually orientated in a rotated position rather than perpendicular to the yz plane. While MIL-47(AIMD) is obtained by time-averaging over 10 ps, the crystallographic MIL-47 structure results from X-ray diffraction studies in which atomic positions are averaged over significantly longer time scales. Therefore, the linker positions may not be clearly reflected in the experimental diffraction data. In addition, the Rietveld refinement procedure normally employed when determining atomic positions from X-ray diffraction data is not an exact method. The uncertainties associated with Rietveld refinement may have resulted in slight inaccuracies in the MIL-47 structure determined, which then translate to significant errors in the prediction of gas adsorption.

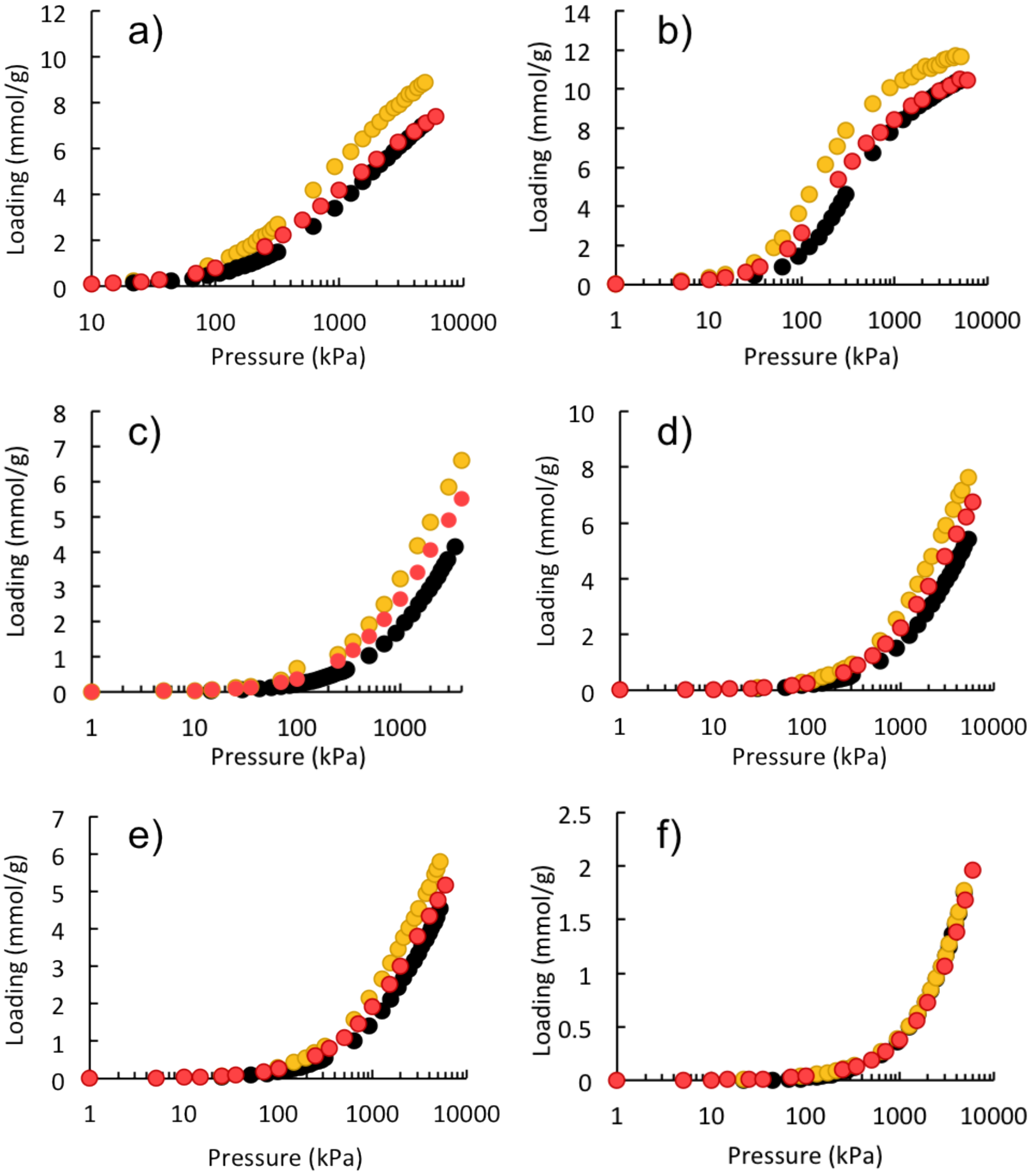

Figure 5-16: Pure component adsorption isotherms for a) CH_4, b) CO_2, c) CO, d) O_2, e) N_2 and f) H_2 in MIL-47. Experimental data - black spheres. Simulated isotherms: MIL-47(original) - yellow spheres, and MIL-47(AIMD) - red spheres.

In the case of the longer-chain hydrocarbons, although the uptake of C_2H_6 is well predicted, the agreement between the low-pressure range MIL-47(AIMD) uptake and the experimental data deteriorates with increasing chain length as shown in Figure 5-17. Furthermore, poorer agreement is observed for propane than for propene. Propane is the slightly larger molecule and unrestricted by the presence of a double bond, and therefore has a greater freedom of movement. These observations suggest that the discrepancies observed for propane, propene and butane might be due to a poor description of steric effects in the simulations performed. In addition, particularly in the case of butane adsorption, the slow diffusion of molecules through the pores may have resulted in a low experimental uptake, that is below equilibrium levels, in the low-pressure region. It should also be mentioned however, that the MIL-47 structure has been reported to undergo significant packing-related structural changes during adsorption of aromatic molecules.[125] The AIMD averaged structures were obtained through simulations using an adsorbate-free framework. It is possible that MIL-47 experiences further structural changes on adsorption of bulky molecules, an effect not described by the simulations performed in this work. The isotherms of propane, propene and butane adsorption in the MIL-47(AIMD) framework are similar to those obtained for the original MIL-47 structure, particularly in the low pressure region. This indicates that the adsorbate – framework interactions experienced by these larger molecules are strong enough to overcome the influence of the structural differences between the two structures.

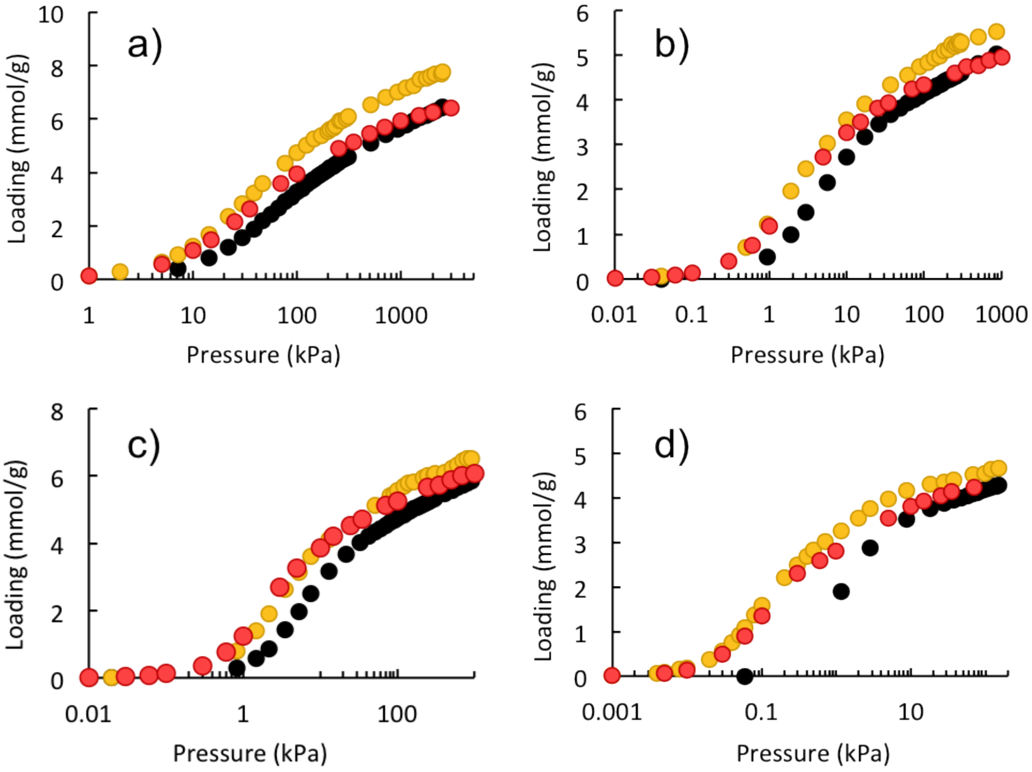

Figure 5-17: Pure component adsorption isotherms for a) C_2H_6, b) C_3H_8, c) C_3H_6 and d) C_4H_{10} in MIL-47. Experimental data - black spheres. Simulated isotherms: MIL-47(original) - yellow spheres, MIL-47(AIMD) - red spheres.

The MIL-47(AIMD) framework was further tested in order to determine whether the configuration is also suitable for predicting mixture adsorption. GCMC simulations were carried out using the Dreiding force field for each of the three gas mixtures in MIL-47(AIMD) and compared to experimental isotherms as well as to simulated isotherms in the original MIL-47 structure. As shown in Figure 5-18, the MIL-47(AIMD) simulations resulted in a significant improvement in mixture adsorption prediction. In the case of CO:CH_4 and C_2H_6:CO_2 mixtures, the agreement between MIL-47(AIMD) isotherms and experimental data is remarkable, as shown in Figure 5-18 a) and c). In the case of CO_2:CO mixtures, the simulated isotherms obtained using MIL-47(AIMD) are in much better agreement with the experimental data than the isotherms simulated using the original structure, however CO_2 uptake is slightly overpredicted while CO uptake is underpredicted. Considering that the experimental error for mixture adsorption was estimated to be ±10%, the agreement observed for mixture adsorption is overall very good.

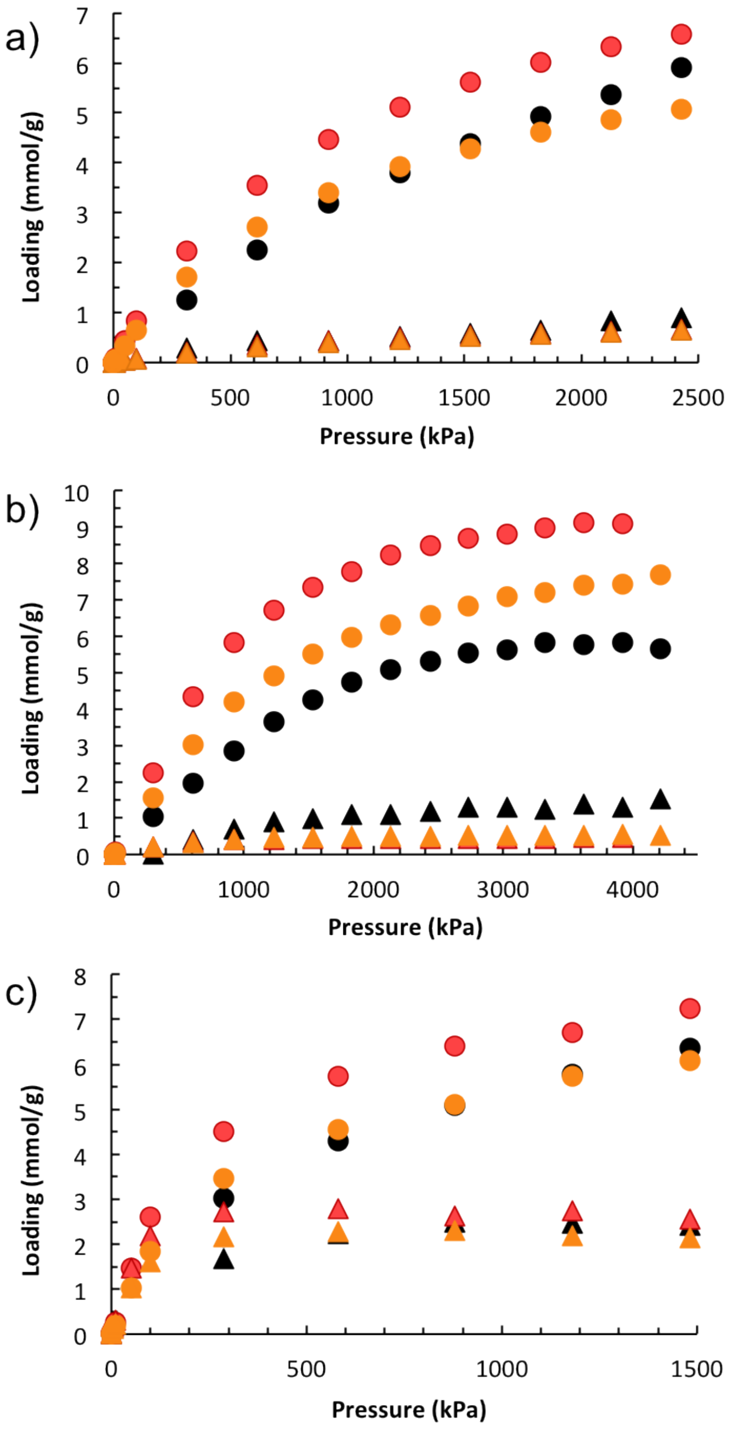

Figure 5-18: MIL-47 binary mixture adsorption isotherms at 303 K: a) 20:80 CO(triangles):CH_4(spheres), b) 20:80 CO_2(spheres):CO(triangles), and c) 20:80 C_2H_6(triangles):CO_2(spheres). Experimental data - black symbols. Simulated isotherms: MIL-47(original) - red symbols, MIL-47(AIMD) - yellow symbols.

5.4.2 The Impact of Linker Rotation On Adsorption and Stability

The MIL-47(AIMD) structure results in simulated isotherms that are in excellent agreement with experimental data. This indicates that the MIL-47 atomic positions may be better described by MIL-47(AIMD) than by the original crystallographic structure. In order to confirm these observations, it is necessary to determine whether the rotation of linkers in MIL-47 results in a stable configuration, and how the energy of a structure with rotated linkers compares to the original crystallographic configuration.

The original crystallographic structure of MIL-47 was modified in order to systematically determine the effect of the extent of linker rotation on the internal energy of the structure. All BDC linkers were incrementally twisted by the same degree around their symmetry axis defined by the carbon atoms belonging to the two carboxylic groups, as depicted in Figure 5-19. This differs from the AIMD averaged structure, in which the angle of rotation varies for each linker.

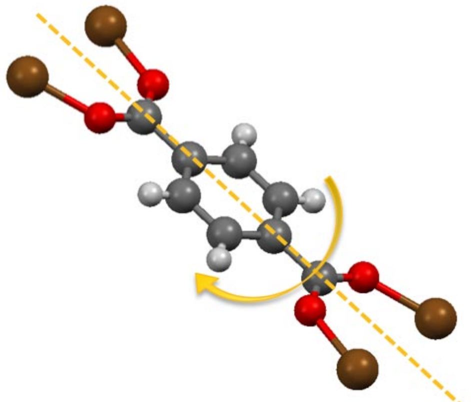

Figure 5-19: Rotation of BDC linkers in MIL-47. Yellow dashed line indicates the axis of rotation. Key: ochre, V; red, O; dark grey, C; light grey, H.

The new structure files obtained by rotating all linkers by 5°, 10°, 15°, 20°, 25° and 30° were then used in order to investigate adsorption of CH_4 in MIL-47. The simulated isotherms (using the Dreiding force field) are compared to the experimental data in Figure 5-20. The best agreement between experimental and simulated data is observed for isotherms obtained using a MIL-47 structure where a 20° twist was applied to the linkers. The MIL-47(20°) isotherm accurately describes methane adsorption across the entire pressure range. As shown in Figure 5-21, the improved agreement with the experimental isotherm achieved with the MIL-47(20°) framework is due to very small structural change.

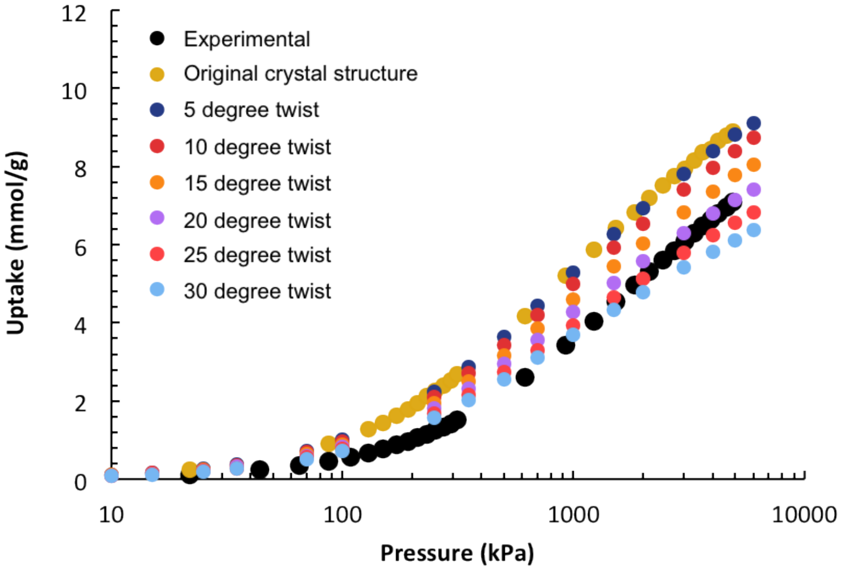

Figure 5-20: Simulated methane isotherms obtained using the original crystallographic structure, and structures modified by applying a twist to all linkers.

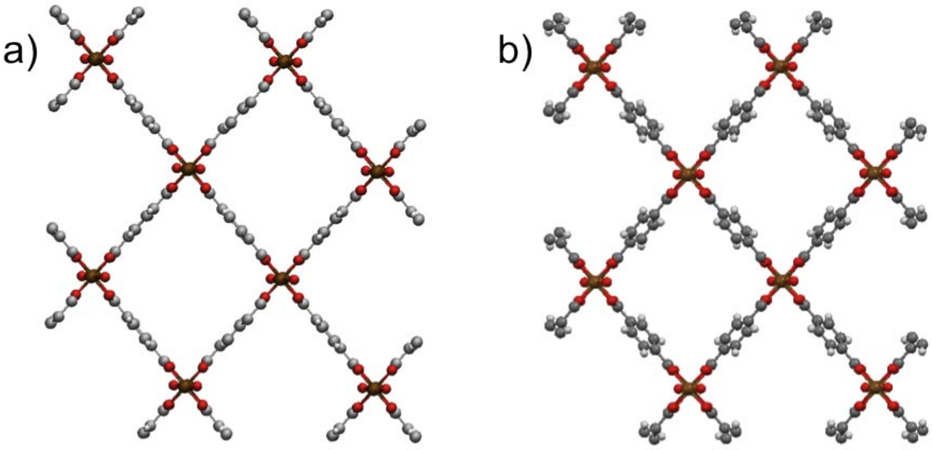

Figure 5-21: a) The original crystallographic MIL-47 structure and b) the MIL-47 structure with linkers twisted by 20°. Key: ochre, V; red, O; dark grey, C; light grey, H.

Ab initio single point energy calculations were performed for the original MIL-47 structure as well as for each of the modified MIL-47 structures with rotated linkers. The energy of the original structure was chosen as the reference point, E_{ref}. The energy difference associated with linker rotation was determined for each modified structure as follows:

$$\Delta E_{linker} = E_{modified} - E_{ref} \qquad \text{Eq 5-1}$$

The calculated change in framework energies due to linker rotation are shown in Figure 5-22. The rotation of linkers in MIL-47 by up to 30° leads to structures with more negative internal energies, which are therefore more favourable than the reference structure. A rotation of 20° results in a structure with one of the most negative energies, indicating that it is a particularly probable configuration of the MIL-47 framework. A rotation of 20° is very similar to the degree of rotation observed in some of the linkers in the AIMD time-averaged configuration. The increase in framework stability corresponding to such a rotation of linkers confirms the trueness of the AIMD time-averaged structure, and validates that the positions of the MIL-47 framework atoms are more accurately represented by using MIL-47(AIMD) than the original crystallographic coordinates.

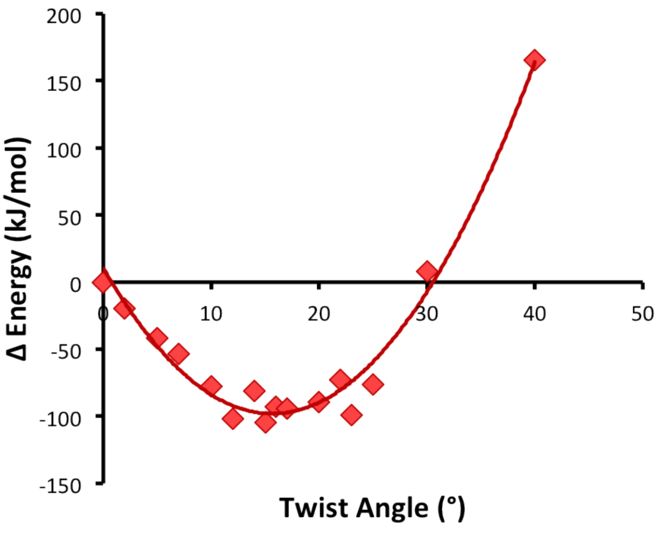

Figure 5-22: Change in framework energy due to linker rotation with respect to the reference structure energy – the original crystallographic MIL-47 structure. Calculated data points are represented using red diamonds. The red trendline is only a guide for the eye.

5.5 Conclusions

By studying the effects of scaling factors on the adsorption isotherms of a wide variety of gases in MIL-47, it became clear that the differences between simulated and experimental isotherms cannot be attributed to the presence of non-porous effects. The scaling of adsorption isotherms, that is reducing the simulated uptake by a factor proportional to the ratio between experimental and simulated uptake at saturation, to account for a lower accessible pore volume gave poor predictions of uptake in the low and medium pressure regions, overpredicting the amount adsorbed. Similarly, simulations with partial blocking of the pore corners of the framework failed to account for the overprediction observed in the low pressure region, thus indicating that the adsorbate-framework interactions simulated are too strong.

In order to determine whether the Dreiding LJ parameters overpredict adsorbate-framework interactions, the transferability of a new set of parameters, Dreiding*, was tested. The modified force field was obtained by reducing the Lennard Jones parameter ε for all framework atoms by 25 % compared to the original Dreiding force field, in order to yield qualitative agreement between simulated and experimental uptake for a single isotherm (methane). In the Henry region, the Dreiding* simulated isotherms showed excellent agreement with the experimental data, indicating a correct representation of adsorbate-framework interactions. Quantitative agreement between simulated and experimental adsorption isotherms was observed for all pure components and mixtures, indicating that Dreiding* is indeed transferable. In other words, the framework LJ parameters require the same adjustment in order to accurately model the adsorbate-framework interaction strength for all of the gases considered. While the Dreiding* force field can be used to successfully predict the adsorption of a variety of pure gases and gas mixtures in MIL-47, this method is not supported by a physical explanation for the necessary adjustment of framework LJ parameters.

A study of the dynamic behavior of the MIL-47 framework through the use of AIMD simulations revealed that the crystallographic positions of the MIL-47 framework atoms do not provide a sufficiently accurate representation of the structure. AIMD simulations provided time-averaged configurations of the guest free MIL-47 framework, featuring a rotation in linker orientation. GCMC simulations carried out using Dreiding and the AIMD time-averaged structure resulted in pure component and mixture adsorption isotherms that were in excellent agreement with experimental data. In addition, single point energy calculations obtained on MIL-47 structures with incrementally rotated linkers showed that linker rotations of up to 30° lead to more energetically favourable configurations. The agreement achieved using MIL-47(AIMD) indicates that the cause for the original discrepancies observed between simulated and experimental isotherms was due to a misrepresentation of framework atomic positions. In MIL-47 the freedom of the benzene rings to rotate about their axis, and the lower framework energy associated with such rotations, confirm that at any discrete moment in time the framework will likely contain linkers with some degree of twist. It is therefore not surprising that in GCMC adsorption studies, the MIL-47(AIMD) configuration is a more appropriate representation of atomic positions than the original crystallographic configuration.

The discrepancies between experimental and simulated isotherms reported in previous MIL-47 studies are very similar in magnitude and shape to the differences presented in this chapter resulting from simulations performed with the crystallographic MIL-47 structure. As a result, the AIMD findings provide an explanation for the overprediction of methane,[100] CO_2,[83] and light hydrocarbon[99] uptake in earlier studies. Generic force fields such as Dreiding and UFF were not designed specifically for MOFs, and can be expected to result in slight inaccuracies in the representation of adsorbate-framework interactions. These force fields however, have been used to successfully simulate adsorption isotherms for numerous MOFs. In the case of MIL-47 the reduction in interaction strength required is large, and unexpected considering the relatively simple nature of the framework. It is much more likely that the discrepancies between the simulated and experimental isotherms in MIL-47 are due to a rotated linker orientation, as revealed by the AIMD investigation. Of course, force field errors may still be present, and may influence MIL-47(AIMD) simulations, but to a much smaller degree.

6 The Impact of Structural Changes on Adsorption in Sc_2BDC_3

The design and synthesis of small pore MOFs is often driven by the proven potential of such materials for gas separation applications.[4] A restricted pore size can result in a molecular sieving effect if the kinetic diameter of one mixture component is smaller than the pore diameter, while the remaining mixture components are too large to enter the pores.[4] On the other hand, if all mixture components are able to fit through the MOF pores, a sufficiently narrow opening will result in a kinetic separation process, as larger molecules will diffuse with greater difficulty than smaller molecules.[4,128]

$Sc_2(O_2CC_6H_4CO_2)_3$, also known as Sc_2BDC_3, is a small pore scandium terephthalate MOF with an orthorhombic unit cell at room temperature, first reported by Miller et al.,[129] as well as Perles et al.,[130] in 2005. The framework is composed of chains of ScO_6 octahedra each of which is linked to neighbouring chains by six terephthalate groups,[129,130] resulting in triangular 1D channels with maximum diameters of 3.5 Å and pore limiting diameters of 2.5 Å. This material, considered to be potentially useful for adsorption and separation processes, has a high thermal stability – crystallinity is maintained up to 400 °C – and a high capacity for H_2 and N_2 at 77 K.[129,130] Although the free diameter of each triangular channel in Sc_2BDC_3 is smaller than the N_2 kinetic diameter of 3.6 Å, the structure easily adsorbs N_2, O_2, CH_4, CO_2, C_2H_6 and C_3H_8, indicating the presence of an inherent structural flexibility which allows such molecules to diffuse into the pores.[131] The orthorhombic Sc_2BDC_3 unit cell contains two symmetrically different linkers, Type 1, and Type 2, shown in blue and yellow in Figure 6-1, arranged in such a way that all triangular channels formed are identical. Adsorption of CO_2 results in a structural change from the orthorhombic form to a monoclinic form, in which the rotation of half of Type 2 linkers about their symmetry axis results in two different types of channels. Follow-up studies revealed temperature changes are also capable of driving this reversible structural change from the orthorhombic to the monoclinic form in Sc_2BDC_3.[132]

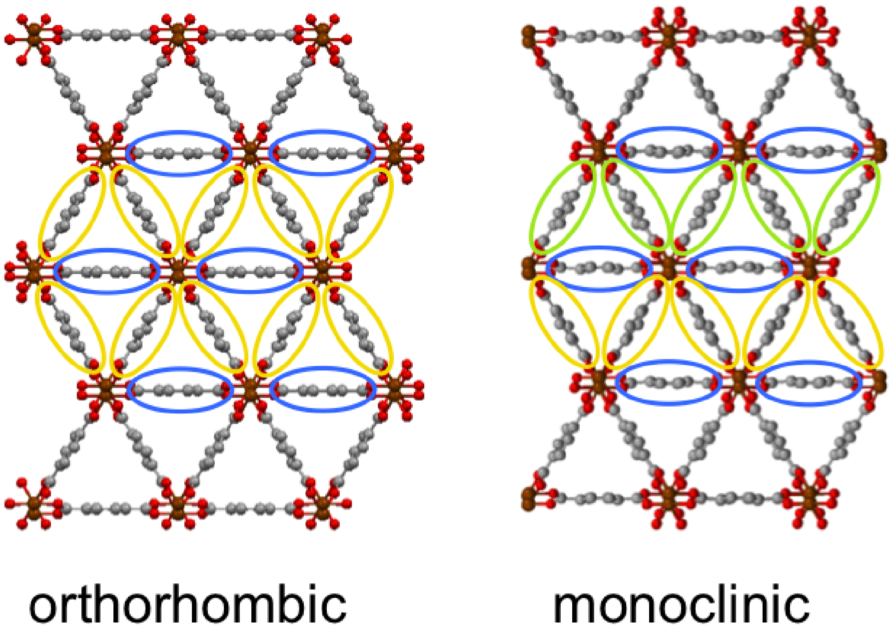

Figure 6-1: Two crystallographic forms of Sc_2BDC_3: orthorhombic and monoclinic. Yellow, blue, and green highlighting is used to indicate symmetrically different linkers. Colour key: O – red, H – light grey, C – dark grey, Sc – brown.

The studies presented in this chapter focus on understanding the adsorption process for CO_2 molecules and methanol molecules in Sc_2BDC_3, using a variety of molecular simulation methods that are described in Section 6.1. In Section 6.2.1, CO_2 adsorption is studied at three different temperatures: 304 K, 273 K and 196 K. The influence of framework configuration on uptake, as well as on CO_2 adsorption sites is investigated using GCMC simulations. Furthermore, in Section 6.2.2, the dynamic response of the Sc_2BDC_3 structure is studied as a function of CO_2 loading at 196 K using ab initio molecular dynamics (AIMD) simulations, and the results are used in order to describe the adsorption of CO_2 over a wide pressure range. Section 6.3 of this chapter looks at methanol adsorption for pressures up to 3 GPa using a diamond anvil cell. The presence of two adsorption sites, observed experimentally by Moggach et al.,[133] is investigated through GCMC and MD simulations. Density distributions of adsorbed methanol molecules as a function of loading elucidate the order in which sites are filled, and radial distribution functions of adsorbed methanol molecules provide an explanation for the observed adsorption site preference. All findings are summarized in Section 6.4.

6.1 Computational Details

6.1.1 GCMC Simulations

Grand canonical Monte Carlo (GCMC)[29] simulations were performed in order to study CO_2 and methanol adsorption in various forms of Sc_2BDC_3. The framework atoms were maintained fixed at their crystallographic positions.[132] All framework atoms were represented using Lennard-Jones parameters taken from the Dreiding force field,[41] with the exception of scandium which was modeled using the Universal Force Field (UFF).[40] Mülliken partial charges for the framework atoms were taken from the work of Mowat et al..[132] All framework LJ parameters and partial charges are presented in Table 6-1 and Figure 6-2. LJ parameters and partial charges describing CO_2 and methanol molecules were obtained from the TraPPE force field,[43,47,50] and are provided in Table 2 – 1 of Chapter 2. The simulations consisted of a minimum of 6×10^6 simulation steps, the first 40% of which were used for system equilibration. In the case of methanol, density distributions were obtained by recording the centre of mass locations of methanol molecules at regular intervals once equilibrium was reached.

Table 6-1: LJ parameters and partial charges assigned to Sc_2BDC_3 framework atoms.[132]

	σ [Å]	ε/kB [K]	q [e]
Sc1	2.936	9.561	1.846
C1	3.473	47.856	-0.113
C2	3.473	47.856	0.916
C3	3.473	47.856	-0.083
C4	3.473	47.856	-0.053
C5	3.473	47.856	-0.163
C6	3.473	47.856	0.866
O1	3.033	48.158	-0.693
O2	3.033	48.158	-0.743
H1	2.846	7.649	0.126
H2	2.846	7.649	0.146

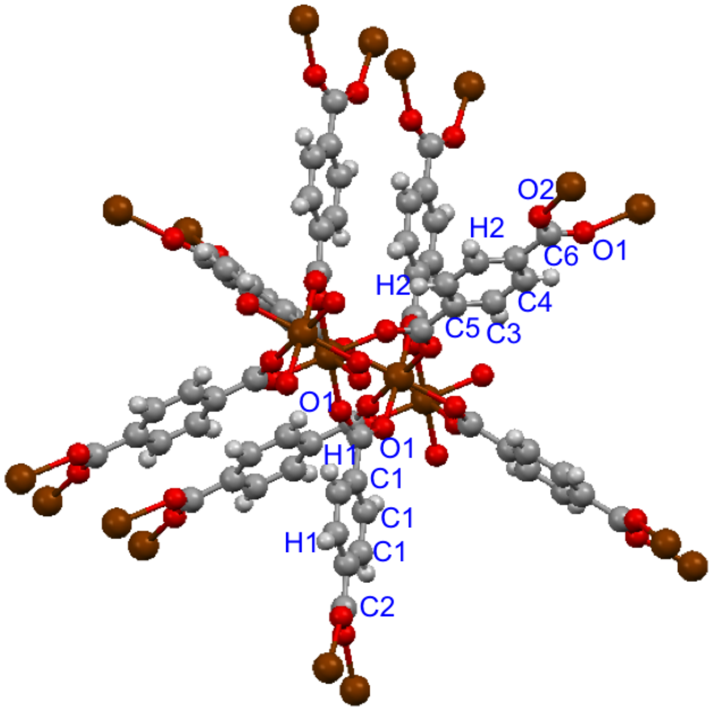

Figure 6-2: Sc_2BDC_3 with atoms labelled corresponding to the partial charges assigned. Colour Key: O – red, H – light grey, C – dark grey, Sc – brown.[132]

6.1.2 MD Simulations

The initial configurations used for the MD simulations were obtained by carrying out GCMC simulations at 298 K and high pressure until a desired methanol loading of 39-42 molec/uc was reached. The loaded frameworks, consisting of 4×2×1 unit cells, were then used directly as starting configurations for molecular dynamics simulations. The MD simulations were performed with the RASPA simulation package,[134] in the NVT (canonical) ensemble. Each simulation was first equilibrated using 2×10^5 MD steps, equivalent to 0.2 ns, ensuring that the system temperature and adsorbate velocities were well equilibrated. The production run consisted of 2×10^5 MD steps, with a time step of 1.0 fs, resulting in a total simulation time of 0.2 ns. The MD simulations used a Nosé-Hoover thermostat in order to maintain the temperature at 298 K, and the velocity-Verlet algorithm[29] for calculating molecular trajectories. The positions of the methanol molecules within each of the Sc_2BDC_3 structures were recorded every 100 fs. For each structure, the 2000 stored configurations were analysed further in order to obtain site-specific radial distribution functions for the positions of methanol molecules.

6.1.3 AIMD Simulations

AIMD simulations were performed using the QUICKSTEP module[66] of the CP2K package.[67] The simulations were carried out using the BLYP exchange correlation functional,[59,60] and dispersion corrections were included using the DFT-D3 method developed by Grimme.[117] All atoms were represented using double-ζ valence plus polarization basis sets optimized for the Goedecker-Teter-Hutter (GTH) pseudopotential[64,65,118] and the BLYP functional. A plane wave basis set energy cutoff of 300 Ry and a corresponding Gaussian basis set relative cutoff energy of 40 Ry were applied. The self-consistent field (SCF) cycles were assigned an energy convergence criteria of 1.0×10^{-6} Hartree. The AIMD simulations were carried out in the NPT ensemble, in order to allow the unit cell parameters to change. The simulation cell contained 1×1×1 Sc_2BDC_3 unit cells for the 0, 4 and 8 molec/uc CO_2 loadings, while 1×1×2 unit cells were used for the 16 molec/uc CO_2 studies, and periodic boundary conditions were applied. The temperature was set to 196 K and controlled using a Nosé-Hoover thermostat.[120] The pressure was set to 1.0 bar and a barostat coupling time constant of 300 fs was applied. In all simulations, the equations of motion were integrated using a time step of 1.0 fs, with the exception of the 16 molec/uc CO_2 study, which employed a 0.5 fs time step. In order to maintain a constant grid point density, a reference cell of constant volume was used. This approach allowed for a more accurate calculation of Coulombic and exchange correlation energies based on a constant number of grid points, despite changes in unit cell size.

6.2 CO_2 Adsorption

6.2.1 The Influence of Temperature on Framework Form

Synchrotron powder X-ray diffraction measurements carried out *in vacuo* by John Mowat (University of St. Andrews) show that at temperatures below 225 K, the Sc_2BDC_3 structure is in a monoclinic configuration.[132] At 225 K the structure undergoes a change from the monoclinic to an orthorhombic configuration, and no additional structural changes are observed upon further heating to 523 K.[132] Interestingly, the work of Miller et al.[131] shows that the structure of Sc_2BDC_3 at 1 bar and 235 K, containing 3.5 mmol/g CO_2, that is, Sc_2BDC_3•$2CO_2$ is monoclinic, yet not identical to the low temperature guest-free configuration, as shown in Figure 6-3. At 235 K the guest-free framework is orthorhombic, however the CO_2-loaded framework under the same conditions is monoclinic, which suggests that CO_2 – framework interactions stabilize the monoclinic configuration, and impede the change towards an orthorhombic form.

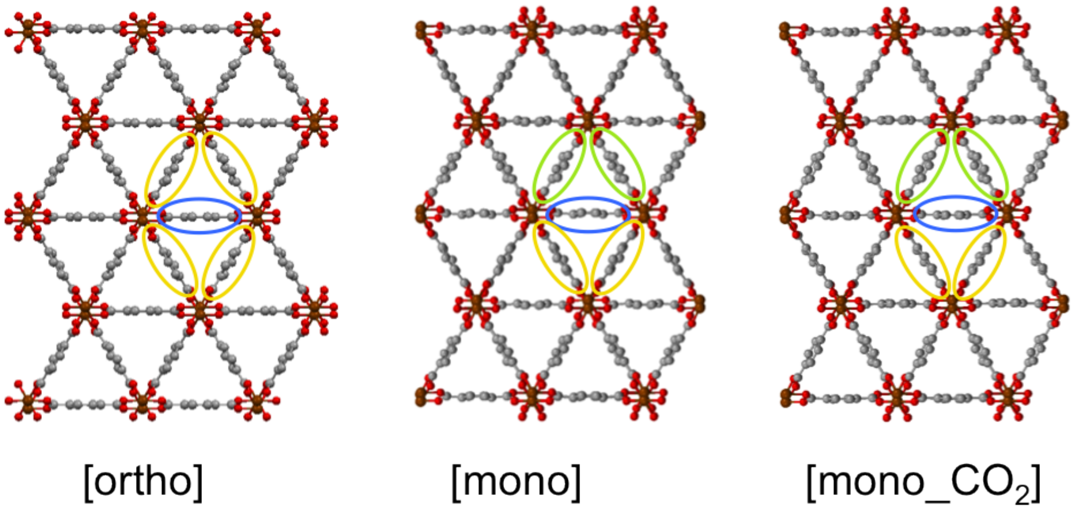

Figure 6-3: Three crystallographic forms of Sc_2BDC_3: orthorhombic – [ortho], low temperature monoclinic – [mono], and CO_2 loaded monoclinic – [mono-CO_2]. Yellow, blue, and green highlighting is used to indicate different linker types the two types of linker orientations. Colour key: O – red, H – light grey, C – dark grey, Sc – brown.

In order to further understand the behavior of Sc_2BDC_3 upon CO_2 adsorption GCMC simulations were carried out using three crystallographic Sc_2BDC_3 configurations: the orthorhombic form, [ortho], the low temperature monoclinic form, [mono], and the configuration obtained during CO_2 adsorption at 1 bar and 235 K, [mono-CO_2]. Isotherms were simulated at 304 K, 273 K and 196 K, and were compared with experimental data from the literature,[131] and with new measurements provided by John Mowat at the University of St. Andrews.[132] The simulated and experimental isotherms are presented in Figure 6-4.

At 304 K the simulations performed using [ortho] are in excellent agreement with the experimental[131] isotherm, whereas the [mono] and [mono-CO_2] isotherms underpredict uptake at high pressure. In addition, at low pressure the [mono-CO_2] greatly overpredicts the experimental loading. Figure 6-4 a) therefore indicates that at 304 K, Sc_2BDC_3 retains its initial orthorhombic form on CO_2 uptake even at pressures as high as 40 bar. At 273 K the experimental isotherm[132] is well described by both, the [mono] and the [ortho] simulations. The similarity between the [mono] and [ortho] simulated isotherms suggests that there is no incentive for a structural change, such as the ability to accommodate additional CO_2 molecules. Considering that the framework is initially in its orthorhombic form at 273 K, and that the [ortho] simulated isotherm is in excellent agreement with the experimental loading, it is likely that the structure remains orthorhombic across the entire pressure region shown in Figure 6-4 b).

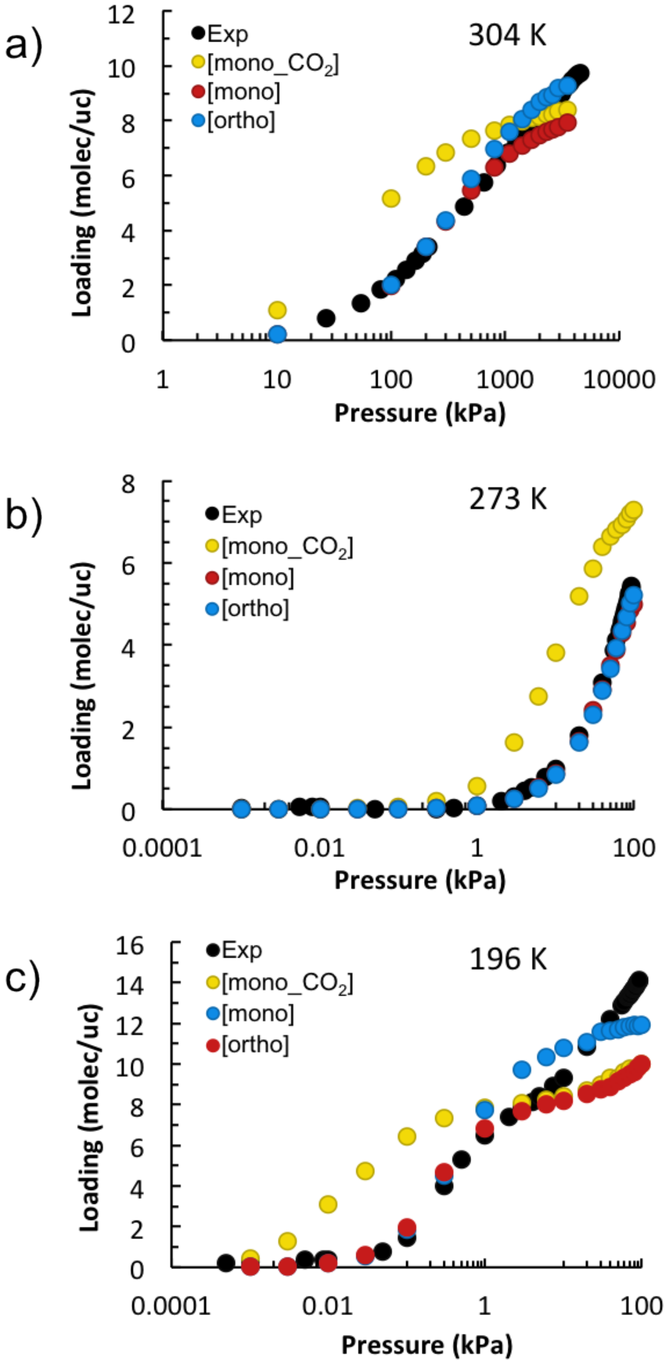

Figure 6-4: CO_2 adsorption isotherms in Sc_2BDC_3 at a) 304 K, b) 273 K and c) 196 K, obtained experimentally, or through GCMC simulations using [ortho], [mono], or [mono-CO_2].

Unlike the 304 K, and 273 K isotherms, the experimental isotherm[132] measured at 196 K contains a step in the 1–10 kPa region. The low pressure section of the isotherm is well described by the [mono] and the [ortho] simulated isotherms. Above 0.3 kPa however, the [ortho] simulation overpredicts the experimental loading, and the step that can be observed experimentally is missing altogether from the [ortho] isotherm. This indicates that under these conditions, the configuration of Sc_2BDC_3 is not the orthorhombic form. The [mono] simulated isotherm matches the experimental loading up to approximately 3 kPa, and contains a step at approximately 8 molec/uc, similar to the experimental data. A good agreement between the [mono] and the experimental isotherms is to be expected considering that the configuration of Sc_2BDC_3 at 196 K is initially [mono]. High pressure uptake however, is underpredicted by the [mono] isotherm as shown in Figure 6-4 c). Simulations carried out using [mono-CO_2] overpredict low pressure loading and underpredict high pressure uptake. This indicates that the interactions between the CO_2 molecules and the [mono-CO_2] framework are stronger than what is observed experimentally at low pressure, and also stronger than the interactions simulated for the [mono] and [ortho] forms. The only instance of agreement between the experimental data and the [mono-CO_2] isotherm coincides with the location of the step. At this point in the isotherm the amount of CO_2 adsorbed is approximately 8 molec/uc, or 3.5 mmol/g, which is the same loading at which the [mono-CO_2] structure was determined from X-ray diffraction.

The two monoclinic forms are only differentiated by a slight tilt of the BDC linkers highlighted in yellow and green in Figure 6-3, and by a small change in the monoclinic β angle from 111.48 ° to 110.95 °. The differences are shown in more detail in Figure 6-5. By undergoing these slight changes the framework allows the CO_2 molecules to orientate themselves in a more energetically favourable fashion.

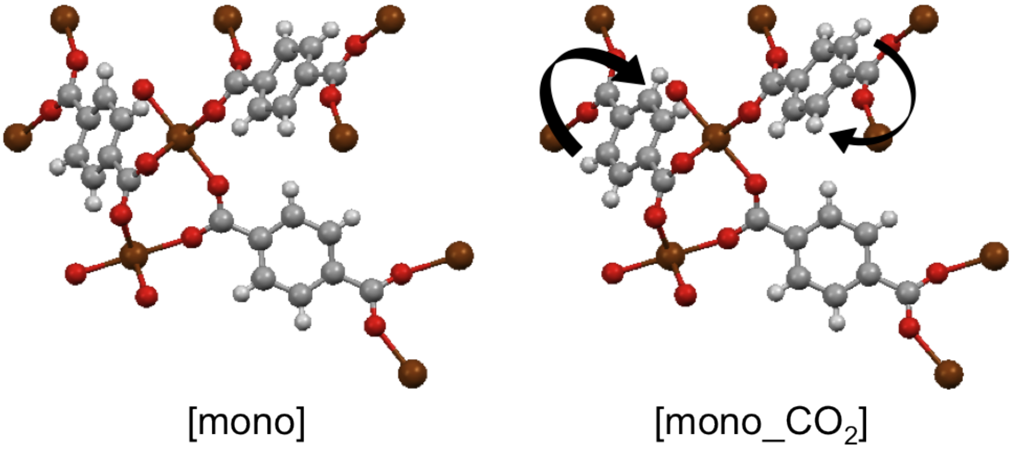

Figure 6-5: Differences in the orientation of linkers in [mono] and [mono-CO$_2$]. Colour key: O – red, H – light grey, C – dark grey, Sc – brown.

The good agreement between the [mono] isotherm and the experimental isotherm at low pressure suggests that in the low loading region the framework is arranged in the [mono] configuration, and only adopts the [mono-CO$_2$] arrangement once approximately 3.5 mmol/g of CO$_2$ has been adsorbed. The slight configurational change from [mono] to [mono-CO2] results in an increase in adsorbate-framework interaction strength. Single crystal X-ray diffraction of Sc$_2$BDC$_3$ at a loading of 3.5 mmol/g indicates that CO$_2$ molecules align themselves in an alternating pattern according to each of the two pore types as shown in Figure 6-6 d), and two distinct adsorption sites are observed. Snapshots from molecular simulations carried out in each of the three configurations, at 235 K, and a loading of 3.5 mmol/g, are compared to the crystallographic arrangement of CO$_2$ molecules in Figure 6-6. While no preferred orientation is observed for [ortho] (Figure 6-6 a)), in [mono-CO$_2$] the CO$_2$ molecules are arranged similarly to the crystallographic pattern, (Figure 6-6 c)). In the [mono] structure, shown in Figure 6-6 b) only one of the experimentally observed adsorption sites, resembling two sites of a triangle, is present in all pores.

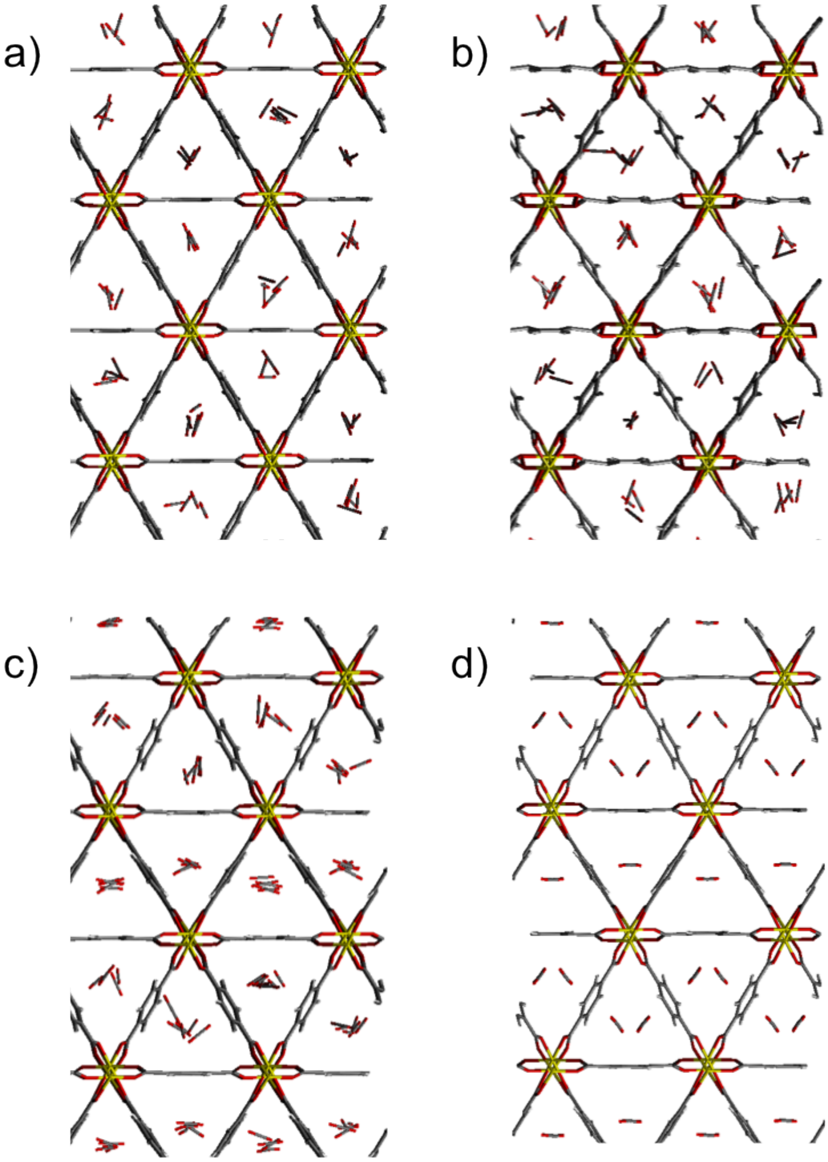

Figure 6-6: Snapshots of simulated CO_2 adsorption at 235 K and a loading of 3.5 mmol/g inside a) [ortho], b) [mono], and c) [mono-CO2], compared to d) the positions identified by single crystal X-ray diffraction. Colour key: O – red, H – light grey, C – dark grey, Sc – yellow.

6.2.2 AIMD Investigation of Adsorption at 196 K

As the adsorption studies using experimentally determined structures can be used to describe the 196 K CO_2 experimental isotherm only up to a loading of 8 molec/uc, or 3.5 mmol/g, ab initio molecular dynamics simulations were carried out to shed light on the structural changes induced by CO_2 uptake over the entire pressure range. Simulations were performed on [mono-CO_2] starting structures containing 0, 4, 8 and

16 molec/uc of CO_2 at 196 K, and the structures were allowed to evolve in response to their loading for a minimum of 10 ps. The positions of the framework atoms were averaged over the simulation time in order to obtain average AIMD configurations, which will be referred to as [avgAIMD 0], [avgAIMD 4], and so on. The ability of each of the average configurations to adsorb CO_2 was assessed by performing GCMC simulations, and the resulting isotherms were compared to experimental data.

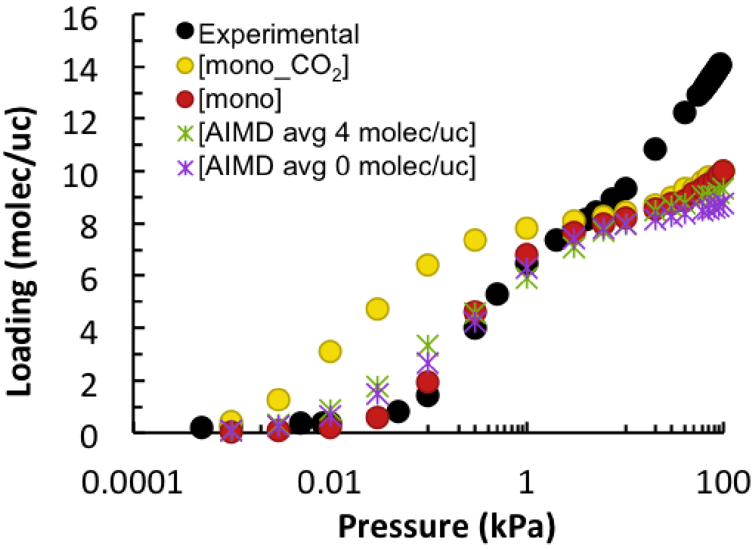

Figure 6-7: Adsorption isotherms of CO_2 in Sc_2BDC_3 at 196 K obtained from GCMC simulations on average structures from AIMD simulations of 0 and 4 molec/uc CO_2 loaded structures, compared to experimental data.

CO_2 isotherms obtained by simulating adsorption in the [avgAIMD 0] and [avgAIMD 4] structures are compared to simulated isotherms for the monoclinic and CO_2 monoclinc configurations, as well as to the experimental CO_2 isotherm in Figure 6-7. Both the [avgAIMD 0] and the [avgAIMD 4] isotherms are very similar to the [mono] simulated isotherm. This indicates that over the course of the two AIMD simulations, the low CO_2 loadings resulted in a subtle structural change of the Sc_2BDC_3 framework from the [mono-CO_2] to the [mono] form. The observed behaviour is in agreement with the experimental data, indicating that for a 0 or 4 molec/uc CO_2 uptake the framework is in its low temperature monoclinic configuration.

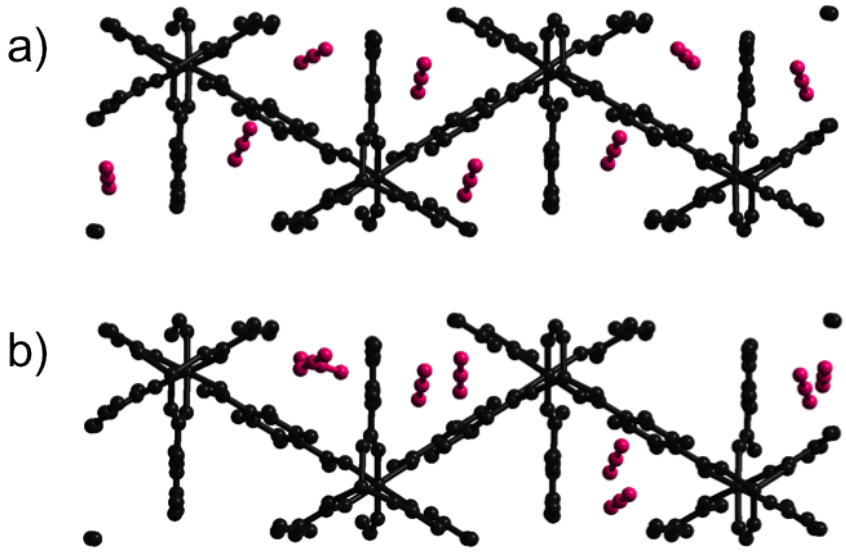

Figure 6-8: Initial configurations for AIMD simulations of Sc_2BDC_3 in the [mono_CO_2] form loaded with 8 molec/uc CO_2, arranged a) as one molecule per channel, and b) in pairs. CO_2 molecules are shown in pink, and framework atoms are in black.

The study of Sc_2BDC_3 with an 8 molec/uc CO_2 loading is particularly important, as this concentration corresponds to a step in the experimental isotherm. At this concentration the structure changes in order to better accommodate the adsorbed molecules, and reach a more energetically favourable form. AIMD simulations performed on [mono-CO_2] loaded with 8 molec/uc CO_2 in two different arrangements, as shown in Figure 6-8, provide insight into the influence of adsorbate arrangement on the configuration of Sc_2BDC_3. Adsorption isotherms determined using average AIMD configurations from each of the 8 molec/uc simulations, referred to as [avgAIMD 8 single] and [avgAIMD 8 paired] are strikingly different as shown in Figure 6-9. The in situ results of Miller et al.[131] indicate that molecules are arranged evenly throughout the pores (1 molecule per pore per unit cell). The study of the paired arrangement was performed in order to determine whether the shape/size of the pores could change in order to accommodate a greater loading (2 molecules per pore per unit cell).

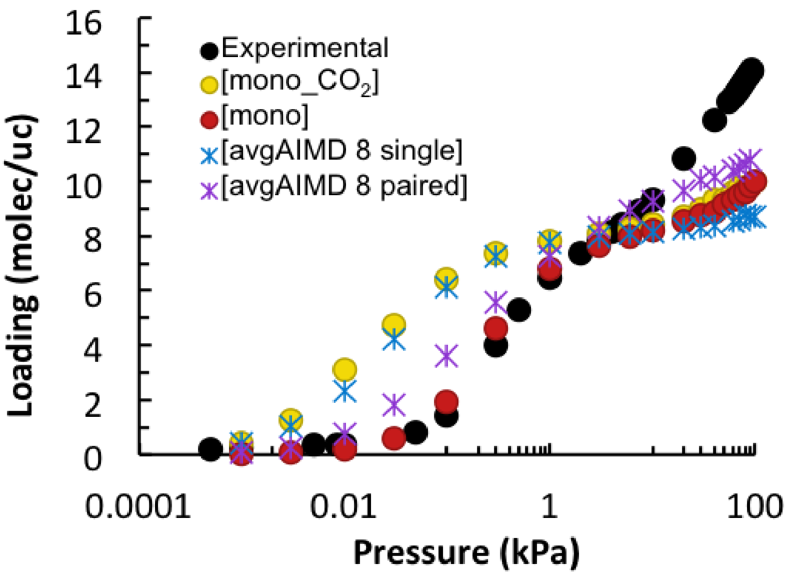

Figure 6-9: Adsorption isotherms of CO_2 in Sc_2BDC_3 at 196 K obtained from GCMC simulations on average structures from AIMD simulations of 8 molec/uc CO_2 loaded structures in the single and paired arrangements, compared to experimental data.

Arranging the 8 CO_2 molecules evenly throughout the unit cell by placing one molecule in each channel results in a reproduction of the [mono-CO_2] isotherm. On the other hand, pairing of CO_2 molecules results in an isotherm similar to that achieved with [mono]. Interestingly, the higher pressure loading using the [avgAIMD 8 paired] configuration is greater than what is observed with the two crystallographic structures. These results indicate that the low energy [mono-CO_2] configuration corresponds to a homogeneous filling of pores, and cannot be reached when CO_2 molecules are arranged in pairs. The presence of pairs of CO_2 molecules in half of the triangular channels, however, results in a facilitated uptake in the high pressure region.

The pore occupancy during the GCMC simulations performed in the [avgAIMD 8 single] and [avgAIMD 8 paired] structures is presented in Figure 6-10. While all pores are filled evenly during adsorption in the [avgAIMD 8 single] structure, in [avgAIMD 8 paired] the occupancy is higher in pores that were filled with pairs of CO_2 molecules during the AIMD simulation. These observations further highlight the flexibility of Sc_2BDC_3, as they show that over the course of the AIMD simulation, structural changes occur in the occupied pores in order to better accommodate the pairs of CO_2 molecules, while the vacant pores retain their ability to adsorb CO_2.

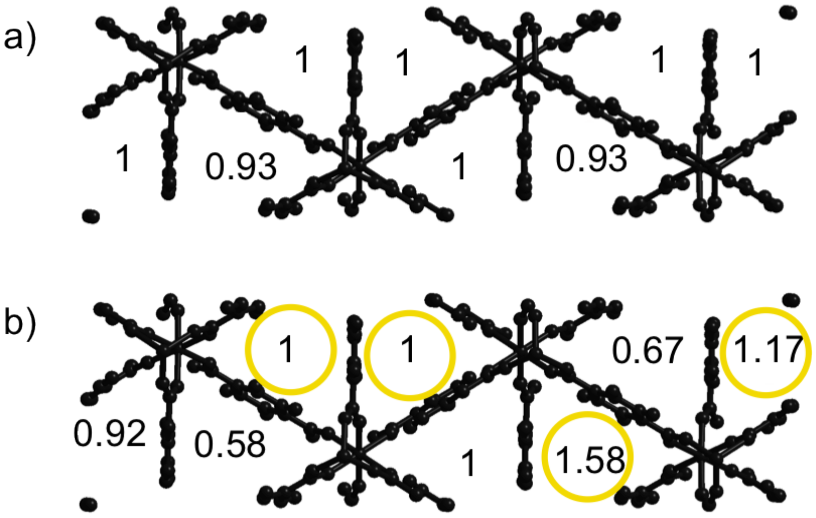

Figure 6-10: Pore occupancy from GCMC simulations using a) [avgAIMD 8 single], and b) [avgAIMD 8 paired]. Yellow highlighting is used to indicate pores filled with pairs of CO_2 molecules during AIMD simulations. Occupancies were evaluated at CO_2 loadings of approximately 8 molec/uc.

Both the [avgAIMD 8 paired] and the [avgAIMD 8 single] structures, as well as the experimentally determined structures result in an underprediction of CO_2 uptake at 196 K and pressures above 3 kPa. In order to examine the arrangement of CO_2 molecules at higher loadings, and the resulting dynamic behaviour of the framework, the [mono-CO_2] structure was filled with 16 molec/uc CO_2 and studied over 15 ps using AIMD at 196 K. In order to ensure that the simulation time was sufficiently long, the first 10 ps of simulation time were used for equilibration, and a time averaged configuration was determined using stored atomic coordinates between 10 and 15 ps. Considering that the starting configuration was obtained at a loading of 8 molec/uc, a doubling of the number of CO_2 molecules present in the small, triangular pores was expected to result in structural changes in the framework. The unit cell parameters were observed to change only slightly over the simulation time. In Table 6-2 the unit cell parameters for the time averaged structures are shown along with the unit cell parameters of Sc_2BDC_3 in the low temperature monoclinic form, and in the CO_2 filled monoclinic form. Once again, the changes observed in unit cell lengths and angles are very small.

Table 6-2: Unit cell parameters of Sc_2BDC_3 from crystallographic data for [mono], and the [mono-CO_2] form, compared to the time averaged unit cell parameters of

Sc_2BDC_3 obtained from AIMD simulations performed at 196 K, and a loading of 16 molec/uc CO_2.

	[mono]	**[mono-CO_2]**	**[avgAIMD 16]**
a (Å)	8.7545	8.747	8.76
b (Å)	34.384	34.464	34.43
c (Å)	11.146	11.092	10.86
α (°)	90.0	90.0	91.68
β (°)	111.48	110.95	107.82
γ (°)	90.0	90.0	87.71

The effect of the observed structural changes on CO_2 adsorption sites were investigated by analyzing the positions of the CO_2 molecules within the pores of Sc_2BDC_3 over the course of the simulation. The time averaged positions of CO_2 molecules within the [avgAIMD 16] structure are shown in Figure 6-11. The two distinct adsorption sites previously identified for a CO_2 loading of 8 molec/uc, are conserved over the course of the AIMD run, and are shown in blue, and yellow. In addition, as the framework adjusts in order to accommodate the high CO_2 loading, a third adsorption site is formed, as shown in Figure 6-11 in pink.

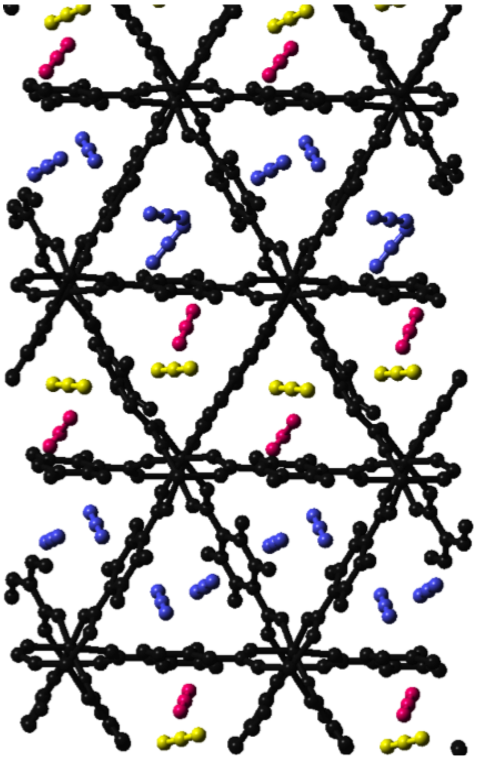

Figure 6-11: Time averaged positions of CO_2 molecules within the pores of the [avgAIMD 16]. Blue, yellow and pink are used to indicate CO_2 molecules adsorbed at three different adsorption sites, while framework atoms are shown in black.

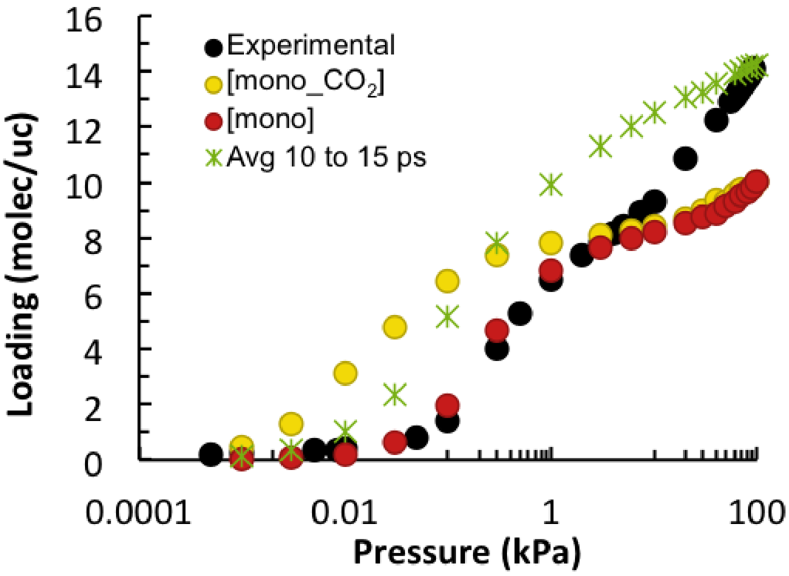

Figure 6-12: Simulated CO_2 adsorption isotherms at 196 K using the time averaged configuration of Sc_2BDC_3 from AIMD simulations with a CO_2 loading of 16 molec/uc. Experimental data and simulated [mono] and [mono-CO_2] isotherms are included.

In order to study CO_2 adsorption over the whole pressure range in [avgAIMD 16] GCMC simulations were performed at 196 K. The resulting isotherm is compared to experimental CO_2 adsorption data at 196 K, as well as to [mono] and [mono-CO_2] simulated isotherms in Figure 6-12. The time averaged AIMD configuration results in a much higher maximum uptake than [mono] and [mono-CO_2], and is able to match the experimental uptake at high pressure. However, the experimental CO_2 uptake between 0.01 and 50 kPa is greatly overpredicted in [avgAIMD 16], an effect that is similar to the low pressure overprediction observed with the [mono-CO_2] form. This indicates that over the course of the adsorption experiment, the Sc_2BDC_3 framework adapts gradually to the increasing CO_2 loading and undergoes structural changes resulting in stronger adsorbate-framework interactions and an increased CO_2 capacity partly facilitated by the formation of a new adsorption site. The time averaged structure obtained from high loading AIMD is therefore able to more easily accommodate additional CO_2 molecules, and can accurately predict the high pressure loading observed experimentally. The structural rearrangements taking place during CO_2 adsorption is accompanied by a gentle rather than a steep slope in the isotherm, indicating the presence of a slow kinetic process. In such a case, it would be beneficial to compare the adsorption isotherm to the desorption process, as the presence of a hysteresis loop would indicate that a structural transition is taking place.

6.3 High Pressure Methanol Adsorption

The investigation into the framework structural changes, and their effect on adsorption sites was extended by studying the behavior of the framework at high pressure. The flexible nature of Sc_2BDC_3 has been shown to be driven by temperature changes, as well as by the adsorption of a variety of molecules, most notably CO_2, at moderate pressures.[131,132] Further insight into the flexible nature of MOFs can be obtained using diamond anvil cells in order to study the frameworks at pressures in the 1 – 5 MPa range.[135-138] High pressure experiments on IRMOF-1 using diethyl formamide (DEF), found that the unit cell volume initially increases with a pressure change of 0.33 – 0.78 GPa, corresponding to the inclusion of adsorbate molecules into the pores of the structure. A reduction in unit cell volume is only observed once pressure is increased beyond 0.78 GPa. Similarly, in the case of HKUST-1, increasing external pressure is initially offset by the hyperfilling of pores, a mechanism which results in an increase of internal pressure.[138] The study of Fairen-Jimenez et al. on ZIF-8 on the other hand, made use of high-pressure diamond anvil cell experiments in order to understand the gate-opening effect observed during gas adsorption, and elucidate a new framework configuration.[137]

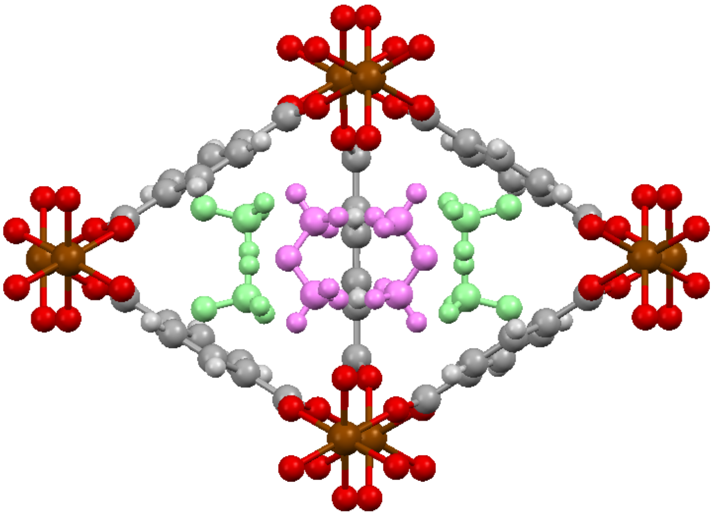

Figure 6-13: Adsorption sites of methanol in Sc_2BDC_3 determined experimentally.[133] Methanol molecules adsorbed at Site 1 and Site 2 are shown in pink, and green, respectively. Colour key: O – red, H – light grey, C – dark grey, Sc – brown.

In this work, GCMC and MD simulations were performed in order to study the adsorption sites occupied by methanol molecules at high pressure. The flexibility of Sc_2BDC_3 was tested by Moggach et al.[133] by carrying out methanol adsorption studies at pressures as high as 3 GPa. Moggach et al. determined the configuration of Sc_2BDC_3 immersed in methanol at ambient pressure, as well as at various pressure points during the high pressure experiment. Methanol molecules were found to occupy two different adsorption sites, Site 1 and Site 2 as shown in Figure 6-13, and a maximum loading of 42 molec/uc was observed at 1.6 GPa.[133] Although the molecular orientations are slightly different, the methanol molecules are centred at locations similar to those observed for CO_2, that is in front of each of the three linkers making up the triangular pores. Here, molecular simulations were carried out using each of the Sc_2BDC_3 configurations in order to confirm the sites at which methanol molecules are adsorbed, and to determine the order in which these sites are occupied. In addition, the computation of radial distribution functions are calculated to reveal the nature of the adsorbate-adsorbate interactions and their role in the adsorption site filling mechanism.

The order in which Sc_2BDC_3 adsorption sites are filled by methanol molecules was determined using GCMC simulations. Density distribution plots of adsorption sites were obtained as a function of loading for the ambient immersed Sc_2BDC_3 structure, [ScBDC im], as well as for seven Sc_2BDC_3 configurations determined by Moggach et al.[133] at various pressure points of the methanol compression experiment: [0.0 GPa], [0.3 GPa], [0.6 GPa], [1.1 GPa], [1.4 GPa], [1.6 GPa], and [2.3 GPa]. The structures elucidated at each pressure point were very similar to one another and to [ScBDC im], however the unit cell of the framework was observed to slightly expand with increasing pressure up to 0.6 GPa, a behaviour which was associated with the movement of methanol molecules into the triangular pores. Further increase in pressure, beyond 0.6 GPa, resulted in a gradual decrease in the volume of the unit cell, and above 3.0 GPa amorphization occured. The adsorption sites observed through simulations shown in Figure 6-14 are in agreement with the experimental data. Site 1 molecules are located in-between the equatorially oriented linkers, while Site 2 molecules are adsorbed near the remaining two linkers making up the triangular pores. At low loading molecules are preferentially adsorbed at Site 1. As loading increases, Site 1 becomes saturated, and adsorption of molecules at Site 2 begins. A further increase in loading, that is beyond 32 molec/uc corresponding to the filling of one of the Site 2 locations, results in uptake at the second Site 2 locations in each channel. The same mechanism of pore filling is observed for all Sc_2BDC_3 structures investigated.

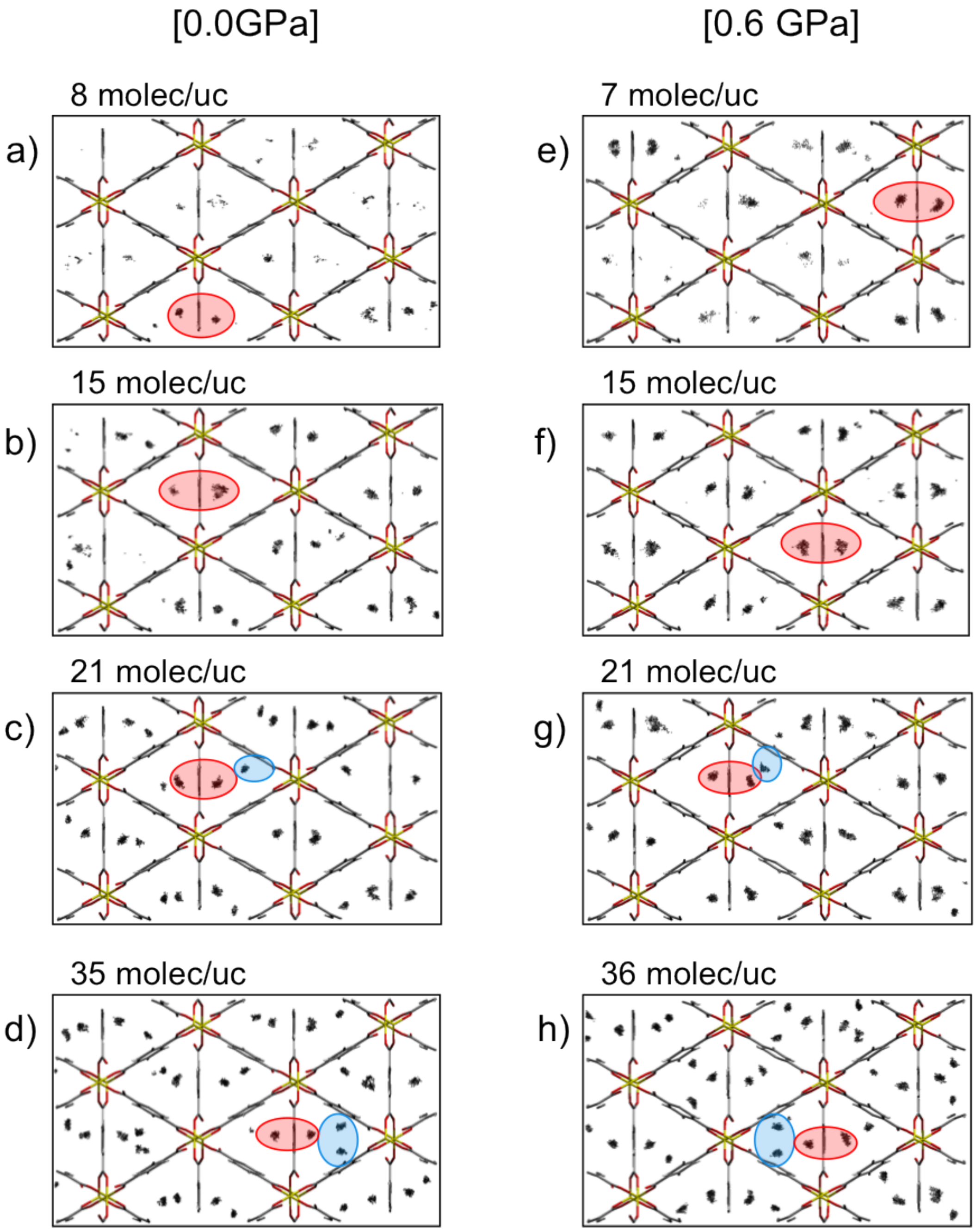

Figure 6-14: Density distributions for the adsorption of methanol in (a to d) [0.0 GPa] and (e to h) [0.6 GPa]. Each plot shows the locations of methanol molecules adsorbed at a particular loading. Each dot represents the position of the centre of mass of a molecule during the GCMC simulation. Red and blue regions indicate adsorption at Site-1 and Site-2, respectively.

In an effort to determine what role hydrogen bonds play in the pore filling mechanism, molecular dynamics simulations were performed for the immersed Sc_2BDC_3 structure, as well as for each of the high pressure structures, at a loading of

39-41 molec/uc. Over the course of the MD simulations, the dynamic locations of the methanol molecules were simulated over time, and the positions were stored at regular intervals. Radial distribution functions were then evaluated by analysing the distances between the oxygen and hydrogen atoms in the OH groups of adsorbed methanol molecules for each stored MD configuration. Considering that methanol molecules were observed to saturate Site 1 before being adsorbed at Site 2, it was essential to identify differences in the methanol-methanol interactions at each site, and assess whether they play a stabilizing role in Site 1 adsorption. Therefore, site specific radial distribution functions were determined by distinguishing between pairs of methanol molecules adsorbed at Site 1 in adjacent pores, and pairs at Site 2 in adjacent pores. In addition, distances between molecules located at Site 1 and molecules located at Site 2 within the same pore were also analyzed. The results for the [0.0 GPa] and [0.6 GPa] structures are presented in Figure 6-15.

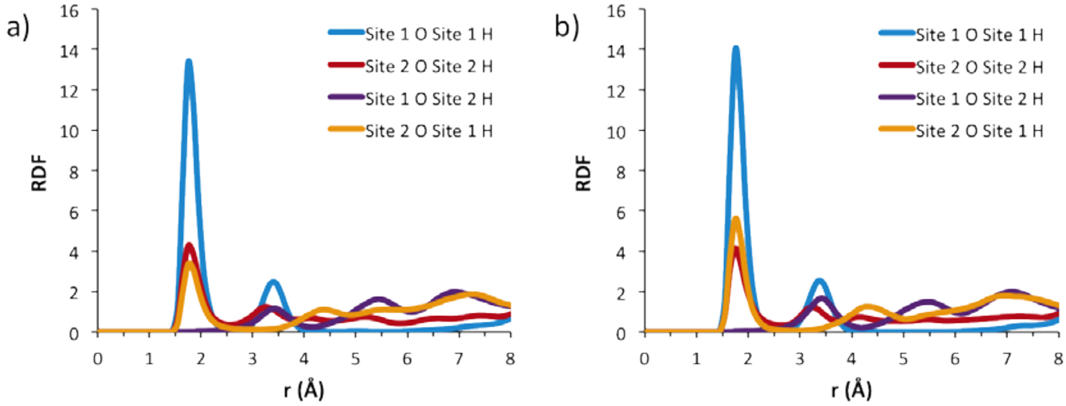

Figure 6-15: Radial distribution functions for methanol molecules adsorbed in a) [0.0 GPa] and b) [0.6 GPa] where Site 1 O corresponds to the oxygen atom of a methanol molecule adsorbed on Site 1, Site 2 H to the OH group hydrogen atom of a methanol molecule adsorbed on Site 2, and so on.

For three of the four atomic pairs analysed, the separation distance between oxygen and hydrogen atoms is between 1.5 and 2.25 Å, which is characteristic for hydrogen bonds. The highest occurrence of hydrogen bonds corresponds to methanol molecules adsorbed at Site 1s in neighbouring pores. The oxygen atoms of methanol molecules adsorbed on Site 2 are equally likely to form hydrogen bonds with methanol molecules adsorbed at Site 2 as with hydrogen atoms of methanol molecules adsorbed within the same pore at Site 1. In contrast, oxygen atoms of methanol molecules adsorbed on Site 1 only rarely form hydrogen bonds with hydrogen atoms of methanol molecules at Site 2. Similar results were observed for all other structures.

The presence of hydrogen bonds between the three atomic pairs is illustrated in the simulation snapshot of the methanol-filled [0.0 GPa] structure presented in Figure 6-16. Methanol molecules adsorbed at Site 1 exhibit a strong preference for interacting with methanol molecules adsorbed at Site 1 in adjacent pores, indicating that the arrangement of framework atoms near Site 1 is more conducive to hydrogen bond formation than the geometry at Site 2. The high incidence of hydrogen bonds between Site 1 molecules increases the site stability and results in a preferential filling of Site 1. In contrast, methanol molecules adsorbed at Site 2 are able to form hydrogen bonds less frequently, and exhibit no preference in interacting with Site 1 or Site 2 methanol molecules. As a result these adsorption sites are occupied only once Site 1 is saturated.

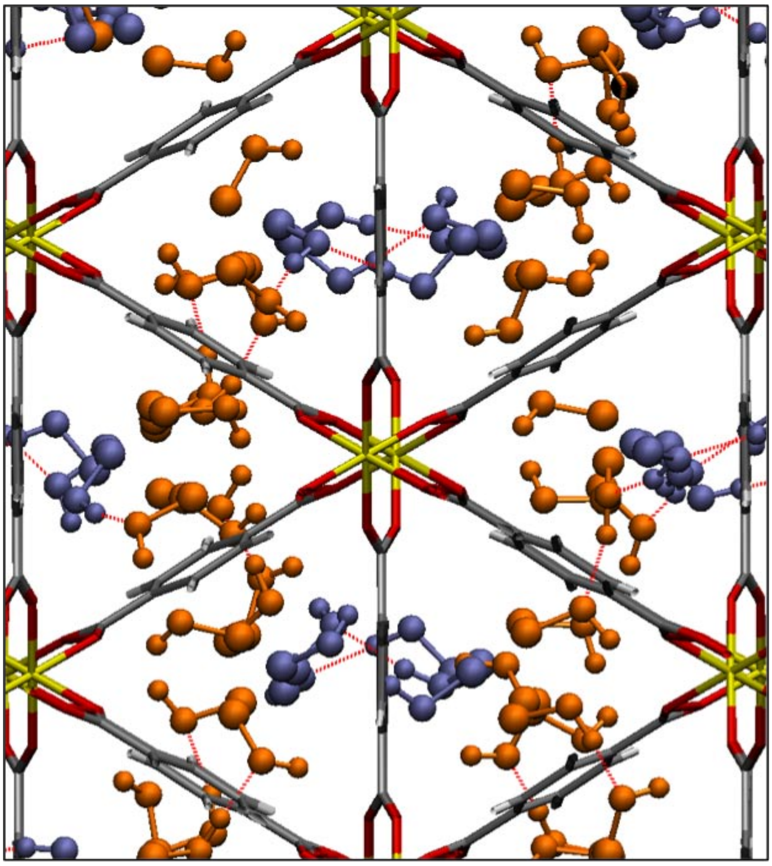

Figure 6-16: Arrangement of methanol molecules within the [0.0 GPa] structure. Molecules adsorbed at Site 1 are shown in blue, while molecules adsorbed at Site 2 are shown in orange. Hydrogen bonds are indicated using red dashed lines.

6.4 Conclusions

At first glance, the triangular pores of Sc_2BDC_3 appear to be insufficiently large for use in gas adsorption and separation applications. Surprisingly, this MOF shows a high degree of flexibility in the presence of various adsorbates, and is able to accommodate not only small molecules, but also linear alkanes. In this chapter, the structural changes of the Sc_2BDC_3 framework upon adsorption of CO_2, and methanol were studied using a variety of classical and ab initio simulation methods. GCMC simulations of CO_2 adsorption at 273 K and 304 K using the orthorhombic framework are in excellent agreement with experimental data, confirming that under these conditions, no structural changes occur. At 196 K however, two instances of changes in the configuration of Sc_2BDC_3 are observed. In the low pressure region, the framework adopts the low temperature monoclinic form, as indicated by the agreement between the low temperature monoclinic simulated isotherm and the experimental data. At a loading of 8 molec/uc, the monoclinic structure undergoes configurational changes in order to better accommodate 1 CO_2 molecule in each pore of the unit cell. This slight modification creates two distinct CO_2 adsorption sites, as detected in the simulation snapshots of [mono-CO_2], which are in agreement with crystallographic data of CO_2-loaded Sc_2BDC_3 at the same temperature. These preferred adsorption sites are not observed in the [ortho] or in the [mono] configurations. CO_2 adsorption beyond the 8 molec/uc loading cannot be accurately described by any of the three crystallographically determined structures. AIMD simulations performed on Sc_2BDC_3 loaded with 16 molec/uc CO_2 result in time-averaged configurations that are able to reproduce the maximum experimental loading at 196 K. For a 16 molec/uc loading, the time averaged positions of CO_2 molecules reveal the presence of a third adsorption site. Therefore, at 196 K and high CO_2 partial pressure, the configuration of Sc_2BDC_3 changes further in order to accommodate additional CO_2 molecules. These changes include the formation of an additional adsorption site.

The locations of preferred adsorption sites within Sc_2BDC_3 was further investigated through high pressure methanol adsorption studies. Density distributions of adsorbed methanol molecules from GCMC simulations show that two distinct adsorption sites are occupied. Site 1 locations are filled first, followed by Site 2. Radial distribution functions calculated for the oxygen and hydrogen atoms of methanol molecules adsorbed in the pores of Sc_2BDC_3 indicate that hydrogen bonds are formed between molecules in neighbouring Site 1s, neighbouring Site 2s, as well between molecules adsorbed at Site 1 and molecules adsorbed at Site 2. The highest incidence of hydrogen bonds corresponds to pairs of Site 1 molecules. In addition, methanol molecules adsorbed at Site 1 show a strong preference for forming hydrogen bonds with Site 1 molecules in neighbouring pores, rather than molecules located at Site 2 in the same pore. It can therefore be concluded that the formation of hydrogen bonds stabilizes the adsorption of methanol molecules at Site 1, resulting in the observed preferential filling of Site 1 before Site 2.

The work presented in this chapter contributes to the understanding of the guest – induced flexibility and high pressure stability of Sc_2BDC_3. The limits of this small pore MOF have yet to be defined however, and further studies are needed in order to fully characterize its adsorptive and separative capabilities.

7 Zirconium MOFs as Adsorbents for H_2 Purification using PSA

7.1 Introduction

In a hydrogen PSA unit, gas streams are separated mainly based on equilibrium selectivity, i.e. the relative adsorption strengths of the components, which is determined by molecular volatility and polarity. One of the most common feed streams used in hydrogen PSA systems is steam methane reformer offgas (SMROG), which normally has a hydrogen content of 70-80%.[139] The remainder of the mixture is composed of CO_2, CH_4, CO, and N_2, which must be removed in order to produce high purity H_2. Water is also normally present; however it is the most strongly adsorbed component and can be easily removed from the stream either prior to the PSA unit, or by using additional adsorbent layers in the PSA column.

PSA units require high-performance adsorbents that have large capacities and selectivities for the impurities to be removed, and which can be easily regenerated at low pressure.[139] Feed streams generally enter a PSA process at 4 – 30 atm, while the waste streams containing desorbed impurities leave the columns at 1.1 – 1.7 atm.[139] Depending on the process temperature and pressure, frequently utilized adsorbents include activated aluminas, silica gels, activated carbons (ACs) and zeolites. Activated carbons are beneficial for the removal of CO_2 and hydrocarbons due to their high capacities and low adsorption enthalpies, however their non-polar structures and large pore diameters render them less advantageous in the removal of N_2 and CO. Zeolites on the other hand, have high selectivities for (quadru)polar adsorbates, but are difficult to regenerate upon CO_2 adsorption due to the high interaction strength between the CO_2 molecules and the charged zeolite pore surface. In order to increase separation efficiency, adsorption columns often contain two or more adsorbent layers, each of which is designed to target specific impurities.[140-144] Such columns allow for CO_2 to be retained in easily regenerated activated carbon particles, while lighter impurities are adsorbed in highly selective zeolite layers. The overall performance of the PSA unit is highly dependent on the adsorbents chosen and is limited by the selectivity of the adsorbent for the most weakly interacting impurity – N_2 in the case of SMROG. Once this impurity breaks through the adsorption column, the feed cycle must be stopped and the adsorbent must be regenerated.

In the continuous search for high-performance adsorbent materials required in order to improve PSA product yield, purity and energy requirements, metal-organic frameworks (MOFs) have been identified as promising candidates. While many MOF studies have focused on adsorption of binary, and ternary mixtures[4] containing the more abundant impurities, that is CO_2 and CH_4, only a few have analyzed CO/H_2 and N_2/H_2 mixture adsorption. It is important to bear in mind that PSA performance is determined by the adsorption behavior of each of the impurities, and that adsorption strength can vary widely depending on the polarity of the impurity and on the properties of the MOF such as pore size, topology and chemical functionality. Furthermore, the impurities are competing with each other for the adsorption sites available, therefore in order to identify the most promising MOFs for H_2 purification a study of the adsorption as well as the micropore and macropore diffusion behavior of the complete mixture is required. A study of diffusion through the micropores is necessary in order to verify the dominant mass transfer resistance. According to the detailed report of Sircar and Golden, the criteria by which PSA adsorbents should be selected include multicomponent adsorption capacities, desorption behaviour, selectivities and isosteric heats of adsorption.[145] None of these factors however, can be used as a single selection criterion, as separation efficiency is affected by each parameter to some degree, as was shown in Chapter 3.[146-148]

The most effective method for testing the selective properties of materials to be used in separating H_2 from multicomponent mixtures is the use of laboratory scale breakthrough and PSA cycle experiments, such as the dual piston PSA setup,[149] as well as mathematical models, which simulate column adsorption. As a result, numerous zeolite and activated carbon studies seeking to identify promising PSA adsorbents have presented breakthrough studies and PSA process modeling for multicomponent H_2 mixtures through single as well as layered beds.[144,150-154] Recently, breakthrough models have been employed to investigate whether MOFs can be used in PSA separations for various applications with mixtures containing up to four gases. A study carried out by Krishna and Long compared several MOFs to zeolites and activated carbons using breakthrough studies of $CO_2/CH_4/H_2$ mixtures as well as binary combinations of the three gases.[146] Their work highlighted the advantage of using breakthrough calculations for separation studies, and showed that Mg MOF-74 was the best material for CO_2/H_2, CO_2/CH_4 and CH_4/H_2 separations.[146] Herm et al. investigated CO_2/CH_4, CH_4/H_2 and $CO_2/CH_4/H_2$ separations, processes which are relevant for CO_2 capture and storage as well as for H_2 purification, and found Mg MOF-74 to outperform Zeolite 13X for all three mixtures.[11] Finally, the recent work of Wu et al. tested the performance of MOFs and zeolites in separating $CO_2/CO/CH_4/H_2$, CO_2/H_2, CH_4/H_2 and CO_2/CH_4 mixtures, and identified Cu-TDPAT as a particularly effective adsorbent for H_2 PSA purification from SMROG.[155]

In this work, a combination of simulation tools is used in order to perform a multi-scale study on the separation of five-component SMROG mixtures, consisting of H_2, N_2, CO, CH_4 and CO_2, through columns containing four MOFs. The stream entering the PSA column is assumed to be water-free. The four MOFs, namely dehydroxylated UiO-66(Zr), UiO-66(Zr)-Br, UiO-67(Zr) and Zr-Cl_2AzoBDC, are assessed through adsorption and desorption studies, and their potential for hydrogen purification is evaluated. These MOFs, which share the same topology, consist of zirconium oxide clusters bridged by different organic linkers (see Figure 7-1) resulting in different pore sizes, pore volumes, and adsorption site strength. They were selected for their stability and resistance to solvents and mechanical pressure.[156,157] In addition, the water stability studies of Yang et al.[9] and Biwas et al.[158] have shown that the four MOFs retain their crystallinity upon immersion in water. The high connectivity of metal centres to organic linkers, which is characteristic of the UiO-66 family, results in high shear and bulk moduli and is responsible for the excellent mechanical stability of these materials.[157]

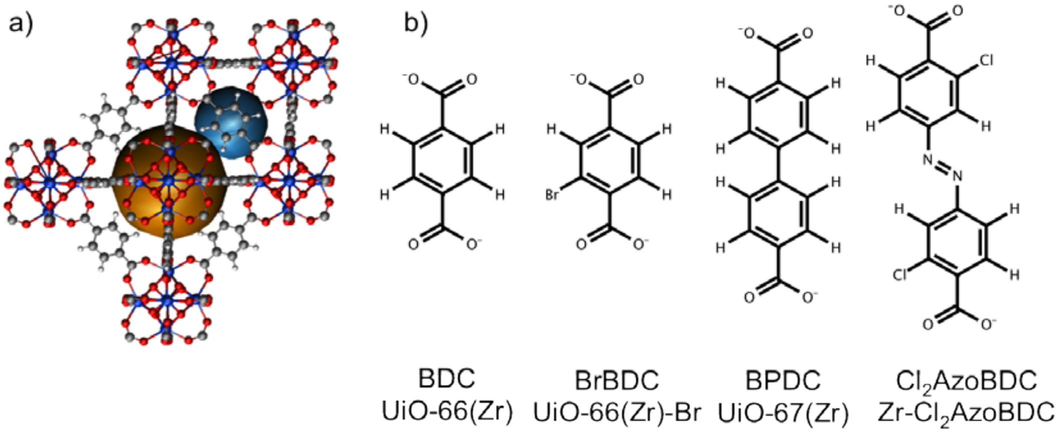

Figure 7-1. a) Octahedral (brown sphere) and tetrahedral (blue sphere) pores of UiO-66(Zr) b) Linkers joining the zirconium clusters in each of the four MOFs. Colour key: zirconium – blue, oxygen – red, carbon – dark grey, hydrogen – light grey.

The materials are first characterized using GCMC and MD methods, as described in Section 7.2. Single component and binary mixture results from grand canonical Monte Carlo (GCMC) simulations are presented in Sections 7.4.1, and 7.4.2, and used to determine the working capacities and selectivities for each of the impurities to be removed. With the help of external field non-equilibrium molecular dynamics (EF-NEMD) simulations micropore transport diffusivities of the mixture components in each of the four MOFs were calculated. The adsorption and diffusion data obtained through molecular simulations were then directly introduced as input into a PSA unit model, as described in Section 7.3. The adsorption column model was employed in order to study mixture adsorption and diffusion through columns containing each of the four MOFs alone (Section 7.4.3), or containing a layered bed consisting of activated carbon and a MOF (Section 7.4.4). The breakthrough curves for each of the mixture components are analyzed, and the impact of the impurities on the overall performance of different MOFs for hydrogen purification from SMROG is discussed. The breakthrough study is extended to include the commercial zeolite and activated carbon materials, studied in detail by Rodrigues and co-workers,[150,159] as well as Zeolite 5A and Calgon PCB,[151,160] This comparison is used to assess whether MOFs are able to compete with commercial PSA adsorbents, and to identify which of the four MOFs is the most promising adsorbent for H_2 PSA purification. In Section 7.4.5 desorption studies are presented and the ease of regeneration of each MOF is discussed. The findings are summarised in Section 7.5.

7.2 Molecular Simulation Methods

7.2.1 GCMC Simulations

Grand canonical Monte Carlo simulations were carried out using the multipurpose simulation code (MuSiC)[79] in order to determine the adsorption isotherms of each of the pure gases as well as the binary mixtures at 298 K. Each MOF was treated as a rigid structure and the framework atoms were maintained fixed at their crystallographic positions.[9,156,158,161] Dispersion, or van der Waals interactions, were modeled using a 12.8 Å cut-off. CO was described using the three-centred model of Martín-Calvo et al.[49] The Lennard Jones parameters used to represent framework atoms were taken from the Universal Force Field (UFF),[40] and the partial charges were adopted from previous studies.[9,161,162]

The differential enthalpy of adsorption, also referred to as the isosteric heat of adsorption, was calculated as was described in Chapter 2, directly from GCMC simulations using the following expression:[87]

$$\Delta h = \mathrm{R}T - \frac{\langle U_{ads} N_{ads} \rangle - \langle U_{ads} \rangle \langle N_{ads} \rangle}{\langle N_{ads}^2 \rangle - \langle N_{ads} \rangle \langle N_{ads} \rangle} \qquad \text{Eq 7-1}$$

Here Δh denotes the differential enthalpy of adsorption, R is the universal gas constant, T is the simulation temperature, $<U_{ads}>$ is the average potential energy per molecule, and $<N_{ads}>$ is the average number of molecules adsorbed. The pore diameters were evaluated using the pore size distribution method of Gelb and Gubbins[75] which gives the diameter of the largest sphere that can be inserted without overlapping with any of the framework atoms. The pore volumes were determined using a numerical Monte Carlo algorithm to carry out random trial insertions using a 0 Å probe molecule. This purely geometrical method in essence calculates all the space inside the unit cell that surrounds the framework atoms.

7.2.2 MD Simulations

Molecular dynamics (MD) simulations were performed in order to determine the micropore transport diffusivities of each of the SMROG components through the pores of the four MOFs studied. EF-NEMD simulations in the NVT ensemble were carried out using the Gromacs package.[163] Each simulation was run for 5.5 ns, where the first 0.5 ns were used for equilibration. A temperature of 298 K was maintained using the Nosé-Hoover thermostat[29] and a time step of 1 fs was employed. The equilibrium configurations obtained from GCMC simulations at 298 K and 10 bar were used as starting configurations for each MD simulation. An external force of 0.1 to 1.0 kJ/mol/Å was applied to each adsorbate molecule inside the simulation box such that a linear response was achieved. The MOFs were assumed to be rigid, and the framework atoms were fixed at their crystallographic coordinates. The framework atoms and the adsorbate molecules were represented using the same Lennard-Jones parameters that were used in the GCMC simulations. Each NEMD simulation was repeated five times, and the average displacement correlation function (DCF) values were obtained. The statistical errors for the DCFs were determined using the Student t-test with a 95% confidence interval.

7.3 Breakthrough Simulation Details

Breakthrough simulation studies of five component mixtures were performed using the CySim adsorption cycle simulator developed by Friedrich et al.[149] By performing mass, momentum and energy balance calculations on an adsorption column (Figure 7-2), including additional units such as valves and inlet and outlet feed lines, the progression of the mixture components along the length of the column is determined. Extensive details regarding the model and the numerical algorithms implemented are provided in the literature,[149] therefore only a brief summary of the model, and the assumptions made, is included here.

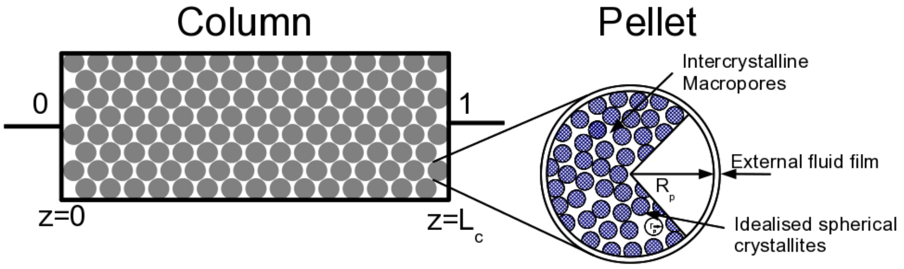

Figure 7-2. Characteristics of adsorption column model containing adsorbent pellets used in the breakthrough simulations.[164] The inset shows a pellet of radius R_p, containing spherical crystallites separated by intercrystalline macropores.

The model assumes that the mixture behaves as an ideal gas at the reference temperature. An axially dispersed plug flow model is employed, and the pressure drop inside the column is described using the Ergun equation. The velocity at the column inlet is set and the outflow velocity is calculated from the mass balance. Initially the column is at uniform pressure, temperature and gas phase concentration. The adsorbate concentration is assumed to be in equilibrium with the set gas phase concentration.

The mass balances along the column are described as follows:

$$\frac{\partial c_i}{\partial t} + \frac{(1-\varepsilon)}{\varepsilon} \cdot \frac{\partial Q_i}{\partial t} + \frac{\partial (c_i \cdot v)}{\partial z} + \frac{\partial J_i}{\partial z} = 0 \qquad \text{Eq 7-2}$$

where c_i is the gas concentration of component i, ε is the bed void fraction, v is the interstitial flow velocity, J_i is the diffusive flux of component i, and z is the position along the column. Q_i is the average adsorbed concentration of component i inside the pellet, and is defined as follows:

$$Q_i = \varepsilon_p c_i^m + \left(1 - \varepsilon_p\right) q_i \qquad \text{Eq 7-3}$$

where ε_p is the pellet void fraction, c_i^m is the gas concentration of i inside the macropore, and q_i is the average adsorbed concentration of i inside the crystal. The diffusion process through the macropores and the micropores is described using linear driving force models as follows:

$$\varepsilon_p \frac{dc_i^m}{dt} + \left(1 - \varepsilon_p\right) \frac{dq_i}{dt} = k_i^p \frac{A_p}{V_p} \left(c_i - c_i^m\right) \qquad \text{Eq 7-4}$$

$$\frac{dq_i}{dt} = k_i^{cr}\frac{3}{r_c}(q_i^* - q_i) \qquad \text{Eq 7-5}$$

where A_p is the pellet surface area, V_p is the pellet volume, and k_i^p and k_i^{cr} are the LDF mass transfer coefficients through the pellet, and through the crystal respectively. q_i^* is the adsorbed concentration of i at equilibrium, which is determined using a dual site Langmuir isotherm model for multi-component streams:

$$q_i^* = \frac{q_{i,s}^1 b_i^1 exp\left(\frac{-\Delta\tilde{H}_i^1}{RT}\right)Px_i}{1+\sum_{j=1}^{N_c} b_j^1 exp\left(\frac{-\Delta\tilde{H}_j^1}{RT}\right)Px_j} + \frac{q_{i,s}^2 b_i^2 exp\left(\frac{-\Delta\tilde{H}_i^2}{RT}\right)Px_i}{1+\sum_{j=1}^{N_c} b_j^2 exp\left(\frac{-\Delta\tilde{H}_j^2}{RT}\right)Px_j} \qquad \text{Eq 7-6}$$

where $q_{i,s}^1$ and $q_{i,s}^2$ are the saturation loadings of i at site 1 and 2, b_i^1 and b_i^2 are the equilibrium constants at site 1 and site 2, $\Delta\tilde{H}_i^1$and $\Delta\tilde{H}_i^2$are the heats of adsorption at site 1 and 2 (the tilde denotes molar units), x_i is the molar fraction of i, P is the total pressure, T is the temperature, R is the universal gas constant, and N_c is the number of components in the stream.

The non-isothermal process is modeled by accounting for heat transfer between the column wall and the bed, as well as between the column wall and the surroundings. The temperature inside the adsorbent pellets is assumed to be uniform. The energy balance in the column is described as follows:

$$\varepsilon\frac{\partial U_f}{\partial t} + (1-\varepsilon)\frac{\partial U_p}{\partial t} + \varepsilon\frac{\partial(H_f\cdot v)}{\partial z} + \frac{\partial J_T}{\partial z} + \sum_{i=1}^{N_c}\frac{\partial(J_i\tilde{H}_i)}{\partial z} + h_w\frac{A_c}{V_c}(T_f - T_w) \qquad \text{Eq 7-7}$$

where U_f is the internal energy of the fluid phase, H_f is the enthalpy of the fluid phase, v is the interstitial flow velocity, J_t is the thermal diffusive flux, A_c and V_c are the internal surface area and the volume of the column, T_f and T_w are the are the fluid and the wall temperatures, and h_w is the heat transfer coefficient at the column wall. For a linear driving force model, the change in the internal energy in the pellet, U_p, over time is expressed as:

$$\frac{dU_p}{dt} = \varepsilon_p\frac{dU_{p,f}}{dt} + \left(1-\varepsilon_p\right)\frac{dU_{p,s}}{dt} = h_p\frac{A_p}{V_p}(T_f - T_p) \qquad \text{Eq 7-8}$$

where $U_{p,f}$ and $U_{p,s}$ are used to denote the internal energies in the macropore, and in the solid phase of the pellet, A_p and V_p are the pellet surface area and volume, h_p is the heat transfer coefficient between the pellet and the fluid, and T_p is the pellet temperature.

An energy balance on the column wall is expressed as:

$$\rho_w c_{P,w} \frac{dT_w}{dt} + h_w \frac{A_c}{V_w}\left(T_w - T_f\right) + U_{ext}\alpha_{wl}(T_w - T_\infty) = 0 \qquad \text{Eq 7-9}$$

where ρ_w and $c_{P,w}$ are the density and constant pressure heat capacity of the column wall, T_w and T_∞ are the wall and oven temperatures, h_w is the heat transfer coefficient between the fluid and the wall, V_w is the volume taken up by the column wall, U_{ext} is the external heat transfer coefficient, and α_{wl} is the logarithmic mean surface area to volume ratio of the column wall.

The momentum balance is then expressed using the Ergun equation as follows:

$$-\frac{\partial P}{\partial z} = \frac{150\mu_f(1-\varepsilon)^2}{\left(2R_p\right)^2\varepsilon^2}v + \frac{1.75\rho_f(1-\varepsilon)}{2R_p\varepsilon}v|v| \qquad \text{Eq 7-10}$$

Here μ_f is the viscosity of the fluid, R_p is the pellet radius, ρ_f is the fluid phase density, and v is the interstitial flow velocity.

7.3.1 Model Input Data

The column characteristics and operating conditions were maintained constant for all materials and were taken from Ribeiro et al, including a feed flow rate of 12.2 m^3/h, and an inlet pressure of 7 bar.[150] SMROG feed is normally available between 21 and 38 °C,[145] therefore the feed temperature was set to a value within this range, that is 298 K. The mixture composition was defined as shown in Table 7-1, and a complete list of the simulation process parameters is provided in Table 7-2.

Table 7-1. Feed gas composition (SMROG)[150]

	Composition (mole%)
H_2	73.0
CO_2	16.0
CO	3.0
CH_4	4.0
N_2	4.0

Table 7-2 Column parameters and properties of adsorbents used in this work, which were taken from the work of Ribeiro et al. [150,165]

Feed flow rate (adsorption) (Nm^3/h)	12.2
Purge gas flow rate (desorption (Nm^3/h)	5.0
Inlet pressure (bar)	7
Column length (m)	1
Column diameter (m)	0.2
Wall density (kg/m^3)	8238
Wall specific heat (J/kg/K)	500
Void fraction of bed	0.38
Void fraction of pellet	0.25
Particle radius (m)	Activated carbons: 1.17×10^{-3} Zeolites : 0.85×10^{-3}
Heat transfer coefficient pellet-bed ($J/m^2/s/K$)	219
Heat transfer coefficient column wall ($J/m^2/s/K$)	94
Particle specific heat capacity (J/kg/K)	Activated carbons: 709 MOFs and zeolites: 920

Single component and binary mixture adsorption isotherms for each of the four MOFs as well as the differential enthalpies of adsorption and Henry constants were calculated using GCMC simulations. The isotherms were fitted to the dual-site Langmuir (DSL) model using the weighted least squares fitting technique detailed in the work of Brandani and Ruthven.[166] This method allowed for the model parameters to be determined by simultaneously fitting single component and binary mixture data while satisfying Henry constant restrictions. As a first step, the simulated pure component adsorption isotherms were fitted to the DSL equation in order to obtain an initial set of parameters. The same set of starting parameters was used to describe the uptake of each gas from a binary mixture following the expression in Eq 7-6. In order to ensure that a good fit would be achieved in the Henry region, the following relationships were used to restrict the fitting of the DSL parameters:

$$K_A = b_{1A} q_{s1} + b_{2A} q_{s2}$$
$$K_B = b_{1B} q_{s1} + b_{2B} q_{s2} \qquad \text{Eq 7-11}$$

where K_A and K_B are the Henry constants of components A and B, respectively. Considering that each binary mixture was composed of hydrogen and one SMROG impurity, the value of q_{s1} was set to equal the value of q_{s1} obtained from the single component isotherm of the impurity. The initial DSL parameters were then optimized in order to reduce the squared differences between the simulated isotherms (both, pure component and binary mixture isotherms) and the fitted values. As shown in Figure 7-3 and Figure 7-4, the DSL curves are in good agreement with the simulated isotherms. It should be noted that although the DSL model as formulated here does not account for the impact of fugacity on adsorption, the PSA simulations in which they were employed were carried out for inlet pressures ranging from 5 to 20 bar. Isotherm fitting focused on the low pressure region, where the ideal gas law is a reasonable approximation, in order ensure an accurate representation of loading at pressures equivalent to the partial pressure of each component in an SMROG mixture. The fitted pure component isotherm parameters, provided in Appendix F, were used directly as inputs for the transient breakthrough simulations. In the case of Zeolite 5A and Calgon PCB as well as the commercial zeolite and activated carbon described by Ribeiro et al., isotherm parameters found in the literature[150,151] were refitted to the DSL model.

Kinetic properties were represented using a bidisperse porous model, where macropore and micropore diffusivities are treated as resistances in series. Single component micropore transport diffusivities for the MOFs were calculated using EF-NEMD simulations and are given in Table 7-3, whereas the micropore diffusivities for the commercial zeolite and activated carbon were taken from Ribeiro et al.[150] In the case of Zeolite 5A and Calgon PCB, the dominant resistance was assumed to be the diffusion of molecules through the macropores, which is consistent with diffusion measurements reported in the literature,[167] therefore micropore diffusion was not needed in the predictions obtained from the breakthrough model.

Table 7-3. Micropore Transport Diffusivities calculated from EF-EMD simulations

Adsorbate	**Micropore Transport Diffusivity $D_c \times 10^9 (m^2/s)$**			
	UiO-66(Zr)	**UiO-66(Zr)-Br**	**UiO-67(Zr)**	**Zr-Cl_2AzoBDC**
H_2	44.5 ± 3.23	10.80 ± 1.23	154.00 ± 1.28	193.00 ± 3.33
CO_2	5.96 ± 0.30	2.80 ± 0.30	26.60 ± 1.80	31.70 ± 0.89
CO	5.83 ± 0.59	0.46 ± 0.06	23.40 ± 1.13	34.60 ± 1.94
CH_4	8.25 ± 0.68	0.22 ± 0.04	23.10 ± 2.12	28.10 ± 1.45
N_2	4.46 ± 0.65	0.25 ± 0.05	22.80 ± 1.45	28.70 ± 2.38

The macropore diffusivities were determined using molecular diffusivities alone, which were calculated according to the Chapman-Enskog equation:[168]

$$D_{ij} = 0.0018583\sqrt{\frac{1}{M_i}+\frac{1}{M_j}}\left(\frac{1}{\sigma_{ij}^2}\right)\left(\frac{T^{3/2}}{P\Omega_{ij}}\right) \qquad \text{Eq 7-12}$$

where M_i and M_j are the molar masses of each binary mixture component, and Ω_{ij} is the "collision integral" and is a function of k_BT/ε_{ij}. σ_{ij} is the separation distance between i and j at the lowest point of the Lennard-Jones potential well, while ε_{ij} is the energy at the lowest point of the well. The Ω_{ij} parameters were taken from the appendix tables of Bird et al.[168] The Chapman-Enskog equation was extended to the five-component mixture as follows:

$$D_{im} = \frac{1-X_i}{\sum_{j\neq i}^{n}\frac{X_j}{D_{ij}}} \qquad \text{Eq 7-13}$$

Here X_i and X_j are the molar fractions of the components in the mixture. The macropore diffusivity was then determined by dividing D_{im} by a tortuosity factor of $\tau = 2$, which falls within the tortuosity range of 1.7 – 4.5 for macropores in the binders of zeolite adsorbents.[2]

$$D_p = \frac{D_{im}}{\tau} \qquad \text{Eq 7-14}$$

The relative impact of micropore diffusivities was compared to the macropore diffusivities using the criterion developed by Ruthven and Loughlin[169] as shown in Eq 7-15.

$$\gamma = \frac{D_c / r_c^2 (1+K)}{D_p / r_p^2} \qquad \text{Eq 7-15}$$

where $K = \frac{(1-\varepsilon_p)H_{ad}}{\varepsilon_p}$ and $H_{ad} = \frac{\rho_s \mathrm{R} T H}{M_w}$

Here D_c and D_p are the micropore and macropore diffusivities through crystallites and pellets of radii of r_c and r_p, respectively, and H denotes the Henry constant. The γ parameters evaluated for the four MOFs are given in Table 7-4. For $\gamma < 0.1$ the process is micropore diffusion limited, while for $\gamma > 10$ macropore diffusion is the governing process. In the case of $0.1 < \gamma < 10$ both macropore and micropore diffusion must be taken into account.[169] The MOF crystallite and pellet radii were set to 3 μm and 0.85 mm, respectively. The crystallite size was chosen at the high end of the Zr MOF crystal size range[170], in order to account for the longest possible micropore diffusion path. The pellet radius for MOFs was chosen to be equal to the zeolite pellets of Ribeiro et al..[150] As all calculated γ values are greater than 10, the macropore diffusion process is much slower than diffusion through the micropores. This analysis demonstrates that for all mixture components and for all four MOFs the uptake rate is macropore diffusion limited.

Table 7-4. Micropore/macropore comparison criterion, γ

	UiO-66(Zr)	**UiO-66(Zr)-Br**	**UiO-67(Zr)**	**Zr-Cl$_2$AzoBDC**
H_2	2,037	491	7,379	9,105
CO_2	39,492	54,095	49,277	31,414
CO	4,556	555	8,515	9,241
CH_4	19,010	915	22,992	15,363
N_2	2,376	178	5,991	6,246

7.4 Results and Discussion

7.4.1 Pure Component Adsorption Isotherms

The adsorption isotherms of each of the impurities in the four structures investigated were determined through GCMC simulations up to a pressure of 50 bar, and are shown in Figure 7-3. They provide information not only about the relative capacities of the MOFs, but also about the relative strength of the adsorbate-framework interactions. A validation of the simulated isotherms for CO_2 and CH_4 adsorption in UiO-66(Zr) is provided in Appendix G. Due to a lack of available experimental data in the literature, it was not possible to validate the isotherms simulated for the remaining three MOFs. Considering the very good agreement observed in the case of UiO-66(Zr) however, the simulated isotherms can be expected to be accurate. Many studies have shown that the adsorption properties of MOFs are governed by a combination of the free volume and the enthalpy of adsorption.[71,88,171] The influence of the free volumes and adsorption enthalpies presented in Table 7-5 on the isotherms shown in Figure 7-3 is a reflection of this relationship.

Table 7-5. Simulated differential enthalpies of adsorption at 7 bar and 300 K for each of the mixture components, as well as free volumes and pore sizes for the four MOFs.

Material	**Δh (kJ/mol)**					**Pore Volume (cm^3/g)**	**Pore Size (Å)**
	H_2	**CO_2**	**CO**	**CH_4**	**N_2**		
UiO-66(Zr)	6.75	26.53	15.89	18.60	14.62	0.482	6.6, 7.5
UiO-66(Zr)-Br	7.46	29.67	18.22	21.00	16.69	0.330	6.4, 7.3
UiO-67(Zr)	5.01	20.37	11.89	14.17	10.69	1.011	8.9, 9.7, 11.9
Zr-Cl_2AzoBDC	4.69	17.28	11.31	13.51	10.37	1.118	10.4, 11.8, 13.6

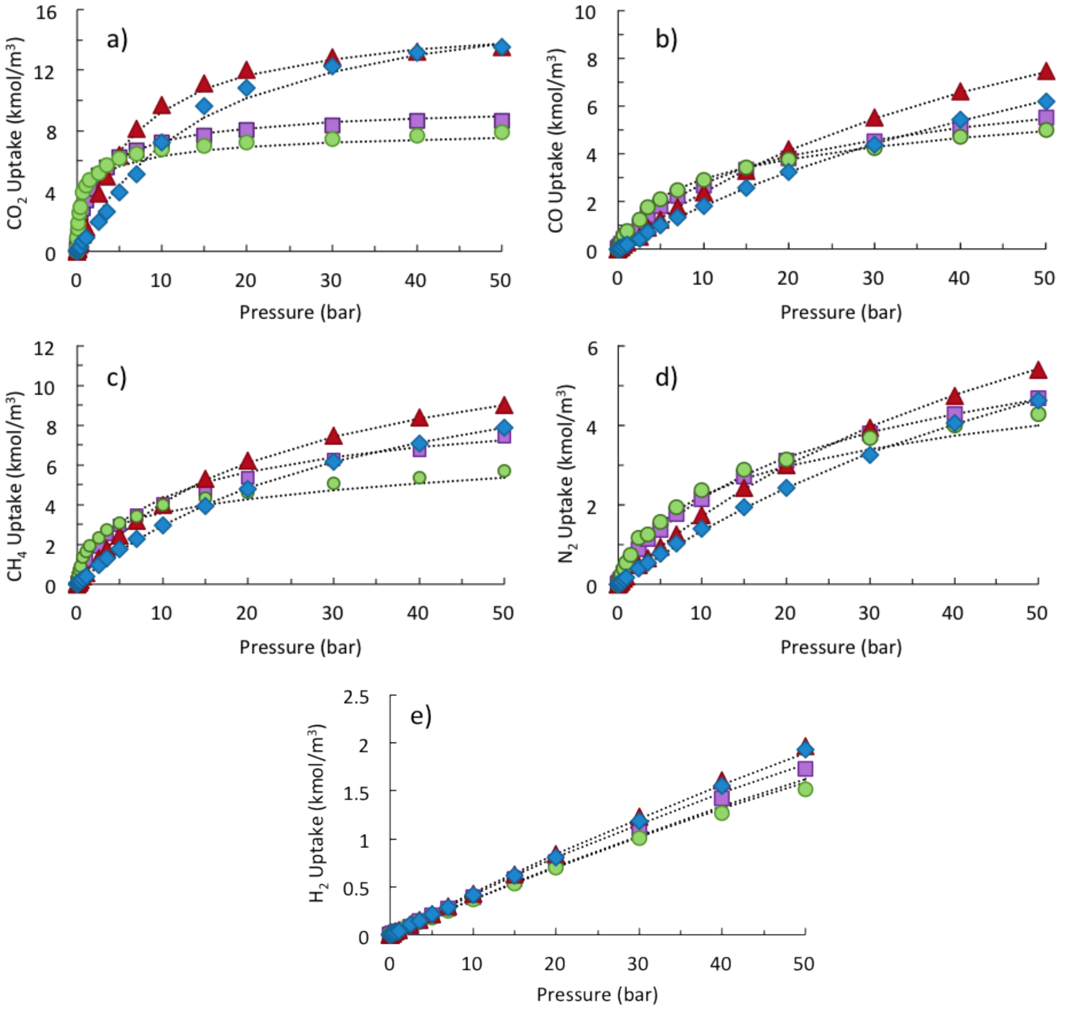

Figure 7-3. Pure component adsorption isotherms obtained using GCMC simulations for a) CO_2, b) CO, c) CH_4, d) N_2 and e) H_2 in each of the four MOFs investigated. UiO-67(Zr) – red triangles, Zr-Cl_2AzoBDC – blue diamonds, UiO-66(Zr)– purple squares, UiO-66(Zr)-Br – green spheres. The dotted lines represent the dual-site Langmuir fitted curves. Loading is expressed in volumetric terms, where the volume represents the space taken up only by MOF crystallites.

At high pressure, the highest uptake of all four adsorbates occurs in UiO-67(Zr). Although Zr-Cl_2AzoBDC has a higher pore volume than UiO-67(Zr), and chlorine functionalized linkers, the slightly shorter linkers of UiO-67(Zr) lead to narrower pores and at the same time to stronger dispersion interactions. At high pressure, the UiO-66(Zr) and UiO-66(Zr)-Br frameworks show the lowest volumetric uptake for each of the adsorbates due to their lower pore volumes as shown in Table 7-5. At low pressure on the other hand, these smaller pore MOFs have the highest uptake of all four adsorbates. As shown in Table 7-5, the highest enthalpies of adsorption for CO,

N_2, CH_4 and CO_2 are observed in UiO-66(Zr)-Br. This can be explained by the presence of narrow pores and pore windows and bromine functional groups, which result in strong dispersion and electrostatic interactions, respectively. It is interesting to note, however, that in the case of CO and N_2 adsorption, all four frameworks have very similar uptake up to a pressure of 20 bar. The highest N_2 enthalpy of adsorption was observed in UiO-66(Zr)-Br, followed by the unfunctionalized UiO-66(Zr), however N_2-framework interactions are relatively weak compared to the other impurities that must be removed during H_2 purification. As a result N_2 will be the most weakly retained impurity, and its breakthrough time dictates the length of the PSA feed step.[139] It is therefore particularly important to identify materials that can selectively adsorb N_2 from H_2 fuel sources such as SMROG.

7.4.2 Adsorption of Binary Mixtures

In order to evaluate the ability of each MOF to selectively adsorb CH_4, CO_2, CO and N_2 from SMROG streams, GCMC simulations were performed for binary mixtures of $CH_4:H_2$, $CO:H_2$, $CO_2:H_2$, and $N_2:H_2$. The hydrogen content of a SMROG mixture is normally at least 70%, therefore the binary mixture simulations were carried out on mixtures with impurity:H_2 ratios of 30:70. The constant hydrogen content across all four mixtures enabled a comparison not only of the selectivities of the four MOFs for each of the impurities, but also of the degree of selectivity relative to the impurity to be removed. It should be noted that in a PSA column the ratio of impurity to H_2 gas is significantly lower, particularly at the leading edge of the concentration front.

The binary mixture adsorption data was used in order to determine the selectivities for each of the impurities, which are shown as a function of pressure in Figure 7-4. The highest selectivities for all four impurities are observed in UiO-66(Zr)-Br. This behavior is a result of the significant potential overlap caused by a narrow pore size, as well as the presence of Br functional groups, both of which lead to increased interactions between the adsorbate molecules and the framework. The lowest CO_2, CH_4, N_2 and CO selectivities correspond to the large pores of UiO-67(Zr) and Zr-Cl_2AzoBDC, where the adsorption enthalpies are the lowest.

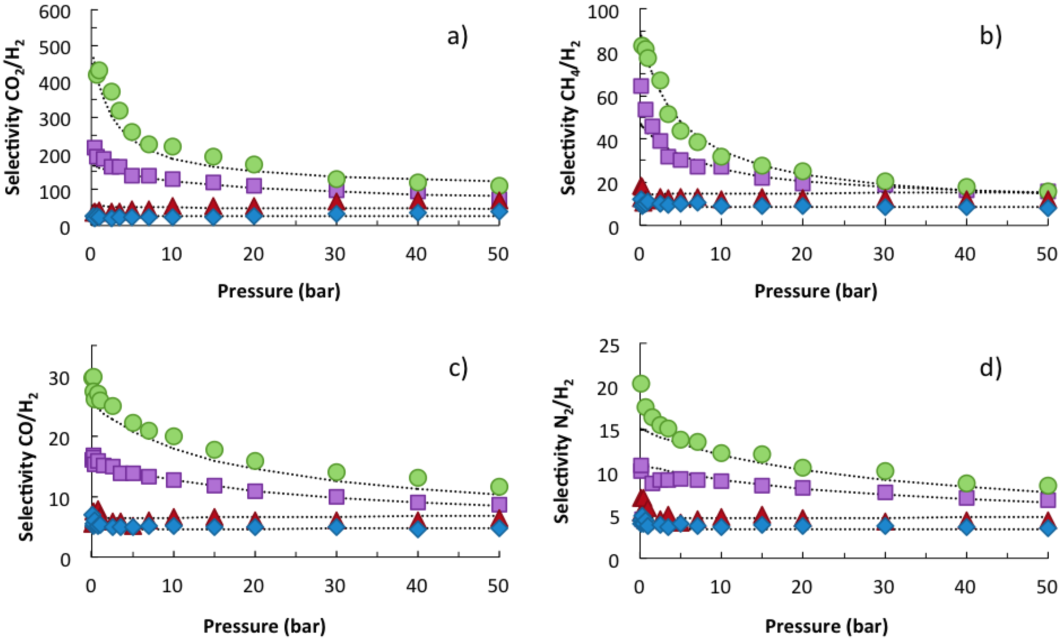

Figure 7-4. Selectivities from binary mixture adsorption of a) CO_2:H_2 30:70, b) CH_4:H_2 30:70, c) CO:H_2 30:70, and d) N_2:H_2 30:70. UiO-67(Zr) – red triangles, Zr-Cl_2AzoBDC – blue diamonds, UiO-66(Zr) – purple squares, UiO-66(Zr)-Br – green spheres. The dotted lines represent the dual-site Langmuir fitted curves.

The working capacities of each MOF, that is the amount of CH_4, CO_2, CO and N_2 that can be adsorbed from each binary mixture at the PSA feed pressure less what remains adsorbed at the purge pressure, were calculated for a 1-7 bar process:

$$\Delta q_i = q_{i,7\,bar} - q_{i,1\,bar} \tag{Eq 7-16}$$

The isothermal working capacity, Δq_i, is a particularly useful measure, as it gives insight into the ease of regeneration of a MOF, as well as its ability to capture impurities. Note, that during a PSA process the temperature inside the bed increases during the adsorption process resulting in a decrease of the working capacity. However the isothermal working capacities presented here provide a suitable measure for comparing different adsorbents. As shown in Figure 7-5, the highest CO and N_2 working capacities correspond to UiO-66(Zr)-Br where stronger adsorbate-framework interactions result in higher uptake at 7 bar than in the other three MOFs. At 1 bar, uptake of CO and N_2 is low in all four structures. UiO-66(Zr) has the highest CH_4 and CO_2 working capacity due to strong adsorbate-framework interactions, as well as a higher pore volume than UiO-66(Zr)-Br. Interestingly, UiO-

67(Zr) has a higher CO_2 working capacity than UiO-66(Zr)-Br, in spite of a large difference in adsorption enthalpies. This indicates that unlike the working capacities of weaker adsorbates, which depend mainly on the enthalpies of adsorption, the amount of CO_2 adsorbed during a PSA cycle is also dependent on the pore volume available.

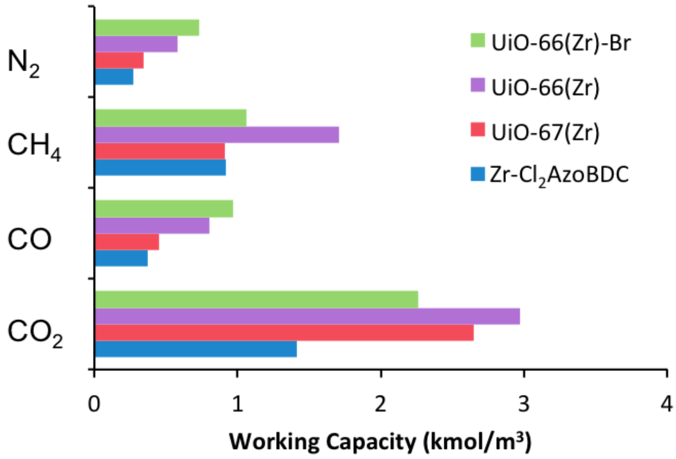

Figure 7-5. Working capacities from binary mixture simulations, for all impurities for a PSA operating range of 1-7 bar, and 298 K.

Each of the impurities however, make up only a small portion of the SMROG stream, therefore a more accurate perspective of the working capacities is achieved by considering the partial pressure of each impurity. Figure 7-6 shows the working capacities calculated from each binary mixture, for pressure ranges that result in impurity partial pressures that are equal to those in an SMROG stream operating between 1 bar and 7 bar, and from 1 bar and 20 bar, respectively. For example, for an SMROG stream operating between 1 and 7 bar, the CO partial pressure ranges from 0.03 bar and 0.21 bar. This results in a binary mixture total pressure of 0.1 – 0.7 bar. The total binary mixture pressures resulting in impurity partial pressures equivalent to those in an SMROG stream at 1, 7 and 20 bar are given in Table 7-6.

Table 7-6: Impurity partial pressures in an SMROG stream at 1, 7 and 20 bar.

P	**Binary Mixture Total Pressure (bar)**			
	CO/H_2	**CH_4/H_2**	**N_2/H_2**	**CO_2/H_2**
1 bar	0.1 (0.03/0.07)	0.13 (0.04/0.09)	0.13 (0.04/0.09)	0.53 (0.16/0.37)
7 bar	0.7 (0.21/0.49)	0.93 (0.28/0.65)	0.93 (0.28/0.65)	3.73 (1.12/2.61)
20 bar	2 (0.6/1.4)	2.67 (0.8/1.87)	26.7 (0.8/1.87)	10.7 (3.2/7.5)

The highest working capacities for CO, N_2 and CH_4 for both SMROG equivalent pressure ranges correspond to UiO-66(Zr)-Br. The highest CO_2 working capacities correspond to UiO-66(Zr) and UiO-66(Zr)-Br in the low pressure range (1 – 7 bar), and to UiO-66(Zr) and UiO-67(Zr) in the high pressure range (1 – 20 bar). This shows that for low adsorption pressures, CO_2 working capacities are highest in the materials with the highest adsorption enthalpies. On the other hand, for high adsorption pressures, it is important to choose materials with large pore volumes in order to obtain a high CO_2 working capacity.

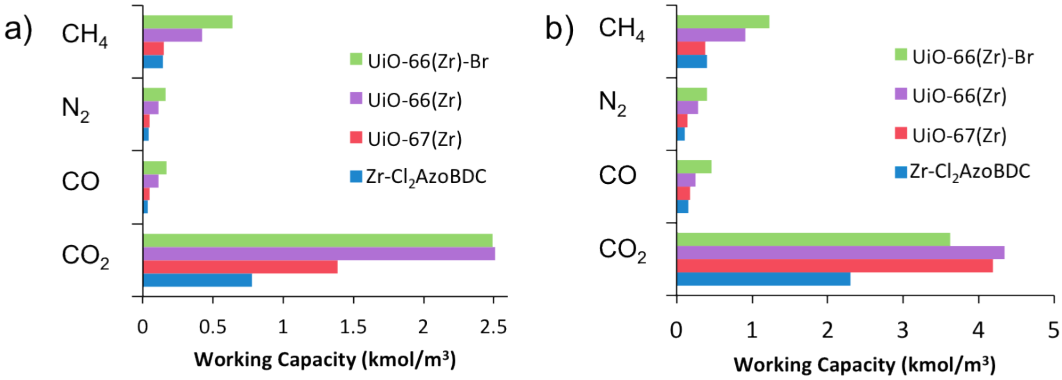

Figure 7-6: Working capacities determined from binary adsorption data for pressure ranges resulting in equivalent SMROG impurity partial pressures in a) the 1 – 7 bar range, and b) the 1 – 20 bar range.

The selectivity plots as well as the working capacities present valuable information about the potential of each MOF as a PSA adsorbent for H_2 purification. However, our results show that a MOF might be very promising in some aspects while showing limitations in others. Based on its high selectivities and N_2 and CO working capacities, UiO-66(Zr)-Br appears to have the greatest ability to retain weakly interacting impurities. Its small pore volume, and hence its lower CO_2 and CH_4 working capacities however, may lead to a shorter overall breakthrough time. UiO-66(Zr) on the other hand, which also exhibits relatively high selectivities, has high CO_2 and CH_4 working capacities and is expected to display good retention of these strongly interacting impurities. Its lower N_2 and CO selectivities however, could lead to a quicker elution of these impurities into the outlet stream. It is difficult to use this information alone in order to determine which material would be able to selectively adsorb the largest amount of impurities, allow for the longest PSA feed step, as well as require the lowest amount of purge gas during the regeneration step.

7.4.3 Breakthrough Curves for Single Layer Beds

In the work of Ribeiro et al., PSA cycles were modeled using five component SMROG mixtures and layered beds composed of a commercial zeolite and an activated carbon.[150] Here, breakthrough curves were simulated for the four MOFs, UiO-66(Zr), UiO-66(Zr)-Br, UiO-67(Zr) and Zr-Cl_2AzoBDC, as well as for beds containing the commercial adsorbents of Ribeiro et al.. The breakthrough curves in Figure 7-7 show the concentration of each impurity as a function of dimensionless time at the column outlet. The dimensionless time, τ, is calculated using

$$\tau = tu / \varepsilon L \qquad \text{Eq 7-17}$$

where u is the velocity of the mixture through the column, L is the column length, and ε is the bed void fraction. The use of dimensionless breakthrough time as opposed to specific time allows for a direct comparison of the breakthrough behavior between processes with different operating parameters. As shown in Figure 7-7, for all six adsorbents, the first impurity to elute is N_2, followed by CO, CH_4 and finally CO_2 as expected considering the weak N_2-framework interactions, and the high heats of adsorption of CO_2 in each of the materials. N_2 breakthrough is therefore confirmed as the limiting factor in determining the duration of the feed step in the PSA process. In addition, the strong interactions between CO_2 and the adsorbents indicate that this impurity is the most difficult to desorb, and could therefore present a constraint during the purge step. In the four MOFs and the activated carbon, CO is adsorbed more weakly than CH_4, and therefore elutes more quickly. Conversely in the commercial zeolite, the nonpolar CH_4 molecules interact more weakly with the framework, and therefore elute earlier than the polar CO molecules. The breakthrough curves of the three intermediate compounds adsorbed, that is N_2, CH_4, and CO, contain regions where the outlet concentrations are higher than their concentrations in the inlet stream. These regions contain one, two or three plateaus each, depending on the order of elution, and are caused by a competitive adsorption behavior, where more strongly adsorbed species displace weaker interacting species from adsorption sites within the column. For example, in Figure 7-7 a) the N_2 curve presents three consecutive steps signifying the displacement of N_2 molecules by CO, CH_4 and CO_2 molecules, respectively.

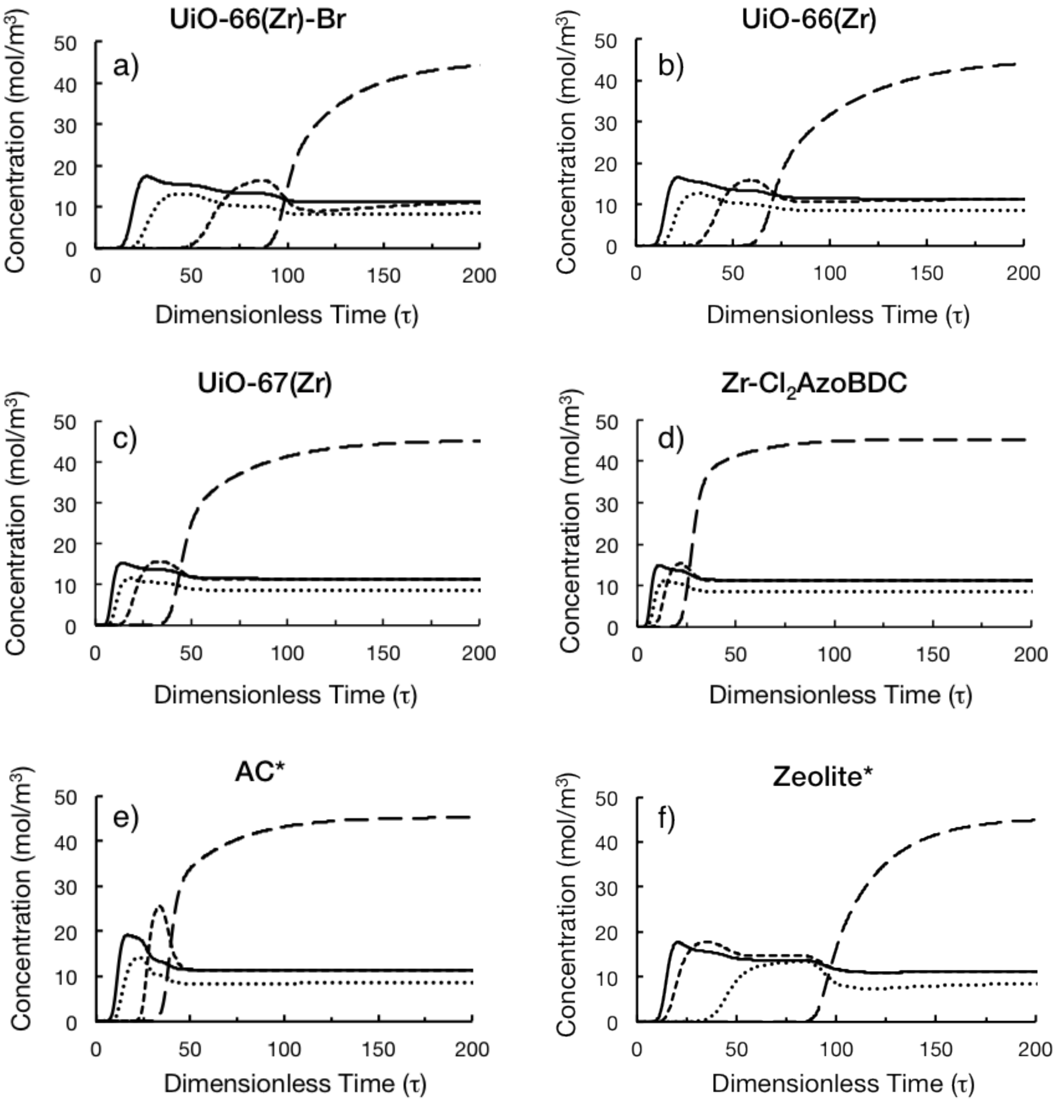

Figure 7-7. Simulated breakthrough curves for a five component mixture through a 1 m long adsorption column containing a) UiO-66(Zr)-Br b) UiO-66(Zr) c) UiO-67(Zr) d) Zr-Cl_2AzoBDC e) AC* f) Zeolite*. long dashed line – CO_2, short dashed line – CH_4, dotted line – CO, solid line – N_2. Zeolite* and AC* are the commercial adsorbents from the work of Ribeiro et al. [150]

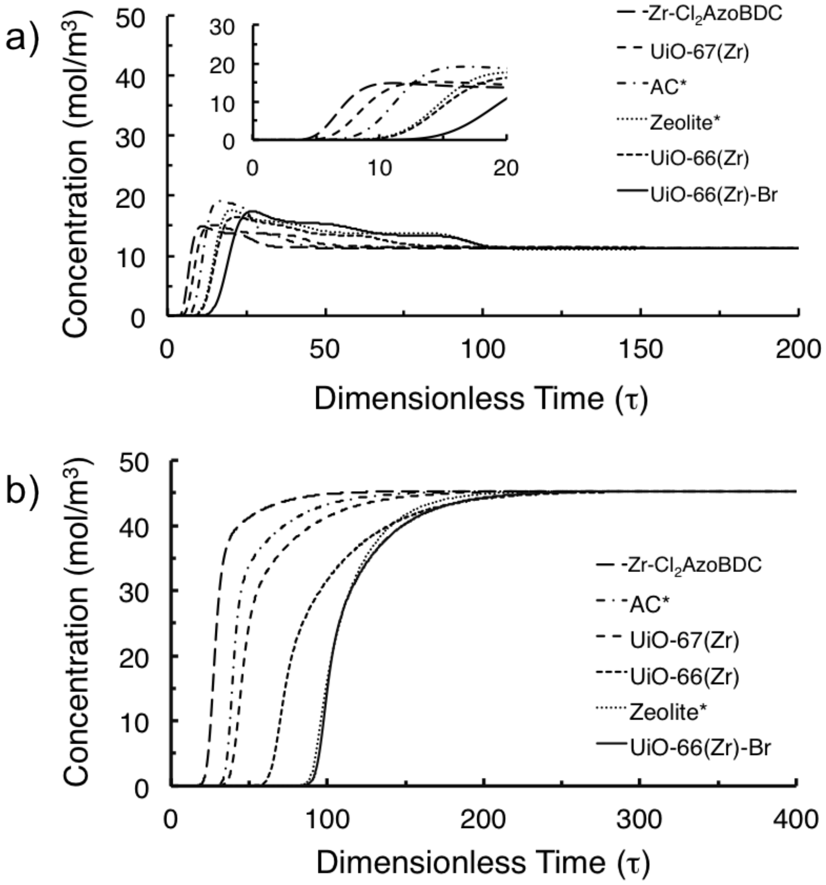

Figure 7-8. a) N_2 and b) CO_2 outlet concentrations as a function of dimensionless time for each of the six adsorbents. The inset in a) focuses on the 0-20 range. Zeolite* and AC* are the commercial adsorbents from the work of Ribeiro et al. [150]

In order to determine how MOFs perform in comparison with the commercial zeolite and activated carbon, it is important to focus on the N_2 and CO_2 breakthrough curves shown in Figure 7-8. Two of the four MOFs considered, namely UiO-66(Zr) and UiO-66(Zr)-Br, have longer N_2 breakthrough times than the zeolite, suggesting that these materials could potentially be used to replace zeolites in hydrogen purification beds in order to optimize the PSA process. The inset in Figure 7-8 a) shows UiO-66(Zr)-Br to have the longest time to breakthrough for N_2 molecules, which makes it the most promising MOF in this study. UiO-67(Zr) and Zr-Cl_2AzoBDC both have significantly shorter N_2 breakthrough times than the zeolite. Figure 7-8 b) shows that the CO_2 breakthrough time of UiO-66(Zr)-Br is similar to that of the zeolite. CO_2 adsorbs weakly in the activated carbon, as well as the large pore MOFs and therefore elutes at an earlier time point.

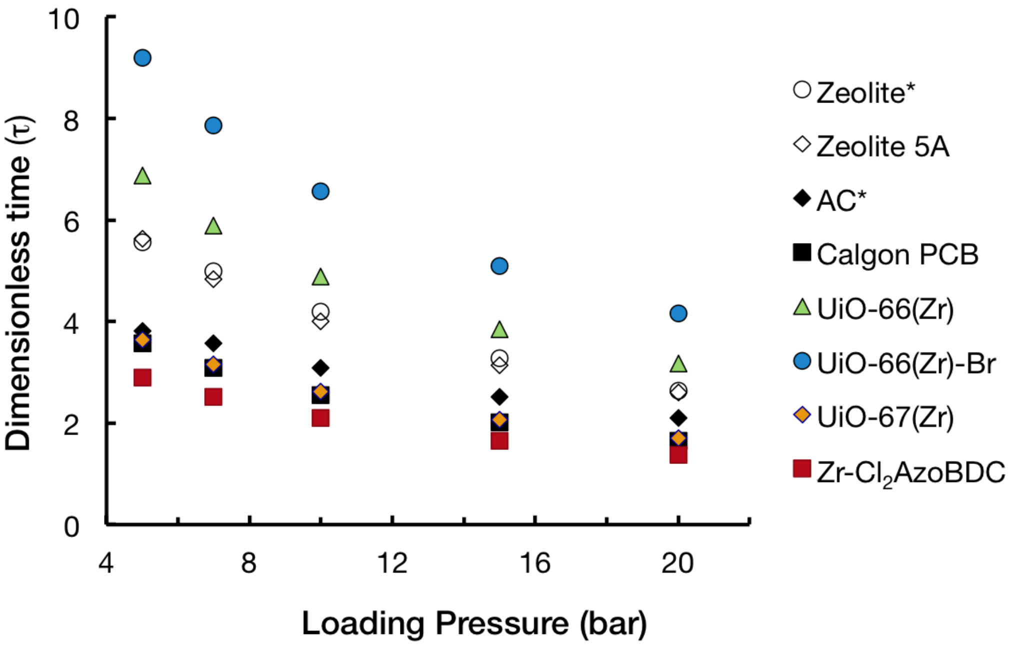

Figure 7-9. N_2 breakthrough time as a function of loading pressure. Zeolite* and AC* are the commercial adsorbents from the work of Ribeiro et al. [150]

The breakthrough curve analysis was extended to include Zeolite 5A and Calgon PCB, in order to further compare the performance of the four MOFs to industrial PSA adsorbents. Breakthrough simulations for these materials were carried out based on the adsorption data provided in the recent PSA work of Ahn et al.[40] In Figure 7-9 breakthrough times for the MOFs, zeolites and activated carbons are plotted as a function of loading pressure. For all adsorbents in this study N_2 is the first impurity to elute into the product stream. Considering that the purity requirement for H_2 fuel and propellant applications is a N_2 concentration lower than 2 ppm,[172] the breakthrough time was defined as the time at which the N_2 content in the outlet stream reached a conservative 1 ppm.

UiO-67(Zr) and Zr-Cl_2AzoBDC have short breakthrough times across the entire pressure range, similar to the activated carbons, which is due to weak N_2 framework interactions. The remaining two MOFs however, have longer breakthrough times than the two zeolite materials. The longest retention of impurities corresponds to UiO-66(Zr)-Br, making this a particularly promising PSA adsorbent.

7.4.4 Layered PSA Columns

As mentioned earlier, the length of the PSA purge step is limited by the ease of CO_2 desorption from the bed. Currently, PSA units employ layered beds containing two or more adsorbents. This technique aims to adsorb each impurity within a layer from which it can be readily desorbed. Alumina or silica layers are used to adsorb water vapor, while activated carbon is used to target CO_2 and long hydrocarbons. These strongly adsorbing impurities are thus prevented from reaching the zeolite layer, from which they would be difficult to remove. In the work of Ribeiro et al., a layered bed containing activated carbon and zeolite is modeled as part of an eight-step PSA cycle, and an outlet stream purity of 99.9994% is obtained.[150] Considering that some MOFs in this study have high heats of adsorption for CO_2, particularly UiO-66(Zr)-Br, it is likely that the use of MOFs in layered adsorption beds along with activated carbon will prove to be more efficient than the use of a MOF-only bed.

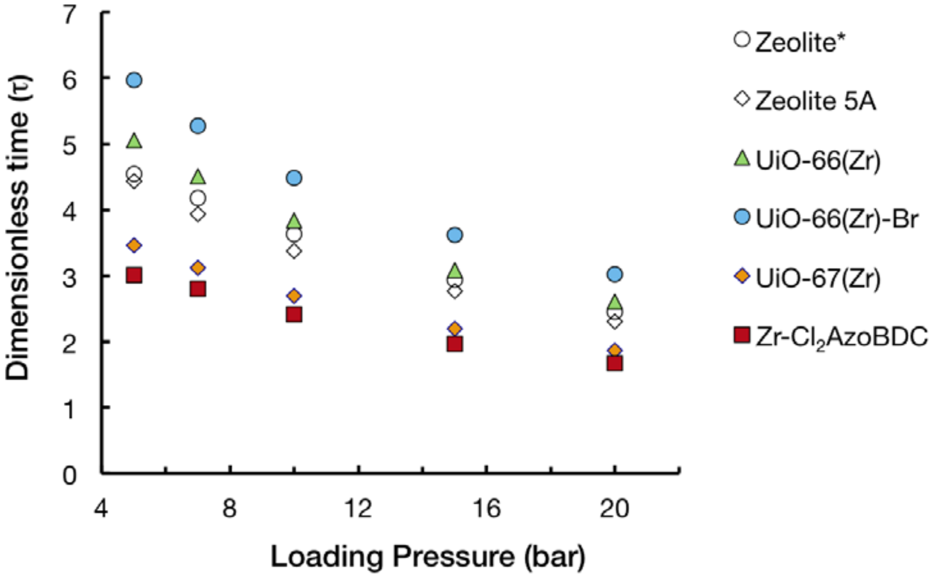

Figure 7-10. N_2 breakthrough time for layered beds as a function of loading pressure. Each bed contains an AC* layer and an equal layer of MOF or zeolite. Zeolite* and AC* are the commercial adsorbents from the work of Ribeiro et al.[150]

Breakthrough curves were modeled for the same SMROG mixture through 1 m long columns containing a 0.5 m bottom layer of the commercial activated carbon used by

Ribeiro et al., followed by a 0.5 m layer of each of the MOFs and the commercial zeolite. The UiO-66(Zr) and UiO-66(Zr)-Br layered bed show similar or longer N_2 breakthrough times than the two zeolite layered beds as shown in Figure 7-10. Generally N_2 breakthrough times are shorter in the case of layered beds than for the single component beds due to the relatively fast movement of molecules through the AC layer. A comparison of the N_2 time to breakthrough for single versus two-layered beds is shown in Figure 7-11. While the addition of an AC layer has the benefit of capturing CO_2 molecules and preventing them from reaching the MOF layer, there is a trade-off in terms of feed step duration, and this effect is most significant in the case of UiO-66(Zr)-Br. Nevertheless, while both UiO-66(Zr) and UiO-66(Zr)-Br perform better than the commercial zeolite of Ribeiro et al. and Zeolite 5A, the most promising framework for H_2 purification using a two-layered bed is UiO-66(Zr)-Br. In UiO-67(Zr) there is only a minor decrease in breakthrough time when the AC layer is included, while in the Zr-Cl_2AzoBDC breakthrough time is actually improved in the two layer setup. This is explained by a weak retention of CO_2 in the two large pore MOFs as shown in Figure 7-8 b), which is similar or worse than that of AC*.

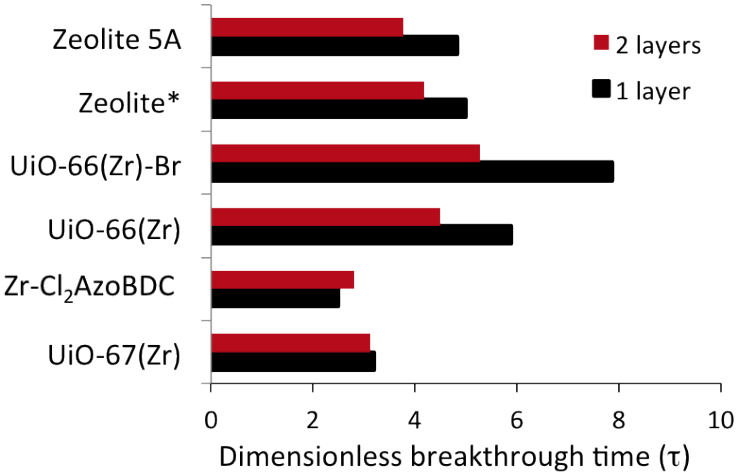

Figure 7-11. Time to N_2 breakthrough (1 ppm in the outlet stream) for 1 m columns containing MOF or zeolite only (black), and layered columns containing equal volumes of AC* and MOF or zeolite (grey). Zeolite* and AC* are the commercial adsorbents from the work of Ribeiro et al.[150]

7.4.5 Ease of Regeneration

In order to compare the ease of column regeneration, layered bed adsorption simulations were carried out for each of the MOFs and zeolites and terminated at their specific N_2 breakthrough times. These simulations were then succeeded by a desorption stage carried out at 1 bar, consisting of a 50 s blow-down and a 450 s purge with pure H_2. In the work of Ribeiro et al. the blow down and desorption steps of the PSA schedule were each set to be ¼ of the feed step duration.[150] Here, the 50 s duration chosen for the blow down is approximately ¼ of the longest feed step duration (UiO-66(Zr)-Br), however a longer purge stage was employed in order to obtain full column regeneration. The impurity loadings at the bottom of the MOF/zeolite layer, approximately in the middle of the column, during the adsorption and desorption stages are shown on the left and right hand sides of Figure 7-12, respectively. Unsurprisingly the lowest loading during adsorption, and quickest regeneration is observed in UiO-67(Zr) and Zr-Cl_2AzoBDC. The two smaller pore MOFs, UiO-66(Zr) and UiO-66(Zr)-Br have the highest impurity loading following the adsorption stage. In particular, UiO-66(Zr)-Br has a N_2 loading that is more than three times those in Zeolite* and Zeolite 5A. Despite the higher amounts of impurities adsorbed inside the small-pore MOFs, full regeneration is achieved after approximately 300 s, which is nearly the same as the regeneration times observed for the two zeolites. This indicates that a layered PSA column containing UiO-66(Zr) or UiO-66(Zr)-Br could be used in order to produce a greater amount of high purity H_2 than the two zeolites, without requiring a longer purge stage.

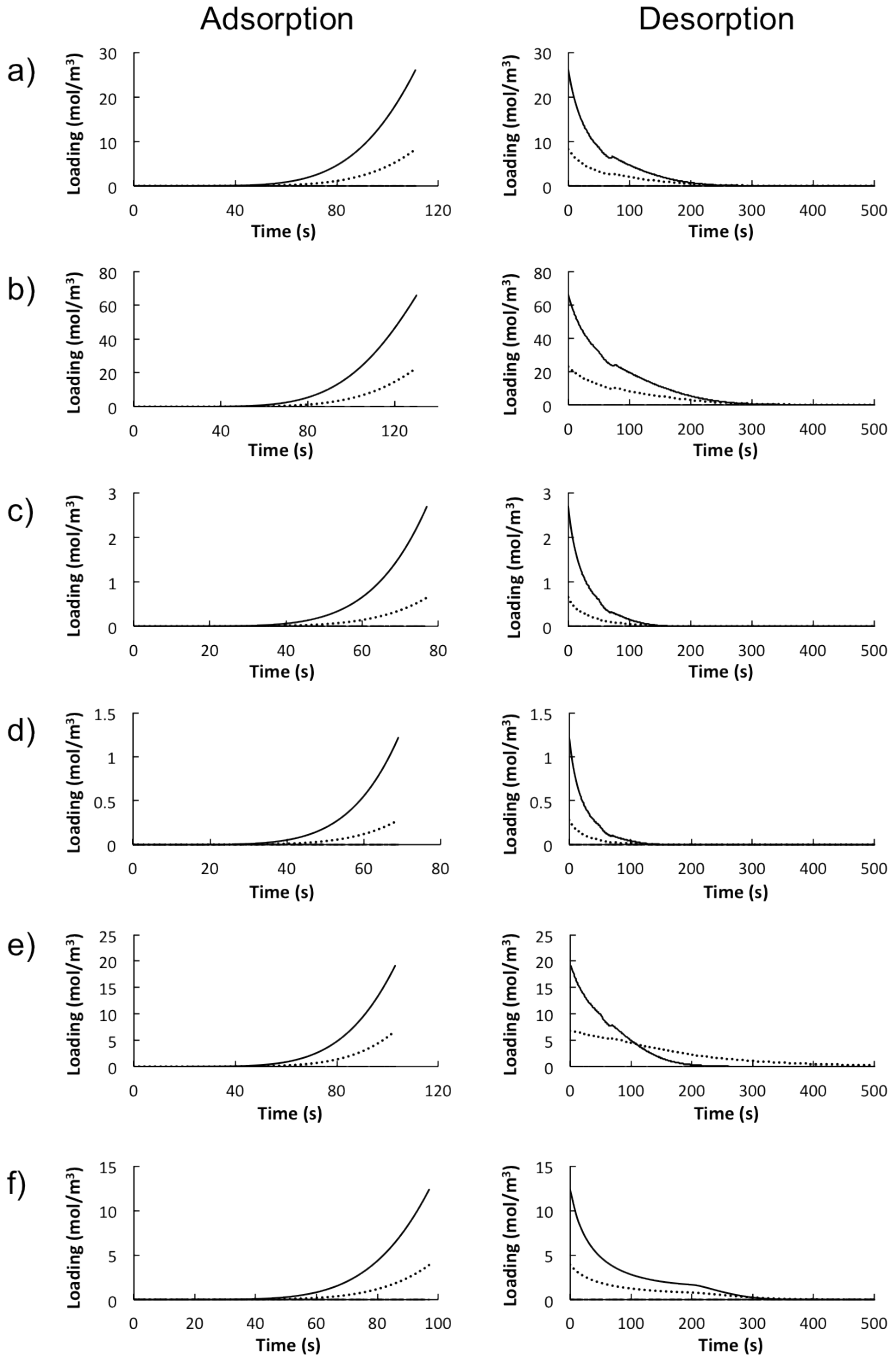

Figure 7-12. Adsorbed impurity concentrations at the bottom of the MOF/zeolite layer from layered bed adsorption simulations terminated at the N_2 breakthrough point (left column) and desorption simulations (right column). Beds contain equal layers of AC* and a) UiO-66(Zr) b) UiO-66(Zr)-Br c) UiO-67(Zr) d) Zr-Cl_2AzoBDC e) Zeolite* and f) Zeolite 5A. Dotted line – CO, solid line – N_2, long dashed line – CO_2, short dashed line – CH_4. The CO_2 and CH_4 curves coincide with the x-axes in all cases. Zeolite* and AC* are the commercial adsorbents from the work of Ribeiro et al.[150]

For all of the frameworks investigated here, the chosen activated carbon layer height of 0.5 m was observed to prevent CO_2 from eluting into the MOF layer before the N_2 breakthrough time was reached. Given the substantial reduction in the overall N_2 breakthrough time caused by the AC layer addition, only the minimum amount of AC required to retain the CO_2 molecules should be used. The structure identified as having the longest N_2 breakthrough time, UiO-66(Zr)-Br was selected in order to investigate the optimum AC layer height. In Figure 7-13, a plot of the CO_2 AC layer breakthrough time is shown along with the overall N_2 breakthrough time for a range of AC and UiO-66(Zr)-Br layer height ratios. The column length was maintained fixed at 1 m. For an AC layer height between 0.2 and 0.4 m, CO_2 (shown as red spheres) reaches the UiO-66(Zr)-Br layer before the N_2 concentration (shown as black spheres) reaches 1 ppm in the product stream. In this region, the duration of the PSA cycle is limited by the CO_2 breakthrough time through the activated carbon. For an AC layer thicker than 0.45 m, all of the CO_2 is retained inside the AC layer for much longer periods of time. However, a thicker activated carbon layer results in poorer N_2 retention. In the case of an AC layer height larger than 0.45 m the PSA cycle duration is limited by the N_2 breakthrough time, which is significantly shorter. The operating range is therefore the area underneath the lowest of the two constraints, and is shown in grey in Figure 7-13. The shortest AC layer height that would render a CO_2 retention time in the AC layer that is longer than the N_2 overall retention time is 0.45 m. Decreasing the AC layer length from 0.5 m to 0.45 m would increase the potential PSA dimensionless breakthrough time from 5.27 to 5.47 (130 s to 135 s).

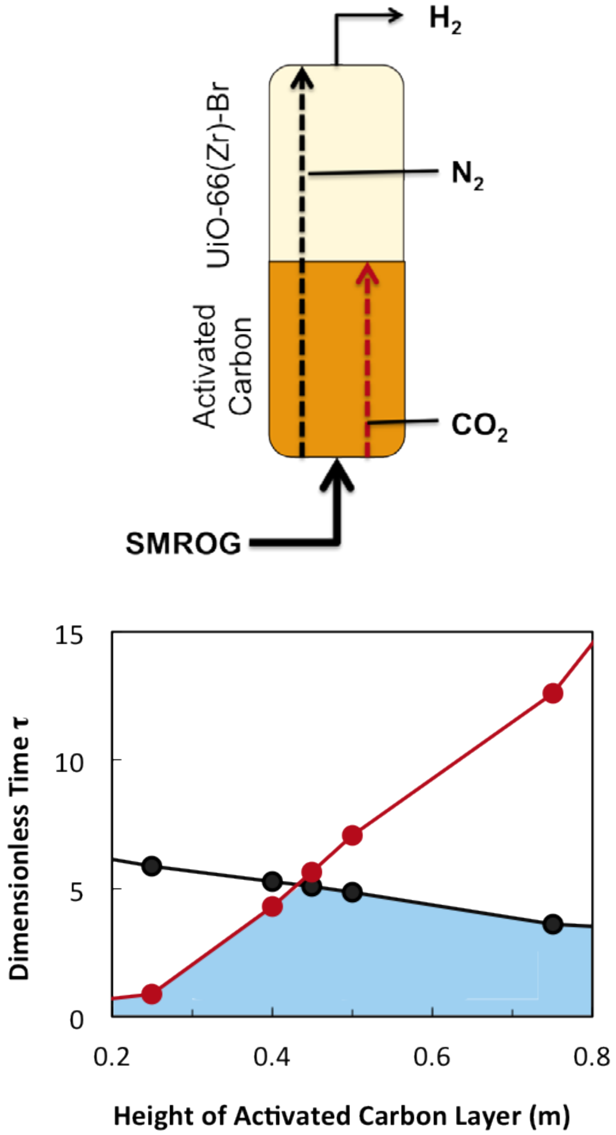

Figure 7-13. For a layered bed of the commercial activated carbon and UiO-66(Zr)-Br: 1 ppm breakthrough time for CO_2 at the end of the activated layer (red spheres) and the N_2 breakthrough time at the end of the column (black spheres). The blue shaded region in the graph denotes the PSA cycle durations for which both operating conditions are satisfied: N_2 retention inside the column and CO_2 retention in the activated carbon layer.

7.5 Conclusions

The work presented in this study demonstrates that some metal-organic frameworks may be able to compete with commercial zeolites as adsorbents for the purification of H_2 from SMROG via pressure swing adsorption. The separation capabilities of four MOFs, namely UiO-66(Zr), UiO-66(Zr)-Br, UiO-67(Zr) and Zr-Cl_2AzoBDC were compared to a commercial zeolite and a commercial activated carbon, as well as Zeolite 5A and Calgon PCB. The MOFs were first evaluated in terms of their pure component adsorption isotherms, working capacities, and adsorption enthalpies for each of the mixture components, as well as binary mixture selectivities. UiO-66(Zr)-Br was observed to have the highest selectivities and working capacities for N_2 and CO, indicating that the presence of narrow pores and functionalized linkers results in improved retention of weakly interacting gases due to stronger adsorbate – framework interactions. UiO-66(Zr) on the other hand displayed the highest CH_4, and CO_2 working capacities for a 1-7 bar pressure range. Considering that CO_2 is the most abundant impurity in the SMROG mixture, and that the most weakly adsorbed impurity is N_2, it is difficult to determine which of the four MOFs would be most efficient in separating H_2 from SMROG based on adsorption and selectivity data alone. Therefore breakthrough curve simulations were performed for five component mixtures composed of H_2, N_2, CO, CH_4 and CO_2. These simulations are exceptionally useful as they enable the study of both adsorptive and diffusive processes, and take into account the contributions of each of the mixture components. The study of single and two-layered beds revealed that UiO-66(Zr) and UiO-66(Zr)-Br have longer breakthrough times than the commercial zeolite studied by Ribeiro et al. and zeolite 5A, and would therefore result in a larger amount of high purity H_2 product per PSA cycle. UiO-66(Zr)-Br was found to be the most effective material for retaining the impurities present in SMROG, having the longest breakthrough time in this study.

It is important to bear in mind that PSA adsorbents are selected not only based on their thermodynamic properties but also on their physical robustness. The UiO-66(Zr) family of MOFs has been shown to have a high resistance to solvents and to mechanical pressure of up to 10 kg/cm^2,[156] making UiO-66(Zr)-Br a particularly promising PSA adsorbent.

8 Summary and Outlook

Many studies have shown that metal organic frameworks are promising materials for a range of adsorption and separation processes. In order to move forward from the conceptual stage towards the application stage, studies must be performed not only on the molecular scale, to understand the MOF structure and the guest-framework interactions taking place, but also on the process scale in order to evaluate the performance of MOFs in their final application environment. Computational work is particularly advantageous as it reduces the need for time-consuming experiments, and provides valuable information about the system that would be difficult to obtain using other methods. The work presented in this thesis was performed in order to obtain a complete evaluation of MOFs as adsorbents for hydrogen purification applications, making use of molecular simulations, as well as experimental work and process simulation studies.

As a first step, pure component and binary mixture adsorption simulation studies on a variety of MOFs were used to identify the connection between structural features and the properties influencing a framework's selectivity for SMROG impurities. It was revealed that a decrease in linker length, the functionalization of linkers using amine groups or additional aromatic rings, and a higher density of linkers result in stronger adsorbate-framework interactions, and lower pore volumes, thereby increasing selectivity. Bearing in mind that separation efficiency is influenced by both selectivity and working capacity, the adsorbent performance indicator (API), which is calculated based on the selectivity, working capacity and adsorption enthalpy, can be used to obtain an overall measure of the suitability of a MOF for a specific binary separation process. The adsorption and selectivity data, and the API factors calculated here for a range of MOFs show that Mn MIL-53 and MIL-47 are promising frameworks for the separation of hydrogen from the impurities present in SMROG. The trends observed in this work are valuable tools that can be used to select or design additional and potentially more promising materials. This study should be extended to determine the influence of additional framework features, including a wider array of functional groups, on selectivity.

Once a MOF is identified as a good adsorbent for a specific separation process, additional work is necessary in order to examine whether the assumptions made during the simulation studies, particularly the rigid framework model, are an accurate representation of the framework. In the case of flexible MOFs, such as Mn MIL-53, the extent of flexibility taking place during the adsorption process must be well understood. Mn MIL-53 was synthesized and studied using a combination of simulation and experimental methods. The framework undergoes significant structural changes at low temperature, and to a lesser extent at room temperature, in order to adsorb CO_2. On the other hand, CH_4 adsorption studies at room temperature resulting in a low uptake suggest that minimal or no structural changes take place. In order to better understand the dynamic behaviour of the structure, future studies should incorporate in situ X-ray diffraction experiments. Such work would help elucidate the exact form of the framework at various temperatures and gas loadings, which is essential for identifying its usefulness for various applications.

In the case of non-flexible MOFs, the use of a rigid framework model based on crystallographic data is a reasonable approximation, leading to a good agreement between simulated isotherms and experimental data. Adsorption simulations of various gases in MIL-47 however, resulted in a significant overprediction of uptake. This discrepancy cannot be explained by the presence of non-porous defects in experimental samples, as low pressure overpredictions persist even after scaling factors are used to account for a pore volume difference. In addition, despite the good agreement obtained using a modified force field, there is no physical justification for a reduction in adsorbate-framework interaction strength. Having ruled out two potential sources for the simulated overpredictions, ab initio molecular dynamics studies were used to determine the positions of the benzene dicarboxylate linkers over time. A significant amount of movement can be observed, as the linkers rotate about their symmetry axis. Linker rotation is energetically favourable, and time averaged structures from ab initio molecular dynamics simulations show that the linkers spend a large amount of time in a rotated position, unlike the orientation described by crystallographic data. This can be explained by the long time over which synchrotron diffraction patterns are measured, compared to the simulation duration. The presence of linker rotation can be used to explain the reason for the initial overpredictions of uptake, as adsorption simulations on time averaged structures, with no force field modifications, result in isotherms that are in excellent agreement with the experimental data. In the case of longer chain hydrocarbons, persisting discrepancies may be due to steric effects, or possibly to additional structural changes. Despite its stable, open-pore nature, MIL-47 exhibits significant dynamic effects. In the case of larger molecules, the form of the framework must be confirmed either experimentally or through ab initio studies of a loaded structure. The use of linkers with dicarboxylate connections is common in MOF synthesis work. These types of linkers have the freedom to rotate about their axis, which can have a strong influence on the adsorption process. As a result, simulations using rigid representations of such MOFs should be preceded by an investigation into the orientations of the linkers, in order to assess the accuracy of the rigid framework representation. On the other hand, from a design point of view, linker rotation could be avoided altogether by incorporating linkers with different binding modes, such as the dihydroxyterephthalic acid linkers of MOF-74 structures.

The flexibility observed in the small pores MOF Sc_2BDC_3 with changes in temperature, or adsorbate-framework interactions, is another example of the effects of linker rotation. CO_2 adsorption at low temperature is accompanied by two stages of structural changes. Starting from a monoclinic configuration, the interactions between CO_2 molecules and the framework drive changes in the framework such that the molecules occupy two distict sites at medium loading, and three distinct sites at high loading. Ab initio molecular dynamics studies indicate that the framework responds to the number of molecules present in each pore, and is able to adjust in order to accommodate them. Whereas CO_2 adsorption is facilitated by structural changes, in the case of methanol adsorption at high pressure, it is the presence of hydrogen bonds that plays a more significant stabilizing role. Methanol molecules are observed to occupy two distinct adsorption sites. Hydrogen bonds form at both sites, and the more favourable adsorption site corresponds to the highest incidence of hydrogen bonds formed. Despite its narrow pores, Sc_2BDC_3 is able to accommodate a surprising variety of molecules. This highly stable MOF may prove beneficial for separation processes, and the limits of its adsorptive properties should be further investigated.

While detailed molecular simulation studies are essential in understanding the behaviour of MOF structures, it is equally important to assess capabilities of promising materials under the working circumstances for which they are targeted. In the case of hydrogen purification from SMROG, such studies can be carried out by performing breakthrough simulations. It is particularly important that the mixtures studied contain all impurities that must be removed, as the molecules compete for the adsorption sites available inside the material. The API factor is a useful indication of a material's separation capabilities for binary mixtures. When working with mixtures of multiple components such as SMROG however, API calculations for a set of binary mixtures although useful, do not account for a competitive adsorption process. In addition, working capacities determined based on the fractional contribution of one mixture component in turn are not a realistic assessment of the material's capacity for the total amount of impurities present. If the total impurity content of the mixture is small, and the volume available inside the pores of a material is sufficiently large, API evaluations based on a set of binary mixtures may provide a reliable assessment of the material's separation capabilities for the complete mixture. Breakthrough curve computational studies on the other hand, can provide consistently accurate evaluations of MOFs as adsorbents for H_2 purification. These process simulations require an accurate description of the adsorption and diffusion of each mixture component within the MOF, information that can be obtained with ease through molecular simulations. A study of the breakthrough behaviour of SMROG through simple as well as layered columns, containing UiO-66(Zr), UiO-66(Zr)-Br, UiO-67(Zr) and Zr-Cl_2AzoBDC shows that certain MOFs can outperform commercial zeolites and activated carbons in separating hydrogen from SMROG impurities. In addition the complete regeneration of columns containing promising MOFs is achieved in a time that is comparable to zeolites, indicating that additional energy would not be required in order to desorb impurities from beds containing MOFs compared to zeolites. The studies performed show that UiO-66(Zr)-Br is a particularly suitable material for hydrogen purification processes, having an excellent retention of impurities. The outstanding separation performance of UiO-66(Zr)-Br deserves further attention, and should be confirmed using experiments.

The work presented in this thesis essentially spans all stages of the selection process of MOFs for hydrogen purification applications. It is clear that such studies require the combination of computer simulations, from the ab initio scale to the unit operations scale, with experimental analyses. Although the main focus of this thesis was hydrogen purification, the methods employed here are transferable to other adsorption and separation applications. Such approaches enable thorough assessments to be performed, and are essential in driving MOF research forward towards industrial applications.

Despite the heavy use of simulation tools, the screening of MOFs based on the steps presented in this thesis, is still a lengthy process. The identification of desirable MOF characteristics for good separation efficiency, as well as the simulation of breakthrough curves on promising structures can be performed in a short amount of time. On the other hand, the assessment of the dynamic properties of MOFs and their impact on adsorption is a more intricate problem. MOFs are diverse, and fairly complex materials that have been shown to exhibit a variety of framework flexibilities, such as gate-opening and breathing properties. As was shown in this work, in some cases even rigid MOFs are able to respond to temperature changes, pressure changes, and interactions with adsorbate molecules. GCMC studies are not able to reflect such properties, therefore adsorption simulations continue to rely on experimental validation. Dynamic effects are often investigated separately, either through experiments, molecular dynamics simulations requiring material-specific flexible force fields, or as was done in this thesis, through ab initio methods which bypass the need for force field development and produce significantly more accurate results. Considering that framework flexibility and adsorption are interrelated, some valuable information is lost when studying these effects independently. Future MOF studies would greatly benefit from the development of new simulation methods that would enable the study of adsorption in all types of MOFs while allowing for structural changes to take place. Such tools could for example combine the classical GCMC method with ab initio techniques, such as energy minimization or AIMD. Adsorption simulations would then theoretically provide a very accurate prediction of uptake and structural behavior, reducing the need for experimental work. Naturally, the development of such tools would require a considerable amount of time, however given the diversity of MOFs, and the great need for quick assessments of adsorption and selectivity, such work would be a worthy investment.

Acronyms

AC	Activated Carbon
AIMD	Ab Initio Molecular Dynamics
API	Adsorbent Performance Indicator
BP	Becke and Perdew (GGA XC functional)
BLYP	Becke, Lee, Yang and Parr (GGA XC functional)
CB-GCMC	Configurational Bias Grand Canonical Monte Carlo
CGTO	Contracted Gaussian Type Orbital
CSD	Cambridge Structural Database
DCF	Displacement Correlation Function
DFT	Density Functional Theory
EF-NEMD	External Field Non-Equilibrium Molecular Dynamics
EMD	Equilibrium Molecular Dynamics
FV	Free Volume
GCMC	Grand Canonical Monte Carlo
GGA	Generalized Gradient Approximation
GTH	Goedecker, Teter and Hutter (pseudopotential)
GTO	Gaussian Type Orbital
HF	Hartree Fock
HKUST	Hong Kong University of Science and Technology
IAST	Ideal Adsorbed Solution Theory
IRMOF	Isoreticular Metal Organic Framework
LDA	Local Density Approximation
LJ	Lennard-Jones
MD	Molecular Dynamics
MIL	Material Institute Lavoisier
MOF	Metal Organic Framework
MSD	Mean Square Displacement
MuSiC	Multipurpose Simulation Code
NMR	Nuclear Magnetic Resonance

PBE	Perdew, Burke and Ernzerhof (GGA XC functional)
PCN	Porous Coordination Network
PCP	Porous Coordination Polymer
PSA	Pressure Swing Adsorption
SA	Surface Area
SCF	Self Consistent Field
SMROG	Steam Methane Reformer Offgas
STO	Slater Type Orbital
TraPPE	Transferable Potential for Phase Equilibria
UFF	Universal Force Field
UiO	University of Oslo
WC	Working Capacity
XC	Exchange-Correlation
XRD	X-ray Diffraction

Nomenclature

A_c	Internal column surface area, m^2
A_c	Internal column surface area
A_p	Pellet surface area
$acc(o \rightarrow n)$	Acceptance probability
b_i^j	Adsorption equilibrium constant of site j for comp. i
c_0	Torsional force constant
c_1	Torsional force constant
c_2	Torsional force constant
c_3	Torsional force constant
c_i	Gas concentration of component i
c_i^m	Gas concentration of component i in the macropore
c_T	Total concentration in the fluid phase
c_T^m	Total concentration in the macropore
$c_{P,sol}$	Specific heat capacity at constant pressure in the solid phase
$c_{P,w}$	Specific heat capacity of the column wall
$\tilde{c}_P$	Molar heat capacity at constant pressure in the fluid phase
$\tilde{c}_{P,ad.}$	Molar heat capacity at constant pressure in the adsorbed phase
$\tilde{c}_V$	Molar heat capacity at constant volume in the fluid phase
d	Number of dimensions
D_c	Micropore diffusivity
D_{ij}	Macropore diffusivity for binary mixtures
D_{im}	Macropore diffusivity for mixtures of more than two gases
D_p	Macropore diffusivity
D_s	Self-diffusivity
D_t	Transport diffusivity
E	Total energy of the system
E_k	Energy of microstate k

E_{known}	Known energy contribution
E_{XC}	Exchange correlation energy term
f	Fugacity of the bulk phase
$\mathbf{F}_i$	Force acting on a molecule i
J	Flux of molecules through micropores
h	Heat transfer coefficient between the pellet and the bed
Δh	Differential enthalpy of adsorption
h_w	Heat transfer coefficient at the column wall
$\hbar$	Plank’s constant
H_{ad}	Dimensionless Henry’s constant
H_f	Enthalpy in the fluid phase per unit volume
$\tilde{\boldsymbol{H}}_i$	Partial molar enthalpy in the fluid phase of comp.i
$\Delta\tilde{\boldsymbol{H}}_i^j$	Heat of adsorption of site j for comp. i
$\hat{H}$	Hamiltonian operator
$\hat{H}_{elec}$	Hamiltonian operator for the electrons
J_i	Diffusive flux of component i
J_T	Thermal diffusive flux
k_B	Boltzmann constant
k_i^p	LDF mass transfer coefficient of component i in the pellet
k_i^{cr}	LDF mass transfer coefficient of component i in the crystal
k_r	Bond force constant
k_θ	Bending force constant
L_c	Column length
L	Onsager coefficient
m	Mass of a particle
M_A	Mass of a nucleus
M_i	Molar mass of binary mixture component i
$M_{observed}$	Value of property M obtained by averaging over time
$\langle M\rangle_{ensemble}$	Ensemble average value of property M
(n)	New configuration
N	Number of molecules in the system

N_{ads}	Number of molecules adsorbed
(o)	Old configuration
P	Pressure
P_i	Probability of finding a particular microstate i in an ensemble
$P_{k,N}$	Probability of encountering a microstate k with N particles
P_{ref}	Reference pressure
q	Matrix of all momenta
q_i	Average adsorbed concentration of component i in the crystal
q_i^*	Adsorbed concentration of component iat equilibrium
$q_{i,s}^j$	Saturation capacity of site j for comp. i
q_T	The total adsorbed concentration in the micropore
Q_i	Average adsorbed concentration of component i in the pellet
r_{eq}	Equilibrium bond length
r_{ij}	Separation distance between particles i and j
r_k	Position of molecule k
r_c	Crystal radius
r_p	Pellet radius
r_i	Position vector of molecule i
$\mathbf{s}$	Matrix of all positions
t	Time
T_f	Fluid temperature
T_{ref}	Reference temperature
T_p	Pellet temperature
T_w	Column wall temperature
T_∞	Outside temperature
T_e	Kinetic energy contribution due to the movement of electrons
T_n	Kinetic energy contribution due to the movement of nuclei
u	Velocity
U_{intra}	Intramolecular potential energy
U_{vdW}	Total dispersion energy contribution
$U_{Coulombic}$	Total Coulombic potential energy contribution
U_{bonded}	Bonded potential energy contribution

$U_{non\text{-}bonded}$	Non-bonded potential energy contribution
$U_{stretch}$	Total potential energy contribution due to bond stretching
U_{bend}	Total potential energy contribution due to angle bending
$U_{torsion}$	Total potential energy contribution due to torsional effects
U_{total}	Total potential energy of the system
U_{ext}	External heat transfer coefficient
U_f	Internal energy in the fluid phase per unit volume
U_p	Internal energy in the pellet per unit volume
$U_{p,f}$	Internal energy in the macropore per unit volume
$U_{p,s}$	Internal energy in the solid phase per unit volume
U_{sol}	internal energy per unit volume in the adsorbent
U_{ads}	Internal energy per unit in the adsorbate
$u(r_{ij})$	Interaction energy for a pair of molecules i and j
V	Unit cell volume
v	Interstitial flow velocity
V_c	Column volume
V_p	Pellet volume
V_w	Column wall volume
V_{total}	Total potential energy in first principles expressions
V_{ne}	the potential energy contributions from electron-nucleus interactions
V_{ee}	the potential energy contributions from electron-electron interactions
V_{nn}	the potential energy contributions from nucleus-nucleus interactions
X_i	Molar fraction of component i in mixture of gases
X_i	Molar fraction of component i in mixture of gases
z	Spatial dimension
Z_A	Atomic number of A

Greek Symbols

α_{wl}	Mean surface area to volume ratio of the column wall
$\alpha(o \rightarrow n)$	Probability of attempting a move
δ	Column wall thickness

ε	Bed void fraction
ε_{ij}	Interaction energy between molecules i and j at the lowest point on the Lennard-Jones potential well
ε_p	Pellet void fraction
ε_0	Permittivity in vacuum
γ_i	Partial charge of sphere i
Ξ	Partition function
λ_L	Axial thermal conductivity and the column wall thickness
Γ	Thermodynamic correction factor
Λ	de Broglie wavelength of a particle
$\Delta\mu$	Chemical potential gradient
μ	Chemical potential
μ_f	Viscosity of the fluid
Ω_{ij}	Collision integral for the Chapman-Enskog diffusivity definition
ρ	Probability distribution
$\rho(\mathbf{r})$	Electron density at a particular point, **r**
ρ_f	Fluid density
ρ_s	Solid density ρ
ρ_w	Column wall density
σ_{ij}	Separation distance between molecules i and j at the lowest point on the Lennard-Jones potential well
$\pi(o \rightarrow n)$	Transition probability
τ_{sim}	Time span of NEMD simulation
τ	Tortuosity factor
Ψ	Wave function
Ψ_{elec}	Electronic wave function
Ψ_i	Wave function for a single electron i
θ_{eq}	Equilibrium bond angle
θ	Angle between the three LJ spheres
ϕ	Dihedral angle of a chain of four bonded atoms
∇^2	Laplacian operator

Appendix A

AIMD Studies on $Mn_2(BDC)_2(BPNO)$

AIMD Simulation Details

The QUICKSTEP module[66] of the CP2K package[67] was used in order to study the atomic positions of [vac], [dmf] and [ben] frameworks over time. In CP2K, an auxiliary plane wave basis set is applied in order to model electron density, while a Gaussian basis set is used to describe wavefunctions. In this work, the AIMD simulations were carried out using the B97-D exchange correlation functional[173,174], making use of the DFT-D2 dispersion correction method developed by Grimme.[173] All atoms were represented using short range double-ζ valence plus polarization MOLOPT basis sets[119] optimized for the Goedecker-Teter-Hutter (GTH)[64,65,118] pseudopotential. A plane wave basis set energy cutoff of 300 Ry and a corresponding Gaussian basis set relative cutoff energy of 40 Ry were applied. The self-consistent field (SCF) cycles were assigned an energy convergence criteria of 1.0×10^{-6} Hartree. The AIMD simulations were carried out in the NPT ensemble, in order to maintain the pressure and temperature constant while allowing the unit cell parameters to change. The simulation cell contained 1×1×1 unit cells, and periodic boundary conditions were applied. In order to ensure that a constant grid point density was maintained despite changes in unit cell size, a reference cell of constant volume was used. This approach allowed for a more accurate calculation of Coulombic and exchange correlation energies based on a constant number of grid points. The temperature was set to 196 K and controlled using a massive Nosé-Hoover thermostat.[120] The pressure was set to 1.0 bar and a barostat coupling time constant of 300 fs was applied. The equations of motion were integrated using time steps of 0.7 fs, as well as 0.2 fs.

Structure Determination Using AIMD

The experimental results presented in Chapter 4 indicate that $Mn_2(BDC)_2(BPNO)$ adopts a relatively open pore configuration during CO_2 adsorption at 196 K and a closed pore form during CH_4 adsorption at 303 K. It is unclear, however precisely what the $[CO_2]$ configuration is, and how it is affected by temperature. AIMD is a powerful computational method, which can be used in order to elucidate structural changes in MOFs. Recently, Chen et al. made use of AIMD in order to investigate the breathing process in MIL-53(Sc) in response to temperature changes, as well as adsorption of CO_2 molecules.[127] In this work, a similar approach was adopted in order to study the [vac], [dmf] and [ben] solvent-free configurations at 196 K. Despite employing relatively lenient convergence criteria, all simulation attempts resulted in the breaking of O-N bonds after 1 – 3 ps. This effect could not be avoided by reducing the time step from 0.7 fs to 0.2 fs, or by increasing the simulation cell size from 1×1×1 to 1×2×2. In all simulations performed with a time step of 0.2 fs the energy drift was maintained below 3×10^{-5} Hartree/atom/step, and the total energy was conserved as shown in Figure 0-1.

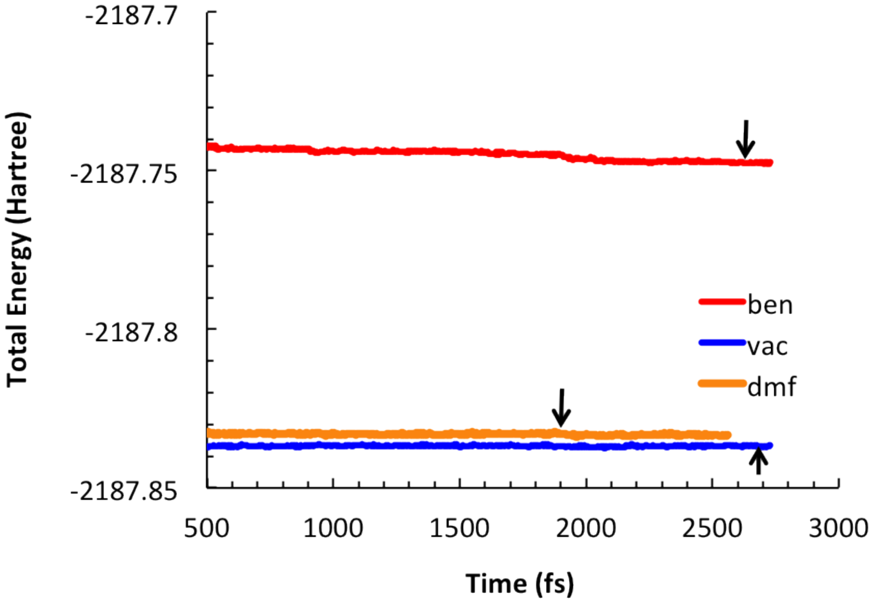

Figure 0-1: The total energy (conserved quantity) over the course of the AIMD simulations performed for [vac], [dmf] and [ben] at 196 K. Arrows are used to show the time point at which the first O-N bond break occurs.

For all three structures the observed breaking of O-N bonds was immediately followed by a relaxation of the structure towards an open pore configuration. One possible reason for this effect could be that unlike other MIL-53 structures, the $Mn_2(BDC)_2(BPNO)$ framework is strained due to the extra connections between MnO chains. The presence of BPNO linkers results in ridged rather than straight MnO chains and severe COO distortions in all $Mn_2(BDC)_2(BPNO)$ configurations.[78] The unusual μ_4-$\eta^2\eta_2$ O-N connections, initially 1.36Å in length, become strained over the course of the AIMD simulations and ultimately break as shown in Figure 0-2. It may be possible to avoid this effect by carrying out simulations with a greater number of unit cells, and a shorter time step. Unfortunately, considering the large density of atoms within each $Mn_2(BDC)_2(BPNO)$, such simulations would require an unfeasibly long computational time.

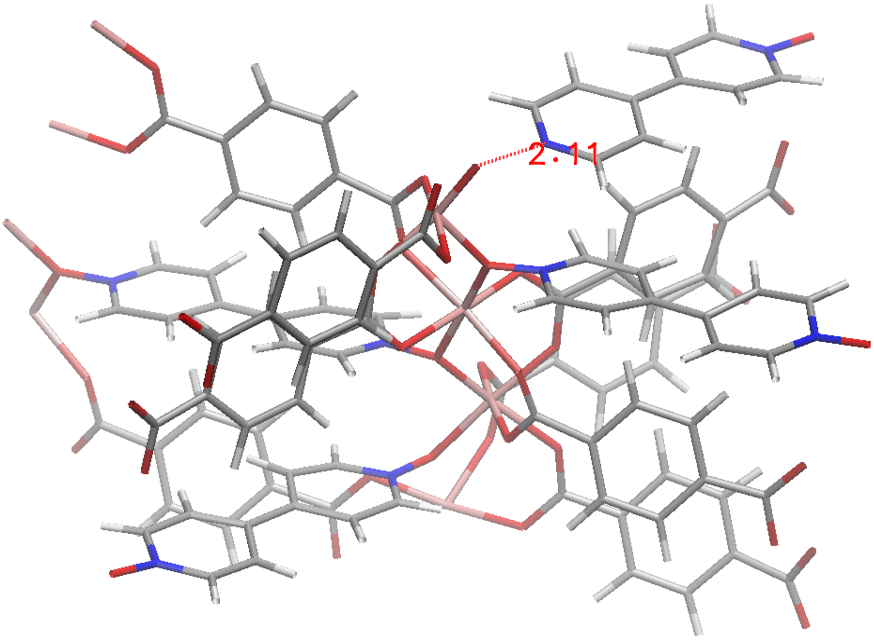

Figure 0-2: AIMD [vac] simulation cell snapshot taken at 2730 fs, showing broken O-N bond as a dashed red line. Colour index: C – dark grey, H – light grey, O – red, Mn – pink, N – blue.

Appendix B

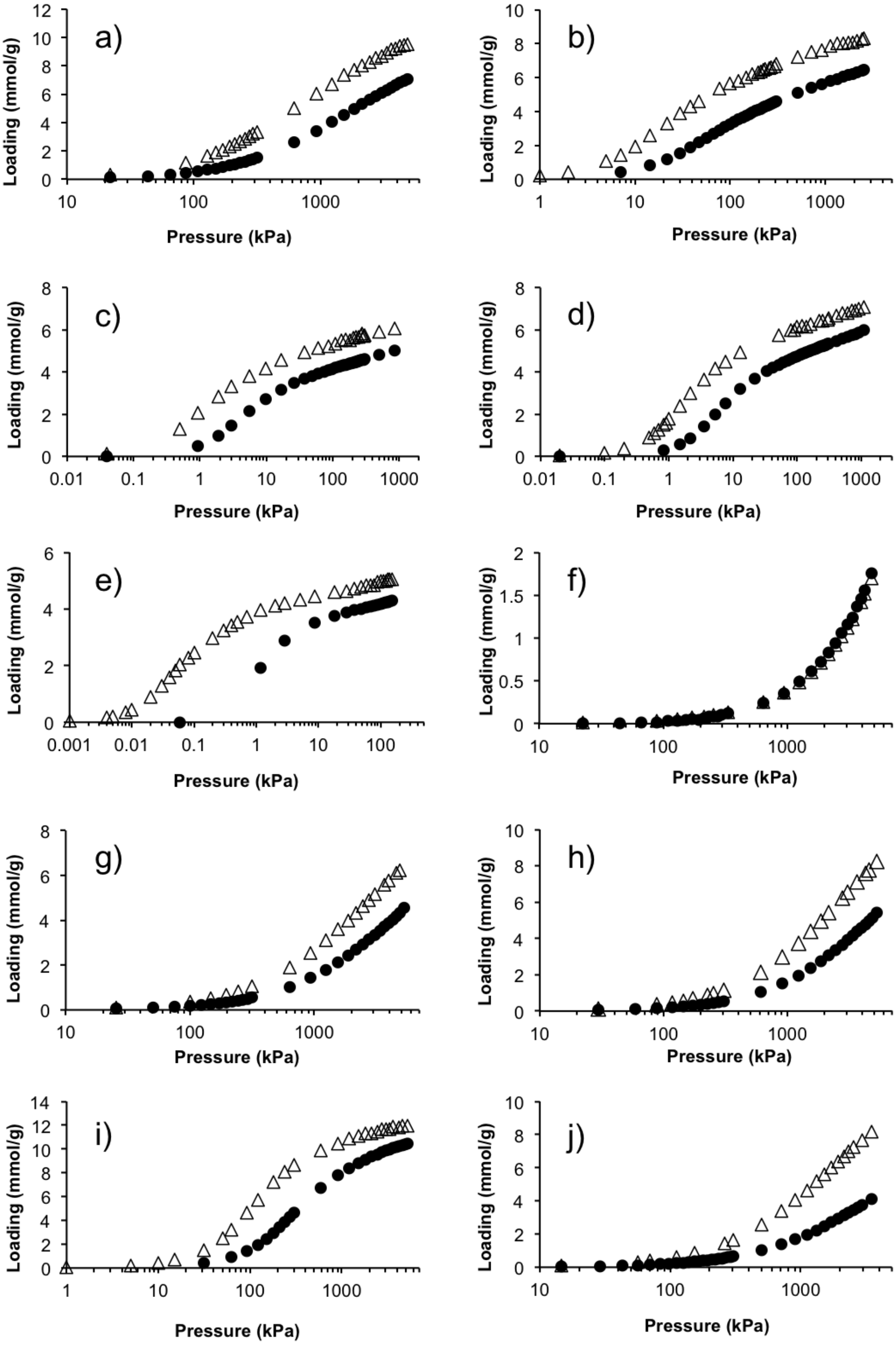

Figure B 1: UFF[40] (open triangles) and experimental (closed spheres) adsorption isotherms in MIL-47 at 303 K for a) methane, b) ethane, c) propane, d) propene, e) butane, f) hydrogen, g) nitrogen, h) oxygen, i) carbon dioxide and j) carbon monoxide.

Appendix C

MIL-47 single gas and mixture isotherm measurement

The static single component and mixture adsorption experiments were performed Sandrine Bourrelly and Phillip Llewellyn at the Université Aix-Marseille. The experiments were carried out at 303 K using a laboratory made gas dosing system connected to a commercial gravimetric adsorption device (Rubotherm Präzisionsmeßtechnik GmbH).[110-112] To obtain the single gas isotherms, the gravimetric apparatus is sufficient. However, the manometric dosing device is coupled to the gravimetric apparatus which are both associated with in situ density measurements and a gas chromatograph, to allow the study of the simultaneous adsorption of several gases.[110]

The experimental protocol starts with sample outgassing using Sample Controlled Thermal Analysis.[175] Such a protocol allows the sample to be outgassed under a controlled reduced pressure (0.02 mbar) thus avoiding problems due to inhomogeneous thermal treatment such as partial degradation. For these experiments, around 1 g of sample was treated to a maximum temperature of 473 K with a final plateau of 16 hours.

The gas mixture is introduced to the sample via a step by step procedure. At each dose, the mixture is circulated around the manifold and across the sample for at least 15 minutes in order to ensure that a homogeneous final mixture is obtained. The sample mass is then collected at 5 minutes intervals with circulation between each measurement and until equilibrium which was assumed attained when the variation of weight remains below 0.03% for 20 minutes. At equilibrium, the sample and sinker weights and the pressure are collected before extraction of a small amount of residual gas to the chromatograph. In this study, the experiments were carried out at 303 K and up to a final pressure of 25 bar. Such an experiment, without the outgassing procedure, takes around 20 hours. Thus, for each point it was possible to measure the total mass m^{tot}, the quantity adsorbed n^{tot}, the total pressure p^{tot} and the density of the gas phase. These measurements of pressure, weight and gas density allow for an estimation of the amount of each component adsorbed. For the calculations of mixture non-ideality, the NIST Refprop dataset was used,[176] and all single component and mixture uptakes are reported in absolute amounts. For the mixture adsorption calculations, a relative error of 10% can be assumed.

The pure gases and mixtures were obtained from Air Liquide, Alphagaz. The as-prepared mixtures were of Quality Crystal (2% uncertainty, Air Liquide).

Appendix D

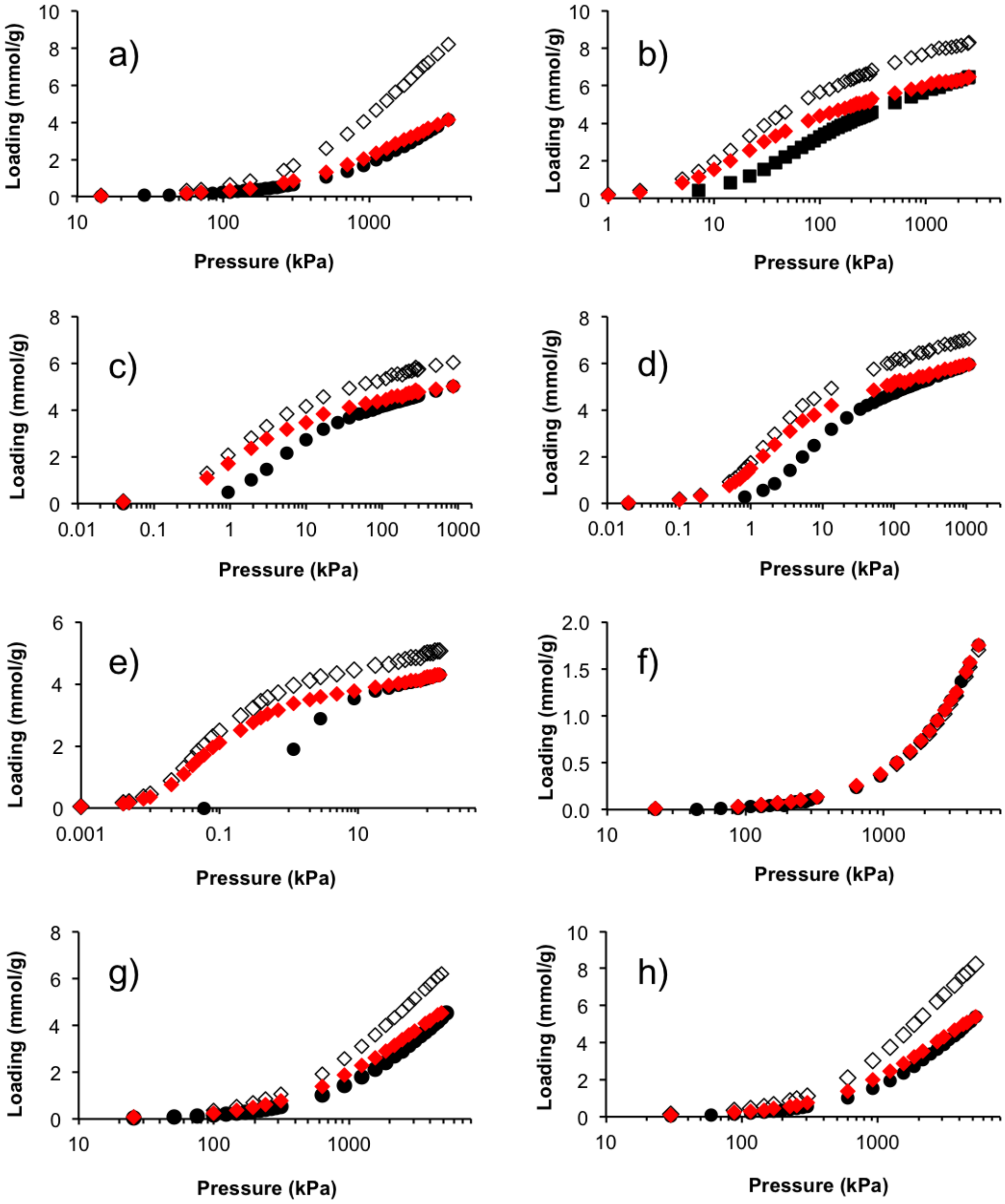

Figure D 1: Experimental (filled spheres), simulated (empty diamonds) and scaled simulated (red diamonds) adsorption isotherms in MIL-47 at 303 K for a) CO, b) C_2H_6, c) C_3H_8, d) C_3H_6, e) C_4H_{10}, f) H_2, g) N_2, and h) O_2. Scaled isotherms were obtained by multiplying the simulated adsorption amounts by a constant factor equal to the ratio between the maximum experimental and simulated uptake.

Appendix E

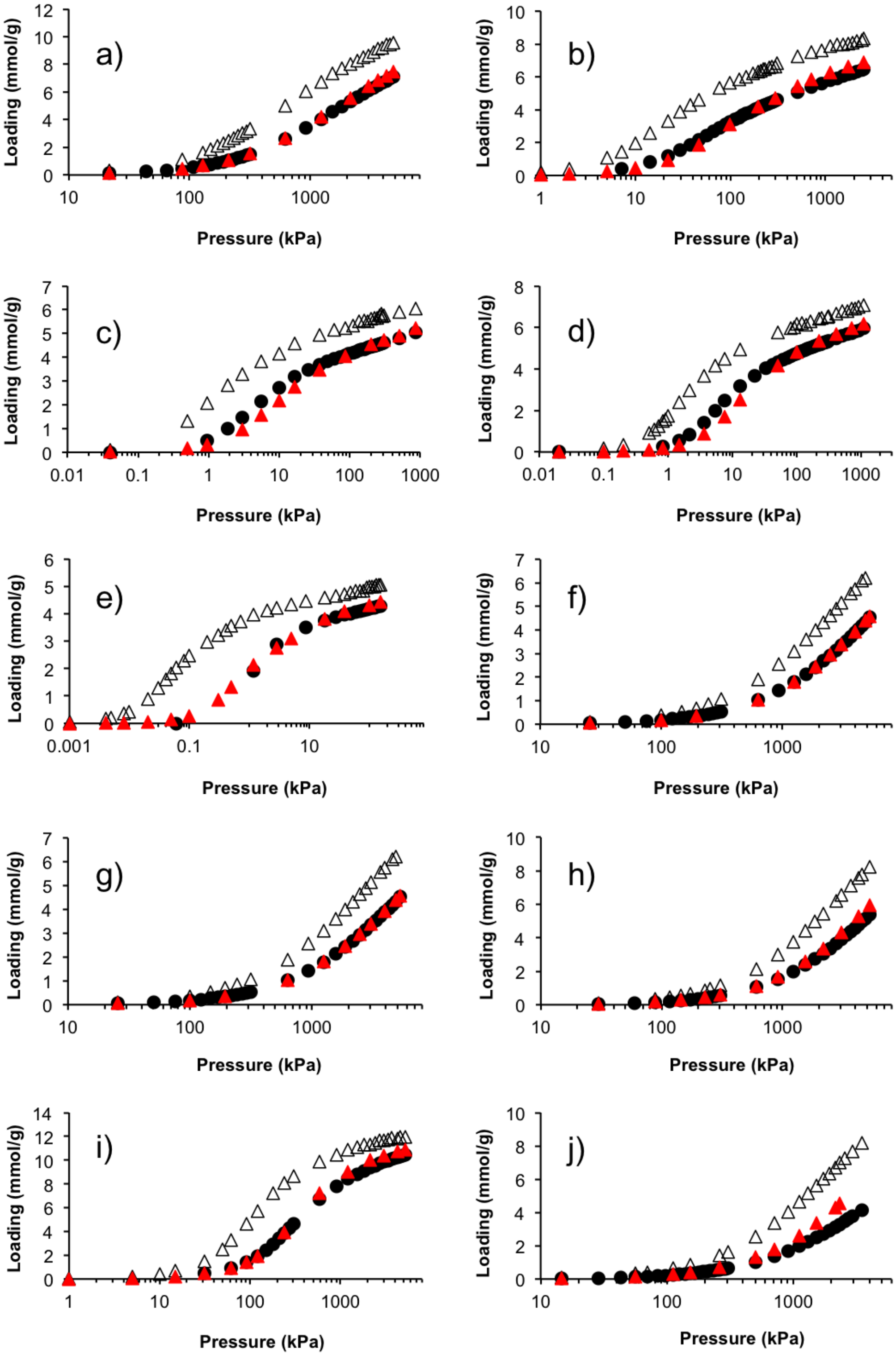

Figure E 1: UFF[40] (open triangles), UFF* (red triangles) and experimental (closed spheres) adsorption isotherms in MIL-47 at 303 K for a) CH_4, b) C_2H_6, c) C_3H_8, d) C_3H_6, e) C_4H_{10}, f) H_2, g) N_2, h) O_2, i) CO_2 and j) CO.

Appendix F

Table F 1: Dual Site Langmuir Parameters for the four MOFs

UiO-67(Zr)

Adsorbate	q^1_s	b^1	q^2_s	b^2	$-\Delta H_{ads}$
	mol/m^3	bar^{-1}	mol/m^3	bar^{-1}	kJ/mol
H_2	6346.78	4.88E-09	9383.60	6.16E-04	5.013
CO_2	6346.78	5.27E-05	9383.60	3.16E-05	20.37
CO	6346.78	1.39E-04	9383.60	1.54E-04	11.87
CH_4	6346.78	2.95E-05	9383.60	2.00E-04	14.17
N_2	6346.78	3.77E-05	9383.60	2.62E-04	10.69

Zr-Cl_2AzoBDC

Adsorbate	q^1_s	b^1	q^2_s	b^2	$-\Delta H_{ads}$
	mol/m^3	bar^{-1}	mol/m^3	bar^{-1}	kJ/mol
H_2	6191.68	1.02E-14	11857.38	5.72E-04	4.69
CO_2	6191.68	6.17E-05	11857.38	5.91E-05	17.28
CO	6191.68	4.47E-05	11857.38	1.58E-04	11.31
CH_4	6191.68	9.59E-06	11857.38	1.34E-04	13.51
N_2	6191.68	1.19E-06	11857.38	1.94E-04	10.37

UiO-66(Zr)

Adsorbate	q^1_s	b^1	q^2_s	b^2	$-\Delta H_{ads}$
	mol/m^3	bar^{-1}	mol/m^3	bar^{-1}	kJ/mol
H_2	4620.80	2.79E-04	5028.37	2.79E-04	6.75
CO_2	4620.80	2.78E-06	5028.37	3.15E-05	26.54
CO	4620.80	1.33E-05	5028.37	1.48E-04	15.89
CH_4	4620.80	1.18E-04	5028.37	1.67E-05	18.60
N_2	4620.80	1.94E-04	5028.37	1.42E-05	14.62

UiO-66(Zr)-Br

Adsorbate	q^1_s	b^1	q^2_s	b^2	$-\Delta H_{ads}$
	mol/m^3	bar^{-1}	mol/m^3	bar^{-1}	kJ/mol
H_2	3460.93	2.30E-04	4618.56	2.28E-04	7.46
CO_2	3460.93	6.85E-07	4618.56	2.47E-05	29.67
CO	3460.93	1.48E-04	4618.56	7.99E-06	18.22
CH_4	3460.93	1.37E-04	4618.56	3.15E-06	21.00
N_2	3460.93	1.59E-04	4618.56	6.29E-06	16.69

Table F 2: Dual Site Langmuir parameters for AC* and Zeolite*, the commercial adsorbents from the work of Ribeiro et al. [150]

AC*

Adsorbate	q^1_s	b^1	q^2_s	b^2	$-\Delta H_{ads}$
	mol/m^3	bar^{-1}	mol/m^3	bar^{-1}	kJ/mol
H_2	811.85	3.38E-05	3785.52	3.39E-05	12.80
CO_2	811.85	4.65E-05	3785.52	3.35E-06	29.10
CO	811.85	1.56E-05	3785.52	9.59E-06	22.60
CH_4	811.85	2.21E-04	3785.52	8.92E-06	22.70
N_2	811.85	4.91E-04	3785.52	2.13E-05	16.30

Zeolite*

Adsorbate	q^1_s	b^1	q^2_s	b^2	$-\Delta H_{ads}$
	mol/m^3	bar^{-1}	mol/m^3	bar^{-1}	kJ/mol
H_2	3888.07	1.07E-06	950.34	5.36E-04	9.23
CO_2	3888.07	2.43E-05	950.34	3.72E-07	36.00
CO	3888.07	5.87E-07	950.34	2.12E-05	29.80
CH_4	3888.07	2.08E-05	950.34	1.30E-04	20.60
N_2	3888.07	8.99E-06	950.34	1.14E-04	20.40

Table F 3: Dual Site Langmuir parameters for Calgon PCB and Single Site Langmuir parameters for Zeolite 5A.[151] Note that in the work of Ahn et al.[151] the heats of adsorption were reported with the wrong units. The units provided here are correct.

Calgon PCB

Adsorbate	q^1_s	b^1	q^2_s	b^2	$-\Delta H_{ads}$
	mol/m^3	bar^{-1}	mol/m^3	bar^{-1}	kJ/mol
H_2	5950.97	1.59E-03	1201.00	1.59E-03	12.06
CO_2	5950.97	4.61E-02	1201.00	3.57E-03	21.93
CO	5950.97	1.33E-02	1201.00	6.33E-08	18.00
CH_4	5950.97	3.04E-02	1201.00	8.23E-05	17.96
N_2	5950.97	2.39E-07	1201.00	8.33E-02	6.95

Zeolite 5A

Adsorbate	q_s	b	$-\Delta H_{ads}$
	mol/m^3	bar^{-1}	kJ/mol
H_2	2594.04	5.32E-03	11.72
CO_2	5089.04	2.86E+00	39.05
CO	2799.63	2.79E-02	22.18
CH_4	2589.98	1.95E-02	22.60
N_2	3066.76	1.10E-02	22.90

Appendix G

The simulated isotherms for CO_2 and CH_4 adsorption in UiO-66(Zr) were compared to the experimental data presented by Yang et al.[161] as shown in Figure G 1. The simulated isotherms are in good agreement with the experimental isotherms. Additional validation studies could not be carried out for the remaining MOFs due to the unavailability of experimental data.

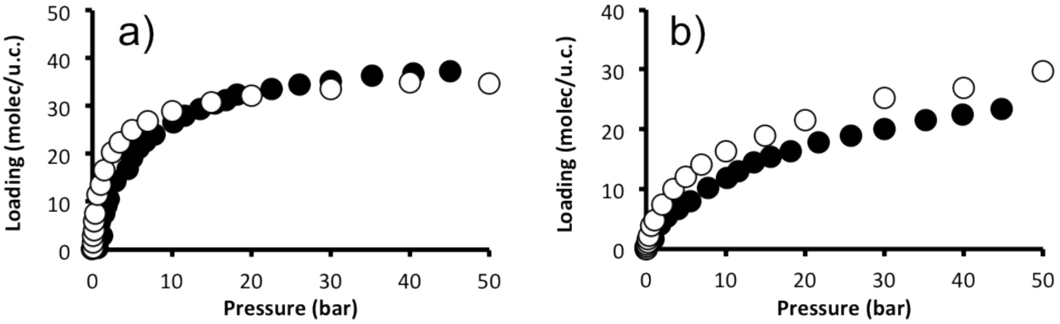

Figure G 1: Dehydroxylated UiO-66(Zr) adsorption isotherms for a) CO_2 and b) CH_4 from simulations (open spheres) and experiment (closed spheres). The experimental data is taken from the work of Yang et al.[161]

References

(1) Stocker, J.; Whysall, M.; Miller, G. Q. *30 Years of PSA Technology for Hydrogen Purification*, UOP, 1998.

(2) Yang, R. T. *Gas Separation By Adsorption Processes*; Imperial College Press: London, 1997; Vol. 1.

(3) Li, J. R.; Kuppler, R. J.; Zhou, H. C. *Chem. Soc. Rev.* **2009**, *38*, 1477.

(4) Li, J. R.; Sculley, J.; Zhou, H. C. *Chem. Rev.* **2012**, *112*, 869.

(5) Cook, T. R.; Zheng, Y. R.; Stang, P. J. *Chem. Rev.* **2013**, *113*, 734.

(6) Babarao, R.; Eddaoudi, M.; Jiang, J. W. *Langmuir* **2010**, *26*, 11196.

(7) Hirscher, M.; Panella, B.; Schmitz, B. *Microporous Mesoporous Mater.* **2010**, *129*, 335.

(8) Morris, R. E.; Wheatley, P. S. *Angew. Chem. Int. Ed.* **2008**, *47*, 4966.

(9) Yang, Q. Y.; Guillerm, V.; Ragon, F.; Wiersum, A. D.; Llewellyn, P. L.; Zhong, C. L.; Devic, T.; Serre, C.; Maurin, G. *Chem. Commun.* **2012**, *48*, 9831.

(10) Castillo, J. M.; Vlugt, T. J. H.; Calero, S. *J. Phys. Chem. C* **2009**, *113*, 20869.

(11) Herm, Z. R.; Krishna, R.; Long, J. R. *Microporous Mesoporous Mater.* **2012**, *151*, 481.

(12) Fischer, M.; Hoffmann, F.; Froba, M. *RSC Advances* **2012**, *2*, 4382.

(13) Ladrak, T.; Smulders, S.; Roubeau, O.; Teat, S. J.; Gamez, P.; Reedijk, J. *Eur. J. Inorg. Chem.* **2010**, 3804.

(14) Liu, Y.; Xuan, W. M.; Cui, Y. *Adv. Mater.* **2010**, *22*, 4112.

(15) Corma, A.; Garcia, H.; Xamena, F. *Chem. Rev.* **2010**, *110*, 4606.

(16) Lu, G.; Hupp, J. T. *J. Am. Chem. Soc.* **2010**, *132*, 7832.

(17) Kreno, L. E.; Leong, K.; Farha, O. K.; Allendorf, M.; Van Duyne, R. P.; Hupp, J. T. *Chem. Rev.* **2012**, *112*, 1105.

(18) Horcajada, P.; Gref, R.; Baati, T.; Allan, P. K.; Maurin, G.; Couvreur, P.; Ferey, G.; Morris, R. E.; Serre, C. *Chem. Rev.* **2012**, *112*, 1232.

(19) Fujita, D.; Suzuki, K.; Sato, S.; Yagi-Utsumi, M.; Kurimoto, E.; Yamaguchi, Y.; Kato, K.; Fujita, M. *Chem. Lett.* **2012**, *41*, 313.

(20) Meek, S. T.; Greathouse, J. A.; Allendorf, M. D. *Adv. Mater.* **2011**, *23*, 249.

(21) Rowsell, J. L. C.; Yaghi, O. M. *Microporous Mesoporous Mater.* **2004**, *73*, 3.

(22) James, S. L. *Chem. Soc. Rev.* **2003**, *32*, 276.

(23) Yaghi, O. M.; O'Keeffe, M.; Ockwig, N. W.; Chae, H. K.; Eddaoudi, M.; Kim, J. *Nature* **2003**, *423*, 705.

(24) Chui, S. S.-Y.; Lo, S. M.-F.; Charmant, J. P. H.; Orpen, A. G.; Williams, I. D. *Science* **1999**, *283*, 1148.

(25) 1987.

(26) Cohen, S. M. *Chem. Rev.* **2012**, *112*, 970.

(27) Ockwig, N. W.; Delgado-Friedrichs, O.; O'Keeffe, M.; Yaghi, O. M. *Accounts Chem Res* **2005**, *38*, 176.

(28) Hill, T. L. *An Introduction to Statistical Thermodynamics*; Dover Publications: Mineola, NY, USA, 1987.

(29) Frenkel, D.; Smit, B. *Understanding Molecular Simulation: From Algorithms to Applications*; 2nd edition ed.; Academic Press: San Diego, 2002.

(30) Allen, M. P.; Tildesley, D. J. *Computer Simulation of Liquids*; Clarendon Press: Oxford, UK, 1987.

(31) Metropolis, N.; Rosenbluth, A. W.; Rosenbluth, M. N.; Teller, A. H.; Teller, E. *J. Chem. Phys.* **1953**, *21*, 1087.

(32) Peng, D.-Y.; Robinson, D. B. *Ind. Eng. Chem. Fundam.* **1976**, *15*, 59.

(33) Macedonia, M. D.; Maginn, E. J. *Mol. Phys.* **1999**, *96*, 1375.

(34) Haile, J. M. *Molecular Dynamics Simulation: Elementary Methods* John Wiley & Sons, Inc.: Canada, 1992.

(35) Rapaport, D. C. *The Art of Molecular Dynamics Simulation*; Cambridge University Press: Cambridge, 1995.

(36) Arya, G.; Chang, H. C.; Maginn, E. J. *J. Chem. Phys.* **2001**, *115*, 8112.

(37) Chempath, S.; Krishna, R.; Snurr, R. Q. *J. Phys Chem. B* **2004**, *108*, 13481.

(38) Williams, J. J.; Seaton, N. A.; Düren, T. *J. Phys. Chem. C* **2011**, *115*, 10651.

(39) Skoulidas, A. I.; Sholl, D. S.; Krishna, R. *Langmuir* **2003**, *19*, 7977.

(40) Rappe, A. K.; Casewit, C. J.; Colwell, K. S.; Goddard, W. A.; Skiff, W. M. *J. Am. Chem. Soc.* **1992**, *114*, 10024.

(41) Mayo, S. L.; Olafson, B. D.; Goddard, W. A. *J. Phys. Chem.* **1990**, *94*, 8897.

(42) Jorgensen, W. L.; Maxwell, D. S.; Tirado-Rives, J. *J. Am. Chem. Soc.* **1996**, *118*, 11225.

(43) Martin, M. G.; Siepmann, J. I. *J. Phys. Chem. B* **1998**, *102*, 2569.

(44) Wick, C. D.; Martin, M. G.; Siepmann, J. I. *J. Phys. Chem. B* **2000**, *104*, 8008.

(45) Yang, Q. Y.; Zhong, C. L. *J. Phys. Chem. B* **2005**, *109*, 11862.

(46) Karra, J. R.; Walton, K. S. *Langmuir* **2008**, *24*, 8620.

(47) Potoff, J. J.; Siepmann, J. I. *Aiche J.* **2001**, *47*, 1676.

(48) Piper, J.; Morrison, J. A.; Peters, C. *Mol. Phys.* **1984**, *53*, 1463.

(49) Martín-Calvo, A.; Lahoz-Martín, F. D.; Calero, S. *J. Phys. Chem. C* **2012**, *116*, 6655.

(50) Chen, B.; Potoff, J. J.; Siepmann, J. I. *J. Phys. Chem. B* **2001**, *105*, 3093.

(51) McQuarrie, D. A. *Quantum Chemistry*; University Science Books: Mill Valley, CA, 1983.

(52) Scholl, D. S.; Steckel, J. A. *Density Functional Theory: A Practical Introduction*; John Wiley & Sons Inc.: Hoboken, New Jersey, 2009.

(53) Born, M.; Oppenheimer, R. *Ann. Phys.* **1927**, *84*, 0457.

(54) Atkins, P. W.; Friedman, R. S. *Molecular Quantum Mechanics*; Oxford University Press: Oxford, UK, 1997.

(55) Hohenberg, P.; Kohn, W. *Physical Review B* **1964**, *136*, B864.

(56) Kohn, W.; Sham, L. J. *Physical Review* **1965**, *140*, 1133.

(57) Martin, R. M. *Electronic Structure: Basic Theory and Practical Methods*; Cambridge University Press: Cambridge, UK, 2004.

(58) Parr, R. G.; Yang, W. *Density-Functional Theory of Atoms and Molecules*; Oxford University Press: Oxford, UK, 1989.

(59) Becke, A. D. *Physical Review A* **1988**, *38*, 3098.

(60) Lee, C.; Yang, W.; Parr, R. G. *Physical Review B* **1988**, *37*, 785.

(61) Miehlich, B.; Savin, A.; Stoll, H.; Preuss, H. *Chem Phys Lett* **1989**, *157*, 200.

(62) Perdew, J. P.; Burke, K.; Ernzerhof, M. *Phys. Rev. Lett.* **1996**, *77*, 3865.

(63) Perdew, J. P. *Physical Review B* **1986**, *33*, 8822.

(64) Goedecker, S.; Teter, M.; Hutter, J. *Physical Review B* **1996**, *54*, 1703.

(65) Hartwigsen, C.; Goedecker, S.; Hutter, J. *Physical Review B* **1998**, *58*, 3641.

(66) VandeVondele, J.; Krack, M.; Mohamed, F.; Parrinello, M.; Chassaing, T.; Hutter, J. *Comput. Phys. Commun.* **2005**, *167*, 103.

(67) .

(68) Lippert, G.; Hutter, J.; Parrinello, M. *Mol. Phys.* **1997**, *92*, 477.

(69) Herm, Z. R.; Swisher, J. A.; Smit, B.; Krishna, R.; Long, J. R. *J. Am. Chem. Soc.* **2011**, *133*, 5664.

(70) Eddaoudi, M.; Kim, J.; Rosi, N.; Vodak, D.; Wachter, J.; O'Keeffe, M.; Yaghi, O. M. *Science* **2002**, *295*, 469.

(71) Frost, H.; Düren, T.; Snurr, R. Q. *J. Phys. Chem. B* **2006**, *110*, 9565.

(72) Liu, B.; Yang, Q.; Xue, C.; Zhong, C.; Chen, B.; Smit, B. *J. Phys. Chem. C* **2008**, *112*, 9854.

(73) Liu, B.; Smit, B. *Langmuir* **2009**, *25*, 5918.

(74) Bae, Y.-S.; Farha, O. K.; Hupp, J. T.; Snurr, R. Q. *J Mater Chem* **2009**, *19*, 2131.

(75) Gelb, L. D.; Gubbins, K. E. *Langmuir* **1999**, *15*, 305.

(76) Rosi, N. L.; Kim, J.; Eddaoudi, M.; Chen, B. L.; O'Keeffe, M.; Yaghi, O. M. *J. Am. Chem. Soc.* **2005**, *127*, 1504.

(77) Barthelet, K.; Marrot, J.; Riou, D.; Férey, G. *Angewandte Chemie-International Edition* **2002**, *41*, 281.

(78) Xu, G.; Zhang, X.; Guo, P.; Pan, C.; Zhang, H.; Wang, C. *J. Am. Chem. Soc.* **2010**, *132*, 3656.

(79) Gupta, A.; Chempath, S.; Sanborn, M. J.; Clark, L. A.; Snurr, R. Q. *Mol. Simul.* **2003**, *29*, 29.

(80) Ma, S. Q.; Sun, D. F.; Simmons, J. M.; Collier, C. D.; Yuan, D. Q.; Zhou, H. C. *J. Am. Chem. Soc.* **2008**, *130*, 1012.

(81) Dietzel, P. D. C.; Morita, Y.; Blom, R.; Fjellvåg, H. *Angew. Chem. Int. Ed.* **2005**, *44*, 6354.

(82) Férey, G.; Serre, C.; Mellot-Draznieks, C.; Millange, F.; Surblé, S.; Dutour, J.; Margiolaki, I. *Angew. Chem. Int. Ed.* **2004**, *43*, 6296.

(83) Ramsahye, N. A.; Maurin, G.; Bourrelly, S.; Llewellyn, P. L.; Devic, T.; Serre, C.; Loiseau, T.; Férey, G. *Adsorption* **2007**, *13*, 461.

(84) Yang, Q.; Zhong, C.; Chen, J.-F. *J. Phys. Chem. C* **2008**, *112*, 1562.

(85) Yazaydin, A. O.; Snurr, R. Q.; Park, T.-H.; Koh, K.; Liu, J.; LeVan, M. D.; Benin, A. I.; Jakubczak, P.; Lanuza, M.; Galloway, D. B.; Low, J. J.; Willis, R. R. *J. Am. Chem. Soc.* **2009**, *131*, 18198.

(86) Xu, Q.; Zhong, C. L. *J. Phys. Chem. C* **2010**, *114*, 5035.

(87) Vuong, T.; Monson, P. A. *Langmuir* **1996**, *12*, 5425.

(88) Frost, H.; Snurr, R. Q. *J. Phys. Chem. C* **2007**, *111*, 18794.

(89) Ockwig, N. W.; Delgado-Friedrichs, O.; O'Keeffe, M.; Yaghi, O. M. *Accounts Chem Res* **2005**, *38*, 176.

(90) Tranchemontagne, D. J.; Mendoza-Cortés, J. L.; O'Keeffe, M.; Yaghi, O. M. *Chem. Soc. Rev.* **2009**, *38*, 1257.

(91) O'Keeffe, M.; Peskov, M. A.; Ramsden, S. J.; Yaghi, O. M. *Accounts Chem Res* **2008**, *41*, 1782.

(92) Wiersum, A. D.; Chang, J.-S.; Serre, C.; Llewellyn, P. L. *Langmuir* **2013**, *29*, 3301.

(93) Maring, B. J.; Webley, P. A. *International Journal of Greenhouse Gas Control* **2013**, *15*, 16.

(94) Frisch, M. J.; Trucks, G. W.; Schlegel, H. B.; Scuseria, G. E.; Robb, M. A.; Cheeseman, J. R.; J. A. Montgomery, J.; T. Vreven, K. N. K.; Burant, J. C.; Millam, J. M.; Iyengar, S. S.; Tomasi, J.; Barone, V.; Mennucci, B.; Cossi, M.; Scalmani, G.;

Rega, N.; Petersson, G. A.; Nakatsuji, H.; Hada, M.; Ehara, M.; Toyota, K.; Fukuda, R.; Hasegawa, J.; Ishida, M.; Nakajima, T.; Honda, Y.; Kitao, O.; H. Nakai; Klene, M.; Li, X.; Knox, J. E.; Hratchian, H. P.; Cross, J. B.; Bakken, V.; Adamo, C.; Jaramillo, J.; Gomperts, R.; Stratmann, R. E.; Yazyev, O.; Austin, A. J.; Cammi, R.; Pomelli, C.; Ochterski, J. W.; Ayala, P. Y.; Morokuma, K.; Voth, G. A.; Salvador, P.; Dannenberg, J. J.; Zakrzewski, V. G.; Dapprich, S.; Daniels, A. D.; Strain, M. C.; Farkas, O.; Malick, D. K.; Rabuck, A. D.; Raghavachari, K.; Foresman, J. B.; Ortiz, J. V.; Cui, Q.; Baboul, A. G.; Clifford, S.; Cioslowski, J.; Stefanov, B. B.; Liu, G.; A. Liashenko; Piskorz, P.; Komaromi, I.; Martin, R. L.; Fox, D. J.; Keith, T.; Al-Laham, M. A.; Peng, C. Y.; Nanayakkara, A.; Challacombe, M.; Gill, P. M. W.; Johnson, B.; Chen, W.; Wong, M. W.; Gonzalez, C.; Pople, J. A.; Revision E.01 ed.; Gaussian, Inc.: Wallingford CT, 2004.

(95) Sarkisov, L.; Harrison, A. *Mol. Simul.* **2011**, *37*, 1248.

(96) Llewellyn, P. L.; Horcajada, P.; Maurin, G.; Devic, T.; Rosenbach, N.; Bourrelly, S.; Serre, C.; Vincent, D.; Loera-Serna, S.; Filinchuk, Y.; Férey, G. *J. Am. Chem. Soc.* **2009**, *131*, 13002.

(97) Devic, T.; Salles, F.; Bourrelly, S.; Moulin, B.; Maurin, G.; Horcajada, P.; Serre, C.; Vimont, A.; Lavalley, J.-C.; Leclerc, H.; Clet, G.; Daturi, M.; Llewellyn, P. L.; Filinchuk, Y.; Ferey, G. *J Mater Chem* **2012**, *22*, 10266.

(98) Espinal, L.; Wong-Ng, W.; Kaduk, J. A.; Allen, A. J.; Snyder, C. R.; Chiu, C.; Siderius, D. W.; Li, L.; Cockayne, E.; Espinal, A. E.; Suib, S. L. *J. Am. Chem. Soc.* **2012**, *134*, 7944.

(99) Rosenbach, N.; Ghoufi, A.; Deroche, I.; Llewellyn, P. L.; Devic, T.; Bourrelly, S.; Serre, C.; Férey, G.; Maurin, G. *Phys. Chem. Chem. Phys.* **2010**, *12*, 6428.

(100) Fairen-Jimenez, D.; Lozano-Casal, P.; Düren, T. In *Characterisation of Porous Solids Viii*; Kaskel, S., Llewellyn, P., RodriguezReinoso, F., Seaton, N. A., Eds.; Royal Soc Chemistry: Cambridge, 2009, p 80.

(101) Surblé, S.; Millange, F.; Serre, C.; Düren, T.; Latroche, M.; Bourrelly, S.; Llewellyn, P. L.; Férey, G. *J. Am. Chem. Soc.* **2006**, *128*, 14889.

(102) Dubbeldam, D.; Frost, H.; Walton, K. S.; Snurr, R. Q. *Fluid Phase Equilib.* **2007**, *261*, 152.

(103) Düren, T.; Bae, Y. S.; Snurr, R. Q. *Chem. Soc. Rev.* **2009**, *38*, 1237.

(104) Sagara, T.; Klassen, J.; Ganz, E. *J. Chem. Phys.* **2004**, *121*, 12543.

(105) Déroche, I.; Rives, S.; Trung, T.; Yang, Q.; Ghoufi, A.; Ramsahye, N. A.; Trens, P.; Fajula, F.; Devic, T.; Serre, C.; Férey, G.; Jobic, H.; Maurin, G. *J. Phys. Chem. C* **2011**, *115*, 13868.

(106) Hamon, L.; Leclerc, H.; Ghoufi, A.; Oliviero, L.; Travert, A.; Lavalley, J. C.; Devic, T.; Serre, C.; Férey, G.; De Weireld, G.; Vimont, A.; Maurin, G. *J. Phys. Chem. C* **2011**, *115*, 2047.

(107) Salles, F.; Jobic, H.; Devic, T.; Llewellyn, P. L.; Serre, C.; Férey, G. r.; Maurin, G. *ACS Nano* **2009**, *4*, 143.

(108) Salles, F.; Kolokolov, D. I.; Jobic, H.; Maurin, G.; Llewellyn, P. L.; Devic, T.; Serre, C.; Férey, G. *J. Phys. Chem. C* **2009**, *113*, 7802.

(109) Babarao, R.; Dai, S.; Jiang, D.-e. *J. Phys. Chem. C* **2011**, *115*, 8126.

(110) Ghoufi, A.; Gaberova, L.; Rouquerol, J.; Vincent, D.; Llewellyn, P. L.; Maurin, G. *Microporous Mesoporous Mater.* **2009**, *119*, 117.

(111) De Weireld, G.; Frère, M.; Jadot, R. *Meas. Sci. Technol.* **1999**, *10*, 117.

(112) Dreisbach, F. S., R.; Losch, H.W. Fundamental of Adsorption 7, 255, 2002. In *Fundamental of Adsorption 7* 2002, p 255.

(113) Ewald, P. P. *Ann. Phys.* **1921**, *369*, 253.

(114) Myers, A. L.; Prausnitz, J. M. *Aiche J.* **1965**, *11*, 121.

(115) Jensen, C. R. C.; Seaton, N. A. *Langmuir* **1996**, *12*, 2866.

(116) Do, D. D. *Adsorption Analysis: Equilibria and Kinetics*; Imperial College Press: London, 1998; Vol. 2.

(117) Grimme, S.; Antony, J.; Ehrlich, S.; Krieg, H. *The Journal of Chemical Physics* **2010**, *132*, 154104.

(118) Krack, M. *Theor. Chem. Acc.* **2005**, *114*, 145.

(119) VandeVondele, J.; Hutter, J. *The Journal of Chemical Physics* **2007**, *127*, 114105.

(120) Martyna, G. J.; Klein, M. L.; Tuckerman, M. *The Journal of Chemical Physics* **1992**, *97*, 2635.

(121) Yang, Q. Y.; Zhong, C. L. *ChemPhysChem* **2006**, *7*, 1417.

(122) Llewellyn, P., MIL47 publication.

(123) Kolokolov, D. I.; Jobic, H.; Stepanov, A. G.; Guillerm, V.; Devic, T.; Serre, C.; Férey, G. *Angew. Chem. Int. Ed.* **2010**, *49*, 4791.

(124) Yot, P. G.; Ma, Q. T.; Haines, J.; Yang, Q. Y.; Ghoufi, A.; Devic, T.; Serre, C.; Dmitriev, V.; Ferey, G.; Zhong, C. L.; Maurin, G. *Chemical Science* **2012**, *3*, 1100.

(125) Wang, X.; Eckert, J.; Liu, L.; Jacobson, A. J. *Inorg. Chem.* **2011**, *50*, 2028.

(126) Brehm, M.; Kirchner, B. *J Chem Inf Model* **2011**, *51*, 2007.

(127) Chen, L.; Mowat, J. P. S.; Fairen-Jimenez, D.; Morrison, C. A.; Thompson, S. P.; Wright, P. A.; Düren, T. *J. Am. Chem. Soc.* **2013**.

(128) Bae, Y.-S.; Snurr, R. Q. *Angew. Chem. Int. Ed.* **2011**, *50*, 11586.

(129) Miller, S. R.; Wright, P. A.; Serre, C.; Loiseau, T.; Marrot, J.; Ferey, G. *Chem. Commun.* **2005**, *0*, 3850.

(130) Perles, J.; Iglesias, M.; Martin-Luengo, M. A.; Monge, M. A.; Ruiz-Valero, C.; Snejko, N. *Chem. Mat.* **2005**, *17*, 5837.

(131) Miller, S. R.; Wright, P. A.; Devic, T.; Serre, C.; Férey, G. r.; Llewellyn, P. L.; Denoyel, R.; Gaberova, L.; Filinchuk, Y. *Langmuir* **2009**, *25*, 3618.

(132) Mowat, J. P. S.; Miller, S. R.; Griffin, J. M.; Seymour, V. R.; Ashbrook, S. E.; Thompson, S. P.; Fairen-Jimenez, D.; Banu, A.-M.; Düren, T.; Wright, P. A. *Inorg. Chem.* **2011**, *50*, 10844.

(133) Graham, A. J.; Banu, A. M.; Düren, T.; Greenaway, A.; McKellar, S. C.; Mowat, J. P. S.; Ward, K.; Wright, P. A.; Moggach, S. A. *Manuscript in Progress* **2013**.

(134) Dubbeldam, D.; Calero, S.; Ellis, D. E.; Snurr, R. Q. In *RASPA 1.0* Northwestern University, Evanston IL, 2008.

(135) Graham, A. J.; Allan, D. R.; Muszkiewicz, A.; Morrison, C. A.; Moggach, S. A. *Angew. Chem. Int. Ed.* **2011**, *50*, 11138.

(136) Moggach, S. A.; Bennett, T. D.; Cheetham, A. K. *Angew. Chem.* **2009**, *121*, 7221.

(137) Fairen-Jimenez, D.; Moggach, S. A.; Wharmby, M. T.; Wright, P. A.; Parsons, S.; Düren, T. *J. Am. Chem. Soc.* **2011**, *133*, 8900.

(138) Chapman, K. W.; Halder, G. J.; Chupas, P. J. *J. Am. Chem. Soc.* **2008**, *130*, 10524.

(139) Liu, K.; Song, C.; Subramani, V. *Hydrogen and Syngas Production and Purification Technologies*; American Institute of Chemical Engineers; John Wiley and Sons, Inc. : Hoboken, New Jersey, 2010.

(140) Golden, T. C.; Kumar, R.; Kratz, W. C. 1990; Vol. US Patent 4957514.

(141) Plee, D. 2002; Vol. United States Patent 6464756.

(142) Le Bec, R. 2005; Vol. US Patent 6849106.

(143) Bomard, O.; Jutard, J.; Moreau, S.; Vigor, X. 1997; Vol. WO 97/45363.

(144) Lee, C. H.; Yang, J. Y.; Ahn, H. W. *Aiche J.* **1999**, *45*, 535.

(145) Sircar, S.; Golden, T. C. *Sep. Sci. Technol.* **2000**, *35*, 667.

(146) Krishna, R.; Long, J. R. *J. Phys. Chem. C* **2011**, *115*, 12941.

(147) Ho, M. T.; Allinson, G. W.; Wiley, D. E. *Ind. Eng. Chem. Res.* **2008**, *47*, 4883.

(148) Kumar, R. *Ind. Eng. Chem. Res.* **1994**, *33*, 1600.

(149) Friedrich, D.; Ferrari, M.-C.; Brandani, S. *Ind. Eng. Chem. Res.* **2013**.

(150) Ribeiro, A. M.; Grande, C. A.; Lopes, F. V. S.; Loureiro, J. M.; Rodrigues, A. E. *Chem. Eng. Sci.* **2008**, *63*, 5258.

(151) Ahn, S.; You, Y.-W.; Lee, D.-G.; Kim, K.-H.; Oh, M.; Lee, C.-H. *Chem. Eng. Sci.* **2012**, *68*, 413.

(152) Lopes, F. V. S.; Grande, C. A.; Rodrigues, A. E. *Chem. Eng. Sci.* **2011**, *66*, 303.

(153) Ahn, H.; Lee, C. H.; Seo, B.; Yang, J.; Baek, K. *Adsorption* **1999**, *5*, 419.

(154) Ahn, H.; Yang, J.; Lee, C. H. *Adsorption* **2001**, *7*, 339.

(155) Wu, H. H.; Yao, K. X.; Zhu, Y. H.; Li, B. Y.; Shi, Z.; Krishna, R.; Li, J. *J. Phys. Chem. C* **2012**, *116*, 16609.

(156) Cavka, J. H.; Jakobsen, S.; Olsbye, U.; Guillou, N.; Lamberti, C.; Bordiga, S.; Lillerud, K. P. *J. Am. Chem. Soc.* **2008**, *130*, 13850.

(157) Wu, H.; Yildirim, T.; Zhou, W. *J. Phys. Chem. Lett.* **2013**, *4*, 925.

(158) Biswas, S.; Van der Voort, P. *Eur. J. Inorg. Chem.* **2013**, 2154.

(159) Lopes, F. V. S.; Grande, C. A.; Ribeiro, A. M.; Loureiro, J. M.; Evaggelos, O.; Nikolakis, V.; Rodrigues, A. E. *Sep. Sci. Technol.* **2009**, *44*, 1045.

(160) Jee, J. G.; Kim, M. B.; Lee, C. H. *Ind. Eng. Chem. Res.* **2001**, *40*, 868.

(161) Yang, Q.; Wiersum, A. D.; Llewellyn, P. L.; Guillerm, V.; Serre, C.; Maurin, G. *Chem. Commun.* **2011**, *47*, 9603.

(162) Yang, Q.; Wiersum, A. D.; Jobic, H.; Guillerm, V.; Serre, C.; Llewellyn, P. L.; Maurin, G. *J. Phys. Chem. C* **2011**, *115*, 13768.

(163) Hess, B.; Kutzner, C.; van der Spoel, D.; Lindahl, E. *J. Chem. Theory Comput.* **2008**, *4*, 435.

(164) Banu, A.-M.; Friedrich, D.; Brandani, S.; Düren, T. *Ind. Eng. Chem. Res.* **2013**, *52*, 9946.

(165) Mu, B.; Walton, K. S. *J. Phys. Chem. C* **2011**, *115*, 22748.

(166) Brandani, F.; Ruthven, D. *Ind. Eng. Chem. Res.* **2003**, *42*, 1462.

(167) Ahn, H.; Yoo, H. K.; Shul, Y.; Hyun, S.; Lee, C. H. *J. Chem. Eng. Jpn.* **2002**, *35*, 334.

(168) Bird, R. B.; Stewart, W. E.; Lightfoot, E. N. *Transport Phenomena*; second ed.; Wiley International: Singapore, 2002.

(169) Ruthven, D. M.; Loughlin, K. F. *Can. J. Chem. Eng.* **1972**, *50*, 550.

(170) Schaate, A.; Roy, P.; Godt, A.; Lippke, J.; Waltz, F.; Wiebcke, M.; Behrens, P. *Chem. Eur. J.* **2011**, *17*, 6643.

(171) Düren, T.; Sarkisov, L.; Yaghi, O. M.; Snurr, R. Q. *Langmuir* **2004**, *20*, 2683.

(172) *CGA G-5.3 Commodity Specification for Hydrogen*; The Compressed Gas Association Inc., 2004.

(173) Grimme, S. *Journal of Computational Chemistry* **2006**, *27*, 1787.

(174) Becke, A. D. *J. Chem. Phys.* **1997**, *107*, 8554.

(175) Rouquerol, J. *Thermochim. Acta* **1989**, *144*, 209.

(176) NIST In *NIST Reference Fluid Thermodynamic and Transport Properties Database (REFPROP)*.